

TECHNICAL REPORTS OF THE METEOROLOGICAL RESEARCH INSTITUTE No. 28

**DESCRIPTION OF A NONHYDROSTATIC MODEL  
DEVELOPED AT THE FORECAST RESEARCH DEPARTMENT  
OF THE MRI**

BY

**Motohki IKAWA and Kazuo SAITO**

気象研究所技術報告

第28号

気象研究所・予報研究部で開発された  
非静水圧モデル

猪川元興・斉藤和雄

気 象 研 究 所

METEOROLOGICAL RESEARCH INSTITUTE, JAPAN

DECEMBER 1991

# Meteorological Research Institute

Established in 1946

Director-General: Mr. Toshiyoshi Tada

Forecast Research Department	Director: Mr. Ryuji Hasegawa
Climate Research Department	Director: Mr. Harushige Koga
Typhoon Research Department	Director: Mr. Shin Ohtsuka
Physical Meteorology Research Department	Director: Mr. Takenori Noumi
Applied Meteorology Research Department	Director: Dr. Koji Shigehara
Meteorological Satellite and Observation System Research Department	Director: Mr. Toyoaki Tanaka
Seismology and Volcanology Research Department	Director: Dr. Masaaki Seino
Oceanographical Research Department	Director: Mr. Masatake Kikuchi
Geochemical Research Department	Director: Mr. Toshiyoshi Tada

1-1 Nagamine, Tsukuba, Ibaraki, 305 Japan

## Technical Reports of the Meteorological Research Institute

Editor-in-chief: Masatake Kikuchi

Editors:	Yukio Misumi	Isamu Yagai	Masahiro Hara
	Shigeru Chubachi	Takahisa Kobayashi	Hiroshi Nirasawa
	Hidemichi Ito	Hiroshi Ishizaki	Yoshimi Suzuki
Managing Editors:	Yoshitsugu Nagasawa	Yukihisa Nakajima	

The *Technical Reports of the Meteorological Research Institute* has been issued at irregular intervals by the Meteorological Research Institute since 1978 as a medium for the publication of survey articles, technical reports, data reports and review articles on meteorology, oceanography, seismology and related geosciences, contributed by the members of the Meteorological Research Institute.

The Editing Committee reserves the right of decision of acceptability of manuscripts and is responsible for the final editing.

---

© 1991 by the Meteorological Research Institute.

The copyright of articles in this journal belongs to the Meteorological Research Institute (MRI). Permission is granted to use figures, tables and short quotes from articles in this journal, provided that the source is acknowledged. Republication, reproduction, translation, and other uses of any extent of articles in this journal, that are not for personal use in research, study, or teaching, require permission from the MRI.

## 序

本報告には、気象研究所予報研究部の猪川元興主任研究官により1980年に開発が始められ、1988年から斉藤和雄研究官が開発に参加して作成された、非静水圧モデルが記述されており、これは10年にわたるモデル開発の集大成である。

今日、日本の天気予報のベースになっている数値予報モデルは、鉛直方向に静力学近似を行ったプリミティブ方程式を用いており、これは総観規模の現象を主対象としたものである。

プリミティブ方程式は高周波内部重力波（音波）を解として持たないので、時間積分のステップが長くとも、計算時間の節約ができるという利点がある。しかし、静力学近似は小さいスケールでは低周波内部重力波を正確に表現できないため、数 km 程度の小スケールの現象、例えば山岳波等を扱う場合には、静力学近似をしない方程式を用いることが望ましい。

近年、電子計算機の進展に伴い、数値モデルも格子間隔や鉛直方向の層を細かくとり、小さいスケールの現象も取り扱えるモデルが実用化されてきている。そして、今や、メソβスケールの現象についてもかなりよく表現できるようになってきた。

しかし、静水圧モデルで更に細かい現象を取り扱うモデルに発展させるには限界がある。これを打開するものとして、非静水圧モデルの開発が期待されるところである。

このような背景のもとに、本報告で述べられたモデルは、2つの目標をもって開発された。

一つは研究の道具として使用するため、対流雲の数値実験や山越え気流の数値実験として実行された。もう一つは、局地的な天気予報を行う将来の数値予報モデル構築への技術的情報を提供することである。

電子計算機が更に能力アップされるのに伴い、短時間、狭領域の数値予報において、近い将来、非静水圧モデルが静水圧モデルにとって変わるであろう。

すでに、イギリス気象局では非静水圧モデルが準ルーチンベースにのっており、カナダでも開発が進んでいるという。

本報告はモデルの3種のスキーム、境界条件の設定、乱流混合過程、雲物理過程のパラメタリゼーション、モデルの数値計算例、実際にモデルを走らせる場合の手法に至るまで、懇切丁寧に述べられている。

しかし、力学フレームや物理過程等について、今後、開発・改良すべき課題はまだ沢山ある。

本報告により、非静水圧モデルについての理解が深まり、開発・改良に携わる人が続き、種々の数値実験（メソモデルの構築）や今後の数値予報の展望が大きく開かれることを期待する。

最後に、本研究を実施した猪川主任研究官、斉藤研究官の功労を多とするとともに、建設的な意見・批判や有用な情報を提供して頂いた関係諸氏に心から感謝の意を表す。本研究の一層の

開発・改良にあたり今後とも御協力・御支援をお願いしたい。

平成3年7月

予報研究部長 長谷川 隆 司

## 追 記

本原稿が完成し、主執筆者の猪川主任研究官から「序」の執筆を依頼されてから、半年間が経過し、発刊が間近に迫った平成3年12月23日、突如として全く予期せぬ病（急性心不全）で猪川主任研究官が急逝された。生前、氏は健康そのものであっただけにその余りに急な鬼籍入りは今だに信じられない思いである。

研究者として脂の乗り切った時の氏の突然の逝去は気象研究所のみならず、世界の気象学の発展のためにも大きな損失であり、御遺族の深い悲しみを思うにつけ、誠に残念でならない。

非静水圧モデルの開発は氏のライフワークとも言えるもので、まさに氏が手塩にかけて畑を耕し、肥料をやり、種子を蒔き、若い樹木として育ててきたものである。今回に至るまでの道のりは決して平坦なものではなかったが、氏の持前の忍耐力と卓越した物理的・数学的センスをもってやりとおしたものであった。氏なくして、この若木を茂り実らせ立派な大樹として成長させていくことは並大抵ではないが、本稿の執筆者の一人であり、氏から直接指導を受けてきた斉藤研究官等の若い研究官がその衣鉢を継いでいくことが、氏への最大の報恩になることと信ずる。

刊行が遅れ遺稿の形になってしまい、完成本をお見せすることができなかったことを深く謝するとともに、慎んで御霊前に献げ、ここに猪川主任研究官の功労にあらためて深い敬意と哀悼の意を表し、御冥福を心よりお祈りする次第である。

平成3年12月

予報研究部長 長谷川 隆 司

# 気象研究所・予報研究部で開発された非静水圧モデル

猪川元興<sup>†</sup>・斉藤和雄<sup>†</sup>

この技術報告に書かれている非静水圧モデルは、気象研究所・予報研究部において1980年より猪川元興により開発がはじめられ、1984年山を取り扱えるように、1987年音波を包含する方程式も取り扱えるように拡張され、1988年斉藤和雄が開発に参加、1990年に一応の完成をみたものである。このモデルは、一つには研究の道具として使用するために、一つには、局地的な天気予報を行なう将来の数値予報モデル構築に対する有益な技術的情報を提供するために開発されてきた。研究の道具として、このモデルは、対流雲の数値実験（猪川他、1987；猪川、1988）や、山越え気流の数値実験（猪川・永沢、1989；猪川、1990；斉藤・猪川、1991）に使用されてきた。

電子計算機の進歩に伴い、短時間・狭領域数値予報においては、近い将来、非静水圧モデルが静水圧モデルにとってかわるであろう。ところで、非静水圧モデルの基本的計算スキームにはいくつか種類がある。このモデルでは、音波が除去された非弾性方程式（anelastic：AE）を用いる方式、音波を包含する弾性方程式を用い、水平・鉛直方向ともインプリシットに時間積分する方式（elastic-horizontally and vertically implicit：E-HI-VI）、弾性方程式を用い、水平方向にはイクスプリシットに、鉛直方向にはインプリシットに時間積分する方式（elastic-horizontally explicit-vertically implicit：E-HE-VI）が使用できて、3種のスキームが容易に相互比較できるようになっている。このモデルは3種のスキームのうち、どのスキームが将来の数値予報モデルにとって一番いいのか評価するのに便利である。

この技術報告の構成は次のようになっている。B章では、モデルの基本方程式とその差分表現が述べられる。3つのスキーム（AE、E-HI-VI、E-HE-VI）の定式化及び、その線形安定性解析がB-1～B-4で述べられる。可変格子上の気圧方程式の解法がB-6で、各種境界条件の設定の仕方が、B-7～B-9で述べられる。B-10では、乱流混合過程のパラメタリゼーションが示される。水蒸気、雲水、雨水、氷晶、雪、あられの混合比と、氷晶、雪、あられの数密度を予報変数に持つ雲物理過程のパラメタリゼーション法がB-11で述べられる。

C章では、モデルの数値計算例が示される。今まで印刷発表されてきた計算例は、ほとんど2次元の計算であったが、ここで示されるのは、3次元の計算例である。C-1では、3次元の非静水圧山岳波の線形解析解と数値解とを比較することによるモデルの検定がおこなわれる。C-2では、日本における局地風（関東地方の海陸風、四国のやまじ風）の計算例が示される。C-3では、

<sup>†</sup>気象研究所予報研究部

雲物理過程のパラメタリゼーション法の性能評価の為に行なった、冬期日本海上で発生する対流性降雪雲の数値実験結果が示される。D章、E章では、ジョブの流れ図、プログラムの流れ図、入力パラメーターの与え方、計算結果の出力法等、実際にモデルを走らせる場合に必要な事項が示される。B章にも、実際にモデルのプログラムを解説する人の便を考えて簡単な「Program Guide」が挿入されている。モデルの概要だけ知りたい読者にとってはB章の「Program Guide」とD及びE章は無視してもよい。

このモデルは多くの改良すべき点がある。力学フレームに関しては、①現在の2次のオーダーの精度から4次の精度をもつ差分法への変更、②ネスティング、③上端境界条件に放射条件を採用すること、④混成鉛直座標系（下層Z\*系、上層Z系）の導入、⑤格子点モデルからスペクトルモデルへの変更などがある。物理過程については、①雲物理過程や乱流混合過程のパラメタリゼーション法の精密化、②放射過程の導入があげられる。さらにプログラムの虫とり、高速化、省記憶容量化などがある。

これらの点の開発・改良は、もはや1人や2人の力では困難である。モデルの詳細が書かれているこの技術報告により、モデルの改良がより多くの人の協力の下で行われることになれば幸いである。又、全く新しいモデルを初めから作り上げる場合にも、この技術報告がなんらかの役に立つことを期待している。

このモデルの開発にあたり、多くの人の協力・助力を得たことに、猪川・斉藤の2人の数値モデラーは感謝したい。内田英治、片山 昭、吉田泰治、相原正彦、久保田 効、嘉味田宗治の前予報研究部長の方々、増田善信、吉住禎夫、近藤洋輝、野口晋孝の前予報研究部・第1研究室長、広瀬元孝、野本真一前第2研究室長の方々、二宮洗三現気象庁海洋気象部長、長谷川隆司現予報研究部長及び丸山健人現第1研究室長にはいろいろお世話になった。特にモデルの力学フレームに関し、相原正彦、吉崎正憲の両氏から貴重なご意見をいただいた。又、雲物理過程のパラメタリゼーション法に関しては、物理気象研究部の松尾敬世、村上正隆、水野 量の三氏にいろいろ教えていただき、建設的な批判をいただいた。水野氏には、プログラムのいくつかのバグを発見・修正していただいた。応用気象研究部の木村富士男（現東北大）、高橋俊二の両氏からは日本の地形データを提供してもらった。さらに、気象研・電子計算機の整備・改善にあたられた歴代、企画室・電計管理班の方々（杉村秀夫、畠山太郎、重久陽亮、青木寿雄、山岬正紀）、本技術報告の印刷発行の事務をしていただいた企画室・調査官、永沢義嗣氏に御礼を申し上げる。

なお、この報告のB-10節以外のB章、C-3節、D及びE章は猪川が、B-10、C-1、C-2節は斉藤が書いた。

**Description of a Nonhydrostatic Model**  
**Developed at the Forecast Research Department**  
**of the MRI**

by

**Motohki Ikawa and Kazuo Saito**

*Forecast Research Department, Meteorological Research Institute*  
*1-1, Nagamine, Tsukuba, Ibaraki, 305 Japan*

**Contents**

A. Preface .....	1
B. Model equations and finite discretization form .....	5
B-1. Governing equations .....	7
B-1-1. Fundamental equations in Cartesian coordinates .....	7
B-1-2. Reference atmosphere and approximate equations .....	9
B-1-3. Governing equations in terrain following coordinates .....	11
B-1-4. Summary .....	13
B-2. AE (anelastic) scheme .....	15
B-2-1. Pressure equation for AE scheme .....	15
B-2-2. Hydrostatic approximation of the anelastic nonhydrostatic model .....	17
B-3. E-HI-VI (elastic-horizontally implicit-vertically implicit) scheme .....	19
B-3-1. Formulation with $\bar{P}^t$ as unknown variables .....	19
B-3-2. A linear stability analysis of E-HI-VI-PI with orography .....	22
B-3-3. E-HI-VI-PI with $\Delta^2 P$ adopted as an unknown variable .....	26
B-3-4. Implicit treatment of gravity waves in addition to sound waves .....	28
B-4. E-HE-VI (elastic-horizontally explicit-vertically implicit) scheme .....	32
B-4-1. Formulation of E-HE-VI scheme with $\bar{P}^r$ as unknown .....	32

B-4-2.	A linear stability analysis of a whole time step integration of E-HE-VI with orography .....	34
B-5.	Grid structure, variable grid and finite discretization form .....	39
B-5-1.	Grid structure .....	39
B-5-2.	Variable grid .....	41
B-5-3.	Finite discretization form on the variable staggered grid .....	41
B-6.	Pressure equation solver on variable grid .....	46
B-6-1.	The case of open (noncyclic) lateral boundary conditions .....	46
B-6-2.	The solvability condition and the constraint of mass conservation .....	53
B-6-3.	The case of cyclic lateral boundary conditions .....	54
B-7.	Lateral boundary conditions .....	56
B-7-1.	Cyclic boundary conditions .....	56
B-7-2.	Open boundary conditons .....	56
B-7-3.	Wall lateral boundary conditions .....	61
B-7-4.	Sponge layer .....	61
B-8.	Lower boundary conditions .....	63
B-8-1.	For velocity .....	63
B-8-2.	For $\Theta$ and $Qv$ .....	63
B-8-3.	For pressure .....	64
B-9.	Upper boundary conditions .....	66
B-9-1.	For velocity .....	66
B-9-2.	For $\Theta$ and $Qv$ .....	66
B-9-3.	For pressure .....	66
B-9-4.	Absorption layer .....	67
B-10.	Subgrid-scale turbulence .....	68
B-10-1.	Turbulent closure model .....	68
B-10-2.	Surface fluxes .....	70
B-11.	Cloud microphysics .....	72
B-11-1.	General features of cloud microphysics .....	72
B-11-2.	Production terms for cloud ice .....	77
B-11-3.	Production terms for snow .....	80
B-11-4.	Production terms for graupel .....	83
B-11-5.	Production terms for cloud water .....	90

B-11-6.	Production terms for rain .....	91
B-11-7.	Some numerical artifices .....	92
Appendix B-11-1.	List of symbols .....	93
Appendix B-11-2.	Figures of production terms for elementary cloud microphysical processes .....	100
B-12.	Computational diffusion .....	105
B-13.	Initial set-up procedures .....	107
B-13-1.	Preparation of eigen-vectors and eigen-values .....	107
B-13-2.	Initial environmental fields .....	107
B-13-3.	Reference atmosphere .....	107
B-13-4.	Reduction methods of initial shocks in the presence of mountains .....	108
B-13-5.	Initialization of pressure in elastic models .....	110
C.	Examples of numerical simulation by the model .....	111
C-1.	Verification of the model against 3-dimensional linear analytic solutions of nonhydrostatic mountain waves .....	113
C-1-1.	Linear analytic solutions of 3-D nonhydrostatic mountain waves .....	113
C-1-2.	Description of the numerical model .....	114
C-1-3.	Comparison between numerical and analytic solutions .....	115
C-2.	3-dimensional simulations of local winds in Japan .....	122
C-2-1.	Land-sea breeze in the Kanto district .....	122
C-2-2.	Local downslope wind "Yamaji-kaze" in Shikoku Island .....	126
C-3.	3-dimensional simulation of the convective snow cloud observed over the Sea of Japan — Sensitivity to ice crystal nucleation rates — .....	134
C-3-1.	Introduction .....	134
C-3-2.	Observations of the convective cloud .....	136
C-3-3.	Numerical model and parameterization of cloud microphysics .....	140
C-3-4.	Experimental design .....	140
C-3-5.	Results of reference experiment (EXDS1) .....	142
C-3-6.	Sensitivity experiments .....	155
C-3-7.	Comparison with observations .....	179
C-3-8.	Summary and conclusion .....	184

D.	Guide to running the model	189
D-1.	Flow charts of the program	191
D-1-1.	Job step	191
D-1-2.	Flow chart of the main program "SIMAIN" for the job step 2	191
D-1-3.	Flow chart of the subroutine CADVC3	193
D-1-4.	Flow chart of the subroutine SVELC	193
D-1-5.	Flow chart of sub.SCPI	195
D-1-6.	Flow chart of the subroutine FTVELC	195
D-1-7.	Flow chart of sub.CPTQVS	197
D-1-8.	Flow chart of sub.CQS3	198
D-2.	Specification of system parameters	200
D-2-1.	P1	200
D-2-2.	P2	200
D-2-3.	P3	201
D-2-4.	P4	203
D-3.	Scheme selection among AE, E-HI-VI and E-HE-VI	204
D-4.	Size of the domain, grid indexing and variable grid generation	205
D-5.	Specification of the boundary conditions	208
D-5-1.	Lateral boundary conditions	208
D-5-2.	Lower boundary conditions	209
D-5-3.	Upper boundary conditions	211
D-6.	Specification of initial environmental fields	212
D-7.	Initiation method of convection	213
D-7-1.	Thermal bubble initiation	213
D-7-2.	Cold dome initiation	213
D-8.	Generation of mountain shape and metric tensors	214
D-9.	Specification of computational diffusion	215
D-9-1.	Nonlinear damping $Dn$	215
D-9-2.	Fourth-order linear damping	215
D-9-3.	Rayleigh damping near the upper boundary	216
D-9-4.	Rayleigh damping near the lateral boundary	216
D-9-5.	Damping in the time integrations schemes	217
D-10.	Store of the results and restart	218

E.	Plotting of the model results . . . . .	219
E-1.	Format of the stored results in magnetic tape . . . . .	221
E-2.	Plot of the $(x-z, y-z, x-y)$ cross sections at the fixed time . . . . .	224
E-3.	Plot of the $(x-t, y-t, z-t)$ cross sections for the fixed plane . . . . .	227
E-4.	An example of input parameter list for the program "PLPMN" . . . . .	228
F.	References . . . . .	231

## **A. Preface**

The nonhydrostatic model presented in this technical report has been developed by M. Ikawa since 1980 and K. Saito since 1988. This model is intended for a research tool and for providing useful information about the scheme to be adopted by a future operational model which will be used in forecasting regional weather. As a research tool, this model has been used for simulations of convective clouds (Ikawa *et al.*, 1987; Ikawa, 1988) and mountain waves (Ikawa and Nagasawa, 1989; Ikawa, 1990; Saito and Ikawa, 1991).

With the advent of computer facilities, nonhydrostatic models will replace hydrostatic models in short-range weather forecasting for a limited area in the near future. There have been many schemes used in nonhydrostatic models so far developed. In this model, AE (anelastic), E-HI-VI (elastic-horizontally and vertically implicit) and E-HE-VI (elastic-horizontally explicit-vertically implicit) schemes are implemented, and these three schemes are easily compared with each other under the same numerical environment. Therefore, this model is regarded as an *evaluation kit* of these three schemes. Which is the best scheme among the three still remains to be decided.

This model has to be improved or refined in many points. Further development of the model will be beyond the power of one or two persons. It is hoped that the detailed description of the model and the manual for running the model presented in this technical report will stimulate the cooperative efforts on the further development of this model or provide some useful information for building up a new model.

The points to be revised or improved are as follows:

1. Dynamical framework:
  - a) Change of the finite discretization form of the 2-nd order to that of the 4-th order.
  - b) 1-way or 2-way nesting.
  - c) Change of the grid model to the spectral model by Tatsumi's limited area spectral method (a) is in contradiction to c))
  - d) Hybrid vertical coordinates (the lower part of the domain is  $\xi^*$ , while the upper part is  $z$ ).
  - e) Radiation condition at the upper boundary (Klemp and Durran, 1983).
2. Physical process:
  - a) Refinement of cloud microphysical processes.
  - b) Refinement of the parameterization of subgrid-scale turbulence and incorporation of subgrid-scale condensation.
  - c) Refinement of the parameterization of surface and air-surface interaction.

d) Incorporation of short- and long-wave radiation. No radiation is incorporated in the present model.

3. Others:

- a) Optimization of the program code for the array processor (supercomputer).
- b) Debugs of the program code to make the model more reliable.

The organization of this report is as follows. In Chapter B, governing equations, parameterizations of physical processes and their finite discretization are presented. In Chapter C, examples of 3-dimensional simulation are presented, including the model verification by comparing 3-dimensional linear analytic solutions of nonhydrostatic mountain waves with their numerical counterparts. In Chapters D and E, procedures for running the model and plotting model results are presented. In Chapter B, some notes named 'Program Guide' (abbreviated as P.G.) are inserted in order to give useful comments on how field variables are expressed and governing equations are computed in the program code. These notes and Chapters D and E may be skipped by readers who intend to get general information on the model and have no interest in running this model.

The two modellers, Ikawa and Saito, thank many persons for helping them to develop the model. Specifically, they thank Drs. M. Aihara and M. Yoshizaki for useful comments and discussions on the dynamical framework of the model. They thank Drs. T. Matsuo, M. Murakami and Mr. H. Mizuno for critical and constructive comments and valuable suggestions on parameterizations of cloud microphysical processes. Mr. Mizuno read through the program, and pointed out some bugs.

Chapter B except for B-10, C-3, and Chapters D and E were written by M. Ikawa. B-10, C-1, C-2 were written by K. Saito.

## **B. Model equations and finite discretization form**

## B-1. Governing equations

2-dimensional equations are considered for simplicity in sections B-1 ~ B-4.

### B-1-1. Fundamental equations in Cartesian coordinates

a) State equation of moist air with hydrometeors

$$\begin{aligned}\rho &= \rho_{\text{dry}} + \rho_v + \rho_c + \rho_r + \rho_i + \rho_s + \rho_g \\ &= \rho_{\text{dry}}(1 + Qv + Qc + Qr + Qi + Qs + Qg),\end{aligned}\quad (1-1)$$

$$p = (\rho_{\text{dry}} + \rho_v)R(1 + 0.61Qv)T, \quad (1-2)$$

where  $\rho_{\text{dry}}$ ,  $\rho_v$ ,  $\rho_c$ ,  $\rho_r$ ,  $\rho_i$ ,  $\rho_s$  and  $\rho_g$  are the densities of dry air, water vapor, cloud water, rain, cloud ice, snow and graupel, respectively;  $Qv$ ,  $Qc$ ,  $Qr$ ,  $Qi$ ,  $Qs$  and  $Qg$  are mixing ratios of water vapor, cloud water, rain, cloud ice, snow and graupel, respectively;  $R$  is the gas constant for dry air;  $T$  is temperature (K). By approximation of  $\rho_{\text{dry}} + \rho_v = \rho(1 - Qc - Qr - Qi - Qs - Qg)$ , Eq. (1-2) is rewritten as

$$\begin{aligned}p &= \rho RT_m \\ &= \rho R(1 - Qc - Qr - Qi - Qs - Qg)T_v \\ &= \rho R(1 - Qc - Qr - Qi - Qs - Qg)(1 + 0.61Qv)T,\end{aligned}\quad (1-3a)$$

or alternatively

$$\rho \equiv \frac{p_0}{R\Theta_m} \left( \frac{p}{p_0} \right)^{C_v/C_p}, \quad (1-3b)$$

where

$$\left. \begin{aligned}T_m &\equiv (1 - Qc - Qr - Qi - Qs - Qg)T_v; \\ T_v &\equiv (1 + 0.61Qv)T; \\ \Theta &\equiv \Pi^{-1}T; \quad \Theta_v \equiv \Pi^{-1}T_v; \quad \Theta_m \equiv \Pi^{-1}T_m; \quad \Pi = \left( \frac{p}{p_0} \right)^{R/C_p};\end{aligned} \right\} \quad (1-4)$$

$p$  is pressure;  $\Theta$  is potential temperature;  $C_p$  is the specific heat of dry air at constant pressure;  $C_v$  is the specific heat at constant volume;  $p_0$  equals 1000 hPa.

b) Mass conservation

By neglecting the fall-out of  $Qr$ ,  $Qs$  and  $Qg$ ,  $\rho$  is governed by

$$\sigma \frac{d\rho}{\rho dt} + \frac{\partial u}{\partial x} + \frac{\partial w}{\partial z} = 0, \quad (1-5a)$$

or

$$\sigma \frac{\partial \rho}{\partial t} + \frac{\partial \rho u}{\partial x} + \frac{\partial \rho w}{\partial z} = 0. \quad (1-5b)$$

Here,  $\sigma$  is a switching parameter;  $\sigma = 1$  represents the exact equation, while  $\sigma = 0$  represents an approximate equation from which sound waves are excluded.

c) Momentum equations

$$\rho \frac{du}{dt} + \frac{\partial p}{\partial x} = \text{DIF}.u, \quad (1-6)$$

$$\rho \frac{dw}{dt} + \frac{\partial p}{\partial z} + \rho g = \text{DIF}.w, \quad (1-7)$$

where  $\text{DIF}.f$  denotes the diffusion term for a field variable  $f$ .

d) Thermal equations

$$Qdt + C_v \text{DIF}.Tdt = C_v dT + pd\alpha = (C_v + R)dT - \alpha dp = C_p \Pi d\Theta, \quad (1-8)$$

$$\frac{d\Theta}{dt} = \frac{Q}{C_p \Pi} + \text{DIF}.\Theta, \quad (1-9a)$$

$$C_v \frac{dT}{dt} - \frac{p}{\rho^2} \frac{d\rho}{dt} = C_v \frac{dT}{dt} + \frac{p}{\rho} \left( \frac{\partial u}{\partial x} + \frac{\partial w}{\partial z} \right) = Q + C_v \text{DIF}.T, \quad (1-9b)$$

where  $Q$  is the diabatic heating rate,  $C_p \Pi \text{DIF}.\Theta = C_v \text{DIF}.T$  and  $\alpha = 1/\rho$ .

From (1-3b),

$$\frac{1}{Cs^2} \frac{\partial p}{\partial t} = \frac{\partial \rho}{\partial t} + \frac{\rho}{\Theta_m} \frac{\partial \Theta_m}{\partial t}, \quad (1-10a)$$

or

$$\frac{1}{Cs^2} \frac{dp}{dt} = \frac{d\rho}{dt} + \frac{\rho}{\Theta_m} \frac{d\Theta_m}{dt}, \quad (1-10b)$$

where  $Cs$  is the sound wave speed  $Cs^2 = (C_p/C_v)RT$ .

From Eqs. (1-10) and (1-5b),

$$\frac{\sigma}{Cs^2} \frac{\partial p}{\partial t} + \frac{\partial \rho u}{\partial x} + \frac{\partial \rho w}{\partial z} = \sigma \frac{\rho}{\Theta_m} \frac{\partial \Theta_m}{\partial t}, \quad (1-11a)$$

or

$$\frac{\sigma}{C_s^2} \frac{dp}{dt} + \rho \left( \frac{\partial u}{\partial x} + \frac{\partial w}{\partial z} \right) = \sigma \frac{\rho}{\Theta_m} \frac{d\Theta_m}{dt}. \quad (1-11b)$$

By use of Eq. (1-5) and  $\sigma = 1$ , momentum equations (1-6) and (1-7) are written in flux form as follows:

$$\frac{\partial \rho u}{\partial t} + \frac{\partial p}{\partial x} = - \frac{\partial \rho u u}{\partial x} - \frac{\partial \rho w u}{\partial z} + \text{DIF}.u, \quad (1-12)$$

$$\frac{\partial \rho w}{\partial t} + \frac{\partial p}{\partial z} + \rho g = - \frac{\partial \rho u w}{\partial x} - \frac{\partial \rho w w}{\partial z} + \text{DIF}.w. \quad (1-13)$$

The equation for the scalar variable  $f$  ( $\Theta$ ,  $Qv$ ,  $Qc$ , ...,  $Qg$ )

$$\rho \frac{df}{dt} = \rho \text{SRC}.f + \rho \text{DIF}.f \quad (1-14a)$$

is also written in flux form as

$$\frac{\partial \rho f}{\partial t} = - \frac{\partial \rho u f}{\partial x} - \frac{\partial \rho w f}{\partial z} + \rho \text{SRC}.f + \rho \text{DIF}.f, \quad (1-14b)$$

where  $\text{SRC}.f$  is the source term of  $f$ .

It is noted that the above equations include sound waves, and no approximation is made for a dry case. The thermal equation (1-9b) in combination with Eqs. (1-5), (1-6) and (1-7) yields the equation of the total energy conservation such as

$$\frac{\partial(\rho E)}{\partial t} + \frac{\partial(\rho E u)}{\partial x} + \frac{\partial(\rho E w)}{\partial z} + \frac{\partial p u}{\partial x} + \frac{\partial p w}{\partial z} = (u \text{DIF}.u + w \text{DIF}.w) + \rho(Q + C_v \text{DIF}.T), \quad (1-15)$$

where

$$E = \frac{1}{2} (u^2 + w^2) + gz + C_v T.$$

The above beautiful equation cannot be obtained from Eq. (1-9a). Aihara and Okamura (1985) adopted Eq. (1-9b) instead of Eq. (1-9a), and obtained the scheme of the flux form which conserves the total energy  $E$  exactly.

### B-1-2. Reference atmosphere and approximate equations

The reference basic state is assumed to be horizontally uniform and dependent only on  $z$  and in hydrostatic balance. All field variables are expressed as the sum of the values of the basic state ( $\bar{\quad}$ ) and perturbations ( $\prime$ ) from them as below:

$$p = \bar{p} + p'; \quad \rho = \bar{\rho} + \rho'; \quad \Theta = \bar{\Theta} + \Theta'; \quad T = \bar{T} + T', \quad (1-16)$$

$$\bar{p} = \bar{\rho} R \bar{T}_m, \quad (1-17)$$

$$\bar{\Theta}_m \equiv \bar{\Pi}^{-1} \bar{T}_m; \quad \bar{\Pi} = \left( \frac{\bar{p}}{p_0} \right)^{R/C_p}, \quad (1-18)$$

$$\bar{\rho} \equiv \frac{p_0}{R \bar{\Theta}_m} \left( \frac{\bar{p}}{p_0} \right)^{C_v/C_p}, \quad (1-19)$$

$$\frac{\partial \bar{p}}{\partial z} = -\bar{\rho} g. \quad (1-20)$$

Note that the suffix “-” is different from the averaging operator in the horizontal, and hereafter the subscript ‘ref’ is also used in the same meaning as the suffix “-”.

From Eqs. (1-3b) and (1-16) and (1-19), an approximate relation is obtained as

$$\rho' = \frac{p'}{C_s^2} - \frac{\bar{\rho} \Theta'_m}{\Theta_m}. \quad (1-21)$$

By use of Eqs. (1-20) and (1-21), Eq. (1-13) is rewritten as

$$\frac{\partial \rho w}{\partial t} + \frac{\partial p'}{\partial z} + \frac{g p'}{C_s^2} = -\frac{\partial \rho u w}{\partial x} - \frac{\partial \rho w w}{\partial z} + \frac{g \bar{\rho} \Theta'_m}{\Theta_m} + \text{DIF}.w, \quad (1-22)$$

Eq. (1-11a) is rewritten as

$$\frac{\sigma}{C_s^2} \frac{\partial p'}{\partial t} + \left( \frac{\partial \rho u}{\partial x} + \frac{\partial \rho w}{\partial z} \right) = \sigma \frac{\rho \partial \Theta'_m}{\Theta_m \partial t} \quad (1-23)$$

The reference atmosphere is required to be not only as close as possible to the model atmosphere but also as smooth as possible.

It is noted that Clark's anelastic equations (1977) are obtained by formally setting  $\sigma = 0$  and  $\rho = \bar{\rho}$  in Eqs. (1-12), (1-14b), (1-22) and (1-23).  $\sigma = 1$  includes acoustic modes, while  $\sigma = 0$  filters out them. Hereafter, the governing equations which are formally obtained by setting  $\rho = \bar{\rho}$  in Eqs. (1-12), (1-14b), (1-22) and (1-23) and replacing  $p$  by  $p'$  in Eq. (1-12) are used.

However,  $\sigma = 1$  and  $\rho = \bar{\rho}$  yield errors in the advection term of flux form for a variable  $f$  as shown below;

$$\begin{aligned} \bar{\rho} \frac{\partial f}{\partial t} &= -\frac{\partial \bar{\rho} u f}{\partial x} - \frac{\partial \bar{\rho} w f}{\partial z} + \bar{\rho} \text{SRC}.f + \bar{\rho} \text{DIF}.f \\ &= -\bar{\rho} u \frac{\partial f}{\partial x} - \bar{\rho} w \frac{\partial f}{\partial z} - f \left( \frac{\partial \bar{\rho} u}{\partial x} + \frac{\partial \bar{\rho} w}{\partial z} \right) \\ &\quad \text{--- error ---} \\ &\quad + \bar{\rho} \text{SRC}.f + \bar{\rho} \text{DIF}.f. \end{aligned} \quad (1-24)$$

This error can be reduced so as to be practically free from numerical trouble for some cases by damping sound wave modes as shown by Ikawa (1988). There are several other choices to avoid the error. One is the use of the advection term in advective form. However, this has some problems in making budget analysis. Another choice is the adjustment on the velocity in order to satisfy the non-divergence of the wind proposed by Yoshizaki (1988). Another choice is to predict time change of  $\rho$  by Eq. (1-5) exactly as Aihara and Okamura (1985) did. But this is currently not yet implemented in E-HI-VI and E-HE-VI schemes (see B-3 and B-4).

The anelastic equations of Ogura and Phillips (1962) conserve the total energy (the degenerated version of  $E$ ). They are obtained by selecting the isentropic atmosphere as the reference atmosphere in addition to setting  $\sigma = 0$  and  $\rho = \bar{\rho}$ . However, the isentropic atmosphere differs from the standard atmosphere, and this might result in large error.

### B-1-3. Governing equations in terrain following coordinates

Formulation of the schemes without any special description is the same as that of Clark (1977). The pressure gradient force is expressed, not in terms of an Exner function but in terms of pressure. The terrain following coordinate system is introduced such as

$$\xi = \frac{H(z - Z_s)}{H - Z_s}, \quad (1-25)$$

where  $Z_s$  is the surface height, and  $H$  is the constant height of the top of the model domain.

Applying the chain rule for the coordinate transform from  $(x, z)$  to  $(x, \xi)$ , the following relations are obtained for an arbitrary function  $\phi$ :

$$G^{1/2} \frac{\partial \phi}{\partial x} = \frac{\partial}{\partial x} (G^{1/2} \phi) + \frac{\partial}{\partial \xi} (G^{1/2} G^{13} \phi) \quad (1-26a)$$

and

$$G^{1/2} \frac{\partial \phi}{\partial z} = \frac{\partial \phi}{\partial \xi}, \quad (1-26b)$$

where

$$G^{1/2} \equiv \frac{1}{(\partial \xi / \partial z)_{x=\text{const}}} = 1 - Z_s/H; \quad G^{13} \equiv \left( \frac{\partial \xi}{\partial x} \right)_{z=\text{const}} = \frac{1}{G^{1/2}} \left( \frac{\xi}{H} - 1 \right) \frac{\partial Z_s}{\partial x}. \quad (1-27)$$

The governing equations (Eqs. (1-5b), (1-12), (1-14b), (1-22) and (1-23)) are written in the  $(x, \xi)$  coordinate system as follows:

$$\frac{\partial U}{\partial t} + \frac{\partial}{\partial x} P + \frac{\partial}{\partial \xi} (G^{13} P) = -ADVU, \quad (1-28)$$

$$\frac{\partial W}{\partial t} + \frac{1}{G^{1/2}} \frac{\partial P}{\partial \xi} + \frac{gP}{Cs^2} = \text{BUOY} - \text{ADVW}, \quad (1-29)$$

$$\sigma \frac{\partial(G^{1/2}\rho')}{\partial t} + \frac{\partial}{\partial x} U + \frac{1}{G^{1/2}} \frac{\partial W}{\partial \xi} + \frac{\partial}{\partial \xi} (G^{13}U) = 0, \quad (1-30a)$$

or alternatively

$$\sigma \frac{\partial(G^{1/2}\rho')}{\partial t} + \frac{\partial}{\partial x} U + \frac{\partial W^*}{\partial \xi} = 0, \quad (1-30b)$$

where

$$U \equiv \bar{\rho}G^{1/2}u, \quad W \equiv \bar{\rho}G^{1/2}w, \quad P \equiv G^{1/2}p', \quad (1-31)$$

$$\text{ADVU} \equiv \frac{\partial Uu}{\partial x} + \frac{\partial W^*u}{\partial \xi}, \quad (1-32)$$

$$\text{ADVW} \equiv \frac{\partial Uw}{\partial x} + \frac{\partial W^*w}{\partial \xi}, \quad (1-33)$$

$$W^* \equiv \frac{1}{G^{1/2}} \bar{\rho}G^{1/2}w + \bar{\rho}G^{1/2}G^{13}u \equiv \bar{\rho}G^{1/2}\omega \equiv \bar{\rho}G^{1/2} \frac{d\xi}{dt}, \quad (1-34)$$

$$\text{BUOY} \equiv g \frac{G^{1/2}\bar{\rho}\Theta'_m}{\Theta_m}. \quad (1-35)$$

Here  $\sigma$  is the switching parameter;  $\sigma = 0$  for anelastic equations, and  $\sigma = 1$  for elastic equations.

The thermal equation is given as

$$\frac{\partial \theta}{\partial t} = -\text{ADV}\theta + \frac{Q}{C_p\Pi} + \text{DIF.}\theta, \quad (1-36)$$

$$\text{ADV}\theta \equiv \frac{1}{\bar{\rho}G^{1/2}} \left( \frac{\partial U\theta}{\partial x} + \frac{\partial W^*\theta}{\partial \xi} \right), \quad (1-37a)$$

$$\theta \equiv \Theta - \Theta_{\text{bias}} = \bar{\Theta}(z) + \Theta' - \Theta_{\text{bias}}. \quad (1-37b)$$

Here,  $\Theta_{\text{bias}}$  is a constant prescribed value which is independent of  $z$  and close to the vertically averaged value of  $\bar{\Theta}(z)$ .

Eq. (1-23) is rewritten as

$$\frac{\sigma}{Cs^2} \frac{\partial P}{\partial t} + \frac{\partial}{\partial x} U + \frac{1}{G^{1/2}} \frac{\partial W}{\partial \xi} + \frac{\partial}{\partial \xi} (G^{13}U) = \sigma \text{PFT}, \quad (1-38)$$

where

$$\text{PFT} = \frac{\bar{\rho}G^{1/2}}{\Theta_m} \frac{\partial \Theta'_m}{\partial t} = \frac{1}{g} \frac{\partial \text{BUOY}}{\partial t}. \quad (1-39)$$

Terms related to sound waves are isolated on the left side of Eqs. (1-28), (1-30) and (1-38).

It is noted that the state variables of the reference atmosphere such as  $\bar{\Theta} = \Theta_{\text{ref}}$  and  $\bar{\rho} = \rho_{\text{ref}}$  is dependent only on  $z$  in the Cartesian coordinate system, but dependent not only on

$\xi$  but also on  $x$  in the terrain following coordinate system. However,  $C_s^2_{\text{ref}} = (C_p/C_v)RT_{\text{ref}}$  is assumed to be dependent only on  $\xi$  for simplicity in the program.

The governing equations in the terrain following coordinate system have been derived in two different ways by tensor analysis (Gal-Chen and Somerville, 1975; Pielke and Martin, 1981; Pielke, 1984) and chain rule (Clark, 1977; Carpenter, 1979; Durran and Klemp, 1983; Aihara and Okamura, 1985). The equations between the two differ slightly and are believed to bring about little differences. A concise review is given by Yoshizaki (1988). The equations derived by chain rule predict the velocity components in the Cartesian coordinate system, while those derived by tensor analysis predict the components of the contravariant vector of the velocity in the terrain following coordinate system. Momentum equations by the two methods are the same in appearance (Wong and Hage, 1983; Pielke and Martin, 1981). However, the directions of the unit vector for the  $u$ -velocity component are different, although the equations for the magnitude of  $u$ -velocity component are the same. The diffusion terms are also different; but, usually, subgrid scale turbulence is parameterized with large uncertainty. This difference is also considered to be insignificant.

#### B-1-4. Summary

In summary, Eqs. (1-28), (1-29) (1-30) (1-36) and (1-38) are adopted as governing equations. The anelastic scheme implemented in the model (see B-2) uses  $\sigma = 0$  and  $\rho = \bar{\rho}$ . Elastic schemes (both E-HI-VI and E-HE-VI) currently implemented in the model (see B-3 and 4) uses  $\sigma = 1$  and  $\rho = \bar{\rho}$  instead of explicit calculation of the prognostic equation (1-30) for density  $\rho$  (Eq. (1-30) is treated just as a dummy equation, currently). This is accompanied by errors in advection term as shown by Eq. (1-24). However, no serious problems have occurred as far as sound waves are damped enough ( $|\text{div}(\rho V)|/\bar{\rho} < 10^{-6}\text{s}^{-1}$  seems to be sufficient) (Ikawa, 1988). In the next sections, these schemes are described, with emphasis on their pressure equations and solving methods. For elastic schemes, special attention is paid to the time integration methods which effectively damp sound waves.

Which scheme is the best among AE, E-HI-VI and E-HE-VI, still remains unclear. From limited numbers of simulations of large amplitude hydrostatic mountain waves in a homogeneous atmosphere (horizontal velocity,  $U$ , and Brunt-Väisälä frequency,  $N$ , are constant), it was found by Ikawa (1988) that the numerical results by those schemes are almost the same and that the CPU time consumed by E-HE-VI is almost twice that by AE or E-HI-VI. However, in the simulation of large-amplitude mountain waves of 2 or 4-layered

atmospheres conducted by Ikawa and Nagasawa (1989), the E-HI-VI was found to succeed in longer computation without computational breakdown than AE for some cases. One purpose of the model in which the three schemes are available in the same computational environment is to compare the performance and efficiency of these three schemes, and to provide some information for deciding the best scheme among the three.

## B-2. AE (anelastic) scheme

### B-2-1. Pressure equation for AE scheme

An AE scheme is obtained by setting  $\sigma = 0$  and  $\rho = \bar{\rho}$  in equations in section B-1-3. In this scheme, sound waves are filtered out.

For convenience, operators are introduced as

$$\text{DIVR}(A, B) = \frac{\partial(G^{13}A)}{\partial\xi} + \left( \frac{1}{G^{1/2}} - \frac{\tilde{1}}{G^{1/2}} \right) \frac{\partial B}{\partial\xi}, \quad (2-1)$$

$$\text{DIVS}(A, B) = \frac{\partial A}{\partial x} + \frac{\tilde{1}}{G^{1/2}} \frac{\partial B}{\partial\xi}, \quad (2-2)$$

and

$$\begin{aligned} \text{DIVT}(A, B) &= \frac{\partial A}{\partial x} + \frac{\partial(G^{13}A)}{\partial\xi} + \frac{1}{G^{1/2}} \frac{\partial B}{\partial\xi} \\ &= \text{DIVS}(A, B) + \text{DIVR}(A, B), \end{aligned} \quad (2-3)$$

where the symbol  $\tilde{\phantom{x}}$  indicates a constant value independent of  $x$  and  $\xi$ .

The pressure equation for the AE scheme is obtained from Eqs. (1-28), (1-29) and (1-30) by eliminating  $U^{it+1}$  and  $W^{it+1}$  in  $\text{DIVT}(\partial U/\partial t, \partial W/\partial t) = 0$  as

$$\begin{aligned} pt \frac{\partial^2 P}{\partial x^2} + \frac{1}{(G^{1/2})^2} \frac{\partial^2 P}{\partial \xi^2} + \frac{1}{G^{1/2}} \frac{\partial}{\partial \xi} \left( \frac{g}{Cs^2} P \right) + \frac{\partial^2}{\partial x \partial \xi} (G^{13} P) \\ + \frac{\partial}{\partial \xi} \left[ G^{13} \left\{ \frac{\partial P}{\partial x} + \frac{\partial}{\partial \xi} (G^{13} P) \right\} \right] \\ = -\text{DIVT}(\text{ADVU}, \text{ADVW} - \text{BUOY}) + \frac{\text{DIVT}(U^{it-1}, W^{it-1})}{2\Delta t} \\ = \text{FP.AE.INV}. \end{aligned} \quad (2-4)$$

Here, superscript 'it' denotes the value at the time step 'it'. Theoretically, the term  $\text{DIVT}(U^{it-1}, W^{it-1})$  would be zero, and the above equation would guarantee  $\text{DIVT}(U^{it+1}, W^{it+1}) = 0$ . However, in numerical simulation, the term becomes non-zero due to round-off errors, and this term may be considered as "sound wave"-like noises originated from numerical round-off errors. The purpose of adding this term to the forcing term, FP.AE.INV, of the pressure equation is to suppress the growth of these "sound wave"-like noises and make the continuity equation of AE be more completely fulfilled.

In the case where orography is included,  $G^{1/2}$  is dependent on  $x$ , and  $G^{13}$  is dependent

on  $x$  and  $\xi$ . It is difficult to solve Eq. (2-4) by the direct method (e.g., dimension reduction method: Ogura (1969), Ikawa (1981)) efficiently because of its non-separability. Eq. (2-4) can be solved by an iterative application of the direct method as follows:

$$\begin{aligned} \frac{\partial^2 P_i}{\partial x^2} + \frac{\tilde{1}}{(G^{1/2})^2} \frac{\partial^2 P_i}{\partial \xi^2} + \frac{\tilde{1}}{G^{1/2}} \frac{\partial}{\partial \xi} \left( \frac{\tilde{g}}{Cs^2} P_i \right) \\ = \text{FP.AE.INV} + \text{FP.AE.VAR}(P_{i-1}), \end{aligned} \quad (2-5)$$

where

$$\begin{aligned} \text{FP.AE.VAR}(P_i) = -\text{DIVR} \left( \frac{\partial P_i}{\partial x}, \left( \frac{\tilde{1}}{G^{1/2}} \frac{\partial}{\partial \xi} + \frac{\tilde{g}}{Cs^2} \right) P_i \right) \\ - \text{DIVT} \left( \frac{\partial}{\partial \xi} G^{13} P_i, \left( \left[ \frac{1}{G^{1/2}} \frac{\partial}{\partial \xi} + \frac{g}{Cs^2} \right] - \left[ \frac{\tilde{1}}{G^{1/2}} \frac{\partial}{\partial \xi} + \frac{\tilde{g}}{Cs^2} \right] \right) P_i \right). \end{aligned} \quad (2-6)$$

The suffix  $i$  denotes the  $i$ -th solution obtained from the  $i$ -th iterative procedure.

At the lower and upper boundaries, the following condition must be satisfied (see Eq. (1-34)):

$$\frac{W}{G^{1/2}} + G^{13} U = \bar{\rho} G^{1/2} \frac{d\xi}{dt} = W^* = 0. \quad (2-7)$$

From Eqs. (2-7), (1-28) and (1-29), the upper and lower boundary conditions for pressure are as follows:

$$\frac{1}{G^{1/2}} \frac{\partial P}{\partial \xi} + \frac{g}{Cs^2} P = -G^{1/2} G^{13} \left( \frac{\partial P}{\partial x} + \frac{\partial}{\partial \xi} (G^{13} P) + \text{ADVU} \right) + \text{BUOY} - \text{ADVW}. \quad (2-8)$$

For these boundary conditions, an iterative procedure is also needed.

$$\frac{\tilde{1}}{G^{1/2}} \frac{\partial P_i}{\partial \xi} + \frac{\tilde{g}}{Cs^2} P_i = \text{FPB.AE.VAR}(P_{i-1}) + \text{FPB.AE.INV}, \quad (2-9)$$

$$\begin{aligned} \text{FPB.AE.VAR}(P_i) = \left( \frac{\tilde{1}}{G^{1/2}} \frac{\partial P_i}{\partial \xi} - \frac{1}{G^{1/2}} \frac{\partial P_i}{\partial \xi} \right) + \left( \frac{\tilde{g}}{Cs^2} - \frac{g}{Cs^2} \right) P_i \\ - G^{1/2} G^{13} \left( \frac{\partial P_i}{\partial x} + \frac{\partial}{\partial \xi} G^{13} P_i \right), \end{aligned} \quad (2-10)$$

and

$$\text{FPB.AE.INV} = \text{BUOY} - \text{ADVW} - G^{1/2} G^{13} \text{ADVU}. \quad (2-11)$$

The iterative application of the direct method to Eqs. (2-5) and (2-9) is found to work well. The method is described in detail in section B-6 (pressure equation solver). 3 or 4 iterations

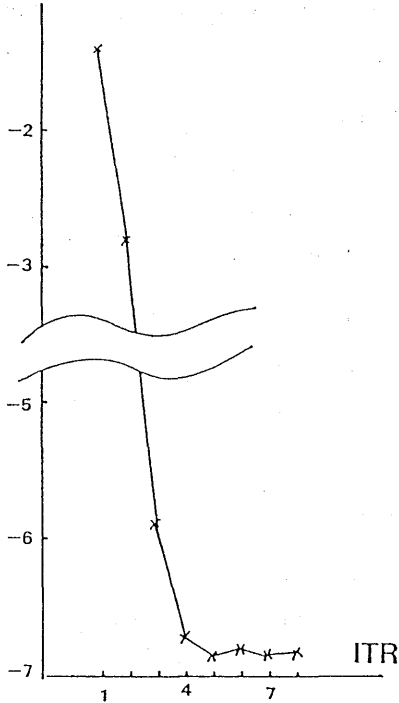


Fig. B-2-1 An example of a convergence of the iterative application of the direct method to Eqs. (2-5) and (2-9) at a certain grid point for the example case in section 3 of Ikawa (1988). The mountain height is set to 2000m and  $\Delta G \doteq \max(\partial Z_s / \partial x) = 0.2$ ,  $\Delta H \doteq \max(Z_s / H) = 0.14$  (for the definition of  $\Delta G$  and  $\Delta H$ , see B-3-2), where  $Z_s(x)$  is a mountain shape function and  $H$  is the height of the model domain. The vertical axis denotes  $\log_{10} |P_i - P_9| / |P_9|$ . The horizontal axis represents  $i$ , the number of iterative applications of the direct method. The first guess  $P_0$  is set to zero and  $P_9$  denotes the solution obtained at the 9-th iteration. (adapted from Ikawa, 1988)

are sufficient to give the well converged solution up to 6 significant digits as shown in Fig. B-2-1.

### B-2-2. Hydrostatic approximation of the anelastic nonhydrostatic model

This is given by Clark and Hall (1988). This hydrostatic version has not been implemented in the model yet. In hydrostatic approximation, the momentum equation for  $w$  is changed as

$$\frac{1}{G^{1/2}} \frac{\partial P}{\partial \xi} + \frac{gP}{C_s^2} = \text{BUOY} \quad (2-12)$$

$$\text{for } k = 1 + 1/2, 2 + 1/2 \dots nz - 1/2,$$

(for  $nz$  and the index  $k$  used in finite discretization form, see B-5).

The vertical velocity is diagnostically determined by use of Eq. (1-30b) with  $\sigma = 0$ . Eq. (2-12) alone is not sufficient for the diagnostic equation for pressure. The horizontal equations of motion are combined with the anelastic continuity equation (1-30b) with  $\sigma = 0$  to form

$$\frac{\partial^2 P}{\partial x^2} + \frac{\partial^2}{\partial x \partial \xi} (G^{1/3} P) = -\text{DIVS}(\text{ADVU}, 0) + \frac{1}{2\Delta t} \frac{\partial (W^{*it+1} - W^{*it-1})}{\partial \xi} \quad (2-13)$$

$$\text{for } k = 2, 3, \dots, nz - 1.$$

Summing Eq. (2-13) over the vertical column results in the following diagnostic column pressure equation:

$$\frac{\partial^2 (\sum_k^k \Delta z_k P_k)}{\partial x^2} + \frac{\partial}{\partial x} [(G^{13} \bar{P}^{xz})_{k=nz} - (G^{13} \bar{P}^{xz})_{k=1}]$$

$$= - \sum_k^k \text{DIVS}(\text{ADVU}, 0)_k \Delta z_k + \frac{(W^{*it+1} - W^{*it-1})_{nz} - (W^{*it+1} - W^{*it-1})_1}{2\Delta t}. \quad (2-14)$$

For the definition of the space averaging operator  $-xz$ , see B-5-3.  $W^*$  at the lower and upper boundaries must be specified from outside.

The diagnostic pressure equations, (2-12) and (2-14) can be solved as follows: From Eq. (2-12),  $P_k$  ( $k > 1$ ) can be expressed as

$$P_k = a_k P_1 + b_k. \quad \text{for } 1 < k \leq nz.$$

Substitution of them into Eq. (2-14) results in the horizontal elliptic equation for  $P_1$ .

In this system, no external gravity waves are allowed, if the upper boundary condition is the rigid wall condition as is often used. On the other hand, the primitive (hydrostatic) equations currently used in many operational forecasting centers have the prognostic equation for the surface pressure and allow the external gravity waves, because the free upper surface is used instead of the rigid wall. The nesting of the hydrostatic version of the anelastic model into the primitive model may have difficulty in this point.

### B-3. E-HI-VI (elastic-horizontally implicit-vertically implicit) scheme

In this scheme, sound waves are included, and the equations in B-1-3 with substitution of  $\sigma = 1$  and  $\rho = \bar{\rho}$  are used. In the time integration, terms related to sound waves are treated implicitly in both the horizontal and the vertical directions.

#### B-3-1. Formulation with $\bar{P}^t$ as unknown variables

Carpenter (1979) extended the non-orographic E-HI-VI of Tapp and White (1976) to that with orography, having slightly different governing equations from the present E-HI-VI. In this section, three kinds of E-HI-VI are formulated, *i.e.*, E-HI-VI-FI (full iteration, fully implicit), E-HI-VI-PI (partial iteration, partially implicit) and E-HI-VI-NI (no iteration, partially implicit).

##### a) E-HI-VI-FI

First, the E-HI-VI-FI is considered by handling all terms associated with sound waves implicitly as follows:

$$\delta_t U + \frac{\partial}{\partial x} \bar{P}^t + \frac{\partial}{\partial \xi} (G^{13} \bar{P}^t) = -ADVU, \quad (3-1)$$

$$\delta_t W + \frac{1}{G^{1/2}} \frac{\partial \bar{P}^t}{\partial \xi} + \frac{g \bar{P}^t}{C_s^2} = BUOY - ADVW, \quad (3-2)$$

$$\delta_t P + C_s^2 \text{DIVT}(\bar{U}^t, \bar{W}^t) = C_s^2 \text{PFT} \quad (3-3a)$$

$$\frac{1}{C_s^2} \delta_t P + \frac{\partial}{\partial x} \bar{U}^t + \frac{1}{G^{1/2}} \frac{\partial \bar{W}^t}{\partial \xi} + \frac{\partial}{\partial \xi} (G^{13} \bar{U}^t) = \text{PFT}, \quad (3-3b)$$

$$\bar{f}^t = \frac{1 + \alpha}{2} f^{it+1} + \frac{1 - \alpha}{2} f^{it-1}, \quad (3-4)$$

and

$$\delta_t f = \frac{f^{it+1} - f^{it-1}}{2\Delta t}, \quad (3-5)$$

where  $f^{it}$  indicates the value of  $f$  at the ' $it$ ' time step,  $\alpha$  is a constant parameter for time averaging and an operator DIVT is defined by Eq. (2-3).

The upper and lower conditions are the same as Eq. (2-7). In these equations,  $\bar{P}^t$ ,  $\bar{U}^t$  and  $\bar{W}^t$  are regarded as unknown variables. After some manipulation, the equation of  $\bar{P}^t$  is obtained, which is similar to the pressure equation of AE. To solve the equation, an iterative method must be needed. Then, E-HI-VI-FI (see section B-3-3) has no advantage in simplicity of solving the elliptic equation over the AE scheme.

b) E-HI-VI-PI

Next, formulation of E-HI-VI-PI is made by handling the part of terms associated with sound waves implicitly as follows:

$$\delta_t U + \frac{\partial}{\partial x} \bar{P}^t = -ADVU - \frac{\partial}{\partial \xi} (G^{13}P), \quad (3-6)$$

$$\begin{aligned} \delta_t W + \frac{\tilde{1}}{G^{1/2}} \frac{\partial \bar{P}^t}{\partial \xi} + \frac{\tilde{g}}{Cs^2} \bar{P}^t = & BUOY - ADVW + \left( \frac{\tilde{1}}{G^{1/2}} \frac{\partial}{\partial \xi} - \frac{1}{G^{1/2}} \frac{\partial}{\partial \xi} \right) P \\ & + \left( \frac{\tilde{g}}{Cs^2} - \frac{g}{Cs^2} \right) P, \end{aligned} \quad (3-7)$$

and

$$\delta_t P + Cs^2 \text{DIVS}(\bar{U}^t, \bar{W}^t) = Cs^2 (\text{PFT} - \text{DIVR}(U, W)) \quad (3-8a)$$

$$\frac{1}{Cs^2} \delta_t P + \frac{\partial}{\partial x} \bar{U}^t + \frac{\tilde{1}}{G^{1/2}} \frac{\partial \bar{W}^t}{\partial \xi} = \text{PFT} + \left( \frac{\tilde{1}}{G^{1/2}} - \frac{1}{G^{1/2}} \right) \frac{\partial W}{\partial \xi} - \frac{\partial}{\partial \xi} (G^{13}U). \quad (3-8b)$$

Here, operators DIVR and DIVS are defined by Eqs. (2-1) and (2-2). From Eqs. (2-7), (3-6) and (3-7), boundary conditions are obtained as follows:

$$\frac{\tilde{1}}{G^{1/2}} \frac{\partial \bar{P}^t}{\partial \xi} + \frac{\tilde{g}}{Cs^2} \bar{P}^t + G^{1/2} G^{13} \frac{\partial}{\partial x} \bar{P}^t = \text{FPBE}. \quad (3-9)$$

All terms on the righthand sides of Eqs. (3-6), (3-7), (3-8) and (3-9) are known.  $\bar{P}^t$ ,  $\bar{U}^t$  and  $\bar{W}^t$  are regarded as unknown variables, and the equation for  $\bar{P}^t$  is obtained, which is similar to that of AE for the case of no-orography, except for the boundary conditions. However, the boundary condition Eq. (3-9) requires iteration since  $G^{1/2} G^{13}$  is dependent on both  $x$  and  $\xi$ .

## c) E-HI-VI-NI

To avoid iteration completely, a slight change in the boundary condition Eq. (3-9) is made as follows:

$$\frac{\tilde{1}}{G^{1/2}} \frac{\partial \bar{P}^t}{\partial \xi} + \frac{\tilde{g}}{C_s^2} \bar{P}^t = -G^{1/2} G^{13} \frac{\partial}{\partial x} P + \text{FPBE}. \quad (3-10)$$

The elliptic equation for  $\bar{P}^t$  obtained from Eqs. (3-6), (3-7), (3-8) and (3-10) needs no iteration. However, this boundary condition is not consistent with Eqs. (2-7), (3-6), (3-7) and (3-8) unless  $U$  at the lower boundary is always zero due to the non-slip condition at the lower boundary, and imposes erroneous forcing at the boundary which is large for a steep slope. This method will be called E-HI-VI-NI hereafter.

## d). Discussion on the stability of E-HI-VI scheme

If the mountain is very high or steep, the terms associated with sound waves, which are transferred to the righthand sides for convenience, become large in both E-HI-VI-PI and E-HI-VI-NI. For E-HI-VI-NI, the boundary condition, Eq. (3-8), is not exact for the free-slip lower boundary condition. Kurihara (1965) examined the instability of a partially implicit method for a simple hyperbolic equation. The partially semi-implicit method for the primitive equations has experienced instability for the case in which the deviation from the basic reference state is large (Simmons *et al.*, 1978). The conjecture that E-HI-VI-PI and E-HI-VI-NI are subject to instability should be checked in a linear stability analysis and numerical experiments.

The linear stability analysis for sound waves in a nonorographic E-HI-VI for the case of  $\alpha = 0$  was given by Tapp and White (1976). That of E-HI-VI-PI for  $0 < \alpha < 1$  with orography will be given in the next subsection B-3-2, where both acoustic and gravity wave modes are taken into account simultaneously. The analysis for only the sound waves shows that, in the case of orography incorporated,  $\alpha = 0$  causes an instability, and  $\alpha > 0$  becomes necessary. However, for a very steep mountain, E-HI-VI-PI is found unstable, no matter what value of  $\alpha$  is chosen in the range  $0 \leq \alpha \leq 1$ . The analysis for both fast and slow modes shows that a weak destabilization occurs even for the case which is shown to be stable by a linear analysis taking into account only sound waves. However, Asselin's (1972) time filter works effectively to suppress this weak destabilization.

**B-3-2. A linear stability analysis of E-HI-VI-PI with orography**

In order to conduct a linear analysis, we simplify the governing equations ((3-6)-(3-9)) of E-HI-VI-PI as follows:

$$\frac{1}{Cs^2} \delta_t P + \frac{\partial}{\partial x} \bar{U}^t + \frac{\partial \bar{W}^t}{\partial \xi} = -\Delta H \frac{\partial W}{\partial \xi} - \Delta G \frac{\partial \bar{U}^{x\xi}}{\partial \xi}, \quad (3-11)^\dagger$$

$$\delta_t U + \frac{\partial}{\partial x} \bar{P}^t = -U_m \frac{\partial U}{\partial x} - \Delta G \frac{\partial}{\partial \xi} \bar{P}^{x\xi}, \quad (3-12)$$

$$\delta_t W + \frac{\partial \bar{P}^t}{\partial \xi} = N\Theta'' - \Delta H \frac{\partial P}{\partial \xi} - U_m \frac{\partial W}{\partial x}, \quad (3-13)$$

$$\delta_t \Theta'' = -NW - U_m \frac{\partial \Theta''}{\partial x}, \quad (3-14)$$

$$\Theta'' = (\Theta'/N)(g\bar{\rho}/\bar{\Theta}), \quad (3-15)$$

where  $U_m$  is the constant of the basic state wind velocity,  $N$  the Brunt-Väisälä frequency defined as  $N^2 \equiv g(\partial\Theta/\partial z)/\bar{\Theta}$ ,  $\Delta H \equiv [1/(1 - Z_s/H) - 1]$  a measure of mountain height,  $\Delta G \equiv G^{13}$  a measure of mountain steepness.

The grid structure is a staggered one, as in Clark (1977) (see section B-5). We substitute the finite difference operators as follows:

$$\left. \begin{aligned} \frac{\partial}{\partial x} &\longrightarrow ik_x^* = i \frac{2 \sin(k_x \Delta x / 2)}{\Delta x}, \\ \frac{\partial}{\partial \xi} &\longrightarrow ik_z^* = i \frac{2 \sin(k_z \Delta \xi / 2)}{\Delta \xi}, \\ \frac{\partial^{-x\xi}}{\partial \xi} &\longrightarrow ik_z^{**} = i \frac{\sin(k_z \Delta \xi) \cos(k_x \Delta \chi)}{\Delta \xi}, \end{aligned} \right\} \quad (3-16)$$

where  $k_x$  and  $k_z$  are horizontal and vertical wave numbers respectively, and  $\Delta \chi$  and  $\Delta \xi$  are horizontal and vertical grid distances respectively, and  $i^2 = -1$ .

<sup>†</sup> Eq. (3-11) should be replaced by

$$\frac{1}{Cs^2} \delta_t P + \frac{\partial}{\partial x} \bar{U}^t + \frac{\partial \bar{W}^t}{\partial \xi} = -\frac{N^2}{g} \left[ W + \frac{U_m}{N} \frac{\partial \Theta''}{\partial x} \right] - \Delta H \frac{\partial W}{\partial \xi} - \Delta G \frac{\partial \bar{U}^{x\xi}}{\partial \xi}.$$

Ikawa (1988) used Eq. (3-11) by mistake. The additional term is assumed to be related to slow modes in the program, and this term is expected to bring about little difference in the qualitative conclusion of the linear analysis made by Ikawa (1988). This expectation is supported by the recent linear analysis made by Gohda and Kurihara (1991).

The equations (3-11)–(3-14) are rewritten in matrix form as follows:

$$S^{it+1} = (\mathbf{A} + 2\Delta t\mathbf{C})^{-1}\mathbf{B}S^{it} + (\mathbf{A} + 2\Delta t\mathbf{C})^{-1}(\mathbf{A} - 2\Delta t\mathbf{D})S^{it-1} \quad (3-17)$$

where

$$\left. \begin{aligned} (S^{it})^{tr} &= (P^{it}, U^{it}, W^{it}, \Theta^{it}) \\ \mathbf{A} &\equiv \begin{bmatrix} 1/Cs^2 & 0 & 0 & 0 \\ 0 & 1 & 0 & 0 \\ 0 & 0 & 1 & 0 \\ 0 & 0 & 0 & 1 \end{bmatrix}, \\ \mathbf{B} &\equiv 2\Delta t \begin{bmatrix} 0 & -\Delta Gik_z^{**} & -\Delta Hik_z^* & 0 \\ -\Delta Gik_z^{**} & -U_m ik_x^* & 0 & 0 \\ -\Delta Hik_z^* & 0 & -U_m ik_x^* & N \\ 0 & 0 & -N & -U_m ik_x^* \end{bmatrix}, \\ \mathbf{C} &\equiv \frac{(1+\alpha)}{2} \begin{bmatrix} 0 & ik_x^* & ik_z^* & 0 \\ ik_x^* & 0 & 0 & 0 \\ ik_z^* & 0 & 0 & 0 \\ 0 & 0 & 0 & 0 \end{bmatrix}, \\ \mathbf{D} &\equiv (1-\alpha)/(1+\alpha)\mathbf{C}, \end{aligned} \right\} \quad (3-18)$$

where superscript  $tr$  denotes the transposed matrix.

If we use Asselin's time filter

$$S^{*it} = S^{it} + \nu(S^{it+1} - 2S^{it} + S^{*it-1}), \quad (3-19)$$

Eq. (3-17) is modified as follows:

$$\begin{bmatrix} S^{it+1} \\ S^{*it} \end{bmatrix} = \begin{bmatrix} (\mathbf{A} + 2\Delta t\mathbf{C})^{-1}\mathbf{B} & (\mathbf{A} + 2\Delta t\mathbf{C})^{-1}(\mathbf{A} - 2\Delta t\mathbf{D}) \\ [(1-2\nu)\mathbf{I} + \nu(\mathbf{A} + 2\Delta t\mathbf{C})^{-1}\mathbf{B}] & \nu(\mathbf{I} + (\mathbf{A} + 2\Delta t\mathbf{C})^{-1}(\mathbf{A} - 2\Delta t\mathbf{D})) \end{bmatrix} \begin{bmatrix} S^{it} \\ S^{*it-1} \end{bmatrix} \quad (3-20)$$

The amplification factor is the eigenvalue of the  $(8 \times 8)$  matrix in Eq. (3-20), and satisfies the 8-th order algebraic equation.

For the case of  $N = 0$ ,  $U_m = 0$  and  $\nu = 0$  (*i.e.*, only the acoustic mode is considered without Asselin's time filter), the characteristic equation is factorized into  $(\lambda^2 - 1)^2$  and the 4-th order algebraic equation with real number coefficients which are given as below:

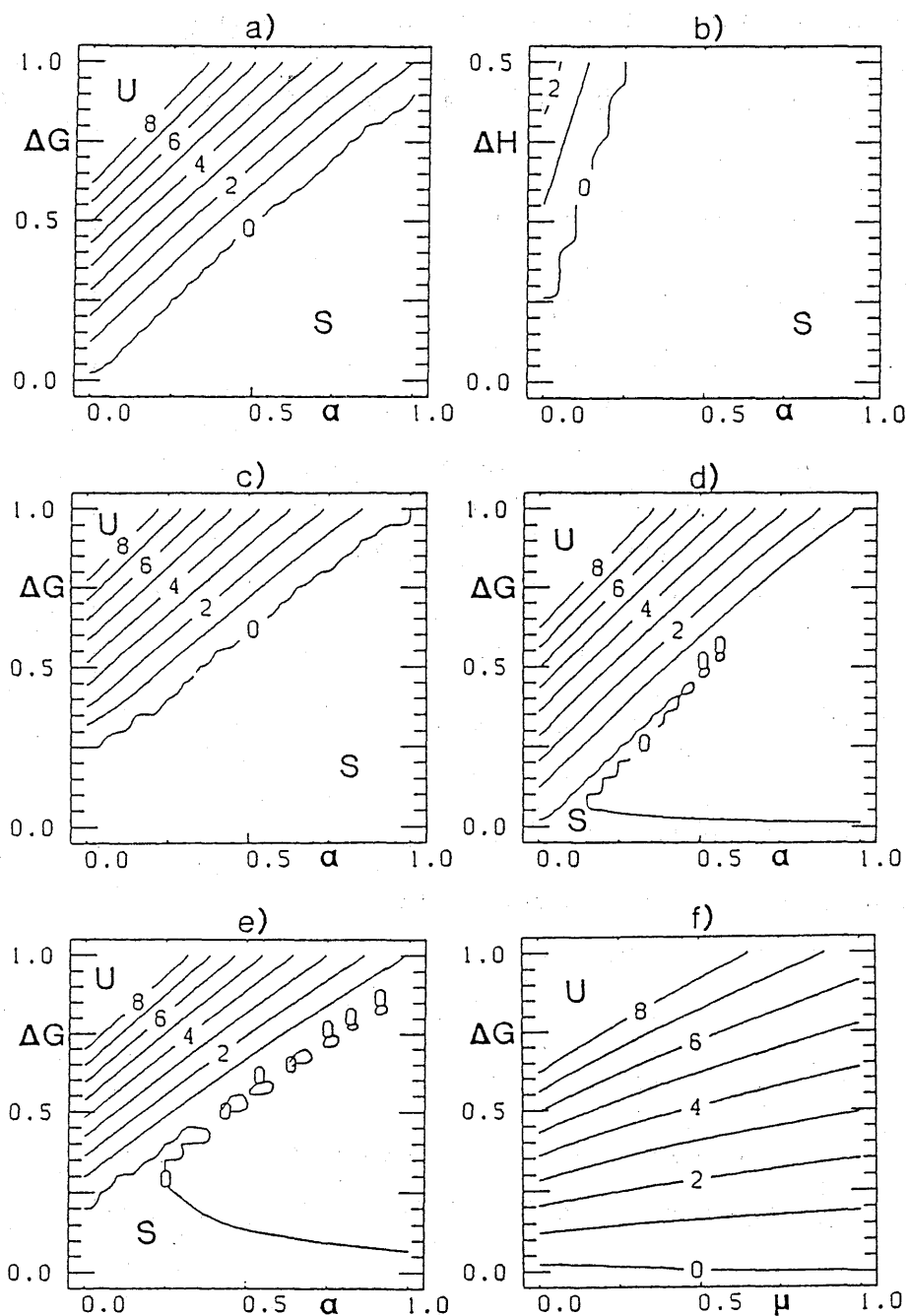


Fig. B-3-1 a, b, c, d, e, f) Amplification factor  $|\lambda|$  of E-HI-VI. The horizontal axis indicates  $\alpha$  varying from 0 to 1 with intervals of 0.05. The vertical axis indicates  $\Delta G = 2\Delta H$  varying from 0 to 1 with intervals of 0.05 unless specifically mentioned. The maximum amplification factor among the cases of  $k_x = 2\pi/\Delta x(i/20)$  (from  $i = -20$  to 20) and  $k_x = 2\pi/\Delta \xi(j/20)$  (from  $j = -20$  to 20) is plotted. The contour line numbered by the integer  $n$  denotes  $|\lambda| = 1 + n \times 0.1$  (the contour interval  $\Delta n$  is 1). The area of  $|\lambda| < 1.00009$  is indicated by S. a) The case of  $N = U_m = 0$ ,

$\nu = 0$ ; analytic solution. **b)** The case of  $N = U_m = 0$ ,  $\nu = 0$  and  $\Delta G = 0$ ; Vertical axis indicates  $\Delta H$ , varying from 0 to 0.5; analytic solution. **c)** The same as a) but for  $\Delta t = 2$  sec; analytic solution. **d)** The case of  $N = 10^{-2}/s$ ,  $U_m = 4m/s$  and  $\nu = 0$ ; numerical solution. **e)** The case of  $N = 10^{-2}/s$ ,  $U_m = 4m/s$  and  $\nu = 0.2$ ; numerical solution. **f)** The case of time averaging by Eq. (3-22),  $N = U_m = 0$ ,  $\nu = 0$ ; numerical solution. The horizontal axis indicates  $\mu$  varying from 0 to 1 with intervals of 0.05. (adapted from Ikawa, 1988)

$$\begin{aligned}
 & \left[ 1 + \left( \frac{1+\alpha}{2} \right)^2 X \right] \lambda^4 + (Cs2\Delta t)^2 (1+\alpha) (k_x^* k_z^{**} \Delta G + k_z^{*2} \Delta H) \lambda^3 \\
 & + 2 \left[ -1 + \left( \frac{1+\alpha}{2} \right) \left( \frac{1-\alpha}{2} \right) X + \frac{(\Delta G k_z^{**})^2 + (\Delta H k_z^*)^2}{2} (Cs2\Delta t)^2 \right] \lambda^2 \\
 & + (Cs2\Delta t)^2 (1-\alpha) (k_x^* k_z^{**} \Delta G + k_z^{*2} \Delta H) \lambda + 1 + \left( \frac{1-\alpha}{2} \right)^2 X = 0, \quad (3-21)
 \end{aligned}$$

where  $X = (Cs2\Delta t)^2 (k_z^{*2} + k_z^{**2})$ . This equation can be solved analytically by Ferrari method<sup>†</sup>. In case of  $\Delta G = \Delta H = 0$  (without orography), we see that the scheme is unconditionally stable;  $\alpha > 0$  gives damping of sound wave mode, and  $\alpha = 0$  gives neither damping nor amplification.

Now, we examine the dependence of stability on  $\alpha$ ,  $\Delta H$  and  $\Delta G$ . Hereafter, parameters  $\Delta x$ ,  $\Delta \xi$ ,  $\Delta t$ ,  $Cs$ ,  $N$  and  $U_m$  are 1200m, 200m, 12s, 340m/s, 0.01/s, 4m/s, respectively, which are the same as were used in the experiments in section 3 of Ikawa (1988). If orography is included, as shown in Fig. B-3-1a,  $\alpha = 0$  gives amplification, and  $\alpha > 0$  becomes necessary for stable time integration. When the ( $\Delta H = a$ ,  $\Delta G = 0$ ) case (Fig. B-3-1b) is compared with the ( $2\Delta H = 0$ ,  $\Delta G = a$ ) case (not shown here) or ( $2\Delta H = a$ ,  $\Delta G = a$ ) (Fig. B-3-1a) with  $0 \leq a \leq 1.0$ , the destabilized area of the case of ( $2\Delta H = a$ ,  $\Delta G = 0$ ) is small. So, it might be said that the steepness ( $\Delta G$ ) destabilizes the scheme more than the height ( $2\Delta H$ ) does. As shown in Fig. B-3-1c, this instability is not suppressed much by a smaller  $\Delta t$ , especially for  $\Delta G > 0.5$ .

For the case of  $N \neq 0$ ,  $U_m \neq 0$  and  $\nu \neq 0$  (i.e., both the gravity wave and the acoustic modes are considered with Asselin's time filter), the amplification factor is obtained numerically<sup>††</sup>. The accuracy of this numerical procedure was checked against the analytical

<sup>†</sup>HITAC mathematical subprogram library 2: subroutine ¥DNAQM is used.

<sup>††</sup>HITAC mathematical subprogram library 2: subroutine ¥ZEFIM is used. First, the matrix is similarly transformed in Hessenberg form. Next, eigenvalues of the Hessenberg matrix are solved by the modified LR method with double precision calculation, where 'L' and 'R' denote lower and upper triangular matrices, respectively.

solution by Ferrari method for the case of  $N = 0$ ,  $U_m = 0$  and  $\nu = 0$ . The difference between the two was found to be below  $2 \times 10^{-6}$ . As shown in Fig. B-3-1d, the inclusion of the slow mode gives a small amplification ( $|\lambda| \geq 1.001$ ) even if  $\alpha > 0$  is used. However, as shown in Fig. B-3-1e, an appropriate Asselin's time filter can reduce the amplification factor below  $|\lambda| \leq 1.00009$  which may cause no trouble in practice. It is noted that, for the case of a very high or very steep mountain ( $2\Delta H = \Delta G = a$ ,  $1 \leq a$ ), no  $\alpha$  ( $0 \leq \alpha \leq 1$ ) or  $\nu$  ( $0 \leq \nu \leq 1$ ) can reduce  $|\lambda|$  below 1.01 ( $\alpha > 1$  degrades the accuracy, so is not considered here).  $\Delta H$  can be decreased by increasing the height of the model domain  $H$ . Therefore, in principle, E-HI-VI-PI cannot be used for the case of a very steep mountain ( $\Delta G \geq 1$ ). This imposes a severe limitation on E-HI-VI-PI, as contrasted with E-HE-VI (see B-4-2).

A different time averaging from the present one Eq. (3-4) such as

$$\bar{f}^t = \frac{1 + \mu}{2} (f^{it+1} + f^{it-1}) - \mu f^{it} \quad (3-22)$$

was proposed by Simmons *et al.* (1978) in order to prevent the instability of a partially semi-implicit method for primitive equations. However, as shown in Fig. B-3-1f, their time averaging is not applicable to the present case. The time averaging is equivalent to the present case of  $N = 0$  and  $U_m = 0$ , if the parameters are set as follows:

$$\begin{aligned} \alpha &= 0, \\ \Delta t &\longrightarrow (1 + \mu)\Delta t, \\ \Delta H \text{ } ikz^* &\longrightarrow ikz^* (\Delta H - \mu)/(1 + \mu) \\ \Delta G \text{ } ikz^{**} &\longrightarrow (\Delta G \text{ } ikz^{**} - i\mu \text{ } kz^*)/(1 + \mu). \end{aligned}$$

Therefore, the method can reduce  $\Delta H$ , but not  $\Delta G$ . The effective  $\Delta G$  depends on  $(kx^*, kz^{**})$  and may have larger values than original ones for some  $(kx^*, kz^{**})$ . Usually, at both slopes of an isolated mountain in the model, the sign of  $\Delta G$  (steepness of a mountain) is opposite to each other and the magnitude of  $\Delta G$  is almost equal to each other.  $\alpha = 0$  and a large  $\Delta G$  cause instability. This is the reason for the futility of the time averaging Eq. (3-22).

### B-3-3. E-HI-VI-PI with $\Delta^2 P$ adopted as an unknown variable

In the program,  $\Delta^2 P$ ,  $\Delta^2 U$  and  $\Delta^2 W$  are adopted instead of  $P$ ,  $U$  and  $W$  as unknown variables in coding E-HI-VI schemes, following Tapp and White (1976). The operator  $\Delta^2$  is defined for any predicted variable  $f$  as

$$\Delta^2 f = 2\bar{f}^t - 2f^{it}, \quad (3-23)$$

$$\bar{f}^t = \frac{1+\alpha}{2} f^{it+1} + \frac{1-\alpha}{2} f^{it-1} = \Delta^2 f/2 + f^{it}, \quad (3-24)$$

$$\begin{aligned} \delta_t f &= \frac{f^{it+1} - f^{it-1}}{2\Delta t} = \frac{\Delta^2 f}{2\Delta t \alpha''} + \frac{(f^{it} - f^{it-1})}{\alpha'' \Delta t} \\ &= \frac{2}{\Delta t \alpha''} (\bar{f}^t - f^{it-1}), \end{aligned} \quad (3-25)$$

$$\alpha'' = 1 + \alpha. \quad (3-26)$$

Prognostic equations for  $U$ ,  $W$  and  $P$  are given in terms of  $\bar{P}^t$ ,  $\bar{U}^t$  and  $\bar{W}^t$  as follows:

$$\delta_t U + \frac{\partial}{\partial x} \bar{P}^t = -ADVU - \frac{\partial}{\partial \xi} (G^{13}P), \quad (3-27)$$

$$\begin{aligned} \delta_t W + \frac{\tilde{1}}{G^{1/2}} \frac{\partial \bar{P}^t}{\partial \xi} + \frac{\tilde{g}}{Cs^2} \bar{P}^t \\ = BUOY - ADVW + \left( \frac{\tilde{1}}{G^{1/2}} - \frac{1}{G^{1/2}} \right) \frac{\partial P}{\partial \xi} + \left( \frac{\tilde{g}}{Cs^2} - \frac{g}{Cs^2} \right) P, \end{aligned} \quad (3-28)$$

and

$$\delta_t P + \tilde{C}s^2 \text{DIVS}(\bar{U}^t, \bar{W}^t) = Cs^2 (\text{PFT} - \text{DIVT}(U, W)) + \tilde{C}s^2 \text{DIVS}(U, W). \quad (3-29)$$

Here, the operators DIVT and DIVS are defined by Eqs. (2-3) and (2-2). The above equations are rewritten in terms of  $\Delta^2 P$ ,  $\Delta^2 U$  and  $\Delta^2 W$  as follows:

$$\frac{\Delta^2 W}{\Delta t \alpha''} + \left( \frac{\tilde{1}}{G^{1/2}} \frac{\partial}{\partial \xi} + \frac{\tilde{g}}{Cs^2} \right) \Delta^2 P = -2ADVW'', \quad (3-30)$$

$$ADVW'' \equiv ADVW - BUOY + \frac{W^{it} - W^{it-1}}{\Delta t \alpha''} + \left( \frac{1}{G^{1/2}} \frac{\partial}{\partial \xi} + \frac{g}{Cs^2} \right) P^{it}. \quad (3-31)$$

$$\frac{\Delta^2 U}{\Delta t \alpha''} + \frac{\partial}{\partial x} \Delta^2 P = -2ADVU'', \quad (3-32)$$

$$ADVU'' \equiv ADVU + \frac{(U^{it} - U^{it-1})}{\Delta t \alpha''} + \frac{\partial P^{it}}{\partial x} + \frac{\partial (G^{13}P^{it})}{\partial \xi}. \quad (3-33)$$

$$\frac{\Delta^2 P}{\tilde{C}s^2 \alpha'' \Delta t} + \text{DIVS}(\Delta^2 U, \Delta^2 W) = -2ADVP'', \quad (3-34)$$

$$ADVP'' \equiv \left( \frac{P^{it} - P^{it-1}}{\Delta t \alpha''} - Cs^2 (\text{PFT} - \text{DIVT}(U, W)) \right) / \tilde{C}s^2. \quad (3-35)$$

Helmholtz equation for  $\Delta^2 P$  is obtained by eliminating  $\Delta^2 U$  and  $\Delta^2 W$  in Eq. (3-34) by use of Eqs. (3-30) and (3-32) as follows:

$$\begin{aligned} & \frac{\Delta^2 P}{(\tilde{C}_s \alpha'' \Delta t)^2} - \frac{\partial^2}{\partial x^2} \Delta^2 P - \frac{\tilde{I}}{G^{1/2}} \frac{\partial}{\partial \xi} \left( \frac{\tilde{I}}{G^{1/2}} \frac{\partial}{\partial \xi} + \frac{\tilde{g}}{C_s^2} \right) \Delta^2 P \\ & = \text{FP.HIP.INV} \equiv -2 \left( \frac{\text{ADVP}''}{\Delta t \alpha''} - \text{DIVS}(\text{ADVU}'', \text{ADVW}'') \right). \end{aligned} \quad (3-36)$$

It is noted that the forcing term for the pressure equation, FP.HIP.INV, includes no  $\Delta^2 P$ . Therefore iteration is not needed from this part. Iteration is needed in order to incorporate exactly the upper and lower boundary conditions.

The upper and lower boundary conditions for E-HI-VI-PI are derived as follows. From Eq. (2-7).

$$\Delta^2 W^* = 0 = \frac{1}{G^{1/2}} \Delta^2 W + G^{13} \Delta^2 U. \quad (3-37)$$

Eliminating  $\Delta^2 U$  and  $\Delta^2 W$  from Eq. (3-37) by use of Eqs. (3-30) and (3-32) yields

$$\left( \frac{\tilde{I}}{G^{1/2}} \frac{\partial}{\partial \xi} + \frac{\tilde{g}}{C_s^2} \right) \Delta^2 P = -2(\text{ADVW}'' + G^{1/2} G^{13} \text{ADVU}'') - G^{1/2} G^{13} \frac{\partial}{\partial x} \Delta^2 P. \quad (3-38)$$

For the iteration procedure, the above equation is written as

$$\left( \frac{\tilde{I}}{G^{1/2}} \frac{\partial}{\partial \xi} + \frac{\tilde{g}}{C_s^2} \right) \Delta^2 P_i = \text{FPB.HIP.INV} + \text{FPB.HIP.VAR}(P_{i-1}), \quad (3-39)$$

$$\text{FPB.HIP.INV} = -2(\text{ADVW}'' + G^{1/2} G^{13} \text{ADVU}''), \quad (3-40)$$

$$\text{FPB.HIP.VAR}(P_{i-1}) = -G^{1/2} G^{13} \frac{\partial}{\partial x} \Delta^2 P_{i-1}. \quad (3-41)$$

Here, suffix  $i$  denotes the value at the  $i$ -th iteration. Eqs. (3-36) and (3-39) are solved by an iterative application of the pressure equation solver mentioned in section B-6.

#### Program Guide

ADVU'', ADVW'' and ADVP'' are set in sub.MODADV in mem.SFXCV. FP.HIP.INV is set in sub.SPFORI in mem.SFXTPG1. FPB.HIP is set in sub.SFPBD and SPFCBD in mem.SFXTPG1.

#### **B-3-4. Implicit treatment of gravity waves in addition to sound waves**

Recently, Tanguay *et al.* (1990), Cullen (1990) and Gouda and Kurihara (1991) independently proposed E-HI-VI schemes which treat implicitly not only sound waves but also

gravity waves. In these schemes, a longer time step can be taken with little computational overhead than an ordinary E-HI-VI scheme. However, these schemes artificially reduce frequencies of gravity wave oscillations which may be of meteorological interest. Here, this version of an E-HI-VI scheme is formulated, although it is not implemented at present.

Prognostic equations for  $U$ ,  $W$ ,  $P$  and  $\theta' \equiv \Theta - \bar{\Theta}(z)$  are given in terms of  $\bar{P}^t$ ,  $\bar{U}^t$ ,  $\bar{W}^t$  and  $\bar{\theta}^t$  as follows:

$$\delta_t U + \frac{\partial}{\partial x} \bar{P}^t = -\text{ADV}U - \frac{\partial}{\partial \xi} (G^{13} P), \quad (3-42)$$

$$\begin{aligned} \delta_t W + \frac{\tilde{1}}{G^{1/2}} \frac{\partial \bar{P}^t}{\partial \xi} + \sigma_g g \left( \frac{\tilde{1}}{C_s^2} \bar{P}^t - \frac{\rho G^{1/2} \bar{\theta}^t}{\bar{\Theta}} \right) \\ = -g G^{1/2} (\rho - \bar{\rho}) - \text{ADV}W + \left( \frac{\tilde{1}}{G^{1/2}} - \frac{1}{G^{1/2}} \right) \frac{\partial P}{\partial \xi} + \sigma_g g \left( \frac{\tilde{1}}{C_s^2} P - \frac{\rho G^{1/2} \theta'}{\bar{\Theta}} \right) \end{aligned} \quad (3-43)$$

$$\rho \equiv \frac{p_0}{R \Theta_m} \left( \frac{\bar{p} + P/G^{1/2}}{p_0} \right)^{C_v/C_p}, \quad (3-44a)$$

$$N^2 \equiv \frac{g}{\bar{\Theta}(z)} \frac{\partial \bar{\Theta}(z)}{\partial z}, \quad (3-44b)$$

$$\rho G^{1/2} \frac{\partial \theta'}{\partial t} + \sigma_g \frac{N^2}{g} \bar{\Theta}(z) \bar{W}^t = -\rho G^{1/2} (\text{ADV}\Theta - \text{DIF}\cdot\Theta - Q/C_p \Pi) + \sigma_g \frac{N^2}{g} \bar{\Theta}(z) W, \quad (3-45)$$

and

$$\begin{aligned} \delta_t P + \tilde{C}_s^2 \left( \text{DIVS}(\bar{U}^t, \bar{W}^t) + \sigma_g \frac{N^2}{g} \bar{W}^t \right) \\ = C_s^2 (\text{PFT} - \text{DIVT}(U, W)) + \tilde{C}_s^2 \left( \text{DIVS}(U, W) + \sigma_g \frac{N^2}{g} W \right), \end{aligned} \quad (3-46)$$

$$\text{PFT} \equiv \frac{\rho G^{1/2}}{\Theta_m} \frac{\partial \Theta'_m}{\partial t} \simeq \frac{\rho G^{1/2}}{\bar{\Theta}} \frac{\partial \theta'}{\partial t} = \frac{\rho G^{1/2} (-\text{ADV}\Theta + \text{DIF}\cdot\Theta + Q/C_p \Pi)}{\bar{\Theta}}$$

$\sigma_g$  is a switching parameter;  $\sigma_g = 1$  for implicit treatment of gravity waves;  $\sigma_g = 0$  for explicit treatment of gravity waves. The operators DIVT and DIVS are defined by Eqs. (2-1) and (2-2). It is noted that the exact buoyancy term  $-g(\rho - \bar{\rho})$  is employed instead of the approximated term by linearization around the basic state. Replacing  $\bar{\rho}$  in Eqs. (1-30)–(1-37) by  $\rho$  given by Eq. (3-44) eliminates errors associated with the advection term shown in Eq. (1-24).

The above equations are rewritten in terms of  $\Delta^2 P$ ,  $\Delta^2 U$ ,  $\Delta^2 W$  and  $\Delta^2 \theta'$  as follows:

$$\frac{\Delta^2 W}{\Delta t \alpha''} + \left( \frac{\tilde{1}}{G^{1/2}} \frac{\partial}{\partial \xi} + \frac{\sigma_g \tilde{g}}{C s^2} \right) \Delta^2 P - \frac{\sigma_g g \rho G^{1/2} \Delta^2 \theta'}{\bar{\Theta}} = -2 \text{ADVW}'' \quad (3-47)$$

$$\text{ADVW}'' \equiv \text{ADVW} + g G^{1/2} (\rho - \bar{\rho}) + \frac{W^{it} - W^{it-1}}{\Delta t \alpha''} + \frac{1}{G^{1/2}} \frac{\partial}{\partial \xi} P^{it}. \quad (3-48)$$

$$\rho G^{1/2} \frac{\Delta^2 \theta'}{\Delta t \alpha''} + \frac{\sigma_g N^2}{g} \bar{\Theta}(z) \Delta^2 W = -2 \text{ADV}\theta'' \quad (3-49)$$

$$\text{ADV}\theta'' \equiv \rho G^{1/2} \left( \text{ADV}\bar{\Theta} - \text{DIF.}\bar{\Theta} - \frac{Q}{C p \Pi} + \frac{\theta'^{it} - \theta'^{it-1}}{\Delta t \alpha''} \right). \quad (3-50)$$

$$\frac{\Delta^2 U}{\Delta t \alpha''} + \frac{\partial}{\partial x} \Delta^2 P = -2 \text{ADV}U'', \quad (3-51)$$

$$\text{ADV}U'' \equiv \text{ADV}U + \frac{(U^{it} - U^{it-1})}{\Delta t \alpha''} + \frac{\partial P^{it}}{\partial x} + \frac{\partial(G^{13} P^{it})}{\partial \xi}. \quad (3-52)$$

$$\frac{\Delta^2 P}{\tilde{C} s^2 \alpha'' \Delta t} + \text{DIVS}(\Delta^2 U, \Delta^2 W) + \frac{\sigma_g N^2}{g} \Delta^2 W = -2 \text{ADVP}'' \quad (3-53)$$

$$\text{ADVP}'' \equiv \left( \frac{P^{it} - P^{it-1}}{\Delta t \alpha''} - C s^2 (\text{PFT} - \text{DIVT}(U, W)) \right) / \tilde{C} s^2 \quad (3-54)$$

Eliminating  $\Delta^2 \theta'$  from Eqs. (3-47) and (3-49) yields

$$\frac{\bar{A} \Delta^2 W}{\Delta t \alpha''} + \left( \frac{\tilde{1}}{G^{1/2}} \frac{\partial}{\partial \xi} + \frac{\sigma_g \tilde{g}}{C s^2} \right) \Delta^2 P = -2 \text{ADVW}''''', \quad (3-55)$$

where

$$\bar{A} \equiv 1 + \sigma_g (\Delta t \alpha'')^2 N^2, \\ \text{ADVW}'''' \equiv \text{ADVW}'' + \frac{\sigma_g g \Delta t \alpha'' \text{ADV}\theta''}{\bar{\Theta}}.$$

The Helmholtz equation for  $\Delta^2 P$  is obtained by eliminating  $\Delta^2 U$  and  $\Delta^2 W$  in Eq. (3-53) by use of Eqs. (3-51) and (3-55) as follows:

$$\frac{\Delta^2 P}{(\tilde{C} s \alpha'' \Delta t)^2} - \frac{\partial^2}{\partial x^2} \Delta^2 P - \left( \frac{\tilde{1}}{G^{1/2}} \frac{\partial}{\partial \xi} + \frac{\sigma_g N^2}{g} \right) \bar{A}^{-1} \left( \frac{\tilde{1}}{G^{1/2}} \frac{\partial}{\partial \xi} + \frac{\sigma_g \tilde{g}}{C s^2} \right) \Delta^2 P \\ = \text{FP.HIP.INV} \\ \equiv -2 \left( \frac{\text{ADVP}''}{\Delta t \alpha''} - \text{DIVS}(\text{ADV}U'', \bar{A}^{-1} \text{ADVW}''''') - \frac{\sigma_g N^2 \bar{A}^{-1} \text{ADVW}'''''}{g} \right). \quad (3-56)$$

It is noted that the forcing term for the pressure equation, FP.HIP.INV, includes no  $\Delta^2 P$ . Therefore iteration is not needed from this part. Iteration is needed in order to incorporate exactly the upper and lower boundary conditions.

In finite discretization form,  $\bar{A}$  is a matrix. Unless  $W$  and  $\theta'$  are placed on the same vertical level, the matrix  $\bar{A}$  is not a diagonal matrix, and finite discretization of Eq. (3-56) becomes complex due to the complexity of  $\bar{A}^{-1}$ , the inverse of  $\bar{A}$ .

The upper and lower boundary conditions for E-HI-VI-PI are derived as follows. From Eq. (2-7),

$$\Delta^2 W^* = 0 = \frac{1}{G^{1/2}} \Delta^2 W + G^{13} \Delta^2 U. \quad (3-57)$$

Eliminating  $\Delta^2 U$  and  $\Delta^2 W$  from Eq. (3-57) by use of Eqs. (3-51) and (3-55) yields

$$\begin{aligned} & \left( \frac{\tilde{1}}{G^{1/2}} \frac{\partial}{\partial \xi} + \frac{\tilde{g}}{Cs^2} \right) \Delta^2 P \\ & = -2(\text{ADVW}'''' + \bar{A}G^{1/2}G^{13}\text{ADVU}'') - \bar{A}G^{1/2}G^{13} \frac{\partial}{\partial x} \Delta^2 P. \end{aligned} \quad (3-58)$$

For the iteration procedure, the above equation is written as:

$$\left( \frac{\tilde{1}}{G^{1/2}} \frac{\partial}{\partial \xi} + \frac{\tilde{g}}{Cs^2} \right) \Delta^2 P_i = \text{FPB.HIP.INV} + \text{FPB.HIP.VAR}(P_{i-1}) \quad (3-59)$$

$$\text{FPB.HIP.INV} = -2(\text{ADVW}'''' + \bar{A}G^{1/2}G^{13}\text{ADVU}'') \quad (3-60)$$

$$\text{FPB.HIP.VAR}(P_{i-1}) = -\bar{A}G^{1/2}G^{13} \frac{\partial}{\partial x} \Delta^2 P_{i-1}. \quad (3-61)$$

Here, suffix  $i$  denotes the value at the  $i$ -th iteration. Eqs. (3-56) and (3-58) are solved by an iterative application of the pressure equation solver mentioned in section B-6.

## B-4. E-HE-VI (elastic-horizontally explicit-vertically implicit) scheme

In this scheme, sound waves are included, and the equations in B-1-3 with substitution of  $\sigma = 1$  and  $\rho = \bar{\rho}$  are used. In the time integration, terms related to sound waves are treated explicitly in the horizontal direction and implicitly in the vertical direction. In addition, a time-splitting method is used for economical computation. There are a variety of so called "time splitting" methods. The time splitting technique used here is illustrated in Fig. B-4-1, and is the same as is used by Durran and Klemp (1983) and Horibata (1986, 1987).

### B-4-1. Formulation of E-HE-VI scheme with $\bar{P}^\tau$ as unknown

The formulation is as follows:

$$\delta\tau U + \frac{\partial}{\partial x} P + \frac{\partial}{\partial \xi} (G^{13} P) = -ADVU, \quad (4-1)$$

$$\delta\tau W + \frac{1}{G^{1/2}} \frac{\partial \bar{P}^{\tau\beta}}{\partial \xi} + \frac{g \bar{P}^{\tau\beta}}{Cs^2} = \text{BUOY} - ADVW, \quad (4-2)$$

$$\frac{1}{Cs^2} \delta\tau P + \frac{\partial}{\partial x} \bar{U}^{\tau\gamma} + \frac{1}{G^{1/2}} \frac{\partial \bar{W}^{\tau\beta}}{\partial \xi} + \frac{\partial}{\partial \xi} (G^{13} \bar{U}^{\tau\gamma}) = \text{PFT}, \quad (4-3)$$

$$\bar{f}^{\tau\beta} = \frac{1+\beta}{2} f^{\tau+\Delta\tau} + \frac{1-\beta}{2} f^\tau, \quad (4-4)$$

$$\bar{f}^{\tau\gamma} = \frac{1+\gamma}{2} f^{\tau+\Delta\tau} + \frac{1-\gamma}{2} f^\tau \quad (4-5)$$

and

$$\delta\tau f = \frac{f^{\tau+\Delta\tau} - f^\tau}{\Delta\tau} = \frac{2}{\Delta\tau(1+\beta)} (\bar{f}^{\tau\beta} - f^\tau), \quad (4-6)$$

where  $\tau$  denotes a small time step.

Small time step integration is made for terms related to sound waves on the left side of Eqs. (4-1)–(4-3), with the other terms fixed which are evaluated at the large time step,  $t$ . The leap-frog method is used for the large time step integration. The upper and lower boundary conditions are given by Eq. (2-7). From Eqs. (4-1) through (4-6), the one-dimensional Helmholtz-type elliptic equation for  $\bar{P}^{\tau\beta}$  is obtained as follows:

$$\begin{aligned} & \frac{1}{(G^{1/2})^2} \frac{\partial^2 \bar{P}^{\tau\beta}}{\partial \xi^2} + \frac{1}{G^{1/2}} \frac{\partial}{\partial \xi} \left( \frac{g}{Cs^2} \bar{P}^{\tau\beta} \right) - \frac{1}{(Cs\Delta\tau)^2} \left( \frac{2}{1+\beta} \right)^2 \bar{P}^{\tau\beta} \\ & = \text{FP.HE.INV} + \text{FP.HE.VAR}(\tau), \end{aligned} \quad (4-7)$$

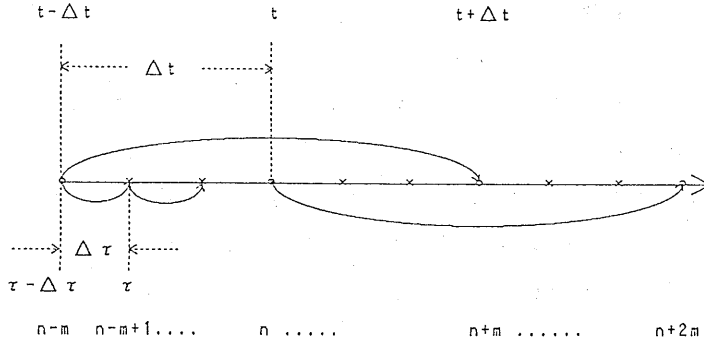


Fig. B-4-1 A schematic illustration of the time "splitting" method used here.  $\Delta\tau$  is the time interval of the small time step integration.  $\Delta t$  is the time interval of the large time step integration.  $Ns = 2\Delta t/\Delta\tau = 2m$  is the number of small time step integration during one large leap-frog time integration. (adapted from Ikawa, 1988)

$$\text{FP.HE.INV} = -\frac{2}{\Delta\tau(1+\beta)} \text{PFT} + \frac{1}{G^{1/2}} \frac{\partial}{\partial\xi} (\text{BUOY} - \text{ADVW}) \quad (4-8)$$

$$\begin{aligned} \text{FP.HE.VAR}(\tau) = \frac{2}{\Delta\tau(1+\beta)} & \left( \frac{\partial \bar{U}^{\tau\gamma}}{\partial x} + \frac{\partial G^{13} \bar{U}^{\tau\gamma}}{\partial \xi} + \frac{1}{G^{1/2}} \frac{\partial \bar{W}^{\tau}}{\partial \xi} \right) \\ & - \frac{1}{(Cs\Delta\tau)^2} \left( \frac{2}{1+\beta} \right)^2 P^{\tau}. \end{aligned} \quad (4-9)$$

The upper and lower boundary conditions are obtained from Eqs. (2-7), (4-1) and (4-2) as:

$$\frac{1}{G^{1/2}} \frac{\partial \bar{P}^{\tau\beta}}{\partial \xi} + \frac{g\bar{P}^{\tau\beta}}{Cs^2} = \text{FPB.INV.HE} + \text{FPB.VAR.HE}(\tau), \quad (4-10)$$

$$\text{FPB.INV.HE} = -\text{ADVW} + \text{BUOY}, \quad (4-11)$$

$$\text{FPB.VAR.HE}(\tau) = \frac{W^{\tau} + G^{1/2} G^{13} U^{\tau+\Delta\tau}}{\Delta\tau}. \quad (4-12)$$

The one-dimensional elliptic equation is solved more easily than 2- or 3-dimensional elliptic equations for AE and E-HI-VI schemes.

A linear stability analysis for the small time step integration is given by Horibata (1986, 1987) with  $\gamma = 1$ , who emphasized the merit of using  $\beta = 1$ . That with  $\gamma \geq 1$  for a whole time step integration is given in the next subsection B-4-2. The analysis shows that, even if the small time step integration is stable, the whole time step integration becomes weakly unstable. In order to prevent instability of the whole time step integration,  $\gamma > 1$  and Asselin's time filter work well. Using  $\gamma > 1$  effectively damps sound waves with infinite or

large vertical wavelengths.

#### B-4-2. A linear stability analysis of a whole time step integration of E-HE-VI with orography

A linear stability analysis of the small time step integration only is given by Horibata (1986, 1987) for  $\gamma = 1$ . That for the whole time step integration and  $\gamma \geq 1$  is given as follows. We simplify the governing equations (4-1), (4-2), (4-3) as below:

$$\frac{1}{Cs^2} \delta\tau P + \frac{\partial}{\partial x} \bar{U}^{\tau\gamma} + (1 + \Delta H) \frac{\partial \bar{W}^{\tau\beta}}{\partial \xi} + \Delta G \frac{\partial \bar{U}^{\tau\gamma}}{\partial \xi} = 0, \quad (4-13)$$

$$\delta\tau U + \frac{\partial}{\partial x} P + \Delta G \frac{\partial \bar{P}^{x\xi}}{\partial \xi} = -U_m \frac{\partial U}{\partial x}, \quad (4-14)$$

$$\delta\tau W + (1 + \Delta H) \frac{\partial \bar{P}^{\tau\beta}}{\partial \xi} = N\Theta'' - U_m \frac{\partial W}{\partial x}, \quad (4-15)$$

$$\delta\tau \Theta'' = -NW - U_m \frac{\partial \Theta''}{\partial x}. \quad (4-16)$$

For the meaning of symbols,  $\Theta''$ ,  $\Delta H$  and  $\Delta G$ , see B-3-2. Eq. (4-13) should be replaced by

$$\frac{1}{Cs^2} \delta\tau P + \frac{\partial}{\partial x} \bar{U}^{\tau\gamma} + (1 + \Delta H) \frac{\partial \bar{W}^{\tau\beta}}{\partial \xi} + \Delta G \frac{\partial \bar{U}^{\tau\gamma}}{\partial \xi} = -\frac{N^2}{g} \left[ W + \frac{U_m}{N} \frac{\partial \Theta''}{\partial x} \right].$$

Ikawa (1988) used Eq. (4-13) by mistake. The additional term is related to slow modes in the program, and this term is expected to bring about little difference in the qualitative conclusion of the linear analysis made by Ikawa (1988) which will be shown below.

The large time step is at every  $m = \Delta t / \Delta\tau$  small time step, indicated as  $n-m$ ,  $n$ ,  $n+m$ ,  $n+2m$  (see Fig. B-4-1). The terms on the righthand side are evaluated by the values at the large time step  $n$ , and kept constant during the small time step integration from  $(n-m)$  to  $(n+m)$ . One small time step integration from  $(n-m)$  to  $(n-m+1)$  time step is expressed in matrix form using the same symbols defined in subsection B-3-2 as below:

$$S^{n-m+1} = (\mathbf{A} + \Delta\tau \mathbf{C})^{-1} \mathbf{B} S^n + (\mathbf{A} + \Delta\tau \mathbf{C})^{-1} (\mathbf{A} - \Delta\tau \mathbf{D}) S^{n-m} \quad (4-17)$$

where

$$S^{n,tr} \equiv (P^n, U^n, W^n, \Theta''^n)$$

$$\mathbf{A} \equiv \begin{bmatrix} 1/Cs^2 & 0 & 0 & 0 \\ 0 & 1 & 0 & 0 \\ 0 & 0 & 1 & 0 \\ 0 & 0 & 0 & 1 \end{bmatrix}$$

$$\mathbf{B} \equiv \Delta\tau \begin{bmatrix} 0 & 0 & 0 & 0 \\ 0 & -U_m i k_x^* & 0 & 0 \\ 0 & 0 & -U_m i k_x^* & N \\ 0 & 0 & -N & -U_m i k_x^* \end{bmatrix} \quad (4-18)$$

$$\mathbf{C} \equiv \begin{bmatrix} 0 & \frac{1+\gamma}{2} i(k_x^* + \Delta G k_z^{**}) & \frac{1+\beta}{2} \tilde{H} i k_z^* & 0 \\ 0 & 0 & 0 & 0 \\ \frac{1+\beta}{2} \tilde{H} i k_z^* & 0 & 0 & 0 \\ 0 & 0 & 0 & 0 \end{bmatrix} \quad (4-19)$$

$$\mathbf{D} \equiv \begin{bmatrix} 0 & \frac{1-\gamma}{2} i(k_x^* + \Delta G k_z^{**}) & \frac{1-\beta}{2} \tilde{H} i k_z^* & 0 \\ i(k_x^* + \Delta G k_z^{**}) & 0 & 0 & 0 \\ \frac{1-\beta}{2} \tilde{H} i k_z^* & 0 & 0 & 0 \\ 0 & 0 & 0 & 0 \end{bmatrix}$$

$$\tilde{H} = 1 + \Delta H = 1/G^{1/2}.$$

First, we consider only the linear stability of the small time step of the acoustic mode by setting  $\mathbf{B} = \mathbf{0}$ . The amplification factor  $\lambda$  is the eigenvalue of the  $(4 \times 4)$  matrix  $(\mathbf{A} + \Delta\tau\mathbf{C})^{-1}(\mathbf{A} - \Delta\tau\mathbf{D})$ . The characteristic equation for  $\lambda$  is factorized into  $(\lambda - 1)^2$  and the following equation:

$$\begin{aligned} & \left[ \frac{1}{(C_s \Delta\tau)^2} + (k_z^* \tilde{H})^2 \left( \frac{1+\beta}{2} \right)^2 \right] \lambda^2 \\ & + \left[ \frac{1+\gamma}{2} (k_x^* + G k_z^{**})^2 - \frac{2}{(C_s \Delta\tau)^2} + \frac{1-\beta^2}{2} (k_z^* \tilde{H})^2 \right] \lambda \\ & + \frac{1}{(C_s \Delta\tau)^2} + (k_z^* \tilde{H})^2 \left( \frac{1-\beta}{2} \right)^2 + \frac{1-\gamma}{2} (k_x^* + \Delta G k_z^{**})^2 = 0. \end{aligned} \quad (4-20)$$

The necessary and sufficient condition for  $|\lambda| \leq 1$  is

$$\begin{aligned} & \beta \geq 0, \quad \gamma \geq 1, \\ & \frac{1}{(C_s \Delta\tau)^2} \geq \frac{(k_x^* + \Delta G k_z^{**})^2}{4} \gamma - \frac{(k_z^* \tilde{H})^2}{4} \beta^2. \end{aligned} \quad (4-21)$$

Under this condition, a measure of the amplification factor is given as

$$|\lambda_1 \lambda_2| = \frac{\frac{1}{(Cs\Delta\tau)^2} + (k_z^* \tilde{H})^2 \left(\frac{1-\beta}{2}\right)^2 + \frac{1-\gamma}{2} (k_x^* + \Delta G k_z^*)^2}{\frac{1}{(Cs\Delta\tau)^2} + (k_z^* \tilde{H})^2 \left(\frac{1+\beta}{2}\right)^2}, \quad (4-22)$$

where  $\lambda_1$  and  $\lambda_2$  are the two roots of Eq. (4-20).

Neutral amplification for all  $k_x^*$ ,  $k_z^{**}$  and  $k_x^*$  is given only by  $\beta = 0$  and  $\gamma = 1$ . When  $\beta > 0$  and  $\gamma = 1$ , sound waves of  $k_z^* \neq 0$  are damped, but sound waves of  $k_z^* = 0$  are not. In order to damp sound waves of  $k_z^* = 0$ ,  $\gamma > 1$  becomes necessary. As pointed out by Horibata (1987), inclusion of orography requires the time step interval  $\Delta\tau$  to be restrictive. The condition of  $\beta > 0$  relaxes the criterion of  $\Delta\tau$  for stability of the scheme in addition to damping sound waves, but the condition of  $\gamma > 1$  requires a smaller  $\Delta\tau$  for stability of the scheme than  $\gamma = 1$ .

Using the eigen-vector matrix of  $(\mathbf{A} + \Delta\tau\mathbf{C})^{-1}(\mathbf{A} - \Delta\tau\mathbf{D})$  which is obtained analytically, we simplify the equation (4-17) as below.

$$T^{n-m+1} = \mathbf{F}T^n + \mathbf{E}T^{n-m} \quad (4-23)$$

$$T^n = \mathbf{X}^{-1}\mathbf{S}^n; \quad \mathbf{F} = \mathbf{X}^{-1}(\mathbf{A} + \Delta\tau\mathbf{C})^{-1}\mathbf{B}\mathbf{X}$$

$$(\mathbf{A} + \Delta\tau\mathbf{C})^{-1}(\mathbf{A} - \Delta\tau\mathbf{D})\mathbf{X} = \mathbf{X}\mathbf{E} \quad (4-24)$$

$\mathbf{X}$ :  $(4 \times 4)$  eigen-vector matrix;

$\mathbf{E}$ :  $(4 \times 4)$  diagonal matrix with diagonal elements of eigen-values.

This transformation makes the numerical computation more accurate as well as making clear the relation between the small and the large time step integration. A whole time step integration from  $(n - m)$  to  $(n + m)$  is expressed as

$$T^{n+m} = (\mathbf{I} + \mathbf{E} + \dots + \mathbf{E}^{2m-1})\mathbf{F}T^n + \mathbf{E}^{2m}T^{n-m}. \quad (4-25)$$

The linear stability analysis of the case  $\mathbf{F} = \mathbf{0}$  (sound wave modes only) is modified by  $\mathbf{F}$  and  $Ns = 2m$  in a large time step integration. If Asselin's time filter is applied at every large time step integration, the whole equation is given as below:

$$\begin{bmatrix} T^{n+m} \\ T^{*n} \end{bmatrix} = \begin{bmatrix} (\mathbf{I} + \mathbf{E} + \dots + \mathbf{E}^{2m-1})\mathbf{F} & \mathbf{E}^{2m} \\ (1 - 2\nu)\mathbf{I} + \nu(\mathbf{I} + \mathbf{E} + \dots + \mathbf{E}^{2m-1})\mathbf{F} & \nu(\mathbf{I} + \mathbf{E}^{2m}) \end{bmatrix} \begin{bmatrix} T^n \\ T^{*n-m} \end{bmatrix}, \quad (4-26)$$

where

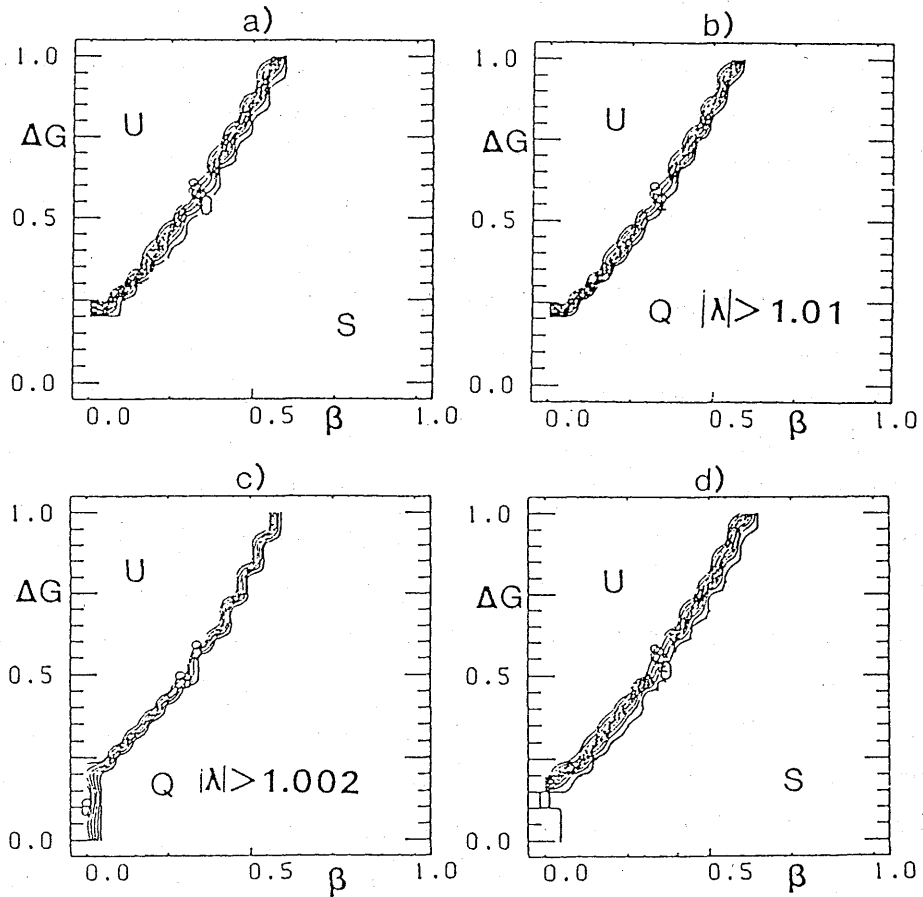


Fig. B-4-2 a, b, c, d) Amplification factor  $|\lambda|$  of E-HE-VI. The horizontal axis indicates  $\beta$ , varying from 0 to 1. The vertical axis indicates  $\Delta G = 2\Delta H$  varying from 0 to 1 with an interval of 0.05. The maximum amplification factor among the cases of  $kx = 2\pi/\Delta x(i/20)$  (from  $i = -20$  to 20) and  $kz = 2\pi/\Delta z(j/20)$  (from  $j = -20$  to 20) is plotted. The contour line numbered by  $n$  denotes  $|\lambda| = 1 + n \times 0.1$  (the contour interval  $\Delta n$  is 1), except for c). The area of  $|\lambda| > 1.8$  is indicated by U except for c); the area of  $|\lambda| < 1.00009$  is indicated by S. a) The case of  $F = 0$  ( $N = U_m = 0$ ) and  $(\gamma, \nu) = (1, 0)$ ; analytic solution. b) The case of  $F \neq 0$  ( $N = 10^{-2}/s$ ,  $U_m = 4\text{m/s}$ ) and  $(\gamma, \nu) = (1, 0)$ ; numerical solution; the area of  $1.01 < |\lambda| < 1.1$  is indicated by Q. c) The case of  $F \neq 0$  ( $N = 10^{-2}/s$ ,  $U_m = 4\text{m/s}$ ) and  $(\gamma, \nu) = (1, 0.2)$ ; numerical solution; The contour line numbered by  $n$  denotes  $|\lambda| = 1 + n \times 0.001$  (the contour interval  $\Delta n$  is 1). The area of  $|\lambda| > 1.008$  is indicated by U; the area of  $1.002 < |\lambda| < 1.003$  is indicated by Q. d) The case of  $F \neq 0$  ( $N = 10^{-2}/s$ ,  $U_m = 4\text{m/s}$ ) and  $(\gamma, \nu) = (1.1, 0.2)$ ; numerical solution. (adapted from Ikawa, 1988)

$$T^{*n} = T^n + \nu(T^{n+m} - 2T^n + T^{*n-m}).$$

The amplification factor is the eigenvalue of the  $(8 \times 8)$  matrix in Eq. (4-26), and solved numerically by the same procedure mentioned in the subsection B-3-2.

Next, the dependence of stability on  $\beta$ ,  $\gamma$ ,  $\nu$ ,  $\Delta H$  and  $\Delta G$  is examined for the parameters  $(\Delta x, \Delta \xi, \Delta t, \Delta \tau, Cs, N, U_m) = (1200\text{m}, 200\text{m}, 12\text{s}, 3\text{s}, 340\text{m/s}, 0.01/\text{s}, 4\text{m/s})$ , which are the same as used in the experiments in section 3 of Ikawa (1988), unless specifically mentioned. Fig. B-4-2a shows the amplification factor for the case of  $\mathbf{F} = \mathbf{B} = \mathbf{0}$  (acoustic mode only;  $U_m = 0\text{m/s}$  and  $N = 0/\text{s}$ ) with  $\gamma = 1$  and  $\nu = 0$ , which is obtained analytically. The unstable area at  $(0 \leq \beta \leq 0.2, 0.4 \leq 2\Delta H = \Delta G)$  is due to the violation of the stability criterion Eq. (4-21) for  $\Delta \tau$ . This area can be removed by a smaller  $\Delta \tau$ . An appropriate choice of  $\beta$  reduces  $|\lambda|$  below 1.00009, which would practically result in no instability. Fig. B-4-2b shows the amplification factor for the case of  $\mathbf{F} \neq \mathbf{0}$  with  $\gamma = 1$  and  $\nu = 0$ , which is obtained numerically. It is found that, even if a small time step integration is stable, a whole time step integration becomes unstable, even though it is weak ( $1.006 \leq |\lambda| \leq 1.007$ ). Fig. B-4-2c shows the amplification factor of the case of  $\mathbf{F} \neq \mathbf{0}$  with  $\gamma = 1$  and  $\nu = 0.2$ . As compared with Fig. B-4-2b,  $|\lambda|$  becomes small, but the minimum  $|\lambda|$  is above 1.003. This remaining weak instability comes from sound waves with  $kz^* = 0$ . Fig. B-4-2d shows the amplification factor of the case of  $\mathbf{F} \neq \mathbf{0}$  with  $\gamma = 1.1$  and  $\nu = 0.2$ . An appropriate choice of  $\beta$  reduces  $|\lambda|$  below 1.0009. As shown by these figures, in order to be stable in a whole time step integration,  $\beta > 0$ ,  $\gamma > 1$  and Asselin's time filter work well.

## B-5. Grid structure, variable grid and finite discretization form

### B-5-1. Grid structure

The staggered grid shown in Fig. B-5-1 is adopted (see Clark, 1977). Prognostic variables other than velocity components are located on the grid point indexed by integer  $(i, j, k)$ . Velocity components,  $U$ ,  $V$  and  $W$ , are located on the grid points indexed by the half integer  $(i + 1/2, j, k)$ ,  $(i, j + 1/2, k)$  and  $(i, j, k + 1/2)$ , respectively. The density of the reference atmosphere  $\bar{\rho}$  is located on the grid point  $(i, j, k)$ .  $G^{1/2}$  and  $Z_s$  are located on the grid point  $(i, j)$ , independent of  $k$ .

As shown in Figs. B-5-2 and B-5-3, boundaries of the model domain are located at  $(1 + 1/2, j, k)$  and  $(nx - 1/2, j, k)$  for the  $y$ - $z$  boundaries, at  $(i, 1 + 1/2, k)$  and  $(i, ny - 1/2, k)$  for the  $x$ - $z$  boundaries and at  $(i, j, 1 + 1/2)$  and  $(i, j, nz - 1/2)$  for the  $x$ - $y$  boundaries. On these boundary planes, velocity components normal to the planes are placed.

### Program Guide

In the program, the array index  $(IX, JY, KZ)$  is used instead of the logical index, such as  $(i, j + 1/2, k)$ . Hereafter, the array index is expressed by the capital letters  $(IX, JY, KZ)$ , while the logical index is expressed by small letters, such as  $(i, j, k)$  or  $(i + 1/2, j, k)$ . In Figs. B-5-2, B-5-3, B-5-4 and B-5-5, the array index is also shown. The dimension of the array in program is  $(NX, NY, NZ) = (nx, ny, nz)$ .

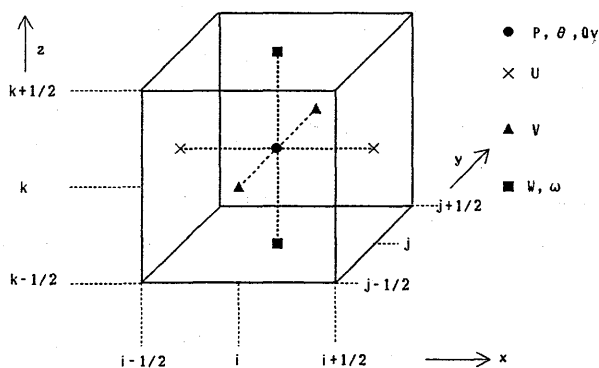


Fig. B-5-1 Staggered grid.



### B-5-2. Variable grid

Figure B-5-4 shows the variable grid structure in the  $z$ -direction. Two kinds of grid intervals are defined.  $\Delta z_k$  represents the grid interval between the two grid points  $(i, j, k - 1/2)$  and  $(i, j, k + 1/2)$ ;  $\Delta z_{k-1/2}$  represents the grid interval between the two grid points  $(i, j, k - 1)$  and  $(i, j, k)$ . As shown in Fig. B-5-4, the following relation between grid intervals  $\Delta z_k$  and  $\Delta z_{k-1/2}$  exists:

$$\Delta z_k = 0.5(\Delta z_{k-1/2} + \Delta z_{k+1/2}). \quad (5-1)$$

The horizontal plane indexed by  $k = 1 + 1/2$  is assumed to be the lower boundary. The height of the grid point  $(i, j, k + 1/2)$  is given as

for  $k = 1$

$$z(k + 1/2) = 0, \quad (5-2)$$

for  $k \geq 2$

$$z(k + 1/2) = \sum_{m=2}^k \Delta z_m.$$

The height of the grid point  $(i, j, k)$  is given as

for  $k = 1$

$$z(k) = -\Delta z_{1+1/2}/2, \quad (5-3)$$

for  $k \geq 2$

$$z(k) = \sum_{m=1}^{k-1} \Delta z_{m+1/2} - \Delta z_{1+1/2}/2. \quad (5-4)$$

The variable grid structure in the  $x$ - and  $y$ -directions is similar to that in the  $z$ -direction. As shown in Fig. B-5-5, the following relations exist:

$$\Delta x_i = 0.5(\Delta x_{i-1/2} + \Delta x_{i+1/2}), \quad (5-5)$$

$$\Delta y_j = 0.5(\Delta y_{j-1/2} + \Delta y_{j+1/2}). \quad (5-6)$$

### B-5-3. Finite discretization form on the variable staggered grid

Averaging operator  $-x$  in the  $x$ -direction is, for any variable  $F$  placed on the grid point indexed by integer, defined by

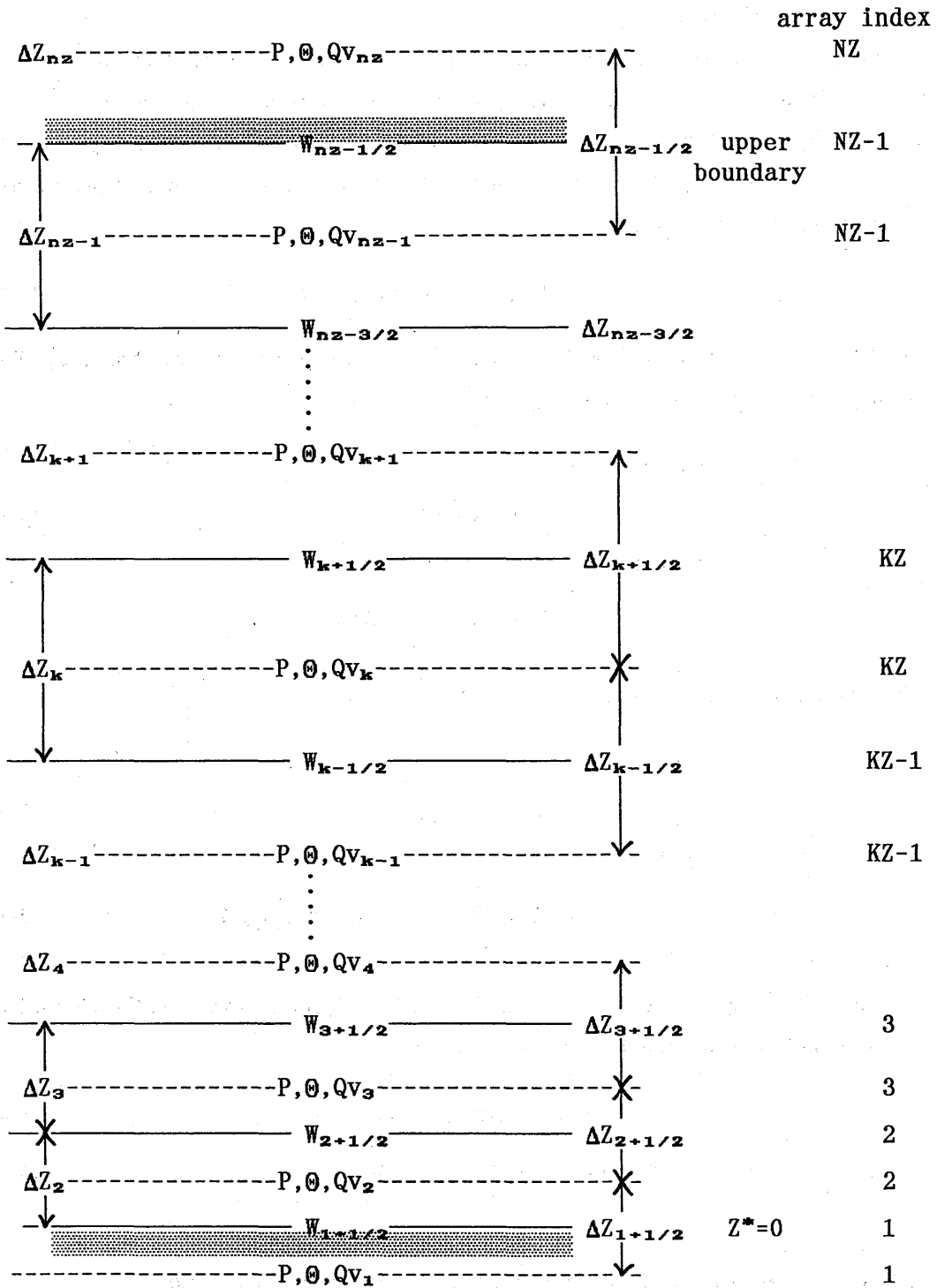


Fig. B-5-4 Variable grid structure in the z-direction.

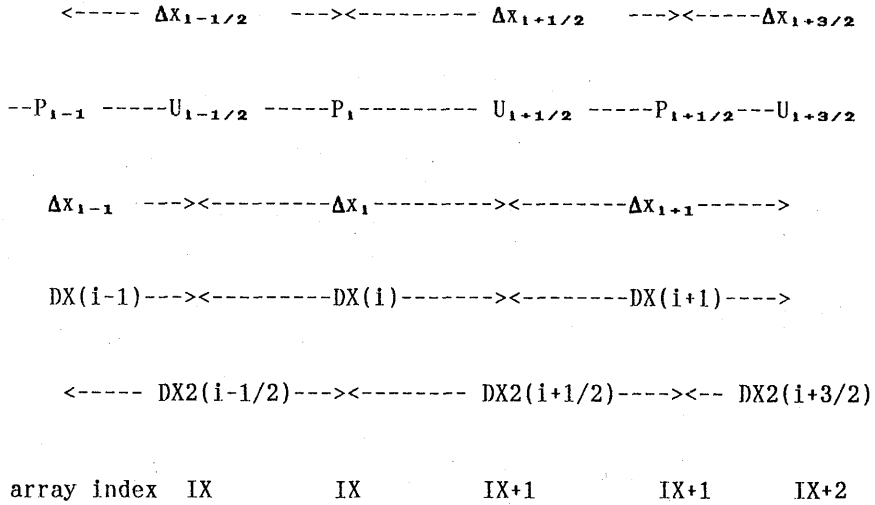


Fig. B-5-5 Variable grid in the  $x$ -direction. Grid interval and grid indexing.

$$\bar{F}^x]_{i+1/2} = \frac{F_i + F_{i+1}}{2}, \quad (5-7)$$

and, for any variable  $U$  placed on the grid point indexed by half integer, by

$$\bar{U}^x]_i = \frac{\Delta x_{i+1/2} U_{i-1/2} + \Delta x_{i-1/2} U_{i+1/2}}{2\Delta x_i}. \quad (5-8)$$

Averaging operators in the  $y$  and  $z$  directions,  $-y$  and  $-z$ , are defined in the same way.

Finite difference operator  $\partial_x$  ( $\partial_y$ ,  $\partial_z$  is defined in the same way) is defined by

$$\partial_x F]_{i-1/2} = \frac{F_i - F_{i-1}}{\Delta x_{i-1/2}}, \quad (5-9a)$$

$$\partial_x U]_i = \frac{U_{i+1/2} - U_{i-1/2}}{\Delta x_i}. \quad (5-9b)$$

Using these operators, terms in governing equations are expressed in finite discretization form as follows (see Clark (1977), p. 193 for more detail):

$G^{13}$  and  $G^{23}$  (Eq. (1-27)) are

$$G^{13}]_{i+1/2, j, k+1/2} = \frac{\bar{I}^x}{G^{1/2}} \left( \frac{\xi}{H} - 1 \right) \frac{\partial Z_s}{\partial x} \quad (5-10a)$$

$$G^{23}]_{i, j+1/2, k+1/2} = \frac{\bar{I}^y}{G^{1/2}} \left( \frac{\xi}{H} - 1 \right) \frac{\partial Z_s}{\partial y} \quad (5-10b)$$

Pressure gradient terms (Eqs. (1-28) and (1-29)) are expressed in discretized form as

$$\text{PFX}]_{i+1/2,j,k} = \partial_x P + \partial_z(G^{13}\overline{P^{xz}}), \quad (5-11)$$

$$\text{PFZ}]_{i,j,k+1/2} = \frac{1}{G^{1/2}} \partial_z P + \frac{g\overline{P^z}}{C_s^2}. \quad (5-12)$$

The operators DIVT and DIVS (see Eqs. (2-3) and (2-2)) are expressed in discretized form as

$$\text{DIVT}(U, W)]_{i,j,k} = \partial_x U + \partial_z(\overline{G^{13}\overline{U^{xz}}}) + \partial_y V + \partial_z(\overline{G^{23}\overline{V^{zy}}}) + \frac{1}{G^{1/2}} \partial_z W, \quad (5-13)$$

$$\text{DIVS}(U, V, W)]_{i,j,k} = \partial_x U + \partial_y V + \frac{\tilde{1}}{G^{1/2}} \partial_z W. \quad (5-14)$$

Eq. (1-31) is expressed in discretized form as

$$U]_{i+1/2,j,k} \equiv \overline{\rho G^{1/2}}^x u, \quad V]_{i,j+1/2,k} \equiv \overline{\rho G^{1/2}}^y v, \quad (5-15)$$

$$W]_{i,j,k+1/2} = \overline{\rho G^{1/2}}^z w, \quad P]_{i,j,k} \equiv G^{1/2} p'.$$

Eqs. (1-32) and (1-33) are expressed in discretized form as

$$\text{ADVU}]_{i+1/2,j,k} = \partial_x(\overline{U^x u^x}) + \partial_y(\overline{V^x v^y}) + \partial_z(\overline{W^{*x} w^z}), \quad (5-16)$$

$$\text{ADV V}]_{i,j+1/2,k} = \partial_x(\overline{U^y v^x}) + \partial_y(\overline{V^y v^y}) + \partial_z(\overline{W^{*y} v^z}), \quad (5-17)$$

$$\text{ADV W}]_{i,j,k+1/2} = \partial_x(\overline{U^z w^x}) + \partial_y(\overline{V^z w^y}) + \partial_z(\overline{W^{*z} w^z}). \quad (5-18)$$

Eq. (1-34) is expressed in discretized form as

$$W^* = \overline{\rho G^{1/2}} \omega]_{i,j,k+1/2} = \frac{1}{G^{1/2}} W + \overline{G^{13}\overline{U^{xz}}} + \overline{G^{23}\overline{V^{zy}}}, \quad (5-19)$$

Eqs. (1-35), (1-36) and (1-37) are expressed in discretized form as

$$\text{BUOY}]_{i,j,k+1/2} = g \frac{\overline{\rho G^{1/2}}^z \theta'_m}{\Theta_m}, \quad (5-20)$$

$$\text{ADV}\theta]_{i,j,k} = \frac{1}{\overline{\rho G^{1/2}}} \{ \partial_x(U\overline{\theta^x}) + \partial_y(V\overline{\theta^y}) + \partial_z(W^*\overline{\theta^z}) \}, \quad (5-21)$$

$$\text{PFT}]_{i,j,k} = \frac{1}{g} \frac{\partial \overline{\text{BUOY}}^z}{\partial t}. \quad (5-22)$$

Program Guide (hereafter, abbreviated as P.G.)

PFX is computed by sub.CPFX where "sub" denotes subroutine.

PFZ is computed by sub.CPFZ.

Conversion from  $W(w)$  to  $OMW = W^*$  (or  $\omega$ ) is made by sub. WCVOMW.

Conversion from  $OMW = W^*$  (or  $\omega$ ) to  $W(w)$  is made by sub. OMWCVW.

Conversion from  $U$  ( or  $V$ ) to  $u(v)$  is made by sub.UCVDNU.

ADVU and ADVW are computed by CADVC3.

ADV $\theta$  or ADVF ( $F = Qv, Qc\dots$ ) is computed by sub.CADVET.

DIVT is computed by sub.SFDIVT in mem.SFXTPG1, where "men" denotes member name in the FORTRAN source file.

DIVS is computed by sub.SFDIV in mem.SFXTPG1.

BUOY is computed by sub.CBUOY3 in mem.SFXTPG1.

## B-6. Pressure equation solver on variable grid

Pressure equation is an elliptic equation (Helmholtz equation for E-HI-VI and Poisson equation for AE) with Neumann type boundary conditions. The solving method of the equation by a direct method (Dimension Reduction Method; e.g., Ogura (1969)) is presented for a non-orographic case here. The elliptic equation to be solved is expressed as

$$\partial_{xx}P + \partial_{yy}P + d\partial_z(d\partial_zP + hP) + eP = F, \quad (6-1)$$

$$d = \frac{\tilde{1}}{G^{1/2}}, \quad h = \frac{\tilde{g}}{Cs^2}, \quad e = \frac{\sigma}{(Cs\alpha''\Delta t)^2}. \quad (6-2)$$

Here,  $\sigma$  is the switching parameter;  $\sigma = 0$  for AE scheme (Eq. (2-5)) and  $\sigma = 1$  for E-HI-VI scheme (Eq. (3-36)). Hereafter,  $d = 1$  is assumed for simplicity.  $h$  and  $e$  are assumed to be dependent on  $z$  but independent of  $x$  and  $y$ .

Lateral boundary conditions are given as

$$\partial_x P = Bx \equiv -\frac{\partial U}{\partial t} - \text{ADVU}, \quad (6-3)$$

$$\partial_y P = By \equiv -\frac{\partial V}{\partial t} - \text{ADVY}. \quad (6-4)$$

Upper and lower boundary conditions are given as

$$\partial_z P + hP = Bz \equiv -\frac{\partial W}{\partial t} - \text{ADVW} + \text{BUOY}. \quad (6-5)$$

### B-6-1. The case of open (noncyclic) lateral boundary conditions

#### a) Finite discretized equation in matrix form

Finite discretization form of Eq. (6-1) on variable grid at  $(i, j, k)$  is as follows:

$$\begin{aligned} & \frac{P_{i+1,j,k}}{\Delta x_{i+1/2}\Delta x_i} - \frac{P_{i,j,k}}{\Delta x_i} \left( \frac{1}{\Delta x_{i+1/2}} + \frac{1}{\Delta x_{i-1/2}} \right) + \frac{P_{i-1,j,k}}{\Delta x_i\Delta x_{i-1/2}} \\ & + \frac{P_{i,j+1,k}}{\Delta y_{i+1/2}\Delta y_i} - \frac{P_{i,j,k}}{\Delta y_i} \left( \frac{1}{\Delta y_{i+1/2}} + \frac{1}{\Delta y_{i-1/2}} \right) + \frac{P_{i,j-1,k}}{\Delta y_i\Delta y_{i-1/2}} \\ & + \frac{1}{\Delta z_k} \left( \frac{1}{\Delta z_{k-1/2}} - \frac{h_{k-1/2}}{2} \right) P_{i,j,k-1} \\ & - \frac{1}{\Delta z_k} \left( \frac{1}{\Delta z_{k-1/2}} + \frac{1}{\Delta z_{k+1/2}} - \frac{h_{k+1/2} - h_{k-1/2}}{2} \right) P_{i,j,k} \\ & + \frac{1}{\Delta z_k} \left( \frac{1}{\Delta z_{k+1/2}} + \frac{h_{k+1/2}}{2} \right) P_{i,j,k+1} + eP_{i,j,k} \\ & = F_{i,j,k}. \end{aligned} \quad (6-6)$$

Finite discretization of boundary conditions Eqs. (6-3)-(6-5) are for  $2 \leq j \leq ny - 1$  and  $2 \leq k \leq nz - 1$

$$\frac{P_{2,j,k} - P_{1,j,k}}{\Delta x_{1+1/2}} = Bx_{;1,j,k}, \quad \frac{P_{nx,j,k} - P_{nx-1,j,k}}{\Delta x_{nx-1/2}} = Bx_{;nx,j,k}, \quad (6-7a)$$

for  $2 \leq i \leq nx - 1$  and  $2 \leq k \leq nz - 1$

$$\frac{P_{i,2,k} - P_{i,1,k}}{\Delta y_{1+1/2}} = By_{;i,1,k}, \quad \frac{P_{i,ny,k} - P_{i,ny-1,k}}{\Delta y_{ny-1/2}} = By_{;i,ny,k}, \quad (6-7b)$$

for  $2 \leq i \leq nx - 1$  and  $2 \leq j \leq ny - 1$

$$\frac{P_{i,j,nz} - P_{i,j,nz-1}}{\Delta z_{k-1/2}} + h_{nz-1/2} \frac{P_{i,j,nz} + P_{i,j,nz-1}}{2} = Bz_{;i,j,nz}, \quad (6-8)$$

$$\frac{P_{i,j,2} - P_{i,j,1}}{\Delta z_{i+1/2}} + h_{1+1/2} \frac{P_{i,j,2} + P_{i,j,1}}{2} = Bz_{;i,j,1}.$$

The element outside the lateral boundary  $P_{1,j,k}$  is eliminated for the practical reason that the same dimension for the matrix  $A$  (see Eq. (6-13)) is applicable to open and cyclic boundary cases as below: At the point  $(2, j, k)$

$$F_{2,j,k} \longleftarrow F_{2,j,k} + \frac{P_{2,j,k} - P_{1,j,k}}{\Delta x_{1+1/2} \Delta x_2} = F_{2,j,k} + \frac{Bx_{;1,j,k}}{\Delta x_2}$$

$$\frac{P_{3,j,k}}{\Delta x_{2+1/2} \Delta x_2} - \frac{P_{2,j,k}}{\Delta x_2 \Delta x_{2+1/2}} \longleftarrow \frac{P_{3,j,k}}{\Delta x_{2+1/2} \Delta x_2} - \frac{P_{2,j,k}}{\Delta x_2} \left( \frac{1}{\Delta x_{2+1/2}} + \frac{1}{\Delta x_{1+1/2}} \right) + \frac{P_{1,j,k}}{\Delta x_2 \Delta x_{1+1/2}}.$$

For other points next to the lateral boundary such as  $(nx-1, j, k)$   $(i, 2, k)$  and  $(i, ny-1, k)$ , the equations are changed in the same manner.

The above equations are written in matrix form as follows:

$$[I \otimes Y_A^{-1} A + Y_B^{-1} B \otimes I] \Pi_{,,k} + r_k \Pi_{,,k+1} + (s_k + e_k) \Pi_{,,k} + t_k \Pi_{,,k-1} = \Phi_{,,k} \quad (6-9)$$

for  $2 \leq k \leq nz - 1$ .

Here  $r_k$ ,  $s_k$  and  $t_k$  are given by Eqs. (6-27)-(6-29) and

$$\Pi_{,,k}^{tr} \equiv (\Pi_{,2,k}^{tr}; \Pi_{,3,k}^{tr}; \dots \dots \dots \Pi_{,ny-1,k}^{tr}), \quad (6-10a)$$

$$\Pi_{,j,k}^{tr} \equiv (P_{2,j,k}; P_{3,j,k}; \dots \dots \dots P_{nx-1,j,k}), \quad (6-10b)$$

$$\Phi_{,,k}^{tr} \equiv (\Phi_{,2,k}^{tr}; \Phi_{,3,k}^{tr}; \dots \dots \dots \Phi_{,ny-1,k}^{tr}), \quad (6-11a)$$

$$\Phi_{j,k}^{tr} \equiv (F_{2,j,k}; F_{3,j,k}; \dots \dots \dots F_{nx-1,j,k}). \quad (6-11b)$$

Superscript  $^{tr}$  denotes the transposed matrix.

$$Y_A \equiv \begin{bmatrix} \Delta x_2 & 0 & 0 & & 0 \\ 0 & \Delta x_3 & 0 & & \\ 0 & 0 & \Delta x_4 & & \\ & & \vdots & & \\ & & & & 0 \\ 0 & & & 0 & \Delta x_{nx-1} \end{bmatrix} \quad (6-12)$$

$$A \equiv \begin{bmatrix} \frac{1}{\Delta x_{2+1/2}}, & \frac{-1}{\Delta x_{2+1/2}}, & & 0, & & 0 \\ \frac{-1}{\Delta x_{2+1/2}}, & \frac{1}{\Delta x_{2+1/2}} + \frac{1}{\Delta x_{3+1/2}}, & \frac{-1}{\Delta x_{3+1/2}}, & & 0, & 0 \\ & & \vdots & & & \\ 0, & \frac{-1}{\Delta x_{i+1/2}}, & \frac{1}{\Delta x_{i+1/2}} + \frac{1}{\Delta x_{i+3/2}}, & \frac{-1}{\Delta x_{i+3/2}}, & 0, & 0 \\ & & \vdots & & & \\ 0, & 0, & \frac{1}{\Delta x_{nx-5/2}}, & \frac{1}{\Delta x_{nx-5/2}} + \frac{1}{\Delta x_{nx-3/2}}, & \frac{-1}{\Delta x_{nx-3/2}} \\ 0 & & 0, & \frac{-1}{\Delta x_{nx-3/2}}, & \frac{1}{\Delta x_{nx-3/2}} \end{bmatrix} \quad (6-13)$$

The matrices,  $Y_B$  and  $B$ , which are associated with finite discretization operators in the  $y$  direction, are defined in a similar way to  $Y_A$  and  $A$  which are associated with finite discretization operators in the  $x$  direction. The symbol  $\otimes$  indicates the tensor product operation, *i.e.*, for the  $(m, m)$  matrix  $M$  and  $(n, n)$  matrix  $N$ ,

$$M \otimes N = \begin{bmatrix} m_{1,1}N & m_{1,2}N & \dots & m_{1,m}N \\ m_{2,1}N & m_{2,2}N & & \\ & & & \\ & & & \\ m_{m,1}N & \dots & \dots & m_{m,m}N \end{bmatrix}, \quad (mn, mn) \text{ matrix.} \quad (6-14)$$

Upper and lower boundary conditions are expressed as

$$-\partial z \Pi_{,,k}|_{k=1+1/2} - h_{1+1/2} \bar{\Pi}_{,,k}^z|_{k=1+1/2} = \Phi_{b,1} \quad (6-15a)$$

$$\partial z \Pi_{,,k}|_{k=nz-1/2} + h_{nz-1/2} \bar{\Pi}_{,,k}^z|_{k=nz-1/2} = \Phi_{b,nz}, \quad (6-15b)$$

where

$$\bar{\Phi}_{b,,1}^{tr} = [\bar{\Phi}_{b,2,1}^{tr}; \bar{\Phi}_{b,3,1}^{tr}; \dots \bar{\Phi}_{b,ny-1,1}^{tr}] \quad (6-15c)$$

$$\bar{\Phi}_{b,j,1}^{tr} = [-Bz_{,2,j,1}; -Bz_{,3,j,1}; \dots -Bz_{,nx-1,j,1}] \quad (6-15d)$$

$$\bar{\Phi}_{b,,nz}^{tr} = [\bar{\Phi}_{b,2,nz}^{tr}; \bar{\Phi}_{b,3,nz}^{tr}; \dots \bar{\Phi}_{b,ny-1,nz}^{tr}] \quad (6-15e)$$

$$\bar{\Phi}_{b,j,nz}^{tr} = [Bz_{,2,j,nz}; Bz_{,3,j,nz}; \dots Bz_{,nx-1,j,nz}]. \quad (6-15f)$$

b) Eigenvector and eigenvalue matrixes

In order to solve Eqs. (6-9) and (6-15) for a variable grid mesh, the generalized eigenvectors for the matrix  $Y_A^{-1}A$  and  $Y_B^{-1}B$  are used. They are defined as follows:

$$AP = Y_A P \Lambda(A), \quad BQ = Y_B Q \Lambda(B) : \quad (6-16a)$$

$P$  and  $Q$ : generalized eigen-vector matrixes normalized as

$$P^{tr} Y_A P = I \text{ and } Q^{tr} Y_B Q = I \quad (\text{note } P^{-1} = P^{tr} Y_A \text{ and } Q^{-1} = Q^{tr} Y_B)$$

$\Lambda(A)$  and  $\Lambda(B)$ : generalized eigenvalue matrixes for  $A$  and  $B$  with only diagonal elements.

$P$  is obtained by a standard procedure, say, Jacobi method, because  $A$  is a symmetric matrix and  $Y_A$  is a positive definite symmetric matrix and written as  $Y_A = L^{tr}L$  for a certain non-singular matrix  $L$ . For the symmetric matrix  $A^* = L^{-1}A(L^{tr})^{-1}$ , the eigen-vector matrix  $P^*$  can be obtained by a standard procedure as

$$A^* P^* = P^* \Lambda(A^*),$$

where  $\Lambda(A^*)$  is the eigen-value matrix of  $A^*$ .

$P$  is calculated from  $P^*$  as

$$P = (L^{tr})^{-1} P^*. \quad (6-16b)$$

Note the following relations:



analogue to taking the Fourier transform of  $P$  in Eq. (6-1)), the following equations are obtained:

$$\begin{aligned}
 & Q^{-1} \otimes P^{-1} [I \otimes Y_A^{-1} A + Y_B^{-1} B \otimes I] \Pi_{,,k} + Q^{-1} \otimes P^{-1} (r_k \Pi_{,,k+1} + s_k \Pi_{,,k} + t_k \Pi_{,,k-1}) \\
 &= Q^{-1} \otimes P^{-1} [I \otimes Y_A^{-1} A + Y_B^{-1} B \otimes I] (Q \otimes P) Q^{-1} \otimes P^{-1} \Pi_{,,k} \\
 &\quad + Q^{-1} \otimes P^{-1} (r_k \Pi_{,,k+1} + s_k \Pi_{,,k} + t_k \Pi_{,,k-1}) \\
 &= [Q^{-1} Q \otimes P^{-1} Y_A^{-1} A P + Q^{-1} Y_B^{-1} B Q \otimes P^{-1} P] Q^{-1} \otimes P^{-1} \Pi_{,,k} \\
 &\quad + Q^{-1} \otimes P^{-1} (r_k \Pi_{,,k+1} + s_k \Pi_{,,k} + t_k \Pi_{,,k-1}) \\
 &= [I \otimes \Lambda(A) + \Lambda(B) \otimes I] Q^{-1} \otimes P^{-1} \Pi_{,,k} \\
 &\quad + (r_k Q^{-1} \otimes P^{-1} \Pi_{,,k+1} + s_k Q^{-1} \otimes P^{-1} \Pi_{,,k} + t_k Q^{-1} \otimes P^{-1} \Pi_{,,k-1}) \\
 &= Q^{-1} \otimes P^{-1} \Phi_{,,k} \tag{6-18}
 \end{aligned}$$

Upper and lower boundary conditions are

$$\begin{aligned}
 & -\partial_z Q^{-1} \otimes P^{-1} \Pi |_{k=1+1/2} - 0.5 h_{1+1/2} (Q^{-1} \otimes P^{-1} \Pi_{,,1} + Q^{-1} \otimes P^{-1} \Pi_{,,2}) \\
 &= Q^{-1} \otimes P^{-1} \Phi_{b,,1} \\
 & \partial_z Q^{-1} \otimes P^{-1} \Pi |_{k=nz} + 0.5 h_{nz-1/2} (Q^{-1} \otimes P^{-1} \Pi_{,,nz-1} + Q^{-1} \otimes P^{-1} \Pi_{,,nz}) \\
 &= Q^{-1} \otimes P^{-1} \Phi_{b,,nz}. \tag{6-19}
 \end{aligned}$$

Define the vectors with  $(nx - 2) \times (ny - 2)$  elements as

$$S_{,,k} \equiv Q^{-1} \otimes P^{-1} \Pi_{,,k}, \tag{6-20}$$

$$R_{,,k} \equiv Q^{-1} \otimes P^{-1} \Phi_{,,k}. \tag{6-21}$$

Let the  $[(nx - 2)(j - 1) + i]$ -th elements of  $S_{,,k}$  and  $R_{,,k}$  be expressed as  $S_{i,j,k}$  and  $R_{i,j,k}$ , respectively, and introduce vectors  $S_{i,j,;}$  and  $R_{i,j,;}$  as

$$S_{i,j,;}^{tr} \equiv (S_{i,j,1}; S_{i,j,2}; \dots S_{i,j,nz}), \tag{6-22}$$

$$R_{i,j,;}^{tr} \equiv (R_{i,j,1}; R_{i,j,2}; \dots R_{i,j,nz}). \tag{6-23}$$



Neumann boundary condition. In this case, the constraint of

$$S_{i_0, j_0, nz-1} + S_{i_0, j_0, nz} = 0 \quad (6-31)$$

is imposed, and the solution is uniquely obtained.

Once  $S_{i,j}$ ; for all  $i$  and  $j$  is obtained,  $\Pi_{,,k}$  is calculated (backward transformation) as

$$\Pi_{,,k} = \mathbf{Q} \otimes \mathbf{P} S_{,,k} \quad (\text{for all } k). \quad (6-32)$$

$P_{i,j,k}$  outside the domain ( $i = 1$  or  $nx$ ;  $j = 1$  or  $ny$ ) are determined from Eqs. (6-7) and (6-8).

The alternative method of solving Eq. (6-24) using the eigen vector matrix  $\mathbf{U}$  for a singular  $\mathbf{C}$  is given as below.

$$\mathbf{C}\mathbf{U} = \mathbf{U}\Lambda(\mathbf{C}); \quad (6-33)$$

$$\mathbf{U}^{-1}\mathbf{C}\mathbf{U}\mathbf{U}^{-1}S_{i,j}; = \Lambda(\mathbf{C})\mathbf{U}^{-1}S_{i,j}; = \mathbf{U}^{-1}R_{i,j}; \quad (6-34)$$

$$S_{i,j}; = \mathbf{U}\Lambda^{-1} * (\mathbf{C})\mathbf{U}^{-1}R_{i,j}; \quad (6-35)$$

where  $\Lambda^{-1} * (\mathbf{C})$  is the quasi-inverse of  $\Lambda(\mathbf{C})$  defined by

$$\Lambda^{-1} * (\mathbf{C}) = \begin{bmatrix} 0 & 0 & & 0 \\ 0 & 1/\lambda_2 & & \\ & & 1/\lambda_2 & \\ & & & 1/\lambda_k \\ 0 & & & & 1/\lambda_{nz} \end{bmatrix} \quad (6-36)$$

with the eigen value  $\lambda_1 = 0$ . This method is not yet implemented.

### B-6-2. The solvability condition and the constraint of mass conservation

The matrix  $\mathbf{C}$  (Eq. (6-25)) becomes singular with rank of  $(nz - 1)$  if  $e = 0$ ,  $\lambda_i(\mathbf{A}) = 0$  and  $\lambda_j(\mathbf{B}) = 0$ , *i.e.*, for the case of Poisson equation (AE scheme) and for the horizontally uniform modes. Here, the singular case ( $e = 0$  case; AE scheme) is considered in detail. Let  $i = 1$  and  $j = 1$  denote the uniform horizontal mode of  $\lambda_i(\mathbf{A}) = 0$  and  $\lambda_j(\mathbf{B}) = 0$ . For simplicity, no mountain is included. For a singular matrix  $\mathbf{C}$ , there exists a nullifying vector  $\mathbf{Z}$  such as

$$\mathbf{Z}^{tr} \mathbf{C} = 0, \quad (6-37)$$

where 0 is the row vector with all elements being zero.

As a result, the following must be satisfied:

$$Z^{tr} CS_{1,1,; } = 0 = Z^{tr} R_{1,1,; } \quad (6-38)$$

$$Z^{tr} = (1, \Delta z_2, \Delta z_3, \dots, \Delta z_{nz-1}, 1). \quad (6-39)$$

Unless  $Z^{tr} R_{1,1,; } = 0$ , Eq. (6-24) is ill-posed, and insolvable. Solvability condition,  $Z^{tr} R_{1,1,; } = 0$ , is related to the mass conservation as delineated below.

Horizontally uniform modes correspond to horizontally averaged modes. Taking horizontal average of Eq. (6-1) yields

$$\begin{aligned} & \iint [\partial_{xx}P + \partial_{yy}P + \partial_{zz}P + \partial_z hP] dx dy \\ & = \iint [-\partial_x ADVU - \partial_y ADVV - \partial_z (ADVW - BUOY)] dx dy \end{aligned} \quad (6-40)$$

By use of lateral boundary conditions Eqs. (6-3) and (6-4), it is rewritten as below.

$$\begin{aligned} \iint [\partial_{zz}P + \partial_z hP] dx dy & = \int \left[ \frac{\partial U_{out}}{\partial t} - \frac{\partial U_{in}}{\partial t} \right] dy + \int \left[ \frac{\partial V_{out}}{\partial t} - \frac{\partial V_{in}}{\partial t} \right] dx \\ & - \partial_z \left( \iint [ADVW - BUOY] dx dy \right). \end{aligned} \quad (6-41)$$

Note that the lefthand side of Eq. (6-41) corresponds to  $CS_{1,1,;}$ ; the righthand side corresponds to  $R_{1,1,;}$ . Roughly speaking, operation of the vector  $Z$  from the left side on Eq. (6-24) corresponds to taking the vertical integration of the above relation, considering upper and lower boundary conditions Eq. (6-5). This yields

$$\int \left( \int \left[ \frac{\partial U_{out}}{\partial t} - \frac{\partial U_{in}}{\partial t} \right] dy + \int \left[ \frac{\partial V_{out}}{\partial t} - \frac{\partial V_{in}}{\partial t} \right] dx \right) dz = 0. \quad (6-42)$$

This is the constraint of the mass conservation over the entire domain. In section B-7, the adjustment to satisfy this constraint on the time derivative of  $U$  and  $V$  on the lateral boundary will be shown. This adjustment is found to be necessary for stable run of the numerical model using both AE and E-HI-VI schemes.

### B-6-3. The case of cyclic lateral boundary conditions

The equation is almost similar to that of the noncyclic case except that the matrix  $A$  (or  $B$ ) is changed as

$A \equiv$

$$\begin{bmatrix} \frac{1}{\Delta x_{1+1/2}} + \frac{1}{\Delta x_{2+1/2}}, & \frac{-1}{\Delta x_{2+1/2}}, & 0, & 0, & \dots & 0, & \frac{-1}{\Delta x_{1+1/2}} \\ \frac{-1}{\Delta x_{2+1/2}}, & \frac{1}{\Delta x_{2+1/2}} + \frac{1}{\Delta x_{3+1/2}}, & & -\frac{1}{\Delta x_{3+1/2}}, & & 0, & 0 \\ & & & \vdots & & & \\ 0, & -\frac{1}{\Delta x_{i+1/2}}, & \frac{1}{\Delta x_{i+1/2}} + \frac{1}{\Delta x_{i+3/2}}, & -\frac{1}{\Delta x_{i+3/2}}, & & 0, & 0 \\ & & & \vdots & & & \\ \frac{-1}{\Delta x_{1+1/2}}, & 0, & \dots & 0, & \frac{-1}{\Delta x_{n-3/2}}, & \frac{1}{\Delta x_{n-3/2}} + \frac{1}{\Delta x_{n-1/2}} \end{bmatrix}$$

(6-43)

Note that  $\Delta x_{1+1/2} = \Delta x_{n-1/2}$  for the cyclic case.

The solving method of the pressure equation for the case of uniform grid and the cyclic boundary conditions is described in detail in Ikawa (1981).

## B-7. Lateral boundary conditions

The model can handle four kinds of lateral boundary conditions as below:

1. Open in the  $x$ -direction and wall in the  $y$ -direction.
2. Open in both  $x$ - and  $y$ -directions.
3. Open in the  $x$ -direction and cyclic in the  $y$ -direction.
4. Cyclic in both  $x$ - and  $y$ -directions.

### B-7-1. Cyclic boundary conditions

For all field variables,  $F$ ,

$$F_{1,j,k} = F_{nx-1,j,k}; \quad F_{nx,j,k} = F_{2,j,k}; \quad \text{for all } j \text{ and } k$$

$$F_{i,1,k} = F_{i,ny-1,k}; \quad F_{i,ny,k} = F_{i,2,k}; \quad \text{for all } i \text{ and } k$$

are imposed.

### B-7-2. Open boundary conditions

- a) For  $\Theta$ ,  $Qv$ ,  $Qc \dots$  and velocity components non-normal to the boundary plane

The boundary is divided into two cases, *i.e.*, inflow and outflow boundaries. The inflow boundary is the boundary where the velocity normal to the boundary plane is directed into the model domain. The outflow boundary is the boundary where the velocity normal to the boundary plane is directed out of the model domain. Let us consider the one dimensional case shown in Fig. B-7-1. In the case of  $U > 0$ , the inflow boundary is the left boundary ( $i = 3/2$ ) and the outflow boundary is the right boundary ( $i = nx - 1/2$ ).

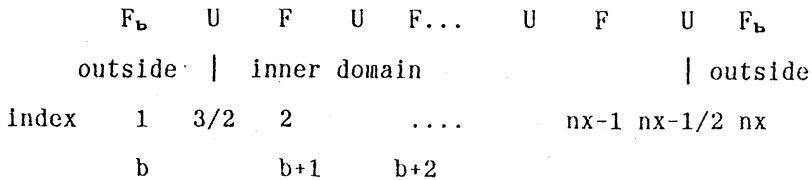


Fig. B-7-1 Grid index used in B-7-2 a).

a-1) At the inflow boundary

Boundary values  $F_b$  are specified as below.

$$F_b^{it+1} = \mu F.\text{ext} + (1 - \mu) F_b^{it-1} \quad (7-1)$$

$F_b$ : the value just outside the boundary

$F.\text{ext}$ : external value specified from outside

a-2) At the outflow boundary

If the left boundary ( $i = 3/2$ ) is the outflow boundary, boundary values are extrapolated from the values of the inner domain as below:

$$F_b^{it+1} = 2F_{b+1}^{it} - F_{b-2}^{it-1} \quad (7-2)$$

For the right boundary case, boundary values are extrapolated in a similar way.

b) Velocity components normal to the boundary plane

For simplicity, the one-dimensional case shown in Fig. B-7-2 is considered. First, the phase speed,  $Cp$ , of waves at the boundary is estimated. Next, it is determined whether waves are outgoing or incoming from the sign of the phase speed. For the outgoing case, a radiation condition is applied.

b-1) At the left boundary (at  $i = JS$ )

The basic equation adopted by Orlanski (1976) is

$$\frac{U^{it}(JS) - U^{it-2}(JS)}{2\Delta t} = \frac{Cp}{\Delta x} \left[ \frac{U^{it}(JS) + U^{it-2}(JS)}{2} - U^{it-1}(JS + 1) \right], \quad (7-3)$$

where  $Cp$  is the phase velocity of waves radiating into outer region.  $Cp$  is estimated as follows: First  $Cp(it - 1)$  is calculated from values at  $it$ ,  $it - 1$  and  $it - 2$  on the inside grid points as

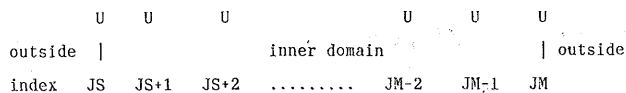


Fig. B-7-2 Grid index used in B-7-2 b).

$$Cp(it-1) = \frac{\Delta x}{\Delta t} \frac{[U^{it}(JS+1) - U^{it-2}(JS+1)]}{[U^{it}(JS+1) + U^{it-2}(JS+1) - 2U^{it-1}(JS+2)]}. \quad (7-4)$$

Next,  $Cp(it-1)$  is modified as

$$Cp^*(it) = \text{MIN} \left( 0, \text{MAX} \left( -\frac{\Delta x}{\Delta t}, Cp(it-1) \right) \right). \quad (7-5)$$

This  $Cp^*(it)$  is an estimator of  $C$ . Substitution of  $C$  by  $Cp^*(t)$  in Eq. (7-3) yields

$$U^{it+1}(JS) = U^{it-1}(JS) + \frac{2\Delta t}{\Delta x} Cp^*(it) \frac{U^{it-1}(JS) - U^{it}(JS+1)}{\left(1 - \frac{\Delta t}{\Delta x} Cp^*(it)\right)}. \quad (7-6)$$

b-2) At the right boundary (at  $i = JM$  in Fig. B-7-2)

In a similar way to the left boundary, the basic equation is

$$\frac{U^{it}(JM) - U^{it-2}(JM)}{2\Delta t} = -\frac{Cp}{\Delta x} \left[ \frac{U^{it}(JM) + U^{it-2}(JM)}{2} - U^{it-1}(JM-1) \right]. \quad (7-7)$$

$Cp$  is estimated as below:

$$Cp(it-1) = -\frac{\Delta x}{\Delta t} \frac{[U^{it}(JM-1) - U^{it-2}(JM-1)]}{[U^{it}(JM-1) + U^{it-2}(JM-1) - 2U^{it-1}(JM-2)]}. \quad (7-8)$$

Modification of  $Cp(it)$  gives  $Cp^*(it)$  as

$$Cp^*(it) = \text{MAX} \left( 0, \text{MIN} \left( \frac{\Delta x}{\Delta t}, Cp(it-1) \right) \right). \quad (7-9)$$

This  $Cp^*(it)$  is an estimator of  $Cp$ . Substitution of  $Cp$  by  $Cp^*(it)$  in Eq. (7-7) yields

$$U^{it+1}(JM) = U^{it-1}(JM) + \frac{2\Delta t}{\Delta x} Cp^*(it) \frac{U^{it}(JM-1) - U^{it-1}(JM)}{\left(1 + \frac{\Delta t}{\Delta x} Cp^*(it)\right)}, \quad (7-10)$$

b-3) Setting of the time tendency of  $U$  at the boundary

Computed phase velocities  $Cp^*$ 's are smoothed by taking average of  $Cp^*$ 's on the adjacent grid points. Judging from the sign of  $Cp^*$ , it is determined whether waves are outgoing or incoming at the boundary.

In an outgoing case, the time tendency of  $U$  at the boundary, DUDTBC, is computed as follows:

at the left boundary (at  $i = JS$ ),  $Cp^* < 0$

$$\text{DUDTBC}(y, z, 1) \equiv \frac{\partial U}{\partial t} \Big|_{b.\text{left}}$$

$$= \frac{U^{it+1}(JS) - U^{it-1}(JS)}{2\Delta t} = \frac{1}{\Delta x} C_{p*}(it) \frac{U^{it-1}(JS) - U^{it}(JS+1)}{\left(1 - \frac{\Delta t}{\Delta x} C_{p*}(it)\right)} \quad (7-11a)$$

at the right boundary (at  $i = JM$ ),  $C_{p*} > 0$

$$\begin{aligned} \text{DUDTBC}(y, z, 2) &\equiv \left. \frac{\partial U}{\partial t} \right|_{b.\text{right}} \\ &= \frac{U^{it+1}(JM) - U^{it-1}(JM)}{2\Delta t} = \frac{1}{\Delta x} C_{p*}(it) \frac{-U^{it-1}(JM) + U^{it}(JM-1)}{\left(1 + \frac{\Delta t}{\Delta x} C_{p*}(it)\right)} \end{aligned} \quad (7-11b)$$

In an incoming case, *i.e.*,

at the left boundary (at  $i = JS$ ),  $C_{p*} \geq 0$

or at the right boundary (at  $i = JM$ ),  $C_{p*} \leq 0$ ,

the time tendency of  $U$  at the boundary, DUDTBC, is computed in order to restore the boundary value to the external value,  $U.\text{ext}$ , to a certain degree as follows:

$$\text{DUDTBC} \equiv \left. \frac{\partial U}{\partial t} \right|_b = [\mu U.\text{ext} + (1 - \mu)U^{it-1} - U^{it-1}]/2\Delta t. \quad (7-11c)$$

Note that  $\mu = 1$  makes  $U^{it+1}$  at the boundary equal to  $U.\text{ext}$ .

#### b-4) Adjustment of the time tendency of $U$ and $V$ at the boundary

In order to satisfy mass conservation in the entire domain,

$$\iiint \{\partial_x U + \partial_y V + \partial_z W^*\} dx dy dz = \iint (U_{\text{in}} - U_{\text{out}}) dz dy + \iint (V_{\text{in}} - V_{\text{out}}) dz dx = 0,$$

the adjustment to the time tendencies of  $U$  and  $V$  at the boundaries, DUDTBC and DVDTBC, is needed. The constant value of adjustment, ADJ, is derived from the equation below:

$$\begin{aligned} &\iint \{[\text{DUDTBC}(y, z, 1) - \text{ADJ}] - [\text{DUDTBC}(y, z, 2) + \text{ADJ}]\} dz dy \\ &+ \iint \{[\text{DVDTBC}(x, y, 1) - \text{ADJ}] - [\text{DVDTBC}(x, y, 2) + \text{ADJ}]\} dz dx = 0. \end{aligned} \quad (7-12)$$

This equation yields

$$\text{ADJ} = 0.5 \times \text{error} / \left( \iint dz dx + \iint dz dy \right), \quad (7-13)$$

where

$$\begin{aligned} \text{error} = & \iint [\text{DUDTBC}(y, z, 1) - \text{DUDTBC}(y, z, 2)] dz dy \\ & + \iint [\text{DVDTBC}(x, z, 1) - \text{DVDTBC}(x, z, 2)] dz dx \end{aligned} \quad (7-14)$$

and index 1 for DUDTBC (or DVDTBC) denotes the value at  $i = 1 + 1/2$  (or  $j = 1 + 1/2$ ) and index 2 denotes the value at  $i = nx - 1/2$  (or  $j = ny - 1/2$ ).

The adjustments on DUDTBC and DVDTBC are

$$\left. \begin{aligned} \text{DUDTBC}(y, z, 1) & \longleftarrow \text{DUDTBC}(y, z, 1) - \text{ADJ}, \\ \text{DUDTBC}(y, z, 2) & \longleftarrow \text{DUDTBC}(y, z, 2) + \text{ADJ}, \\ \text{DVDTBC}(x, z, 1) & \longleftarrow \text{DVDTBC}(x, z, 1) - \text{ADJ}, \\ \text{DVDTBC}(x, z, 2) & \longleftarrow \text{DVDTBC}(x, z, 2) + \text{ADJ}. \end{aligned} \right\} \quad (7-15)$$

As discussed in B-6-2, the requirement of mass conservation in the entire domain is related to the solvability condition of the pressure equation. Adjustment on DUDTBC and DVDTBC is necessary for the realization of the solvability condition of the pressure equation.

#### P.G.

$C_p$  is set in arrays CPHU and CPHV by subs.ORUCPH and ORVCPH, respectively, which are called in sub.SVELC. The setting of DUDTBC and adjustment is done by sub.SUVPBD in mem.SFXHEI. Array DUDTBC and DVDTBC are used in setting lateral boundary condition for pressure and computing boundary values of  $U$  and  $V$ .

c) For the pressure equation of AE and E-HI-VI

c-1) For the pressure equation of AE

Neumann boundary condition for pressure is obtained from Eq. (1-28):

$$\frac{\partial}{\partial x}(P) = -\text{ADVU} - \frac{\partial U}{\partial t} \Big|_b - \frac{\partial}{\partial \xi}(G^{13}P) = -\text{ADVU} - \text{DUDTBC} - \frac{\partial}{\partial \xi}(G^{13}P). \quad (7-16)$$

The time tendency of  $U$  at the boundary, DUDTBC is computed as discussed in B-7-2, b-4).

c-2) For the pressure equation of E-HI-VI

Neumann boundary condition for pressure is obtained from Eq. (3-32):

$$\frac{\partial}{\partial x}(\Delta^2 P) = -2\text{ADVU}'' - \frac{\Delta^2 U}{\Delta t \alpha''} = -2 \left[ \text{ADVU}'' + \text{DUDTBC} - \frac{U^{it} - U^{it-1}}{\Delta t \alpha''} \right] \quad (7-17)$$

P.G.

The righthand side of Eqs. (7-16) and (7-17) are evaluated by sub.SUVPBD in mem.SFXHEL and provided as the lateral boundary condition by sub.SFPBD.

### B-7-3. Wall lateral boundary conditions

The wall is free-slip, and thermally insulated. This condition imposed at  $j = 1 + 1/2$  and  $ny - 1/2$  is described below. For all field variables except for  $V$ , the (mirror image) condition

$$F_{i,1,k} = F_{i,2,k}; \quad F_{i,ny,k} = F_{i,ny-1,k} \quad (7-18)$$

is imposed.

For the velocity component  $V$ , normal to the wall boundary,

$$\left. \begin{aligned} V_{i,1/2,k} &= -V_{i,2+1/2,k}; & V_{i,1+1/2,k} &= 0; \\ V_{i,ny+1/2,k} &= -V_{i,ny-3/2,k}; & V_{i,ny-1/2,k} &= 0; \end{aligned} \right\} \quad (7-19)$$

are imposed.

In the evaluation of ADVV at  $j = 1 + 1/2$ , which is necessary for the boundary condition to pressure,

$$\text{ADV}V \equiv \partial_x(\bar{U}^y \bar{v}^x) + \partial_y(\bar{V}^y \bar{v}^y) + \partial_z(\bar{W}^* \bar{v}^z), \quad (7-20)$$

the following term must be adopted:

$$\partial_y(\bar{V}^y \bar{v}^y) = \frac{\bar{V}^y \bar{v}^y|_2 - \bar{V}^y \bar{v}^y|_1}{\Delta y_{1+1/2}} = \frac{2\bar{V}^y \bar{v}^y|_2}{\Delta y_{1+1/2}}, \quad (7-21)$$

where the following relation is virtually used such as

$$\bar{V}^y \bar{v}^y|_{j=2} + \bar{V}^y \bar{v}^y|_{j=1} = 0. \quad (7-22)$$

This makes dynamic pressure at the wall boundary to be properly calculated (see also Eqs. (8-11), (8-12)).

### B-7-4. Sponge layer

Rayleigh damping near the lateral boundary,  $D_{r\ell}$ , is imposed to prevent the false reflection of internal gravity waves from the lateral boundary, enforce the environmental external conditions (designated by  $f.\text{ext}$  below) and suppress noises.

$$D_{r\ell}(f) = -\frac{1}{2m_{r\ell}\Delta t} \left( 1 + \cos \left( \frac{\pi(LX - x)}{x_d} \right) \right) (f - f.\text{ext}) \quad (7-23)$$

for  $x > LX - x_d$ .

$$D_{r\ell}(f) = -\frac{1}{2m_{r\ell}\Delta t} \left( 1 + \cos \left( \frac{\pi x}{x_d} \right) \right) (f - f.\text{ext}) \quad (7-24)$$

for  $x < x_d$ .

## B-8. Lower boundary conditions

### B-8-1. For velocity

For  $W$ , the kinematical condition,

$$\frac{1}{G^{1/2}} W + \overline{G^{13} \bar{U}^{z^2}} + \overline{G^{23} \bar{V}^{z^2}} \equiv W^* = \bar{\rho} G^{1/2} \omega = \bar{\rho} G^{1/2} \frac{d\xi}{dt} = 0 \quad (8-1)$$

at  $k = 1 + 1/2$  is imposed.

For the case of no friction (free-slip; no subgrid scale momentum flux),

$$\overline{\bar{\rho} u'' w''} = 0 \quad (\text{at } k = 1 + 1/2), \quad U_{k=1} = U_{k=2}, \quad V_{k=1} = V_{k=2}, \quad (8-2)$$

is imposed.

For the case of friction (non-slip; subgrid scale momentum flux is present; see B-10-2),

$$\overline{\bar{\rho} u'' w''} = -\bar{\rho} C_{dm} V_a \frac{(U^* + U_{k=2})}{\bar{\rho} G^{1/2}}, \quad (8-3)$$

$$V_a \equiv \frac{((U^* + U_{k=2})^2 + (V^* + V_{k=2})^2)^{1/2}}{\bar{\rho} G^{1/2}} \quad (8-4)$$

is imposed. The suffix  $k = 2$  denote the lowest level above the ground.  $U^*$  and  $V^*$  are the translation velocity components of the numerical model frame relative to the earth surface. It is noted that  $U$  and  $V$  are velocity components of air relative to the model frame, and those relative to the earth surface are given by  $U^* + U$  and  $V^* + V$ , respectively.

$\overline{\bar{\rho} v'' w''}$  is formulated in a similar way to  $\overline{\bar{\rho} u'' w''}$ .

### B-8-2. For $\Theta$ and $Qv$

For the case of no flux condition,

$$\overline{\bar{\rho} \theta'' w''} = 0 \quad \text{and} \quad \Theta_{k=1} = \Theta_{k=2}, \quad (8-5)$$

$$\overline{\bar{\rho} Qv'' w''} = 0 \quad \text{and} \quad Qv_{k=1} = Qv_{k=2}. \quad (8-6)$$

For the case of flux condition (see B-10-2),

$$\overline{\bar{\rho} \theta'' w''} = -\bar{\rho} C_{dh} V_a (\Theta_2 - \Theta_s) \quad \text{and} \quad \Theta_{k=1} = \Theta_s \quad (8-7)$$

$$\overline{\bar{\rho} Qv'' w''} = -\bar{\rho} C_{dh} V_a (Qv_2 - Qv_s) \quad \text{and} \quad Qv_{k=1} = Qv_s, \quad (8-8)$$

where  $\Theta_s$  and  $Qv_s$  are the potential temperature and mixing ratio of water vapor at the (sea or ground) surface. Over the land,  $C_{dm}$  and  $C_{dh}$  are determined from Monin and Obukhov's similarity law (see Sommeria, 1976). Over the sea, they are determined from the formula by Kondo (1975).

P.G.

For the case of no friction (free-slip; no subgrid-scale momentum flux),  $MSW(1) = 0$  must be specified to the program.

For the case of friction (non-slip),  $MSW(1) = 1$  must be specified to the program.

For the case of no heat flux condition,  $MSW(1) = 0$  or ( $MSW(1) = 1$  and  $MSW(13) = 0$ ) must be specified to the program.

For the case of heat flux condition,  $MSW(1) = 1$  and  $MSW(13) = 1$  must be specified to the program.

**B-8-3. For pressure**

$$PFZ]_{1+1/2} = \frac{1}{G^{1/2}} \partial_z P + \frac{g\bar{P}^z}{C_s^2} = -\frac{\partial W}{\partial t} - ADVW + BUOY \quad (8-9)$$

is specified so as to be consistent with the kinematic condition Eq. (8-1). The estimation of ADVW and BUOY at  $k = 1 + 1/2$  is somewhat ambiguous for the case of non-slip (flux) condition.

$$ADVW \equiv \partial_x(\bar{U}^z \bar{w}^x) + \partial_y(\bar{V}^z \bar{w}^y) + \partial_z(\bar{W}^{*z} \bar{w}^z), \quad (8-10)$$

where

$$\partial_z(\bar{W}^{*z} \bar{w}^z) = \frac{\bar{W}^{*z} \bar{w}^z]_2 - \bar{W}^{*z} \bar{w}^z]_1}{\Delta z_{1+1/2}} = \frac{2\bar{W}^{*z} \bar{w}^z]_2}{\Delta z_{1+1/2}}. \quad (8-11)$$

The above equation comes from the following relation:

$$\bar{W}^{*z} \bar{w}^z]_{k=1} + \bar{W}^{*z} \bar{w}^z]_{k=2} = 0, \quad (8-12)$$

which is required from the vertical momentum conservation (see Clark, 1977. Eq. (3-33)).

Buoyancy term is computed as

$$BUOY \equiv g \frac{\overline{\bar{\rho} G^{1/2} \Theta'_m{}^z}}{\bar{\Theta}_m},$$

$$\Theta'_{m,k=1+1/2} = 0.5(\Theta_{m,k=2} + \Theta_{m,k=1}) - \bar{\Theta}_m.$$

In the case where heat flux is present, currently  $\Theta_{m,k=1} = \Theta_{m,s}$  is used. However, the use of

$$\Theta'_{m,k=1+1/2} = 0.5(\Theta_{m,k=2} + \bar{\Theta}_{m,k=1}) - \bar{\Theta}_{m,k=1+1/2}$$

might be better in this case.

## B-9. Upper boundary conditions

The upper boundary is the slip, thermally insulated rigid wall. Currently, radiation conditions (Klemp and Durran, 1983) is not implemented. Instead, sponge layer (absorption of waves by Rayleigh friction) (see B-12-3) is introduced to realize quasi-radiation conditions.

### B-9-1. For velocity

For  $W$ , the kinematical condition,

$$\frac{1}{G^{1/2}} W + \overline{G^{13} \bar{U}^z x} + \overline{G^{23} \bar{V}^z y} \equiv W^* = \bar{\rho} G^{1/2} \omega = \bar{\rho} G^{1/2} \frac{d\xi}{dt} = 0 \quad (9-1)$$

at  $k = nz - 1/2$  is imposed (note  $G^{13}_{k=nz-1/2} = 0$ , *i.e.*, Eq. (9-1) is equivalent to  $W = 0$ ).

No friction (free-slip; no subgrid scale momentum flux) condition, such as

$$\overline{u'' w''} = 0 \text{ (at } k = nz - 1/2), \quad U_{k=nz} = U_{k=nz-1}, \quad V_{k=nz} = V_{k=nz-1}, \quad (9-2)$$

is imposed.

### B-9-2. For $\Theta$ and $Qv$

No flux condition, such as

$$\overline{\rho \theta'' w''} = 0 \quad \text{and} \quad \Theta_{k=nz-1} + \Theta_{k=nz} = \bar{\Theta}, \quad (9-3)$$

$$\overline{\rho Q v'' w''} = 0 \quad \text{and} \quad Qv_{k=nz-1} = Qv_{k=nz}. \quad (9-4)$$

Note that  $\Theta_{k=nz-1} + \Theta_{k=nz} = \bar{\Theta}$  guarantees  $\text{BUOY}_{k=nz-1/2} = 0$ .

### B-9-3. For pressure

$$\text{PFZ}]_{nz-1/2} = \frac{1}{G^{1/2}} \partial_z P + \frac{g \bar{P}^z}{C_s^2} = -\frac{\partial W}{\partial t} - \text{ADVW} + \text{BUOY} \quad (9-5)$$

is specified so as to be consistent with the kinematic condition Eq. (9-1). The first term of the righthand side of Eq. (9-5) is zero due to  $W_{k=nz-1/2} = 0$ .

$$\begin{aligned} \text{ADVW} &\equiv \partial_x (\bar{U}^z \bar{w}^x) + \partial_y (\bar{V}^z \bar{w}^y) + \partial_z (\bar{W}^{*z} \bar{w}^z) = \partial_z (\bar{W}^{*z} \bar{w}^z) \\ &= \frac{\bar{W}^{*z} \bar{w}^z]_{nz} - \bar{W}^{*z} \bar{w}^z]_{nz-1}}{\Delta z_{nz-1/2}} = \frac{-2 \bar{W}^{*z} \bar{w}^z]_{nz-1}}{\Delta z_{nz-1/2}}, \end{aligned}$$

where the following relation is used:

$$\overline{W^{*z} w^z}]_{k=nz} + \overline{W^{*z} w^z}]_{k=nz-1} = 0.$$

The above relation comes from the vertical momentum conservation (see Clark, 1977, Eq. (3-33)).

#### B-9-4. Absorption layer

Rayleigh damping near the upper boundary,  $D_{ru}$ , is added for a field variable  $f$  ( $f = u, v, w, \theta$ ) in the upper part of the domain ( $z > z_d$ ) to prevent the false reflection of internal gravity waves from the upper right wall.

$$D_{ru}(f) = -\frac{1}{2m_{ru}\Delta t} \left( 1 + \cos \left( \frac{\pi(LZ - z)}{LZ - z_d} \right) \right) (f - f.\text{ext}) \quad (9-6)$$

for  $z > z_d$ . Here,  $LZ$  is the height of the domain.

## B-10. Subgrid-scale turbulence

### B-10-1. Turbulent closure model

To determine the diffusion coefficients, the turbulent closure model is used. The formulation is based on that by Klemp and Wilhelmson (1978) and Deardorff (1980).

The prognostic equation for subgrid-scale turbulent kinetic energy  $E$  is given as follows:

$$\frac{dE}{dt} = \text{BUOYP} - \overline{u_i''u_j''} \frac{\partial u_i}{\partial x_j} + \frac{\partial}{\partial x_j} \left( K_e \frac{\partial E}{\partial x_j} \right) - \frac{C_e}{\ell} E^{3/2}, \quad (10-1)$$

where

$$E = (\overline{u''^2 + v''^2 + w''^2})/2, \quad (10-2)$$

$$\overline{u_i''u_j''} = -K_m \left( \frac{\partial u_i}{\partial x_j} + \frac{\partial u_j}{\partial x_i} \right) + \frac{2}{3} \delta_{i,j} E. \quad (10-3)$$

The subgrid-scale perturbation is denoted by the superscript "", and the overbar denotes the average of the subgrid-scale quantities in one grid box.

The buoyancy production term BUOYP in Eq. (10-1) is calculated taking account of the cloud water loading and the release of latent heat as

$$\text{BUOYP} = gw'' \left( \frac{\theta''}{\Theta} + 0.61Qv'' \right) = \frac{gK_h}{G^{1/2}} \left( -\frac{1}{\Theta} \frac{\partial \Theta}{\partial \xi} - 0.61 \frac{\partial Qv}{\partial \xi} \right) \quad (10-4a)$$

for the unsaturate case ( $Q_c = 0$ ),

and

$$\text{BUOYP} = gw'' \left( \frac{\theta''}{\Theta} + 0.61Qv'' - Qc'' \right) = \frac{gK_h}{G^{1/2}} \left( -A \frac{\partial \Theta_e}{\partial \xi} + \frac{\partial Qc}{\partial \xi} \right) \quad (10-4b)$$

for the saturate case ( $Q_c > 0$ ).

Here

$$A = \frac{1}{\Theta} \left( \frac{1 + \frac{1.61\varepsilon L Qv}{R_d T}}{1 + \frac{\varepsilon L^2 Qv}{C_p R_d T^2}} \right), \quad (10-5)$$

$\varepsilon = 0.622$ ,  $\Theta_e$  is the equivalent potential temperature,  $L$  the latent heat of vaporization, and  $R_d$  the gas constant for dry air. The last two terms in Eq. (10-1) are evaluated at  $(it - 1)$  time step in order to maintain numerical stability.

The subgrid-scale mixing length  $\ell$  is determined depending on the thermal stratification. Near the ground surface, it approaches to the product of Karman constant  $\kappa$  ( $= 0.4$ ) and height from the surface ( $z - Z_s$ ) when the surface friction exists;

$$\frac{1}{\ell} = \frac{1}{\kappa(z - Z_s)} + \frac{1}{\ell_\infty}, \quad (10-6)$$

where

$$\ell_\infty = \Delta s \quad \text{for the unstable case } (N_\ell \leq 0), \quad (10-7a)$$

$$\ell_\infty = \min(\Delta s, 0.76E^{1/2}N_\ell^{-1}) \quad \text{for the stable case } (N_\ell > 0), \quad (10-7b)$$

$\Delta s$  is the typical grid distances,  $N_\ell$  is the local stability and  $\Theta_\ell$  is the liquid water potential temperature defined by

$$\Delta s = (\Delta x \Delta z)^{1/2} \quad \text{for 2-dimensional model,} \quad (10-8a)$$

$$\Delta s = (\Delta x \Delta y \Delta z)^{1/3} \quad \text{for 3-dimensional model,} \quad (10-8b)$$

$$N_\ell = \frac{g}{\Theta} \frac{\partial \Theta_\ell}{\partial z}, \quad (10-9)$$

$$\Theta_\ell = \Theta - \frac{L}{C_p \Pi} Qc. \quad (10-10)$$

The eddy diffusion coefficients for velocity components, turbulent energy and other predicted variables ( $\theta$ ,  $Qv$ ,  $Qc$ , ...) are given as

$$K_m = C_m \ell E^{1/2} \quad (C_m = 0.2 \text{ is used}), \quad (10-11)$$

$$K_e = 2K_m, \quad (10-12)$$

$$K_h = P_r^{-1} K_m. \quad (10-13)$$

The coefficient of the viscosity dispersion term in Eq. (10-1) and the inverse Prandtl number  $P_r^{-1}$  are given as

$$C_e = 0.19 + 0.51\ell/\Delta s, \quad (10-14)$$

$$P_r^{-1} = 1 + 2\ell/\Delta s. \quad (10-15)$$

The diffusion term by subgrid-scale turbulence for turbulent energy  $E$  is given as

$$\text{DIF}.E = -\frac{\overline{\partial u_j'' E''}}{\partial x_j} = \frac{\partial}{\partial x_j} \left( K_e \frac{\partial E}{\partial x_j} \right), \quad (10-16a)$$

and for other scalar variables  $f(\theta, Qv, Qc, \dots)$  as

$$\text{DIF}.f = -\frac{\partial \overline{u_j'' f''}}{\partial x_j} = \frac{\partial}{\partial x_j} \left( K_h \frac{\partial f}{\partial x_j} \right). \quad (10-16b)$$

The diffusion term by subgrid-scale turbulence for each velocity component ( $u = u_1$ ,  $v = u_2$ ,  $w = u_3$ ) is given as

$$\text{DIF}.u_i = \frac{\partial \overline{u_j'' u_i''}}{\partial x_j}. \quad (10-17)$$

The above diffusion terms are evaluated using the values at  $(it - 1)$  time step to maintain numerical stability.

### P.G.

$E$ ,  $K_m$  and  $K_h$  are computed by sub.CTURB5 and CNVED3 in mem.CVTURB, respectively.  $\text{DIF}.f$  is computed by sub.CDIFE1, and  $\text{DIF}.u$  is computed by sub.CRSTUV.  $\text{DIF}.f$  and  $\text{DIF}.u$  are added to array ADVF and ADVU in which advection terms for  $f$  and  $u$  have been stored by sub.CADVET and CADVC3, respectively.

### B-10-2. Surface fluxes

They are given from the resistance law as follows:

for momentum fluxes,

$$\overline{\rho u'' w''} = -\bar{\rho} C_{dm} V_a \frac{(U^* + U_{k=2})}{\bar{\rho} G^{1/2}}, \quad (10-18a)$$

$$\overline{\rho v'' w''} = -\bar{\rho} C_{dm} V_a \frac{(V^* + V_{k=2})}{\bar{\rho} G^{1/2}}; \quad (10-18b)$$

for sensible heat and water vapor fluxes,

$$\overline{\rho \theta'' w''} = -\bar{\rho} C_{dh} V_a (\Theta_2 - \Theta_s), \quad (10-19)$$

$$\overline{\rho Q v'' w''} = -\bar{\rho} C_{dh} V_a (Qv_2 - Qv_s), \quad (10-20)$$

where  $V_a$  is given by Eq. (8-4).  $U^*$  and  $V^*$  are translation velocity components of the numerical model frame relative to the earth surface. It is noted that  $U$  and  $V$  are the velocity components of air relative to the model frame, not to the earth surface. Suffix 2 and  $s$  denotes the values at the lowest grid points above the surface and those at the surface, respectively.

Over the sea,  $C_{dm}$  and  $C_{dh}$  are determined from the formula by Kondo (1975). Over the land,  $C_{dm}$  and  $C_{dh}$  are determined from Monin and Obukhov's similarity law (see Sommeria,

1976) for a given roughness length of the ground,  $z^*$ . The  $C_{dm}$  and  $C_{dh}$  are functions of  $z_a/z^*$  and  $z_a/L$ , where  $z_a = (\Delta z_{1+1/2})/2$  and  $L$  is the local Monin-Obukhov length:

$$L = -\frac{\Theta_s(-u''w'')^{3/2}}{\kappa g \theta'' w''}, \quad (10-21)$$

where  $\kappa$  is 0.4 (Karman constant).

From similarity theory, the drag coefficients can be written as

$$C_{dm} = \frac{1}{\phi^2}, \quad C_{dh} = \frac{1}{\phi\psi}, \quad (10-22)$$

where  $\phi$  and  $\psi$  are universal functions (Businger *et al.* 1971) defined as,

for unstable cases,

$$\left. \begin{aligned} \phi &= \frac{1}{\kappa} \left\{ \log \left( \frac{z_a}{z^*} \right) - \left[ 2 \log \left( \frac{1+\xi}{2} \right) + \log \left( \frac{1+\xi^2}{2} \right) - 2 \arctan(\xi) + \left( \frac{\pi}{2} \right) \right] \right\}, \\ \psi &= \frac{1}{1.35\kappa} \left[ \log \left( \frac{z_a}{z^*} \right) - 2 \log \left( \frac{1+\eta}{2} \right) \right], \end{aligned} \right\} \quad (10-23a)$$

$$\text{with } \xi = \left( 1 - 15 \frac{z_a}{L} \right)^{1/2} \text{ and } \eta = \left( 1 - 9 \frac{z_a}{L} \right)^{1/2},$$

and,

for neutral or stable cases,

$$\left. \begin{aligned} \phi &= \frac{1}{\kappa} \left\{ \log \left( \frac{z_a}{z^*} \right) + 4.7 \frac{z_a}{L} \right\}, \\ \psi &= \frac{1}{\kappa} \left\{ 0.74 \log \left( \frac{z_a}{z^*} \right) + 4.7 \frac{z_a}{L} \right\}. \end{aligned} \right\} \quad (10-23b)$$

Eqs. (10-18)–(10-23) can be solved by iteration (a three-time iteration is sufficient) to yield the converged  $C_{dm}$  and  $C_{dh}$ .

#### P.G.

See sub.CRSTUV in mem.CVTURBXXZ. If MSW(1) = 0, no surface fluxes are assumed (free-slip, thermally insulated). If MSW(1) = 1 and MSW(13) = 0, only momentum flux is calculated on the assumption of no heat fluxes and neutral stratification. If MSW(1) = 1 and MSW(13) = 1, both momentum flux and heat fluxes are calculated. Sub.KONDOH and sub.GRDFXH give  $C_{dm}$  on the sea and land, respectively, both of which are called in sub.CRSTUV.

## B-11. Cloud microphysics

The model can incorporate 5 kinds of parameterization of cloud microphysics:

1. Dry model (no water vapor).
2. Warm rain model (water vapor  $Q_v$ , cloud water  $Q_c$  and rain  $Q_r$ )
3. Cold rain model with the mixing ratios of cloud water, rain, cloud ice  $Q_i$ , snow  $Q_s$  and graupel  $Q_g$  and the number concentration of cloud ice  $N_i$  predicted.
4. Cold rain model with the mixing ratios of cloud water, rain, cloud ice, snow and graupel and the number concentrations of cloud ice  $N_i$  and snow  $N_s$  predicted.
5. Cold rain model with the mixing ratios of cloud water, rain, cloud ice, snow and graupel and the number concentrations of cloud ice  $N_i$ , snow  $N_s$  and graupel  $N_g$  predicted.

In the following, the most sophisticated version of parameterization will be described.

### B-11-1. General features of cloud microphysics

In the model, water substance is categorized into 6 forms (water vapour,  $Q_v$ ; cloud

Table B-11-1

Variable $Q_x$ (kg/kg) $N_x$ ( $m^{-3}$ )	Size distribution $N_x(D)$ ( $m^{-4}$ )	Fall velocity $U_{dx}$ (m/s)	Density $\rho_x$ (kg/ $m^3$ )
$Q_r$	$N_r(D) = N_{r0} \exp(-\lambda D)$ $N_{r0} = 8 \times 10^6$	$a_r D r^{br} \left(\frac{\rho_0}{\rho}\right)^{1/2}$ $a_r = 842$ $b_r = 0.8$	$\rho_w = 1 \times 10^3$
$Q_s$ $N_s$	$N_s(D) = N_{s0} \exp(-\lambda D)$  ( $N_{s0} = 1.8 \times 10^6$ )	$a_s D s^{bs} \left(\frac{\rho_0}{\rho}\right)^{1/2}$  $a_s = 17$ $b_s = 0.5$	$\rho_s = 8.4 \times 10$ $r_{s0} = r_0 = 75 \mu m$ $m_{s0} = (4\pi/3)\rho_s r_{s0}^3$
$Q_g$ $N_g$	$N_g(D) = N_{g0} \exp(-\lambda D)$  ( $N_{g0} = 1.1 \times 10^6$ )	$a_g D g^{bg} \left(\frac{\rho_0}{\rho}\right)^{1/2}$  $a_g = 124$ $b_g = 0.64$	$\rho_g = 3 \times 10^2$  $r_{g0} = r_0 = 75 \mu m$ $m_{g0} = (4\pi/3)\rho_g r_{g0}^3$
$Q_c$	mono $Di = \left(\frac{6\rho Q_c}{\pi\rho_w N_c}\right)^{1/3}$ $N_c = 1 \times 10^8 m^{-3}$	$a_c D c^{bc}$ $a_c = 3 \times 10^7$ $b_c = 2.0$	$\rho_c = 1.0 \times 10^3$
$Q_i$ $N_i$	mono $Di = \left(\frac{6\rho Q_i}{\pi\rho_i N_i}\right)^{1/3}$	$a_i D i^{bi} \left(\frac{\rho_0}{\rho}\right)^{0.35}$ $a_i = 7 \times 10^2$ $b_i = 1.0$	$\rho_i = 1.5 \times 10^2$ $m_{i0} = 1 \times 10^{-12} kg$

water,  $Q_c$ ; rain,  $Q_r$ ; cloud ice,  $Q_i$ ; snow,  $Q_s$  and graupel,  $Q_g$ ) as shown in Table B-11-1. Values in Table B-11-1 are determined referring to observational studies by Locatelli and Hobbs (1974), Kajikawa (1976, 1978), Yagi *et al.* (1979) and Harimaya (1978). For cloud ice, snow and graupel, the number concentrations are predicted in addition to their mixing ratios. For rain, snow and graupel, the inverse exponential functions are hypothesized for their size distribution functions. For cloud water and cloud ice, mono-dispersive distribution is hypothesized, and their precipitation is not taken into account explicitly. Cloud ice designates pristine ice crystal smaller than  $r_0$  in radius, and snow designates snow crystals and aggregates of snow crystals larger than  $r_0$  in radius. As will be shown in C-3,  $r_0$  has a large influence on the number and mass of cloud ice, and  $r_0$  is treated as a tuning parameter ranging from 50 to 100 $\mu\text{m}$ .

The cloud microphysical processes simulated in the model are illustrated in Fig. B-11-1

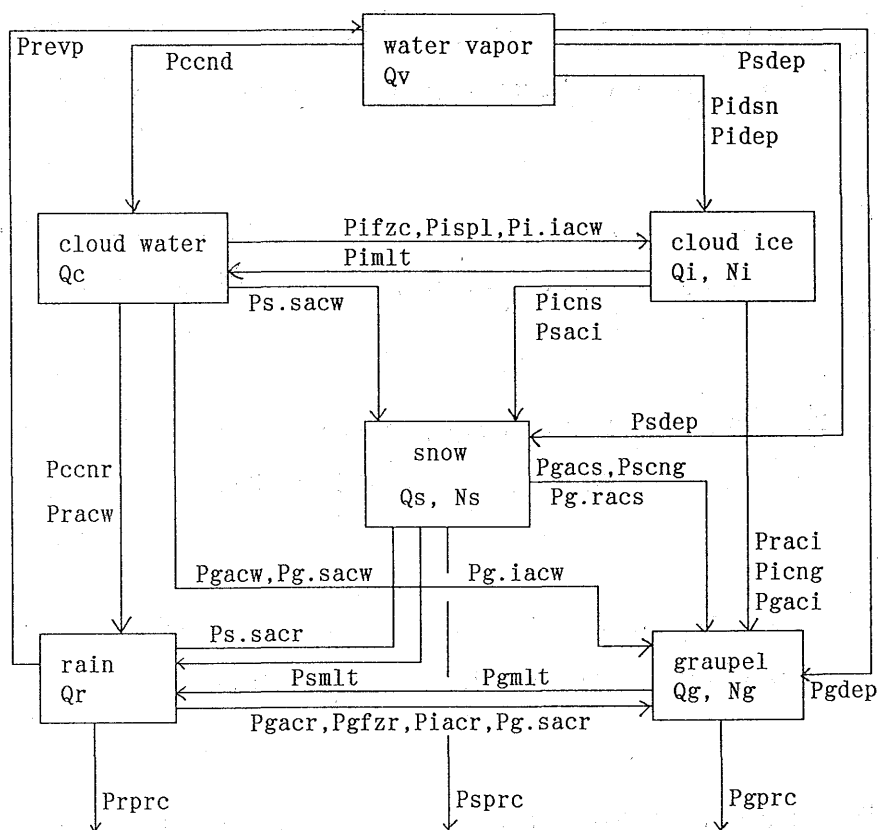


Fig. B-11-1 Cloud microphysical processes in the model. For explanation of the symbols, see Appendix B-11-1.

and the meaning of symbols is explained in the Appendix. Unless specifically mentioned, the parameterizations of microphysical processes are the same as in Ikawa *et al.* (1987). Newly incorporated and revised parts of parameterizations are described below, which are mainly based upon Murakami (1990) and Cotton *et al.* (1986). In the following, (L-*nn*), (CT-*nn*) and (M-*nn*) denote the number of equation appearing in Lin *et al.*, Cotton *et al.* and Murakami, respectively.

The prognostic equations for mixing ratios of 6 water species and potential temperature are as follows:

$$\frac{\partial Q_v}{\partial t} + \text{ADV}(Q_v) - D(Q_v) = \text{PRD}(Q_v) \equiv \text{Prevp} - \text{Pidep} - \text{Psdep} - \text{Pgdep} - \text{Pidsn} - \text{Pccnd}, \quad (11-1)$$

$$\begin{aligned} \frac{\partial Q_c}{\partial t} + \text{ADV}(Q_c) - D(Q_c) = \text{PRD}(Q_c) \equiv & -\text{Pccnr} - \text{Pracw} + \text{Pccnd} - \text{Pifzc} \\ & - \text{Pispl} - (\text{Ps.sacw} + \text{Pg.sacw}) - \text{Pgacw} - (\text{Pi.iacw} + \text{Pg.iacw}) + \delta\text{Pimlt}, \end{aligned} \quad (11-2)$$

$$\begin{aligned} \frac{\partial Q_r}{\partial t} + \text{ADV}(Q_r) - D(Q_r) = \text{PRD}(Q_r) \equiv & -\text{Prprc} + \text{Pracw} + \text{Pccnr} - \text{Prevp} \\ & - \text{Pgfzr} - \text{Piacr} - (\text{Ps.sacr} + \text{Pg.sacr}) - \text{Pgacr} + \delta(\text{Psmlt} + \text{Pgmlt}), \end{aligned} \quad (11-3)$$

$$\begin{aligned} \frac{\partial Q_i}{\partial t} + \text{ADV}(Q_i) - D(Q_i) = \text{PRD}(Q_i) \equiv & \text{Pidsn} + \text{Pifzc} + \text{Pispl} + \text{Pidep} \\ & + \text{Pi.iacw} - \text{Picng} - \text{Praci} - \text{Psaci} - \text{Pgaci} - \text{Picns} - \delta\text{Pimlt}, \end{aligned} \quad (11-4)$$

$$\begin{aligned} \frac{\partial Q_s}{\partial t} + \text{ADV}(Q_s) - D(Q_s) = \text{PRD}(Q_s) \equiv & -\text{Psprc} + \text{Psdep} + \text{Picns} + \text{Ps.sacw} \\ & - \text{Pscng} + \text{Psaci} + \text{Ps.sacr} - \text{Pg.racs} - \text{Pgacs} - \delta\text{Psmlt}, \end{aligned} \quad (11-5)$$

$$\begin{aligned} \frac{\partial Q_g}{\partial t} + \text{ADV}(Q_g) - D(Q_g) = \text{PRD}(Q_g) \equiv & -\text{Pgprc} + \text{Pgdep} + (\text{Pscng} + \text{Pg.sacw}) \\ & + \text{Pgacr} + \text{Pgacw} + \text{Pgaci} + (\text{Piacr} + \text{Praci}) + (\text{Pg.sacr} + \text{Pg.racs}) \\ & + \text{Pgfzr} + (\text{Picng} + \text{Pg.iacw}) - \delta\text{Pgmlt} \end{aligned} \quad (11-6)$$

$$\begin{aligned}
 \frac{\partial \theta}{\partial t} + \text{ADV}(\theta) - D(\theta) = \text{PRD}(\theta) \equiv & -\frac{L_v}{C_p \Pi} (\text{Prevp} - \text{Pcnd}) \\
 & + \frac{L_s}{C_p \Pi} (\text{Pidep} + \text{Pidsn} + \text{Psdep} + \text{Pgdep}) \\
 & + \frac{L_f}{C_p \Pi} ((\text{Pi.iacw} + \text{Pg.iacw}) + (\text{Ps.sacw} + \text{Pg.sacw}) + \text{Pgacw} + \text{Piacr} + \text{Pifzc} \\
 & + \text{Pgfzr} + \text{Psacr} + \text{Pgacr} - \delta(\text{Pimlt} + \text{Psmlt} + \text{Pgmlt})). \quad (11-7)
 \end{aligned}$$

In addition to the prognostic equations for the mixing ratios of water species, prognostic equations for the number concentrations of cloud ice, snow and graupel are also formulated as follows:

$$\begin{aligned}
 \frac{\partial}{\partial t} [Ni] + \bar{\rho} \text{ADV} \left[ \frac{Ni}{\bar{\rho}} \right] - D[Ni] = \text{PRD}(Ni) \\
 \equiv -Niag + Nifzc + \frac{\text{Pidsn} + \text{Pispl}}{m_{i0}} - \frac{Ni}{Qi} (\delta \text{Pimlt} + \text{Praci} + \text{Psaci} + \text{Pgaci}) - \frac{\text{Picns}}{m_{s0}}, \quad (11-8)
 \end{aligned}$$

$$\begin{aligned}
 \frac{\partial}{\partial t} [Ns] + \bar{\rho} \text{ADV} \left[ \frac{Ns}{\bar{\rho}} \right] - D[Ns] = \text{PRD}(Ns) \\
 \equiv -Nsprc - \text{Nscng} - \text{Ng.sacr} - \text{Nsag} + \frac{\text{Picns}}{m_{s0}} - \frac{Ns}{Qs} (\delta \text{Psmlt} + \text{Pssub}), \quad (11-9)
 \end{aligned}$$

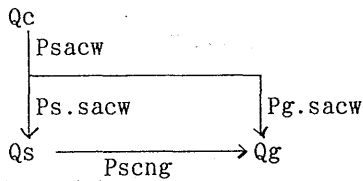
$$\begin{aligned}
 \frac{\partial}{\partial t} [Ng] + \bar{\rho} \text{ADV} \left[ \frac{Ng}{\bar{\rho}} \right] - D[Ng] = \text{PRD}(Ng) \\
 \equiv -Ngprc + \text{Niacr} + \text{Nscng} + \text{Ng.sacr} - \frac{Ng}{Qg} (\delta \text{Pgmlt} + \text{Pgsub}). \quad (11-10)
 \end{aligned}$$

Here  $L_f$ ,  $L_v$ ,  $L_s$  are latent heats of fusion, vaporization and sublimation, respectively.  $\delta$  is 0 or 1 below or above the freezing temperature, respectively. The ADV term in Eqs. (11-1) to (11-10) represent the advection term defined as

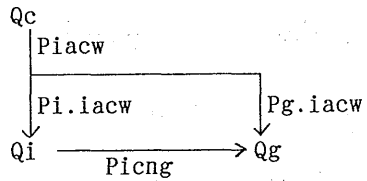
$$\text{ADV}(f) = \frac{1}{\bar{\rho} G^{1/2}} \left[ \frac{\partial}{\partial x} (\bar{\rho} G^{1/2} u f) + \frac{\partial}{\partial y} (\bar{\rho} G^{1/2} v f) + \frac{\partial}{\partial \xi} (\bar{\rho} G^{1/2} \omega f) \right].$$

The  $D$  terms represent the summation of the diffusion due to subgrid scale turbulence (B-10) and artificial computational diffusion (B-12).

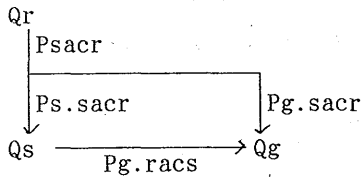
The subscripts  $V$ ,  $C$  (or  $W$ ),  $R$ ,  $I$ ,  $S$ , and  $G$  refer to vapor, cloud water, rain, cloud ice, snow and graupel. Source and sink terms for mass and number are designated by  $\text{Pqqqq}$  and  $\text{Nqqqq}$ , respectively. "qqqq" denotes elementary cloud microphysical processes, defined as "xdep(-xsub)" for depositional growth of  $x$ , "xsub" for sublimation from  $x$ , "xmlt" as



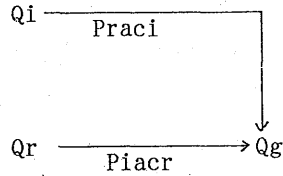
a) Collision between snow and cloud water



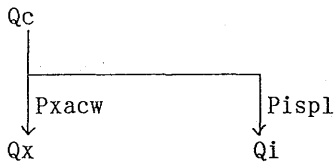
b) Collision between cloud ice and cloud water



c) Collision between rain and snow



d) Collision between cloud ice and rain



e) Collision between cloud water and Qx (snow, graupel)

Fig. B-11-2 Three component accretion processes.

melting of x, "xprc" for precipitation of x, "xag" for aggregation of x, "xcny" for conversion of x into y, "xfzy" for freezing of y to form x, "xacy" for the accretion of y by x, "x.yacz" for generation of x as a result of accretion of z by y (three-component accretion process, see Fig. B-11-2), "idsn" for deposition/sorption nucleation of cloud ice and "ispl" for ice multiplication process by ice splinters ejected during riming.

For the exchange between water vapor and cloud water (Pccnd), the instant adjustment procedure used by Klemp and Wilhelmson (1978) was adopted. Cloud ice is assumed to melt into cloud water instantaneously above the freezing point (Pimlt).

For water substance,  $x$ , whose size distribution function is expressed by the inverse exponential function, the following basic relations hold:

$$N_x = \frac{N_{0x}}{\lambda x}, \quad \rho Q_x = \int_0^\infty \rho_x \frac{\pi}{6} D x^3 N_{0x} \exp(-\lambda x D x) dD x = \frac{\pi \rho_x N_{0x}}{\lambda x^4},$$

$$\lambda x = \left( \frac{\pi \rho_x N_x}{\rho Q_x} \right)^{1/3}, \quad N_{0x} = N_x \left( \frac{\pi \rho_x N_x}{\rho Q_x} \right)^{1/3}. \quad (11-11)$$

The change in the number concentration of the precipitable hydrometeor  $x$  due to precipitation is given as

$$N_{x\text{prc}} = -\frac{\partial(\bar{U}_n x N_x)}{\partial z}, \quad (11-12)$$

where  $\bar{U}_n x$  is the number-weighted mean terminal velocity defined as

$$\bar{U}_n x = \frac{\int U_{dx}(D) N_{0x} \exp(-\lambda x D x) dD x}{N_x} = \frac{a_x \Gamma(1 + b_x)}{\lambda x^{b_x}} \lambda x^{-b_x} \left( \frac{\rho_0}{\rho} \right)^{1/2}. \quad (11-13)$$

The change in the mixing ratio of the precipitable hydrometeor  $x$  due to precipitation is given as

$$P_{x\text{prc}} = -\frac{\partial(\rho \bar{U}_x Q_x)}{\rho \partial z}, \quad (11-14)$$

where  $\bar{U}_x$  is the mass-weighted mean terminal velocity defined as

$$\bar{U}_x = \frac{\int \frac{\pi}{6} \rho_x D x^3 U_{dx}(D x) N_{0x} \exp(-\lambda x D x) dD x}{\rho Q_x} = \frac{a_x \Gamma(4 + b_x)}{6 \lambda x^{b_x}} \left( \frac{\rho_0}{\rho} \right)^{1/2}. \quad (11-15)$$

## B-11-2. Production terms for cloud ice

### a) Ice Nucleation

In the model cloud, cloud ice is produced through deposition/sorption nucleation (Pidsn: M-29), freezing of cloud droplets (Pifrc; heterogeneous (M-30) and homogeneous freezing of cloud droplets above and below  $-40^\circ\text{C}$ , respectively) and the secondary ice crystal production term (Pispl: Hallett and Mossop, 1974).

a-1) *Deposition/sorption nucleation*

The temperature dependency of deposition/sorption nucleation is given by Fletcher's (1962) empirical equation,

$$N_i^* = N_{i0} \exp(\beta_2 T_s). \quad (\text{M-26})$$

The supersaturation dependency of ice nucleation is given by Huffmann and Vali (1973),

$$N_i = A \left( \frac{S_i - 1}{S_0 - 1} \right)^B. \quad (\text{M-27})$$

Replacing  $A$  with  $N_i^*$ , we obtain

$$N_i = N_{i0} \exp(\beta_2 T_s) \left( \frac{S_i - 1}{S_0 - 1} \right)^B, \quad (\text{M-28})$$

where  $N_{i0} = 1.0 \times 10^{-2} (\text{m}^{-3})$ ,  $\beta_2 = 0.6 (\text{K}^{-1})$ ,  $B = 4.5$ .  $(S_0 - 1)$  represents the ice supersaturation of a water saturated cloud  $(Qvsw/Qvsi - 1)$ . It may be reasonable to assume that ice nucleation by deposition/sorption occurs in an ascending air parcel in clouds. Assuming that the vertical change in humidity is negligibly small, we get the following equation for ice nucleation rate in ascending cloud air:

$$\begin{aligned} \text{Pidsn} &= m_{i0} \frac{dN_i}{dt} \approx m_{i0} \frac{\partial N_i}{\partial T_s} \frac{\partial T_s}{\partial z} \frac{dz}{dt} \\ &= m_{i0} \beta_2 N_{i0} \exp(\beta_2 T_s) \left( \frac{S_i - 1}{S_0 - 1} \right)^B \frac{\partial T_s}{\partial z} w, \end{aligned} \quad (\text{11-16})$$

$$\text{Nidsn} = \frac{\text{Pidsn}}{m_{i0}}. \quad (\text{11-17})$$

a-2) *Freezing of cloud droplets*

For heterogeneous freezing of cloud droplets ( $T_c > -40^\circ\text{C}$ ), we obtain the following equation by extrapolating Bigg's (1953) equation down to the cloud droplet size (M-30):

$$\text{Pifrc} = B' [\exp\{A'(T_0 - T)\} - 1] \frac{\rho_w Q_c^2}{\rho_w N_c}, \quad (\text{11-18})$$

$$\text{Nifzc} = \text{Pifzc} \frac{N_c}{Q_c}, \quad (\text{11-19})$$

where  $A' = 0.66 (\text{K}^{-1})$ ,  $B' = 100.0 (\text{m}^{-3} \text{s}^{-1})$  is used.  $\rho_w$  is the density of liquid water,  $N_c$  the number concentration of cloud droplets which is preset in this model.

For homogeneous freezing of cloud droplets ( $T_c < -40^\circ\text{C}$ ), cloud drops are turned into cloud ice instantaneously:

$$\text{Pifzc} = \frac{Qc}{2\Delta t}, \quad \text{Nifzc} = \frac{Nc}{2\Delta t}, \quad (11-20)$$

where  $\Delta t$  is the time interval of the leap-frog time integration.

a-3) *Ice multiplication process*

Hallet and Mossop (1974) reported that approximately 350 ice splinters are produced for every  $10^{-6}$  kg of rime accretion on graupel particles at  $-5^\circ\text{C}$ . Based on their report, ice splinters associated with riming process is parameterized (CT-71) as

$$\text{Nispl} = \rho \times 3.5 \times 10^8 f(T_c)(\text{Ps.sacw} + \text{Pg.sacw} + \text{Pgacw}), \quad (11-21)$$

$$f(T_c) = \begin{cases} 0 & \text{for } T_c > T_1 = -3^\circ\text{C} \\ \frac{T_c - T_1}{T_2 - T_1} & \text{for } T_1 \geq T_c \geq T_2 = -5^\circ\text{C} \\ 1 & \text{for } T_2 \geq T_c \geq T_3 = -5^\circ\text{C} \\ \frac{T_c - T_4}{T_3 - T_4} & \text{for } T_3 \geq T_c \geq T_4 \\ 0 & \text{for } T_c < T_4 = -8^\circ\text{C} \end{cases} \quad (11-22)$$

The increase in mass of cloud ice associated with this process is given as

$$\text{Pispl} = \text{Nispl} \times m_{i0}. \quad (11-23)$$

b) *Depositional growth of cloud ice*

Depositional growth of cloud ice is given as

$$\text{Pidep} = \frac{Qv - Qvsi}{Qvsw - Qvsi} a_1 (m_i)^{a_2} Ni / \rho, \quad (11-24)$$

where  $a_1$  and  $a_2$  are temperature-dependent parameters taken from Koenig (1971).

c) *Riming growth of cloud ice*

The amount of rime on cloud ice is given as

$$\text{Piacw} = Ni \frac{\pi}{4} (Di + Dc)^2 Eic |U_{di} - U_{dc}| Qc. \quad (11-25a)$$

The portion of  $\text{Piacw}$  consumed for riming growth of cloud ice is given as

$$\text{Pi.iacw} = \min(\text{Piacw}, \beta \times \text{Pidep}). \quad (11-25b)$$

The amount of riming greater than  $\beta \times \text{Pidep}$  is consumed to form graupel ( $\text{Pg.iacw}$ ). In this

study,  $\beta = 1.0$  is tentatively used. Collection efficiency,  $E_{ic}$ , is given as follows (Fletcher, 1962; Mizuno and Matuo, 1980):

$$\psi = \left( \frac{\rho_w U_{di}}{18\eta D_i} \right)^{1/2} \cdot D_c = (Stk/2)^{1/2} \quad (Stk : \text{Stokes number}) \quad (11-26)$$

$$\eta = (1.718 + 0.049T_c - 1.2 \times 10^{-5}T_c^2) \times 10^{-5} \quad (\text{viscosity} : \text{Nsm}^{-2})$$

in case of  $\psi > 0.25$ :

for disk ( $-4^\circ\text{C} < T_c < 0^\circ\text{C}$  or  $-20^\circ\text{C} < T_c < -10^\circ\text{C}$ )

$$E_{ic} = 0.572 \times \log_{10}(\psi - 0.25) + 0.967$$

for column ( $-10^\circ\text{C} < T_c < -4^\circ\text{C}$  or  $T_c < -20^\circ\text{C}$ )

$$E_{ic} = 0.556 \times \log_{10}(\psi - 0.25) + 0.632$$

in case of  $\psi < 0.25$ :

$$E_{ic} = 0.$$

### B-11-3. Production terms for snow

#### a) Conversion from cloud ice to snow (Picns)

The conversion from cloud ice (pristine ice crystals) to snow takes place through three processes; depositional and riming growth of ice crystals and aggregation between pristine ice crystals. The time needed for an ice crystal to grow from  $m_i$  to  $m_{s0}$  in mass via depositional and riming growth is

$$\Delta\tau = \frac{Ni(m_{s0} - m_i)}{\text{Pidep} + \text{pi.iacw}}; \quad m_i = \frac{\rho Qi}{Ni}; \quad m_{s0} = (4\pi/3)\rho_s r_{s0}^3. \quad (11-27)$$

Therefore, cloud ice converted into snow in unit time is given as (in case of  $m_i < 0.5m_{s0}$ )

$$\text{CN}_{is}^{\text{dep+ac}} = \frac{1}{\Delta\tau} \rho Qi = \frac{m_i}{m_{s0} - m_i} (\text{Pidep} + \text{Pi.iacw}). \quad (11-28)$$

This term becomes very large for the case of  $m_i \approx m_{s0}$  to yield erroneous results. To prevent this, Eq. (11-28) is applied only to the case of  $m_i < 0.5m_{s0}$ . To the case of  $m_i > 0.5m_{s0}$ , the following is applied:

(in case of  $m_i > 0.5m_{s0}$ )

$$\text{CN}_{is}^{\text{dep+ac}} = (\text{Pidep} + \text{Pi.iacw}) + \left(1 - \frac{0.5m_{s0}}{m_i}\right) \frac{Qi}{2\Delta t}. \quad (11-29)$$

The conversion from cloud ice to snow due to aggregation is parameterized, following Murakami (Eqs. (M-34)...(M-41)). The rate of collision-coalescence among a homogeneous population of ice crystals may be written by

$$\left. \frac{dNi}{dt} \right|_{\text{aggr}} = \frac{1}{2} K_I Ni^2, \quad (\text{M-34})$$

where

$$K_I = \frac{\pi}{6} \bar{D}i^2 \bar{U}_I E_{II} X. \quad (\text{M-35})$$

Here  $\bar{D}i$  represents the mean diameter of ice crystals,  $\bar{U}_I$  the fall velocity of ice crystals,  $E_{II}$  the collection efficiency between ice crystals, and  $X$  the dispersion of the fall velocity spectrum of ice crystals. Using the following equation for the fall velocity

$$\bar{U}_I = a_I \bar{D}i \left( \frac{\rho_0}{\rho} \right)^{\frac{1}{3}}, \quad (\text{M-36})$$

Eq. (M-35) is rewritten as

$$K_I = \frac{C_1}{Ni}, \quad (\text{M-37})$$

where

$$C_1 = \frac{\rho Q i a_I E_{II} X}{\rho_I} \left( \frac{\rho_0}{\rho} \right)^{\frac{1}{3}}. \quad (\text{M-38})$$

Combining Eq. (M-34) and Eq. (M-37), we obtain

$$\left. \frac{dNi}{dt} \right|_{\text{aggr}} = -\frac{C_1}{2} Ni. \quad (\text{M-39})$$

The time needed for cloud ice to grow by aggregation from  $\bar{r}_I$  to  $r_{s0}$  in radius is equal to the time needed for the cloud ice concentration to decrease from  $Ni$  to  $Ni(\bar{r}_I/\bar{r}_{s0})^3$ . Assuming that  $\rho_I$  is constant yields

$$\Delta\tau_2 = -\frac{2}{C_1} \log \left( \frac{\bar{r}_I}{r_{s0}} \right)^3. \quad (\text{M-40})$$

The conversion rate from cloud ice to snow is given by

$$\text{CN}_{\text{IS}}^{\text{Ag}} = \frac{Qi}{\Delta\tau_2}. \quad (\text{M-41})$$

The total conversion rate in mass from cloud ice to snow is given by the sum of

$$\text{Picns} = \text{CN}_{\text{IS}}^{\text{dep+ac}} + \text{CN}_{\text{IS}}^{\text{Ag}}. \quad (\text{11-30})$$

The total conversion rate in number from cloud ice to snow is given by

$$N_{icns} = \frac{P_{icns}}{m_{s0}} \quad (11-31)$$

b) Aggregation among snow particles( $N_{sag}$ )

The decrease in number concentration of snow due to aggregation among snow crystals (or aggregates)(M-44) is obtained using an equation based on the analytical model of aggregational growth by Passarelli (1978).

$$N_{sag} = \left. \frac{dN_s}{dt} \right|_{agg} = - \frac{a_s E_{ss} I(b_s)}{4 \times 720} \pi^{\frac{1-b_s}{3}} \rho^{\frac{2+b_s}{3}} \rho_s^{\frac{-2-b_s}{3}} Q_s^{\frac{2+b_s}{3}} N_s^{\frac{4-b_s}{3}}, \quad (11-32)$$

where

$$I(d) = \int_0^\infty \int_0^\infty x^3 y^3 (x+y)^2 |x^d - y^d| e^{-(x+y)} dx dy.$$

For  $d = 0.6, 0.5$  and  $0.4$ ,  $I(d) = 2566, 1610$  and  $1108$  (Mizuno, 1990).

c) Depositional growth and melting of snow

Depositional growth of snow (L-52) for  $T_c < T_0$  is modified in order to incorporate the warming of the surface temperature of a snow particle due to riming as follows (Cotton and Anthes, 1989, Eq. 4-37)

$$P_{sdep} \text{ (or } -P_{ssub}) = \frac{2\pi(Si-1)}{\rho(A''+B'')} \text{VENT}(a_s, b_s, \lambda_s, N_{s0}) - \frac{L_s L_f}{\kappa_a R_w T^2 (A''+B'')} P_{sacw}, \quad (11-33a)$$

where

$$A'' = \frac{L_s^2}{\kappa_a R_w T^2}, \quad B'' = \frac{1}{\rho Q v s i \psi},$$

$$\text{VENT}(a_s, b_s, \lambda_s, N_{s0})$$

$$= N_{s0} \left[ 0.78 \lambda_s^{-2} + 0.31 S_c^{1/3} \Gamma \left( \frac{b_s+5}{2} \right) a_s^{1/2} \left( \frac{\rho_0}{\rho} \right)^{1/4} \nu^{-1/2} \lambda_{b_s}^{-(b_s+5)/2} \right].$$

The first term on R.H.S of Eq. (11-33a) is the same as  $P_{sdep}$  without modification, (L-52). Similar modification is made for the depositional growth of graupel ( $P_{gdep}$ ). Generally, modification for graupel is much larger than that for snow.

The melting of snow for  $T_c > T_0$  is formulated on heat balance considerations. The

cooling associated with the melting is balanced by the combined effects of conduction and convection of heat to the particle surface, the latent heat of condensation and evaporation of water to or from the particle surface, and the sensible heat associated with the accreted water. The rate of melting of snow to form rain can be expressed as

$$P_{\text{smlt}} = \frac{2\pi}{\rho L_f} (K_a T_c - L_v \psi \rho (Q_{vs} w - Qv)) \times \text{VENT}(a_s, b_s, \lambda_s, N_{s0}) + \frac{C_w T_c}{L_f} (P_{\text{sacw}} + P_{\text{sacr}}), \quad (\text{L-32})$$

If  $P_{\text{smlt}}$  is positive, melting occurs, and  $P_{\text{sdep}}$  ( $-P_{\text{ssub}}$ ) is calculated (see Ikawa *et al.*, 1987, Eq. (2-12)) by

$$P_{\text{sdep}} = -2\pi\psi(Q_{vs}(T = T_0) - Qv) \times \text{VENT}(a_s, b_s, \lambda_s, N_{s0}). \quad (\text{11-33b})$$

If  $P_{\text{smlt}}$  is negative for  $T_c > T_0$ , melting does not occur. In a dry air, evaporative cooling is large enough to prevent melting.  $P_{\text{sdep}}$  ( $-P_{\text{ssub}}$ ) is calculated in a similar way to  $P_{\text{prev}}$  (L-52) by

$$P_{\text{sdep}}(\text{or } -P_{\text{ssub}}) = \frac{2\pi(S_w - 1)}{\rho(A'' + B'')} \text{VENT}(a_s, b_s, \lambda_s, N_{s0}), \quad (\text{11-34})$$

where

$$A'' = \frac{L_s^2}{K_a R_w T^2}, \quad B'' = \frac{1}{\rho Q_{vs} w \psi}.$$

$P_{g\text{dep}}$  for  $T > T_0$  is formulated in a similar way to  $P_{\text{sdep}}$  for  $T > T_0$ .

#### B-11-4. Production terms for graupel

a) Conversion from cloud ice to graupel ( $P_{\text{icng}}$ ; see Fig. B-11-2b)

This occurs via riming on ice crystals, and is parameterized as follows. The mass required for an ice crystal to be converted into a graupel particle of minimum weight,  $m_{g0}$ , is

$$\Delta m_{gi} = m_{g0} - m_i,$$

where

$$m_{g0} = (4\pi/3)\rho_g r_{g0}^3; \quad m_i = \frac{\rho Q_i}{N_i}; \quad r_{g0} = r_0 = 75\mu\text{m}.$$

On the other hand, it is assumed that the portion of the amount of rime on an ice crystal greater than  $\beta \times P_{\text{idep}}$ ,

$$CLic = \max \left( \frac{\pi}{4} (Di + Dc)^2 Eic |U_{di} - U_{dc}| \rho Qc - \beta \frac{Pidep}{Ni}, 0 \right), \quad (11-35)$$

is consumed to form a graupel particle. The time needed for an ice crystal to be converted into a graupel is  $\Delta m_{gi}/CLic$ . The amount of cloud ice in mass converted into graupel in unit time is given as

$$Picng = \frac{CLic}{\Delta m_{gi}} \rho Qi = Nicng m_i \quad (11-36)$$

The number of ice crystals to be converted into graupel is given as

$$Nicng = \frac{CLic}{\Delta m_{gi}} Ni = \frac{Picng + Pg.iacw}{m_{g0}}. \quad (11-37)$$

The amount of rime converted into graupel in unit time is given as

$$Pg.iacw = Ni CLic = Nicng \Delta m_{gi}. \quad (11-38)$$

b) Conversion from snow to graupel (Pscng; see Fig. B-11-2a)

Snow is converted into graupel through the collection of supercooled cloud droplets (riming process). All of the accreted cloud water is not converted into graupel; some is consumed for the riming growth of snow itself. The point of the parameterization is how to determine the dispatcher function  $\eta(D)$  which specifies the portion of the accreted cloud water to be converted into graupel. The remainder  $(1-\eta(D))$  is consumed for the riming growth of snow. Following Murakami (1990) who assumed that the change of snow particle size due to riming is negligibly small, the amount of riming needed for snow with diameter  $D$  to be converted into graupel with diameter  $D$  through the riming process is given by

$$\Delta m_{sg} = (\rho_g - \rho_s) \pi D^3 / 6. \quad (11-39)$$

The amount of riming by snow with the diameter  $D$  is given by

$$CL(D) = \frac{\pi}{4} D^2 Esc U_{ds} \rho Qc, \quad (11-40)$$

$$U_{ds} = a_s D^{b_s} (\rho_0/\rho)^{0.5} \quad (a_s = 17, \quad b_s = 0.5) \quad (11-41)$$

The time needed for a snow particle with diameter  $D$  to be converted into graupel with diameter  $D$  through the riming process (Murakami, 1990, M-42) is given by

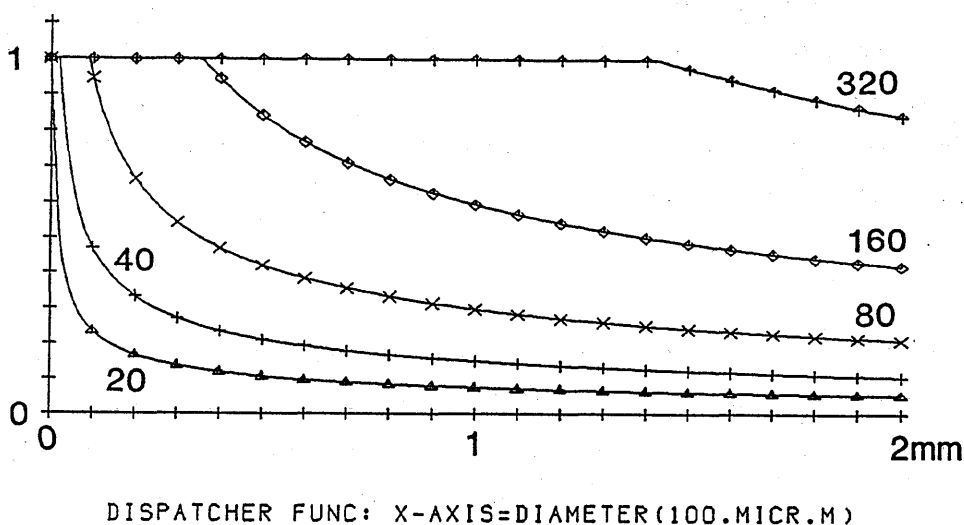


Fig. B-11-3 The dispatcher function (Eq. (11-43)) as a function of the diameter of a snow particle,  $D$ , with the parameters  $\rho_0 = \rho = 1 \text{ kgm}^{-3}$ ,  $\rho Qc = 10^{-3} \text{ kgm}^{-3}$  and  $E_{sc} = 1$  for the case of  $\alpha 2\Delta t = 20, 40, 80, 160$  and  $320$ .

$$\Delta\tau = \frac{\Delta m_{sg}}{CL(D)} = \frac{2(\rho_g - \rho_s)D^{1-b_s}}{3a_s E_{sc} \rho Qc} \left(\frac{\rho}{\rho_0}\right)^{1/2} \quad (11-42)$$

$\Delta\tau$  is small for small  $D$ , and small snow particles are more likely converted into graupel than large snow particles. Therefore the dispatcher function is assumed to be

$$\eta(D) = \min\left(1, \frac{\alpha 2\Delta t}{\Delta\tau}\right) = \min\left(1, \frac{\alpha 2\Delta t CL(D)}{\Delta m_{sg}}\right), \quad (11-43)$$

where  $\alpha$  is a tuning parameter and  $\Delta t$  is the time step of the leap-frog time integration. The amount of riming to be consumed for graupel generation is  $\eta(D)CL(D)$ , while that for riming growth of a snow particle is  $(1 - \eta(D))CL(D)$ . Hereafter, the diameter which yields  $\alpha 2\Delta t = \Delta\tau$  is designated by  $D_{sc}$ :

$$D_{sc} = \left(\alpha 2\Delta t \frac{3a_s E_{sc} \rho Qc}{2(\rho_g - \rho_s)}\right)^2 \quad (11-44)$$

All the amount of riming on snow particles smaller than  $D_{sc}$  in diameter is assumed to form graupel. For the case of  $\alpha 2\Delta t = 80s$ ,  $\rho Qc = 10^{-3} \text{ kg/m}^3$ ,  $D_{sc} = 100\mu\text{m}$  (see Fig. B-11-3).

Figure B-11-3 shows the dispatcher function with the parameters  $\rho_0 = \rho = 1 \text{ kgm}^{-3}$ ,  $\rho Qc = 10^{-3} \text{ kgm}^{-3}$  and  $E_{sc} = 1$  for the case of  $\alpha 2\Delta t = 20, 40, 80, 160$  and  $320$ .

As will be shown in C-3, in the 3-dimensional simulation of convective snow clouds

observed over the Sea of Japan in winter, it is found that  $\alpha = 2 \sim 5$  for  $2\Delta t = 8$  sec gives rise to the observed ratio of the precipitation amount of graupel over that of snow which is about  $0.3 \sim 1.0$ .

In the 2-dimensional simulation of convective snow clouds observed over the Sea of Japan in winter, Ikawa (1988) used Matsuo's method (1986),

$$\eta(D) = \begin{cases} 1 & \text{for } D < Dcr \\ 0 & \text{for } D > Dcr. \end{cases} \quad (11-45)$$

He found  $Dcr = 1 \times 10^{-3}$  m gives rise to the reasonable ratio of the precipitation amount of graupel over that of snow. As can be seen from Fig. B-11-3, the dispatcher function of the form Eq. (11-45) with  $Dcr = 1 \times 10^{-3}$  m is larger than the dispatcher function given by Eq. (11-43) with  $\alpha\Delta t = 32$ . This difference comes from the differences of the dimension of the model (2-D or 3-D) and two parameterizations; his previous parameterization incorporates  $Pg.sacw$ , but not  $Pscng$  explicitly. This dispatcher function is simple enough, but overestimates the number of graupel particles generated, and may cause imbalance between number and mass of graupel.

The amount of rime on snow particles converted into graupel is given as

$$\begin{aligned} Pg.sacw &= \int \eta(D)CL(D)f(D)dD \\ &= \alpha 2\Delta t \frac{3\rho_0\pi N_{s0}(\rho Qc)^2 Esc^2 a_s^2 \Gamma(2b_s + 2)}{8\rho(\rho_g - \rho_s)\lambda_s^{2b_s+2}}. \end{aligned} \quad (11-46)$$

The probability for a snow particle of the diameter  $D$  to be converted into a graupel particle in unit time is given by

$$\text{Prob}(D) = \frac{1}{2\Delta t} \min\left(1, \frac{2\Delta t\eta(D)CL(D)}{\Delta m_{sg}}\right) \simeq \frac{\eta(D)CL(D)}{\Delta m_{sg}}. \quad (11-47)$$

The approximate expression holds for most  $D$  ( $D > Dsc/\alpha^2$ ).

The number generation of graupel due to riming of snow is given as

$$Nscng = \int \text{Prob}(D)f(D)dD \simeq \int \frac{\eta(D)CL(D)}{\Delta m_{sg}} f(D)dD. \quad (11-48)$$

In evaluating the above integral,

$$f(D) = N_{s0}D \exp(-\lambda_s D) \quad (11-49)$$

is used instead of

$$f(D) = N_{s0} \exp(-\lambda_s D), \quad (11-50)$$

in order to avoid over-estimation of the number concentration for small  $D$  (snow particles of  $D < 100\mu\text{m}$  are categorized into pristine ice crystals, and should not be counted).

$N_{\text{scng}}$  is approximated as

$$\begin{aligned} N_{\text{scng}} &= \int_0^{D_{sc}} \frac{CL(D)}{\Delta m_{sg}} f(D) dD + 2\alpha\Delta t \int_{D_{sc}}^{\infty} \frac{CL(D)^2}{\Delta m_{sg}^2} f(D) dD \\ &= \text{coef} \frac{N_{s0}}{\lambda_s^{3/2}} \left[ -z \exp(-z^2) + \int_0^{(\lambda D_{sc})^{1/2}} \exp(-z^2) dz \right] \\ &\quad + (\alpha 2\Delta t) \text{coef}^2 \frac{N_{s0} \exp(-\lambda_s D_{sc})}{\lambda_s}, \end{aligned} \quad (11-51)$$

where

$$\text{coef} = \left( \frac{\rho_0}{\rho} \right)^{1/2} \frac{3a_s E_{sc} \rho Q_c}{2(\rho_g - \rho_s)}. \quad (11-52)$$

The equation might be further simplified as

$$N_{\text{scng}} = \frac{\rho_0}{\rho} \left( \frac{3\pi a_s \rho Q_c E_{cs}}{2(\rho_g - \rho_s)} \right)^2 \frac{N_{s0}}{\lambda_s} \alpha 2\Delta t, \quad (11-53)$$

for the case of small  $\lambda D_{sc}$  (small  $\alpha 2\Delta t$ , small  $Q_c$ , large  $Q_s$  and small  $N_s$ ). For example, Eq. (11-53) gives only 10% overestimation of  $N_{\text{scng}}$  for the case of ( $\lambda D_{sc} = 0.37$ ,  $\alpha 2\Delta t = 100\text{sec}$ ,  $Q_c = 10^{-3}\text{kg/kg}$ ,  $Q_s = 0.5 \times 10^{-3}\text{kg/kg}$ ,  $N_s = 3.4 \times 10^3\text{m}^{-3}$ ), while this gives 50% overestimation of  $N_{\text{scng}}$  for the case of ( $\lambda D_{sc} = 1.5$ ,  $\alpha 2\Delta t = 100\text{sec}$ ,  $Q_c = 2 \times 10^{-3}\text{kg/kg}$ ,  $Q_s = 0.5 \times 10^{-3}\text{kg/kg}$ ,  $N_s = 3.4 \times 10^3\text{m}^{-3}$ ).

The amount of snow converted into graupel as embryo is given as (see Murakami, 1990, (M-43))

$$P_{\text{scng}} = \int \frac{\pi}{6} D^3 \rho_s \text{Prob}(D) f(D) dD \simeq \frac{\rho_s}{\rho_g - \rho_s} P_{g.\text{sacw}}. \quad (11-54)$$

The amount of riming consumed for the growth of snow itself is

$$P_{s.\text{sacw}} = P_{\text{sacw}} - P_{g.\text{sacw}},$$

where  $P_{\text{sacw}}$  is given by (L-24).

Dependency of  $P_{g.\text{sacw}}$  and  $P_{\text{scng}}$  on  $\alpha 2\Delta t$  is shown in Figs. B-11-6. and B-11-8.

c) Collision between rain and snow (see Fig. B-11-2c)

For collision between rain and snow, the accretion rate of rain by snow is

$$\begin{aligned} \text{Psacr} = \frac{1}{\rho} \int_0^\infty \int_0^\infty \frac{\pi}{4} (Dr + Ds)^2 Ers |U_{dr} - U_{ds}| \rho_w \frac{\pi}{6} Dr^3 N_{r0} \exp(-\lambda_r Dr) N_{s0} \\ \times \exp(-\lambda_s Ds) dDr dDs. \end{aligned} \quad (11-55)$$

In most of models so far, the following approximation is used for the differential velocity;

$$|U_{dr} - U_{ds}| \approx |\bar{U}_r - \bar{U}_s|.$$

This approximation underestimates Pracs when the value of  $\bar{U}_r$  is close to  $\bar{U}_s$ . To remedy this underestimation, we used the following approximation proposed by Mizuno (1990a) who obtained the exact value of the intergral of Eq. (11-55) analytically for the case of  $b_r = b_s = 0.5$ ,

$$|U_{dr} - U_{ds}| \approx \sqrt{(\alpha \bar{U}_r - \beta \bar{U}_s)^2 + \gamma \bar{U}_r - \bar{U}_s} \quad (11-56)$$

wiht  $\alpha = 1.2$ ,  $\beta = 0.95$  and  $\gamma = 0.08$ . The approximation expressed by Eq. (11-56) yields

$$\text{Psacr} = \pi^2 Ers \sqrt{(\alpha \bar{U}_r - \beta \bar{U}_s)^2 + \gamma \bar{U}_r \bar{U}_s} \frac{\rho_w}{\rho} N_{r0} N_{s0} \left( \frac{5}{\lambda_r^6 \lambda_s} + \frac{2}{\lambda_r^5 \lambda_s^2} + \frac{0.5}{\lambda_r^4 \lambda_s^3} \right), \quad (11-57)$$

where the collection efficiency of snow for rain (or that of rain for snow),  $Ers$ , is assumed to be unity. Eq. (11-57) is used for the case shown in C-3 where  $b_r$  is not equal to 0.5 but 0.8.

The accretion rate of snow by rain is

$$\text{Pracs} = \pi^2 Ers \sqrt{(\alpha \bar{U}_r - \beta \bar{U}_s)^2 + \gamma \bar{U}_r \bar{U}_s} \frac{\rho_s}{\rho} N_{s0} N_{r0} \left( \frac{5}{\lambda_s^6 \lambda_r} + \frac{2}{\lambda_s^5 \lambda_r^2} + \frac{0.5}{\lambda_s^4 \lambda_r^3} \right) \quad (11-58)$$

with  $\alpha = 1.2$ ,  $\beta = 0.95$  and  $\gamma = 0.08$ .

The number of collisions between snow and rain particles in unit time is given as

$$\begin{aligned} \text{Nsacr} = \text{Nracs} = \int_0^\infty \int_0^\infty \frac{\pi}{4} (Dr + Ds)^2 Ers |U_{dr} - U_{ds}| \\ \times N_{r0} \exp(-\lambda_r Dr) N_{s0} \exp(-\lambda_s Ds) dDr dDs. \end{aligned} \quad (11-59)$$

Mizuno (1990b) obtained the exact value of the above integral analytically, and he proposed the following approximation for the case of  $b_r = b_s = 0.5$  to Eq. (11-59):

$$\begin{aligned} \text{Nsacr} = \text{Nracs} \\ = \frac{\pi}{4} Ers \sqrt{(\alpha \bar{U}_{nr} - \bar{U}_{ns})^2 + \beta \bar{U}_{nr} \bar{U}_{ns}} N_{r0} N_{s0} \\ \times \int_0^\infty \int_0^\infty (Dr + Ds)^2 \exp(-\lambda_r Dr) \exp(-\lambda_s Ds) dDr dDs \\ = \frac{\pi}{2} Ers \sqrt{\alpha (\bar{U}_{nr} - \bar{U}_{ns})^2 + \beta \bar{U}_{nr} \bar{U}_{ns}} N_{r0} N_{s0} \left( \frac{1}{\lambda_r^3 \lambda_s} + \frac{1}{\lambda_r^2 \lambda_s^2} + \frac{1}{\lambda_r \lambda_s^3} \right) \end{aligned} \quad (11-60)$$

where  $\alpha = 1.7$   $\beta = 0.3$  and the collection efficiency of snow for rain (or that of rain for snow),  $Ers$ , is assumed to be unity. Eq. (11-60) is used for the case shown in C-3 where  $b_r$  is not equal to 0.5 but 0.8.

The portion of the accreted rain by snow consumed for production of graupel in mass is

$$Pg.sacr = (1 - \alpha_{rs})Psacr, \quad (11-61)$$

where  $(1 - \alpha_{rs})$  is the ratio at which the collisions between raindrops and snow particles result in graupel production. The equation chosen to express  $\alpha_{RS}$  (Murakami, 1990: (M-25)) is

$$\alpha_{rs} = \frac{\rho_s^2 \left[ \frac{4}{\lambda_s} \right]^6}{\rho_s^2 \left[ \frac{4}{\lambda_s} \right]^6 + \rho_w^2 \left[ \frac{4}{\lambda_r} \right]^6} = \frac{m_s^2}{m_s^2 + m_r^2}. \quad (11-62)$$

The portion of the accreted snow by rain consumed for production of graupel in mass is

$$Pg.racs = (1 - \alpha_{rs})Pracs. \quad (11-63)$$

The portion of the accreted rain by snow consumed for production of snow is

$$Ps.sacr = \alpha_{rs}Psacr. \quad (11-64)$$

The number of graupel particles generated by collision of snow and rain is

$$Ng.racs = (1 - \alpha_{rs})Nracs = Ng.sacr. \quad (11-65)$$

A similar approximation is used in deriving the rates involving collision between graupel and snow and between graupel and rain. Collision between graupel and snow is almost suppressed in the simulation shown in C-3 by setting  $Esg = 0.001$ .

d) Graupel generation via collision between ice and rain

The number of graupel generated via collision between ice and rain is given as

$$\begin{aligned} Niacr = Nraci &= \frac{\pi}{4} \int_0^\infty Dr^2 Ur Ni Nr_0 \exp(-\lambda_r Dr) dDr \\ &= \frac{\pi}{4} \frac{\Gamma(3 + b_r)}{\lambda_r^{3+b_r}} Ni Nr_0 \left( \frac{\rho_0}{\rho} \right)^{1/2} \\ &= Praci(Ni/Qi). \end{aligned} \quad (11-66)$$

The mass of cloud ice accreted by rain,  $P_{aci}$ , is given by (L-25).

e) Graupel generation via immersion freezing of rain

The number of graupel generated via immersion freezing of rain is given, based on Bigg (1953) as

$$N_{gfzr} = B'' \frac{\pi}{6} \int D^3 N_{0r} \exp(-\lambda_r D) dD = B'' \pi N_{0r} \lambda_r^{-4}, \quad (11-67)$$

where  $B'' = B'(\exp(A(T_0 - T)) - 1)$ ,  $B' = 100 \text{ (m}^{-3}\text{s}^{-1}\text{)}$  and  $A' = 0.66 \text{ (K}^{-1}\text{)}$ . The increase in mass,  $P_{gfzr}$ , is given by (L-45).

### B-11-5. Production terms for cloud water

a) Conversion from water vapor into cloud water ( $P_{cnd}$ )

"Instantaneous adjustment procedure" is applied to the newly time-integrated  $Q_c$ ,  $\theta$  and  $Q_v$  in which advection, diffusion and cloud microphysical terms are taken into account except for the term ( $P_{cnd}$ ) discussed here. During condensation or evaporation, pressure is assumed to be invariant. Let  $Q_c + \Delta Q_c$ ,  $Q_v + \Delta Q_v$  and  $\theta + \Delta\theta$  be the adjusted values for  $Q_c$ ,  $Q_v$  and  $\theta$ . Let  $Q_{vsw}(\theta, P)$  be the saturation mixing ratio of water vapor with respect to water.

- 1) If  $Q_{vsw}(\theta, P) > Q_v$  and  $Q_c = 0$ , then no adjustment is made.
- 2) Otherwise, adjustment is made as below. The following equation is solved up to the second-order approximation in  $\Delta\theta$ :

$$\begin{aligned} Q_v + \Delta Q_v &= Q_{vsw}(\theta + \Delta\theta) \\ &\simeq Q_{vsw}(\theta) + (\partial Q_{vsw}/\partial\theta)(\theta)\Delta\theta + 0.5(\partial^2 Q_{vsw}/\partial\theta^2)(\theta)\Delta\theta^2, \end{aligned} \quad (11-68)$$

$$C_p \Pi \Delta\theta = -L_v \Delta Q_v, \quad (11-69)$$

$$\Delta Q_v = -\Delta Q_c. \quad (11-70)$$

The equation to be solved for  $\Delta\theta$  is

$$Q_v - Q_{vsw}(\theta) = (C_p \Pi / L_v + (\partial Q_{vsw}/\partial\theta)(\theta))\Delta\theta + 0.5(\partial^2 Q_{vsw}/\partial\theta^2)(\theta)\Delta\theta^2. \quad (11-71)$$

The first guess of  $\Delta\theta$  is given as

$$\Delta\theta_1 = \frac{Q_v - Q_{vsw}(\theta)}{C_p \Pi / L_v + (\partial Q_{vsw}/\partial\theta)(\theta)}. \quad (11-72)$$

The second guess of  $\Delta\theta$  is given by use of  $\Delta\theta_1$  as

$$\Delta\theta_2 = \frac{Qv - Qvsw(\theta)}{C_p\Pi/L_v + (\partial Qvsw/\partial\theta)(\theta) + 0.5(\partial^2 Qvsw/\partial\theta^2)(\theta)\Delta\theta_1} \quad (11-73)$$

$$Pccnd = (C_p\Pi/L_v) \Delta\theta_2/2\Delta t. \quad (11-74)$$

Usually, this second guess is accurate enough.

A similar procedure is applied for the deposition of water vapor to form cloud ice at  $T_c < -40^\circ\text{C}$  (Pidsn), using  $Qvsi$  and  $L_s$  instead of  $Qvsw$  and  $L_v$ .

### B-11-6. Production term for rain

#### a) Conversion from cloud water into rain

The collision and coalescence of cloud droplets to form raindrops has been parameterized in different ways. "Kessler's parameterization" (Cotton and Anthes, 1989, §4-3-1) is

$$Pccnr = a(Qc - Q_{co})H(Qc - Q_{co}) \quad (11-75)$$

where  $H$  is the Heaviside function ( $Q_{co}$  is the threshold value for conversion). Ikawa (1988) used this parameterization with  $a = 10^{-3}\text{s}^{-1}$ ,  $Q_{co} = 10^{-3}$ .

Cotton (see Cotton and Anthes, 1989) modified this by making  $a$  and  $Q_{co}$  dependent on  $Qc$  and the prescribed number concentration of cloud water,  $Nc$ :

$$Q_{co} = \frac{4\pi\rho_w Nc r_{cm}^3}{3\rho} = 4 \times 10^{-12} Nc \quad (\text{for } r_{cm} = 10^{-5}\text{m}), \quad (11-76)$$

$$a = \pi E c c U_{dc} Nc r_c^2 = 1.3 \times 10^3 Qc^{4/3} Nc^{-1/3} \left( \frac{\rho_0}{\rho} \right). \quad (11-77)$$

Lin *et al.* (1983), Nickerson *et al.* (1986) and Matsuo and Mizuno (1988) proposed the parameterization based upon Berry (1968) or Berry and Reinhardt (1973):

$$Pccnr = aQc^2, \quad (11-78)$$

where  $a$  is function of  $Qc$ ,  $Nc$  and dispersion of the size distribution. Lin *et al.* used a modified form of the relation suggested by Berry (1968). It may be written as

$$Pccnr = \rho(Qc - Q_{co})^2 [1.2 \times 10^{-4} + \{1.569 \times 10^{-12} N_1 / [D_0(Qc - Q_{co})]\}]^{-1}, \quad (L-50)$$

where  $N_1$  is the number concentration of cloud droplets and  $D_0$  the dispersion (0.15) of

cloud droplets distribution. When the amount of cloud water exceeds  $Q_{co}$ , raindrops are formed. The introduction of the threshold in (L-50) is an empirical modification to Berry's original form made to better simulate observations of first echoes. Lin *et al.* reported that, for cold-based clouds typical of the northern High Plains region, they normally turned off Pccnr consistent with observations which indicate that the collision-coalescence process is rarely active.

For the simulation of the convective snow cloud to be shown in C-3, "Kessler's parameterization" is used for simplicity and uncertainty.

### B-11-7. Some numerical artifices

In leap-frog time integration, the values not at the central time step ( $it$ ) but at the old time step ( $it - 1$ ) is used for evaluating cloud microphysical production terms to maintain numerical stability.

Sometimes, some sink terms of cloud microphysical processes become so large that the mixing ratio at the next time step ( $it + 1$ ) becomes negative. A basic remedy for preventing this is to adopt smaller  $\Delta t$  at the expense of computational time. However, instead of doing so, sink terms are always adjusted in order to fulfill the following constraint:

$$P_{qqqq} < \frac{Qx}{2\Delta t} \quad (11-79)$$

Sometimes, mass ( $Qx$ ) becomes negative due to finite discretization errors in advection term in spite of the above-mentioned adjustment on  $P_{qqqq}$ . Negative mixing ratios are forced to be zero. If the values at the neighboring grid points are greater than zero, a certain value is subtracted from them, in order to maintain the conservation property of  $Qx$  as much as possible.

Sometimes, imbalance between mass ( $Qx$ ) and number ( $Nx$ ) occurs mainly due to numerical errors, especially for small  $Qx$  ( $< 10^{-15}$  kg/kg), and gives rise to erroneous results and numerical troubles (overflow etc.). To prevent this,  $Nx$  is adjusted for the given  $Qx$  to fulfill the following constraints:

for cloud ice

$$\frac{0.5 \times \rho Qi}{m_{i \max}} < Ni < 100 \frac{\rho Qi}{m_{i0}} \quad ; \quad m_{i \max} = 0.8 m_{s0} \quad (11-80)$$

for snow and graupel

$$\left(\frac{N_{x0}}{1000}\right)^{3/4} \left(\frac{\rho Q x}{\rho_x \pi}\right)^{1/4} < Nx < (1000N_{x0})^{3/4} \left(\frac{\rho Q x}{\rho_x \pi}\right)^{1/4}, \quad (11-81)$$

$$10^{-7} \times \left(\frac{\rho Q x}{m_{x0}}\right) < Nx < 100 \times \left(\frac{\rho Q x}{m_{x0}}\right). \quad (11-82)$$

The prescribed  $N_{x0}$  and  $m_{x0}$  are shown in Table B-11-1.

### Appendix B-11-1. List of symbols

In this list, L-nn, CT-nn and M-nn indicate that these terms are given by the formula nn in Lin *et al.* (1983), Cotton *et al.* (1986) and Murakami (1990).

Notation	Description		
Value	Unit		
$a_c$	constant in empirical formula for $U_{dc}$	$3 \times 10^{-7}$	$m^{1-bc}s^{-1}$
$a_g$	constant in empirical formula for $U_{dg}$	124	$m^{1-bg}s^{-1}$
$a_i$	constant in empirical formula for $U_{di}$	700	$m^{1-bi}s^{-1}$
$a_r$	constant in empirical formula for $U_{dr}$	842	$m^{1-br}s^{-1}$
$a_s$	constant in empirical formula for $U_{ds}$	17	$m^{1-bs}s^{-1}$
$A'$	constant in Bigg's equation	0.66	$K^{-1}$
$b_c$	constant in empirical formula for $U_{dc}$	2.0	
$b_g$	constant in empirical formula for $U_{dg}$	0.64	
$b_i$	constant in empirical formula for $U_{di}$	1.0	
$b_r$	constant in empirical formula for $U_{dr}$	0.8	
$b_s$	constant in empirical formula for $U_{ds}$	0.5	
$B$	constant in Huffmann and Vali's equation	4.5	
$B'$	constant in Bigg's equation	100	$m^{-3}s^{-1}$
$C_p$	specific heat of air at constant pressure	1005	$Jkg^{-1}K^{-1}$
$Dg$	diameter of graupel		m
$Dr$	diameter of rain		m
$Ds$	diameter of snow		m
$\bar{D}_c$	mean diameter of cloud water		m
$\bar{D}_i$	mean diameter of cloud ice		m
$D_v$	diffusivity of water vapor in the air		$m^2s^{-1}$

<i>Ecg</i>	collection efficiency of graupel for cloud water $Stk^2/(Stk + 0.5)^2$ (Murakami, 1990; Lew <i>et al.</i> , 1986)	
<i>Ecr</i>	collection efficiency of rain for cloud water $Stk^2/(Stk + 0.5)^2$	
<i>Ecs</i>	collection efficiency of snow for cloud water $Stk^2/(Stk + 0.5)^2$	
<i>Eig</i>	collection efficiency of graupel for cloud ice	0.1
<i>Eii</i>	collection efficiency among cloud ice particles	0.1
<i>Eis</i>	collection efficiency of snow for cloud ice	1.0
<i>Erg</i>	collection efficiency of graupel for rain	1.0
<i>Ers</i>	collection efficiency of snow for rain	1.0
<i>Esg</i>	collection efficiency of graupel for snow	0.001
<i>Ess</i>	collection efficiency among snow particles	0.1
<i>g</i>	gravitational acceleration	9.8 $\text{ms}^{-2}$
<i>L<sub>f</sub></i>	latent heat of fusion	$3.34 \times 10^5 \text{ Jkg}^{-1}$
<i>L<sub>s</sub></i>	latent heat of sublimation	$2.83 \times 10^6 \text{ Jkg}^{-1}$
<i>L<sub>v</sub></i>	latent heat of evaporation	$2.5 \times 10^6 \text{ Jkg}^{-1}$
<i>m<sub>i0</sub></i>	mass of the smallest cloud ice	$1 \times 10^{-12} \text{ kg}$
<i>m<sub>g0</sub></i>	mass of the smallest graupel particle	$1.6 \times 10^{-10} \text{ kg}$
<i>m<sub>r</sub></i>	mean mass of rain	kg
<i>m<sub>s</sub></i>	mean mass of snow	kg
<i>m<sub>s0</sub></i>	mass of the smallest snow particle	$4.4 \times 10^{-11} \text{ kg}$
<i>N<sub>c</sub></i>	number concentration of cloud water	$1.0 \times 10^8 \text{ m}^{-3}$
<i>N<sub>g0</sub></i>	parameter of graupel size distribution	$1.1 \times 10^6 \text{ m}^{-4}$
<i>N<sub>i</sub></i>	number concentration of cloud ice	$\text{m}^{-3}$
<i>N<sub>i0</sub></i>	parameter of Fletcher's equation: (M-26)	$1.0 \times 10^{-2} \text{ m}^{-3}$
<i>N<sub>r0</sub></i>	parameter of rain size distribution	$8.0 \times 10^6 \text{ m}^{-4}$
<i>N<sub>s</sub></i>	number concentration of snow	$\text{m}^{-3}$
<i>N<sub>s0</sub></i>	parameter of snow size distribution	$1.8 \times 10^6 \text{ m}^{-4}$
<i>Niacr</i>	number of collisions between rain and cloud ice in unit time: (11-66)	$\text{m}^{-3}\text{s}^{-1}$
<i>Niag</i>	decrease in number concentration of cloud ice by	$\text{m}^{-3}\text{s}^{-1}$

	aggregation (M-39)	
Nicng	number generation rate of graupel due to accretion of cloud water by cloud ice: (11-37)	$m^{-3}s^{-1}$
Nicns	number generation rate of snow due to depositional and riming growth of cloud ice and aggregation of cloud ice: (11-31)	$m^{-3}s^{-1}$
Nidsn	number generation rate for deposition/sorption nucleation of cloud ice at the expense of water vapor (M-29) (11-17)	$m^{-3}s^{-1}$
Nifzc	number generation rate of cloud ice due to homogeneous and heterogeneous freezing (M-30) of cloud water: (11-19)	$m^{-3}s^{-1}$
Nimlt	number generation rate for melting of cloud ice to form cloud water	$m^{-3}s^{-1}$
Nispl	number generation rate for ice splinter multiplication of cloud ice: (11-23)	$m^{-3}s^{-1}$
Ngaci	number of collisions in unit time between cloud ice and graupel	$m^{-3}s^{-1}$
Ngacr	number of collisions in unit time between rain and graupel; similar to Nsacr	$m^{-3}s^{-1}$
Ngacs	number of collisions in unit time between snow and graupel; similar to Nsacr	$m^{-3}s^{-1}$
Ngfzr	number of rain drops which freeze to form graupel: (11-67)	$m^{-3}s^{-1}$
Ng.raci	generation rate of graupel by collision between cloud ice and rain	$m^{-3}s^{-1}$
Ngprc	rate of change in number concentration due to the precipitation of graupel: (11-12)	$m^{-3}s^{-1}$
Ng.racs =Ng.sacr	generation rate of graupel by collision between snow and rain: (11-65)	$m^{-3}s^{-1}$
Nraci	number of collisions in unit time between rain and cloud ice: (11-66)	$m^{-3}s^{-1}$
Nracs	number of collisions in unit time between rain	$m^{-3}s^{-1}$

	and snow: (11-60)	
Nsacr	number of collisions in unit time between snow and rain: (11-60)	$m^{-3}s^{-1}$
Nsaci	number of collisions in unit time between cloud ice and snow: similar to Niacr	$m^{-3}s^{-1}$
Nsag	decrease in number concentration of snow by aggregation (M-44)	$m^{-3}s^{-1}$
Nscng	number generation rate of graupel due to the riming growth of snow to form graupel: (11-51)	$m^{-3}s^{-1}$
Nsprc	rate of change in number concentration due to the precipitation of snow: (11-12)	$m^{-3}s^{-1}$
Pccnd	condensation of water vapor in unit time to form cloud water which is calculated by "instantaneous adjustment procedure": (11-74)	$s^{-1}$
Pccnr	generation term of rain via collision and coalescence of cloud droplets: (11-75 ~ 76)	$s^{-1}$
Piacw	accreted cloud water by cloud ice in unit time which is the sum of $P_{i,acw}$ and $P_{g,acw}$ : (11-25)	$s^{-1}$
$P_{i,acw}$	portion of accreted cloud water by cloud ice in unit time to be consumed for riming growth of cloud ice itself: (11-26)	$s^{-1}$
Piacr	production rate for accretion of rain by cloud ice (L-26)	$s^{-1}$
Picng	generation rate of graupel in mass due to accretion of cloud water by cloud ice: (11-36)	$s^{-1}$
Picns	generation rate of snow in mass due to depositional and riming growth of cloud ice and aggregation of cloud ice: (11-30)	$s^{-1}$
Pidep	production rate for depositional growth of cloud ice: (11-24)	$s^{-1}$
Pidsn	generation rate for deposition/sorption nucleation of cloud ice at the expense of water vapour	$s^{-1}$

	(M-29)	
Pifzc	production rate for homogeneous and heterogeneous freezing (M-30) of cloud water to form cloud ice: (11-20)	$s^{-1}$
Pimlt	production rate for melting of cloud ice to form cloud water	
Pispl	production rate for ice splinter multiplication of cloud ice at riming process (Hallet-Mossop, 1974) (11-21)	$s^{-1}$
Pgaci	production rate for accretion of cloud ice by graupel (L-41)	$s^{-1}$
Pgacr	production rate for accretion of rain by graupel (L-42)	$s^{-1}$
Pgacs	production rate for accretion of snow by graupel (L-29)	$s^{-1}$
Pgacw	production rate for accretion of snow by graupel (L-40)	$s^{-1}$
Pgdep	rate for depositional growth of graupel, similar to (11-33)	$s^{-1}$
Pgfzr	probabilistic freezing of rain to form graupel (L-45)	$s^{-1}$
Pg.iacw	portion of the accreted cloud water by cloud ice which is converted into graupel	$s^{-1}$
Pgmilt	production rate for graupel melting to form rain, $T > T_0$ (L-47)	$s^{-1}$
Pg.racs	portion of the accreted snow by rain which is converted into graupel: (11-63)	$s^{-1}$
Pg.sacw	portion of the accreted cloud water by snow which is converted into graupel: (11-47)	$s^{-1}$
Pg.sacr	portion of the accreted rain by snow which is converted into graupel: (11-61)	$s^{-1}$
Pgwet	wet growth of graupel; may involve Pgacs and Pgaci and must include Pgacw or Pgacr, or both.	$s^{-1}$

Pgdry	dry growth of graupel; involves Pgacs, Pgaci, Pgacw and Pgacr (L-49)	$s^{-1}$
Pgprc	rate of change in mixing ratio due to the precipitation of graupel: (11-14)	$s^{-1}$
Praci	production rate for accretion of cloud ice by rain (L-25)	$s^{-1}$
Pracw	production rate for accretion of cloud water by rain (L-27)	$s^{-1}$
Prevp	production rate for rain evaporation (L-52)	$s^{-1}$
Praci	generatin rate of graupel by collision between cloud ice and rain (L-25)	$s^{-1}$
Pracs	production rate for accretion of cloud water by snow: (11-58)	$s^{-1}$
Prprc	rate of change in mixing ratio due to the precipitation of rain: (11-14)	$s^{-1}$
Psacw	accreted cloud water by snow which is the sum of Ps.sacw and Pg.sacw. (L-24)	$s^{-1}$
Ps.sacw	part of accreted cloud water by snow which is consumed for riming growth of snow itself: Ps.sacw=Psacw-Pg.sacw	$s^{-1}$
Ps.sacr	portion of the accreted rain by snow which is consumed for the growth of snow: (11-64)	$s^{-1}$
Psacr	accreted rain by snow: (11-57)	$s^{-1}$
Psaci	production rate for accretion of cloud ice by snow (L-22)	$s^{-1}$
Pscng	generation of graupel in mass due to the riming of snow: (11-54)	$s^{-1}$
Psdep	production rate for depositional growth of snow: (11-33 ~ 34)	$s^{-1}$
Psmlt	production rate for snow melting to form rain (L-32)	$s^{-1}$
Psprc	rate of change in mixing ratio due to the precipitation of snow: (11-14)	$s^{-1}$

$Q_{vsw}$	saturation mixing ratio for water vapor with respect to water		
$Q_{vsi}$	saturation mixing ratio for water vapor with respect to ice		
$\bar{r}_I$	mean radius of cloud ice		m
$r_{s0}$	radius of the smallest snow	$0.75 \times 10^{-4}$	m
$R_w$	gas constant for water vapor	461.5	$\text{Jkg}^{-1}\text{K}^{-1}$
$S_i$	saturation ratio over ice, $Q_v/Q_{vsi}$		
$S_w$	saturation ratio over water, $Q_v/Q_{vsw}$		
$Stk$	Stokes number for mass-weighted mean size of cloud water and precipitable hydrometeor, $x$ (Eq. (11-26)). $\bar{D}c^2\bar{U}x\rho_w/(9\eta\bar{D}x)$		
$T$	temperature		K
$T_0$	temperature at the freezing point	273.16	K
$T_c$	temperature in Celsius $T - T_0$		$^{\circ}\text{C}$
$T_s$	supercooled temperature ( $T_0 - T$ )		$^{\circ}\text{C}$
$U_{dc}$	terminal velocity of cloud water of radius $Dc$		$\text{ms}^{-1}$
$U_{dg}$	terminal velocity of graupel of radius $Dg$		$\text{ms}^{-1}$
$U_{di}$	terminal velocity of cloud ice of radius $Di$		$\text{ms}^{-1}$
$U_{dr}$	terminal velocity of rain of radius $Dr$		$\text{ms}^{-1}$
$\bar{U}_{ng}$	number weighted mean terminal velocity for graupel		$\text{ms}^{-1}$
$\bar{U}_{nr}$	number weighted mean terminal velocity for rain		$\text{ms}^{-1}$
$\bar{U}_{ns}$	number weighted mean terminal velocity for snow		$\text{ms}^{-1}$
$\bar{U}_c$	mean terminal velocity of cloud water		$\text{ms}^{-1}$
$\bar{U}_g$	mass-weighted mean terminal velocity of rain		$\text{ms}^{-1}$
$\bar{U}_s$	mass-weighted mean terminal velocity of snow		$\text{ms}^{-1}$
$X$	dispersion of the fall velocity spectrum of cloud ice: (11-62)	0.25	
$\alpha_{rs}$	the ratio at which collision between rain and snow generates not graupel but snow		$\text{ms}^{-1}$
$\alpha_{scng}$	tuning parameter associated with the dispatcher function which determines the portion of the ac-	4	

	creted cloud water by snow to be consumed for graupel generation: (11-43)		
$\beta_2$	parameter in Fletcher's equation (M-28)	0.6	$\text{K}^{-1}$
$\kappa_a$	thermal conductivity of air	$2.4 \times 10^{-2}$	$\text{Jm}^{-1}\text{s}^{-1}\text{K}^{-1}$
$\pi$	non-dimensional pressure		
$\lambda_g$	slope parameter in graupel size distribution		$\text{m}^{-1}$
$\lambda_r$	slope parameter in rain size distribution		$\text{m}^{-1}$
$\lambda_s$	slope parameter in snow size distribution		$\text{m}^{-1}$
$\psi$	diffusivity of water vapor		
$\nu$	dynamic viscosity of air		
$\eta$	viscosity of air $\eta = \rho\nu$ .		
$\rho$	air density of the basic state		$\text{kgm}^{-3}$
$\rho_0$	air density of the basic state at $z = 0$ m		$\text{kgm}^{-3}$
$\rho_g$	density of graupel	$2.0 \times 10^2$	$\text{kgm}^{-3}$
$\rho_i$	density of cloud ice	$5.0 \times 10^2$	$\text{kgm}^{-3}$
$\rho_s$	density of snow	$8.4 \times 10^1$	$\text{kgm}^{-3}$
$\rho_w$	density of water	$1.0 \times 10^3$	$\text{kgm}^{-3}$
$\Delta t$	time step of leap-frog time integration	4.0	$\text{s}^{-1}$

#### Appendix B-11-2. Figures of production terms for elementary cloud micro-physical processes

Production terms (Pqqqq) are plotted under several conditions in Fig. B-11-4 ~ B-11-10. The parameters are the same as in Table B-11-1 except for  $r_0 = 50\mu\text{m}$ . For a given  $Q_i$ ,  $Q_s$  and  $Q_g$ ,  $N_i$ ,  $N_s$  and  $N_g$  are computed from Eq. (M-28) and Eq. (11-11) using the prescribed  $N_{s0}$  and  $N_{g0}$  (see Table B-11-1), respectively. The ordinate denotes  $\log_{10}(\text{Pqqqq})$ , where the unit of Pqqqq is  $\text{s}^{-1}$ . Sensitivity of Pscng and Pg.sacw (see Eqs. (11-54), (11-46)) to the parameter  $\alpha 2\Delta t$  used in Eq. (11-43) is shown in Figs. B-11-6 and B-11-8. In the following, the parameter  $\alpha 2\Delta t$  used in Eq. (11-43) is set to 40, unless specifically mentioned.

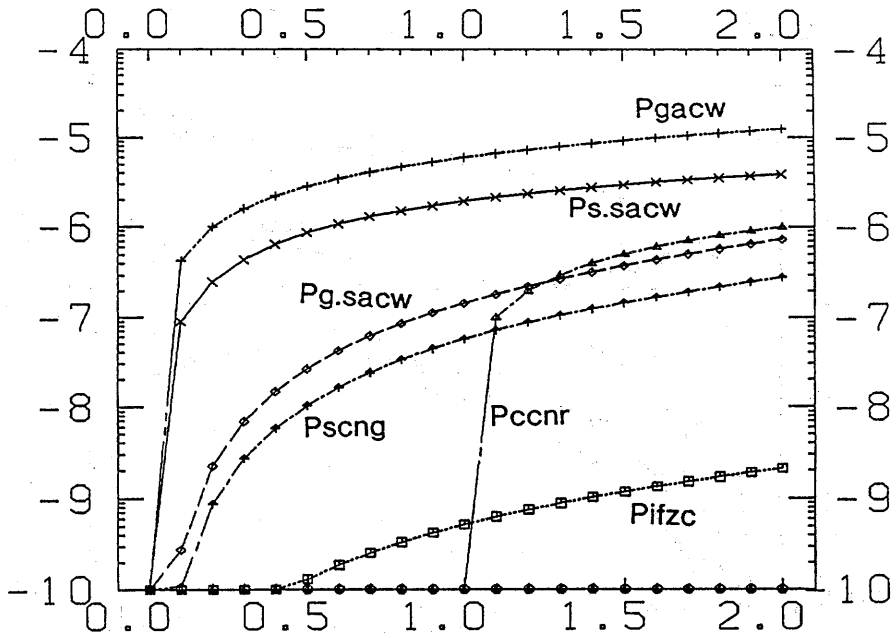


Fig. B-11-4 Cloud microphysical processes involving cloud water as a function of  $Q_c$  varying from 0 to 2 g/kg, under the condition of  $T_c = -20^\circ\text{C}$ ,  $P = 700$  hPa,  $Q_v = Q_{vs w}$ ,  $Q_r = 0$ ,  $Q_i = 0$ ,  $Q_s = 0.5 \times 10^{-3}$  kg/kg and  $Q_g = 0.5 \times 10^{-3}$  kg/kg.

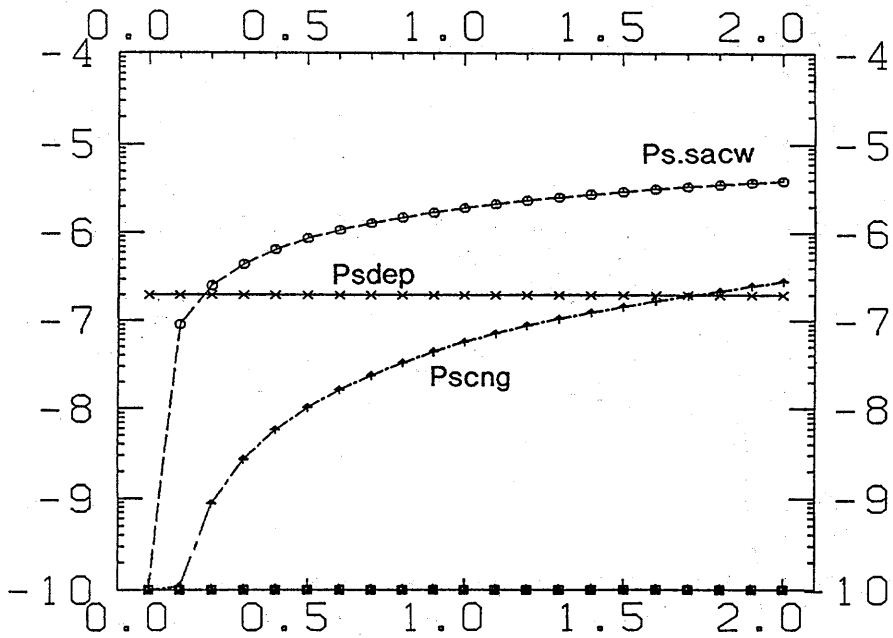


Fig. B-11-5 Cloud microphysical processes involving snow as a function of  $Q_c$  varying from 0 to 2 g/kg, under the condition of  $T_c = -20^\circ\text{C}$ ,  $P = 700$  hPa,  $Q_v = Q_{vs w}$ ,  $Q_r = 0$ ,  $Q_i = 0$ ,  $Q_s = 0.5 \times 10^{-3}$  kg/kg and  $Q_g = 0.5 \times 10^{-3}$  kg/kg.

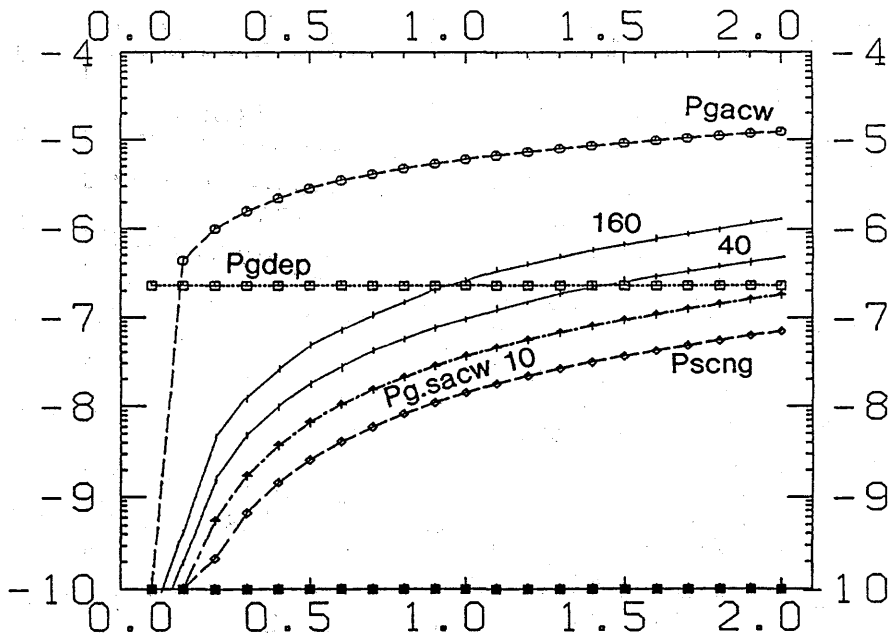


Fig. B-11-6 Cloud microphysical processes involving graupel as a function of  $Q_c$  varying from 0 to 2 g/kg, under the condition of  $T_c = -20^\circ\text{C}$ ,  $P = 700$  hPa,  $Q_v = Q_{vsw}$ ,  $Q_r = 0$ ,  $Q_i = 10^{-11} Ni/\rho$  ( $Ni = 10^3 \text{ m}^{-3}$ ),  $Q_s = 0.5 \times 10^{-3} \text{ kg/kg}$ ,  $Q_g = 0.5 \times 10^{-3} \text{ kg/kg}$  and  $\alpha 2\Delta t = 10$  (see Eq. (11-43)).  $P_{g.sacw}$ 's for  $\alpha 2\Delta t = 40$  and 160 are added for comparison.

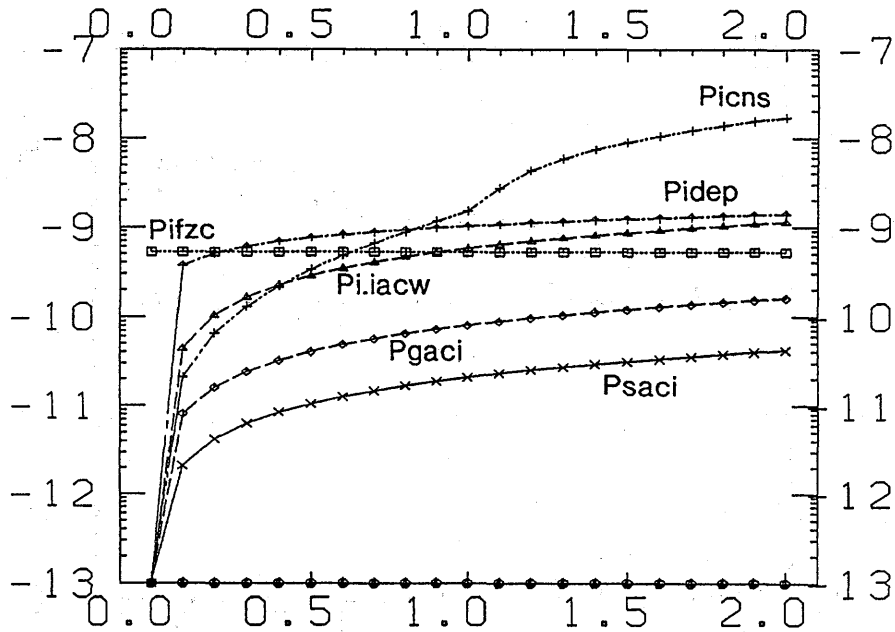


Fig. B-11-7 Cloud microphysical processes involving cloud ice as a function of  $\rho Q_i$  varying from 0 to  $Ni \times m_{s0}$ , under the condition of  $T_c = -20^\circ\text{C}$ ,  $P = 700$  hPa,  $Q_v = Q_{vsw}$ ,  $Q_c = 1.0 \times 10^{-3} \text{ kg/kg}$ ,  $Q_r = 0$ ,  $Q_s = 0.5 \times 10^{-3} \text{ kg/kg}$  and  $Q_g = 0.5 \times 10^{-3} \text{ kg/kg}$ . The abscissa denotes  $\rho Q_i = Ni \times m_{s0} \times (j/20)$ , where  $j$  varies from 0 to 20,  $m_{s0} = 0.44 \times 10^{-10} \text{ kg}$  and  $Ni = 10^3 \text{ m}^{-3}$ .

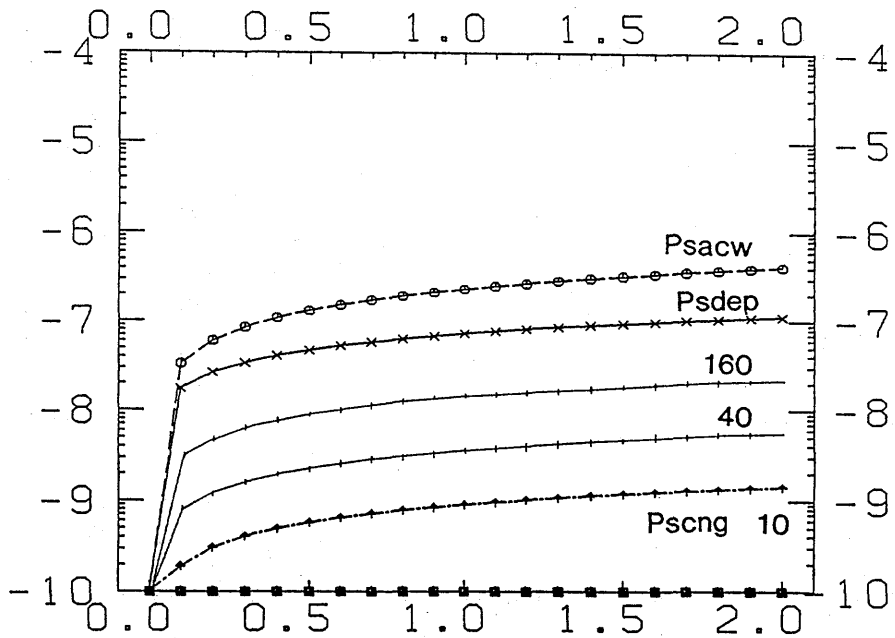


Fig. B-11-8 Cloud microphysical processes involving snow as a function of  $Q_s$  varying from 0 to 2 g/kg, under the condition of  $T_c = -20^\circ\text{C}$ ,  $P = 700$  hPa,  $Q_v = Q_{vs,w}$ ,  $Q_c = 0.5 \times 10^{-3}$  kg/kg,  $Q_r = 0$ ,  $Q_i = 0$ ,  $Q_g = 0.5 \times 10^{-3}$  kg/kg and  $\alpha 2\Delta t = 10$  (see Eq. (11-43)). Pscng's for  $\alpha 2\Delta t = 40$  and 160 are added for comparison.

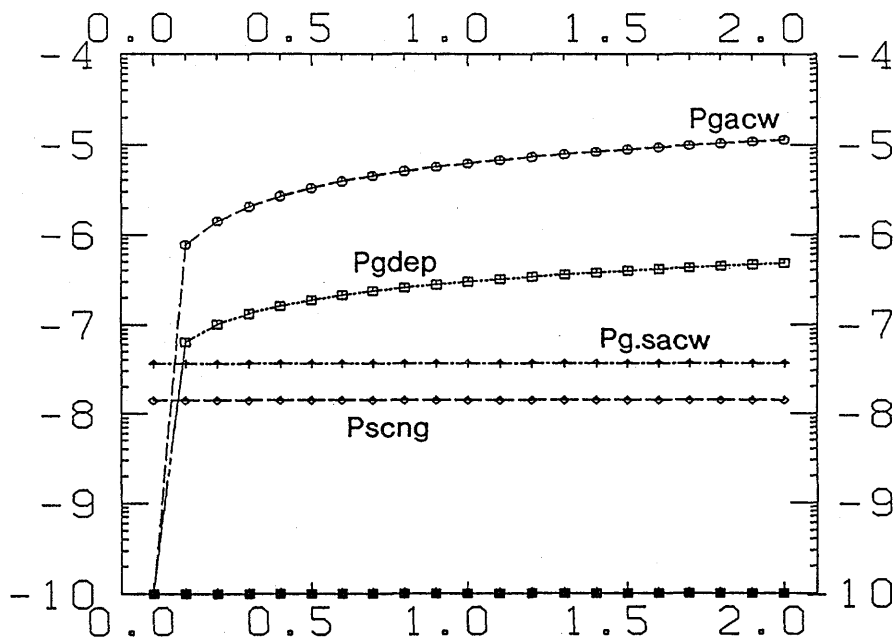


Fig. B-11-9 Cloud microphysical processes involving graupel as a function of  $Q_s$  varying from 0 to 2 g/kg, under the condition of  $T_c = -10^\circ\text{C}$ ,  $P = 850$  hPa,  $Q_v = Q_{vs,w}$ ,  $Q_c = 0.5 \times 10^{-3}$  kg/kg,  $Q_r = 0$ ,  $Q_i = 0$  and  $Q_g = 0.5 \times 10^{-3}$  kg/kg.

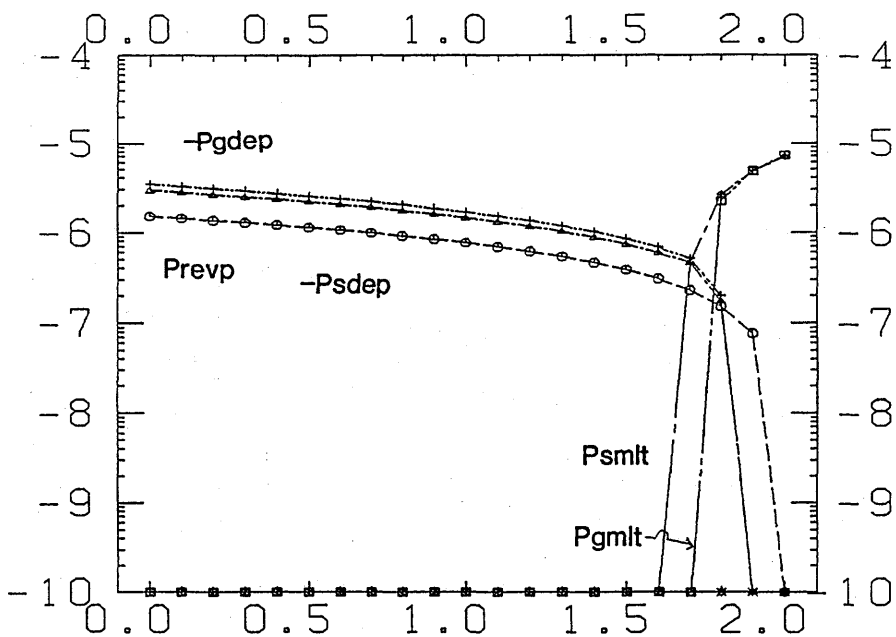


Fig. B-11-10 Cloud microphysical processes relevant to forming a cold dome as a function of relative humidity varying from 0 to 100%, under the condition of  $T_c = 1^\circ\text{C}$ ,  $P = 970$  hPa,  $Q_c = 0$ ,  $Q_r = 0.5 \times 10^{-3}$  kg/kg,  $Q_i = 0$ ,  $Q_s = 0.5 \times 10^{-3}$  kg/kg and  $Q_g = 0.5 \times 10^{-3}$  kg/kg.

## B-12. Computational diffusion

Artificial computational diffusion terms are added to the diffusional term by subgrid scale turbulence (Eqs. (10-16) and (10-17)) in order to suppress computational noises and to overcome some problems near the upper and lateral boundaries. In leap-frog time integration from the time step 'it - 1' to 'it + 1', these terms are evaluated using the values at the time step 'it - 1' instead of 'it' in order to maintain numerical stability.

- i) Nonlinear damping  $Dn$  (Nakamura, 1978)

$$Dn(f) = \frac{DX^3}{8m_n\Delta t|\Delta f|} \frac{\partial}{\partial x} \left( \left| \frac{\partial f}{\partial x} \right| \frac{\partial f}{\partial x} \right) + \frac{DZ^3}{8m_n\Delta t|\Delta f|} \frac{\partial}{\partial z} \left( \left| \frac{\partial(f - f.\text{ext})}{\partial z} \right| \frac{\partial(f - f.\text{ext})}{\partial z} \right), \quad (12-1)$$

where  $f.\text{ext}$  denotes the horizontally averaged value of initial  $f$ .

- ii) Fourth-order linear damping for suppressing mainly 2-grid noises is given as

$$D_{4\ell}(f) = \frac{-DX^4EKH(k)FKMXF(k)}{16m_{4\ell}\Delta t} \frac{\partial^4 f}{\partial x^4}. \quad (12-2)$$

- iii) Rayleigh damping near the upper boundary to prevent the false reflection of internal gravity waves from the upper rigid wall.

$$D_{ru}(f) = -\frac{1}{2m_{ru}\Delta t} \left( 1 + \cos \left( \frac{\pi(LZ - z)}{LZ - z_d} \right) \right) (f - f.\text{ext}) \quad (12-3)$$

for  $z > z_d$ .

Here,  $LZ$  is the height of the model domain.

- iv) Rayleigh damping near the lateral boundary is imposed in order to prevent the false reflection of internal gravity waves from the lateral boundary, enforce the environmental external conditions and suppress noises.

$$D_{r\ell}(f) = -\frac{1}{2m_{r\ell}\Delta t} \left( 1 + \cos \left( \frac{\pi(LX - x)}{x_d} \right) \right) (f - f.\text{ext}) \quad (12-4)$$

for  $x > LX - x_d$ .

$$D_{r\ell}(f) = -\frac{1}{2m_{r\ell}\Delta t} \left( 1 + \cos \left( \frac{\pi x}{x_d} \right) \right) (f - f.\text{ext})$$

for  $x < x_d$ .

Here,  $LX$  is the width of the model domain.

v) Damping in the time integration schemes

v-1) Asselin's time filter

$$f(it) = f^*(it) + 0.5\nu(f^*(it + 1) - 2f^*(it) + f(it - 1)) \quad (12-5)$$

v-2)  $\alpha$  parameter used in E-HI-VI scheme (Eq. (3-4))

v-3)  $\beta$  and  $\gamma$  parameters used in E-HE-VI scheme (Eqs. (4-4) and (4-5))

## B-13. Initial set-up procedures

### B-13-1. Preparation of eigen-vectors and eigen-values

After variable grids are generated (see D-4), matrix  $A$ ,  $Y_A$ ,  $B$  and  $Y_B$  which are used in the finite discretization expression of the pressure equation (see section B-6) are generated, and the generalized eigenvalue problems

$$AP = Y_A P \Lambda(A) \quad \text{and} \quad BQ = Y_B Q \Lambda(B) \quad (\text{see Eq. (6-17)})$$

are solved by Jacobi method. Eigen-vectors,  $P$  and  $Q$ , are arranged in the decreasing order of their eigen-values. They are stored in magnetic tape.

P.G.

```
sub.CVEVSI ----- INIVG1 ----- GMAT ----- VRGDIS
                    ----- JACOBI
                    ----- arrange eigen-vectors
                    ----- normalize eigen-vectors
                    ----- store eigen-vectors and values in magnetic tape.
```

### B-13-2. Initial environmental fields

Currently, vertical profiles of  $u$ ,  $v$ ,  $\theta$  and  $Qv$  without any horizontal variation can be specified in the input parameter list (arrays.KZIN and VALIN). The specified values for  $u$  and  $v$  are not for  $\bar{\rho}G^{1/2}u$  but for  $u$ ; those for  $\theta$  are biased ( $\theta_{\text{init}} = \theta_{\text{input}} + \theta_{\text{bias}}$ ); those for  $Qv$  are specified in relative humidity.

Inputted  $u$  is converted to  $\bar{\rho}G^{1/2}u$  and is stored in array U and is predicted.  $\theta = \theta_{\text{init}} - \theta_{\text{bias}}$  is stored in array PT and is predicted. From inputted relative humidity, the mixing ratio of water vapour is calculated and stored in array QV and is predicted.

P.G.

See D-6 and sub.INIFLD, INIVAL, GENPTD, QVSATU.

### B-13-3. Reference atmosphere

From the given initial vertical profile  $\theta_{\text{init}}(z)$ ,  $\theta_{\text{ref}}(z)$  is determined in the following

form:

$$\left. \begin{aligned} \Theta_{\text{ref}}(z) &= az + \Theta_{\text{ref}}(z_0) && \text{for } z_0 < z < z_1, \\ \Theta_{\text{ref}}(z) &= c(z - z_2)^2 + b(z - z_2) + \Theta_{\text{ref}}(z_2) && \text{for } z_1 < z < z_2, \\ \Theta_{\text{ref}}(z) &= b(z - z_2) + \Theta_{\text{ref}}(z_2) && \text{for } z_2 < z < z_t, \end{aligned} \right\} \quad (13-1)$$

where

$$\left. \begin{aligned} a &= -\frac{\Theta_{\text{ref}}(z_1) - \Theta_{\text{ref}}(z_0)}{z_1 - z_0}, \\ b &= \frac{\Theta_{\text{ref}}(z_t) - \Theta_{\text{ref}}(z_2)}{z_t - z_2}, \\ c &= \frac{\Theta_{\text{ref}}(z_1) - \Theta_{\text{ref}}(z_2) - b(z_1 - z_2)}{(z_1 - z_2)^2}. \end{aligned} \right\} \quad (13-2)$$

Here,  $z_0$  is 0m and  $z_t$  is the height of the model domain.

$\Theta_{\text{ref}}$  is required to be as close as possible to  $\Theta_{\text{init}}$ , and as smooth as possible.

Once  $\Theta_{\text{ref}}$  is determined, nondimensional pressure of the reference atmosphere,  $\Pi_{\text{ref}}$ , is determined from hydrostatic balance as follows:

$$\frac{\partial \Pi_{\text{ref}}}{\partial z} = -\frac{g}{C_p} \Theta_{\text{ref}}(z), \quad (13-3)$$

with the lower boundary condition of  $\Pi_{\text{ref},k=1} = 1$ .  $P_{\text{ref}}$  and  $T_{\text{ref}}$  are obtained from  $\Pi_{\text{ref}}$  and  $\Theta_{\text{ref}}$ ;  $\bar{p} = \rho_{\text{ref}}$  is obtained from the state equation of gas.

P.G.

See sub.ORGINO; sub.CREFST;  $\Theta_{\text{ref}}(x, \xi)$  is set in array VPTREF.

#### B-13-4. Reduction methods of initial shocks in the presence of mountains

a) Mountain growing method

Mountain shape function is expressed as

$$Z_s(x, y) = h(t)Z_{s0}(x, y), \quad (13-4)$$

where the maximum value of  $Z_{s0}$  is one.  $h(t)$  is linearly raised up to  $Z_{\text{top}}$  for the first 600 time steps at every 6 time steps. In accordance with the time change of  $Z_s$ , metric tensors

such as  $G^{1/2}$ ,  $G^{13}$  and  $G^{23}$  and  $\bar{\rho}G^{1/2}$  are changed. In accordance with the time change of  $\bar{\rho}G^{1/2}$ , time derivatives of  $U = \bar{\rho}G^{1/2}u$  and  $V = \bar{\rho}G^{1/2}v$  and  $W = \bar{\rho}G^{1/2}w$  are changed as follows:

$$\begin{aligned}\frac{\partial(\bar{\rho}G^{1/2}u)}{\partial t} &= \frac{\partial(\bar{\rho}G^{1/2})}{\partial t}u + \bar{\rho}G^{1/2}\frac{\partial u}{\partial t} \\ &= \frac{\partial(\bar{\rho}G^{1/2})}{\partial t}u + (-ADVU - PFX)\end{aligned}\quad (13-5a)$$

Eq. (1-34) is changed into

$$\begin{aligned}\bar{\rho}G^{1/2}\frac{d\xi}{dt} = W^* &= \bar{\rho}G^{1/2}\left[\frac{1}{G^{1/2}}w + \frac{H}{H-\xi}\left(\frac{\xi}{H} - 1\right)\left(\frac{\partial Z_s}{\partial x}\frac{dx}{dt} + \frac{\partial Z_s}{\partial t}\right)\right] \\ &= \bar{\rho}G^{1/2}\left[\frac{1}{G^{1/2}}w + G^{13}u + \frac{1}{G^{1/2}}(H-\xi)\frac{\partial G^{1/2}}{\partial t}\right].\end{aligned}\quad (13-5b)$$

At the upper and lower boundaries,  $W^*$  is zero. The upper and lower boundary conditions for the pressure equations such as Eqs. (2-8), (3-58) and (4-10) are changed in accord to the change of Eq. (1-34) into Eq. (13-5b).

#### P.G.

See D-6 and sub.ADJUVW and ORGIN0 in mem.SFXTPG1.  $Z_{top}$  is specified in the input parameter list VALIN(35,4).

#### b) Wind growing method

$U$  is linearly increased from 0 to  $U_{init}$  (initial environmental field of  $U$ ) by Rayleigh friction for the first 600 time steps.  $U_{ext}$  is changed at every 6 time steps for the first 420 time step as follows:

$$U_{ext} = \frac{it}{420}U_{init}\quad (13-6)$$

Rayleigh friction is imposed at every time step over the entire domain for the first 600 time steps as

$$\frac{\partial(\bar{\rho}G^{1/2}u)}{\partial t} = -\left(ADVU - \frac{U_{ext} - U^{it-1}}{2\Delta t}\right) - PFX\quad (13-7)$$

#### P.G.

See sub.WDGRW2 in mem.SFXTPG1.

### B-13-5. Initialization of pressure in elastic models

To prevent the excitation of sound waves from the initial fields,

$$\text{DIVT}(U^{it}, V^{it}, W^{it}) = 0, \quad it = 0$$

is necessary. But this alone is not sufficient to ensure the non-divergence of the wind field at the next time step,  $\text{DIVT}(U^{it+1}, V^{it+1}, W^{it+1}) = 0$ . The condition that pressure satisfy the pressure equation of AE is necessary. This ensures  $\text{DIVT}(U^{it+1}, W^{it+1}) = 0$  as discussed by Ikawa (1988). In E-HI-VI and E-HE-VI, the pressure obtained from the pressure equation of AE is given as the initial pressure.

### **C. Examples of numerical simulation by the model**

So far, the model has been successfully applied to simulations of convective clouds (Ikawa *et al.*, 1987; Ikawa, 1988), mountain waves (Ikawa and Nagasawa, 1989; Ikawa, 1990; Saito and Ikawa, 1991) and orographic convective rainfall (Ikawa, 1985). However, they are mostly 2-dimensional. The verification of the model was made by comparing model results with 2-dimensional nonlinear analytic solutions of hydrostatic mountain waves by Lilly and Klemp (1979) (see Ikawa, 1988; Saito and Ikawa, 1991). In this chapter, the model will be checked against 3-dimensional linear analytic solutions of nonhydrostatic mountain waves. 3-dimensional simulations of local winds and convective snow clouds will be shown, with more refined and sophisticated parameterizations of physical processes than the older ones.

## C-1. Verification of the model against 3-dimensional linear analytic solutions of nonhydrostatic mountain waves

In this section, the model-simulated mountain flow over a 3-dimensional mountain is verified by comparing it with the linear analytic solutions by Smith (1980).

### C-1-1. Linear analytic solutions of 3-D nonhydrostatic mountain waves

For the steady flow of a vertically unbounded stratified Boussinesq fluid over a 3-dimensional small-amplitude topography, the following equation for vertical displacement of stream line  $\delta(x, y, z)$  is obtained:

$$\frac{\partial^2}{\partial x^2} (\nabla^2 \delta) + \frac{N^2}{U^2} \nabla_H^2 \delta = 0, \quad (1-1)$$

where  $\nabla_H^2 = \partial^2/\partial x^2 + \partial^2/\partial y^2$ ,  $\nabla^2 = \nabla_H^2 + \partial^2/\partial z^2$ ,  $N$  is the Brunt-Väisälä frequency, and  $U$  is the environmental wind speed.

With constant  $N^2$  and  $U^2$ , the solution of Eq. (1-1) is easily obtained by using double Fourier transform analysis:

$$\delta(x, y, z) = \int \int_{-\infty}^{\infty} Z_s^{\sim}(k, l) e^{imz} e^{i(kx+ly)} dkdl, \quad (1-2)$$

where  $Z_s^{\sim}(k, l)$  is the double Fourier transform of the mountain shape  $Z_s(x, y)$  defined as

$$Z_s^{\sim}(k, l) = \frac{1}{4\pi^2} \int \int_{-\infty}^{\infty} Z_s(x, y) e^{-i(kx+ly)} dx dy, \quad (1-3)$$

$m$  in Eq. (1-2) is calculated by the horizontal wave number vector  $(k, l)$  as follows:

$$m^2 = \frac{k^2 + l^2}{k^2} \left( \frac{N^2}{U^2} - k^2 \right). \quad (1-4)$$

For  $k^2 > N^2/U^2$ , the positive imaginary root of Eq. (1-4) is chosen, and for  $k^2 < N^2/U^2$ , the sign of  $m$  is chosen to be the same as that of  $k$  in order to satisfy the upper radiation condition.

For the case of hydrostatic approximation, Eq. (1-4) is further simplified as follows:

$$m = \frac{N}{U} \frac{(k^2 + l^2)^{1/2}}{k}. \quad (1-5)$$

Once  $\delta$  is obtained, the vertical velocity component  $w$  is easily obtained using the kinematic condition for steady flow

$$w = U \frac{\partial \delta}{\partial x}. \quad (1-6)$$

The bell-shaped mountain with circular contours

$$Z_s(x, y) = \frac{h_m}{(r^2/a^2 + 1)^{3/2}}; \quad r = (x^2 + y^2)^{1/2} \quad (1-7)$$

is used for an example of mountain shape, where “ $h_m$ ” is the height of the mountaintop and “ $a$ ” is the horizontal scale of the mountain.  $h_m$  is set to 100m, and typical atmospheric values of  $U = 8\text{m/s}$  and  $N = 0.01\text{s}^{-1}$  are chosen.

The analytic solution is calculated by using discrete complex Fourier transform. The mountain shape  $Z_s(x, y)$  is discretized on the grid mesh with an interval  $\Delta x = \Delta y = a/3$ . The mesh size  $Nx = Ny = 128$  is used.

### C-1-2. Description of the numerical model

Numerical simulation is also performed and the experimental result is compared. In the simulation, the horizontal grid interval of  $\Delta x = \Delta y = a/3$  is used, while the variable grid interval  $\Delta z = 40\text{m} \sim 1200\text{m}$  is used for the vertical grid interval. The grid number of  $(Nx, Ny, Nz) = (60, 40, 32)$  is used for Cases a) and b), while  $(Nx, Ny, Nz) = (60, 21, 32)$  is used for Case c). The time interval  $\Delta t = 30\text{sec}$  is used. The anelastic scheme with Boussinesq approximation is employed, and an absorbing layer is imposed at the highest 10 layers to prevent a false reflection of mountain wave from the upper boundary. Open lateral boundary condition is employed except for Case c). For the smooth start-up, the mountain height is initially set to zero, and it is raised linearly to the ordinary height (100m) during the first 60 time steps, equivalent to the model time of  $t = 30\text{min}$ .

### C-1-3. Comparison between numerical and analytic solutions

#### a) Case with wide horizontal scale mountain shape

Firstly, we show the comparative results for the case of wide horizontal scale mountain shape. In Eq. (1-7), the horizontal scale “ $a$ ” is set to 6km. In this case, the product of the Scorer number  $N/U$  and “ $a$ ” is 7.5, which means that the horizontal scale of the mountain is much larger than the distance of down-wind drift during a buoyancy oscillation. The nonhydrostatic effect is expected to be small. The horizontal grid interval of  $\Delta x = \Delta y = 2\text{km}$  is used for the calculation of the analytic solution and the numerical simulation.

Figures C-1-1 a) ~ d) show the vertical velocity  $w$  at various levels obtained by the nonhydrostatic analytic solution. In these figures, the altitudes are  $z = 2.44\text{km}$ ,  $1.30\text{km}$ ,  $0.74\text{km}$  and  $0.34\text{km}$  in order, and correspond to  $zN/U \simeq \pi$ ,  $\pi/2$ ,  $\pi/4$  and  $\pi/8$ . The mountaintop is located at  $x = y = 127\text{km}$ , and the area from  $x = 96\text{km}$  to  $x = 190\text{km}$  and  $y = 96\text{km}$  to  $y = 158\text{km}$  is shown. Near the ground, the pattern of the updraft in the windward side and the pattern of the downdraft in the lee side are roughly symmetric as shown in Fig. C-1-1 d). However, the updraft in the windward side diminishes with the height, and it almost disappears in Fig. C-1-1 b) ( $z = 1.3\text{km}$ ). On the other hand, another U-shaped updraft region develops in the lee, and the patterns of the vertical velocity become asymmetric further aloft.

Figures C-1-1 e) ~ h) show the vertical velocity  $w$  at various levels obtained by the numerical simulation after  $240\Delta t$  ( $t = 120\text{min}$ ). In these figures, the altitudes are about  $2.44\text{km}$ ,  $1.30\text{km}$ ,  $0.74\text{km}$  and  $0.34\text{km}$  above the ground surface in order, and correspond to the 12th, 9th, 7th and 4th level of the model. In this case, the dimensions of the model domain are  $(Lx, Ly) = (118\text{km}, 78\text{km})$ , and the mountaintop is located at  $x = y = 39\text{km}$ . The area from  $x = 8\text{km}$  to  $x = 102\text{km}$  and  $y = 8\text{km}$  to  $y = 70\text{km}$  is shown in these figures.

As shown in Figs. C-1-1 g) and h), near the ground the pattern of  $w$  by the model agrees well with those by the analytic solution except for the small numerical noises. Further aloft, although the width of the U-shaped updraft region in the lee in Fig. C-1-1 e) is somewhat smaller than in Fig. C-1-1 a), the characteristics of the pattern of  $w$  by the analytic solution are well reproduced by the simulation.

Figures C-1-3 a), b) show the vertical cross-section of  $w$  through the vicinity of the mountaintop (at  $y = 126\text{km}$ ) obtained by hydrostatic and nonhydrostatic analytic solutions. They quite resemble each other since the hydrostatic approximation is applicable in this case. Fig. C-1-3 c) shows the vertical cross section of  $w$  through the vicinity of the mountaintop

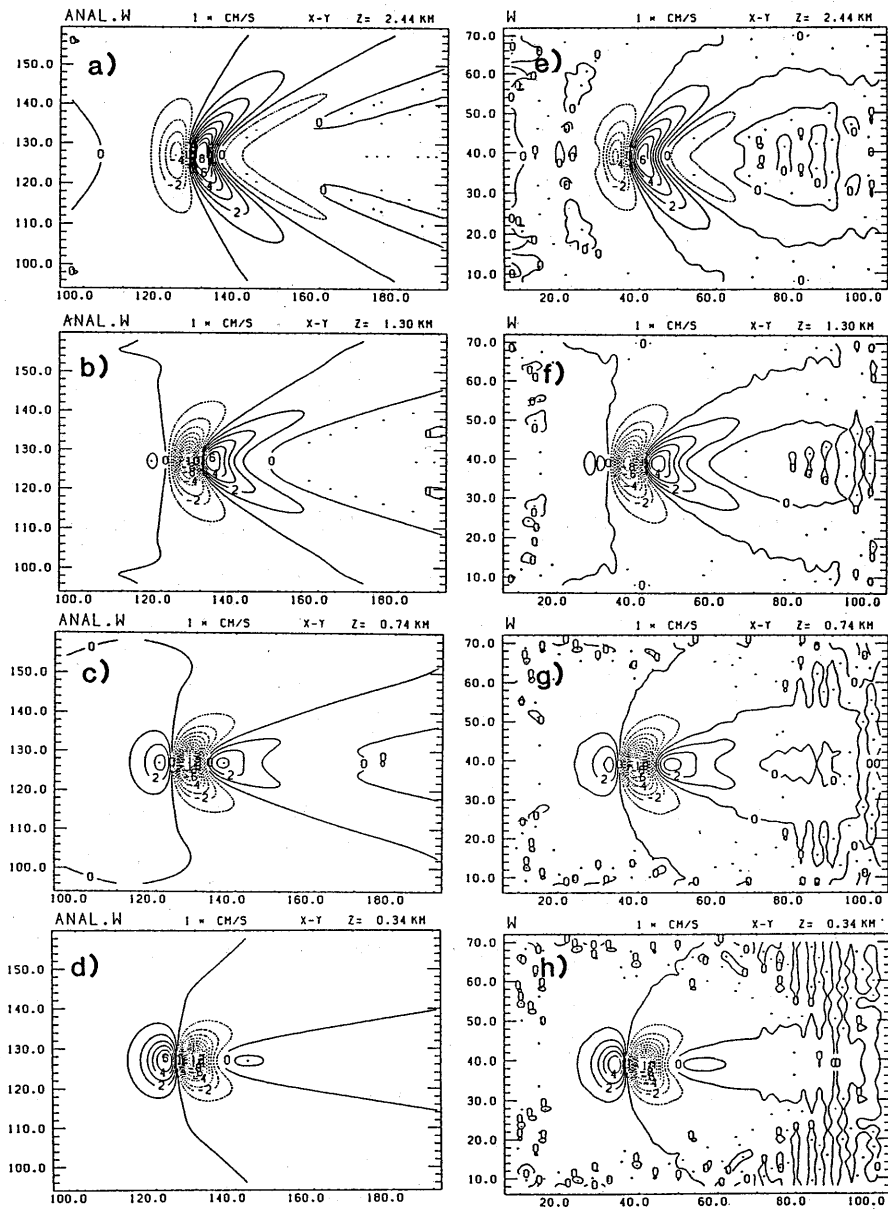


Fig. C-1-1 a) ~ d) Horizontal cross-section of vertical velocity ( $w$ ) at various levels obtained by the non-hydrostatic analytic solution for the case of  $aN/U = 7.5$  ( $U = 8$  m/s,  $N = 0.01$  s $^{-1}$ ,  $a = 6$  km),  $h_m = 100$  m. The altitudes are indicated at the upper right of each figure. The contour interval is 1 cm/s.

e) ~ h) Horizontal cross-section of  $w$  at various levels by the numerical simulation ( $t = 120$  min). The altitudes above the ground surface ( $z^*$ ) are indicated at the upper right of each figure.

(at  $y = 38\text{km}$ ) obtained by numerical simulation. Although the model-simulated mountain wave decreases with the increase of the height mainly by the imposed absorbing layer, the characteristic of the mountain wave which propagates vertically is well reproduced.

b) Case with small horizontal scale mountain shape

Secondly, a comparison is performed for the case of smaller horizontal scale mountain shape. In Eq. (1-7), smaller horizontal scale of  $a = 1.2\text{km}$  is used. The height of the mountaintop  $h_m$ , the atmospheric values  $U$  and  $N$  are the same as those of the former case. In this case, the product of the Scorer number  $N/U$  and " $a$ " is 1.5, and nonhydrostatic effect is expected to become significant. Horizontal grid interval of  $\Delta x = \Delta y = 400\text{m}$  is used for the calculation of the analytic solution and the numerical simulation.

Figures C-1-2 a) ~ d) show the vertical velocity  $w$  at various levels obtained by the nonhydrostatic analytic solution. In these figures, the altitudes are the same as in Figs. C-1-1 a) ~ d). The mountaintop is located at  $x = y = 25.4\text{km}$ , and the area from  $x = 19.2\text{km}$  to  $x = 38.0\text{km}$  and  $y = 19.2\text{km}$  to  $y = 31.6\text{km}$  is shown. The contour interval of these figures is five times larger than that used in Fig. C-1-1 owing to the increasing of the incline of the mountain slope. On comparing these figures with Figs. C-1-1, the trailing lee waves appear in the lee of a U-shaped updraft region. These trailing lee waves with horizontal wavelength of  $2\pi U/N$  ( $\simeq 5\text{km}$ ) are due to the buoyancy oscillation by the nonhydrostatic effect.

Figures C-1-2 e) ~ h) show the vertical velocity  $w$  at various levels obtained by the numerical simulation after  $120\Delta t$  ( $t = 60\text{min}$ ). In these figures, the altitudes are the same as in Figs. C-1-1 e) ~ f). The dimensions of the model domain are  $(Lx, Ly) = (23.6\text{km}, 15.6\text{km})$ , and the mountaintop is located at  $x = y = 7.8\text{km}$ . The area from  $x = 1.6\text{km}$  to  $x = 20.4\text{km}$  and  $y = 1.6\text{km}$  to  $y = 14.0\text{km}$  is shown in these figures, where the model-simulated flows agree quite well with the results of nonhydrostatic analytic solutions shown in Figs. C-1-2 a) ~ d). The lee oscillations due to the nonhydrostatic effect are also well reproduced by the simulation.

Figures C-1-3 d) and e) show the vertical cross-section of  $w$  through the vicinity of the mountaintop (at  $y = 25.2\text{km}$ ) obtained by the hydrostatic and nonhydrostatic analytic solutions. In the case of the hydrostatic solution shown in Fig. C-1-3 d), the pattern of  $w$  is the same as in Fig. C-1-3 a) except for the contour interval. On the other hand, in the case of the nonhydrostatic solution shown in Fig. C-1-3 e), the pattern of  $w$  is quite different from Fig. C-1-3 b). The difference between them is due to the buoyancy oscillation

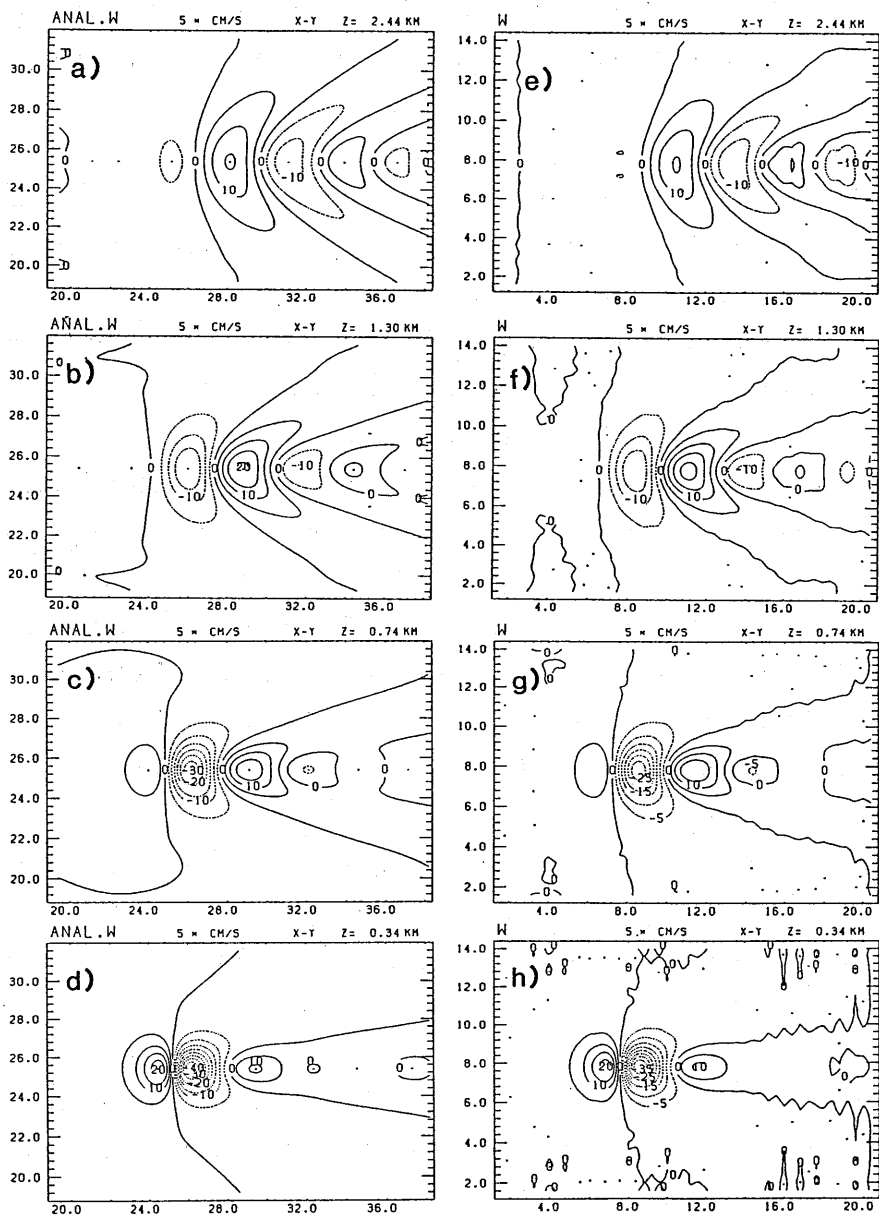


Fig. C-1-2 a) ~ h) As in Figs. C-1-1 a) ~ h) but for  $aN/U = 1.5$  ( $a = 1.2$  km). The contour interval is 5 cm/s.

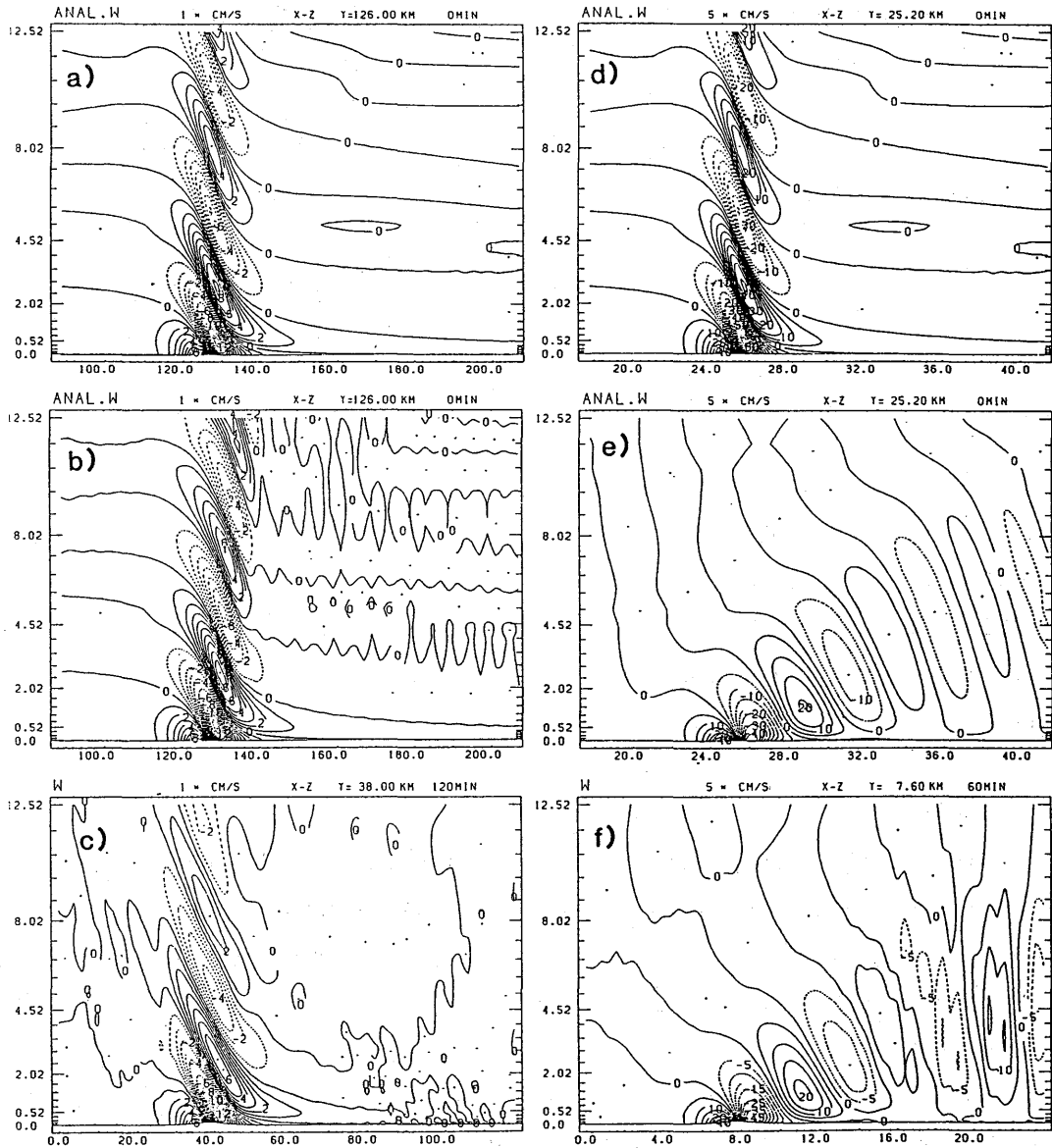


Fig. C-1-3 a) The vertical cross-section of  $w$  in the vicinity of the mountaintop obtained by the hydrostatic analytic solution for the case of  $aN/U = 7.5$  ( $a = 6$  km). The contour interval is 1 cm/s. The graduations on the vertical axis show the altitudes of the levels of the numerical model corresponding to the variable vertical grid interval.  
 b) As in a) but by the nonhydrostatic analytic solution.  
 c) As a) but by the numerical simulation.  
 d) ~ f) As in a) ~ c) but for  $aN/U = 1.5$  ( $a = 1.2$  km). The contour interval is 5 cm/s.

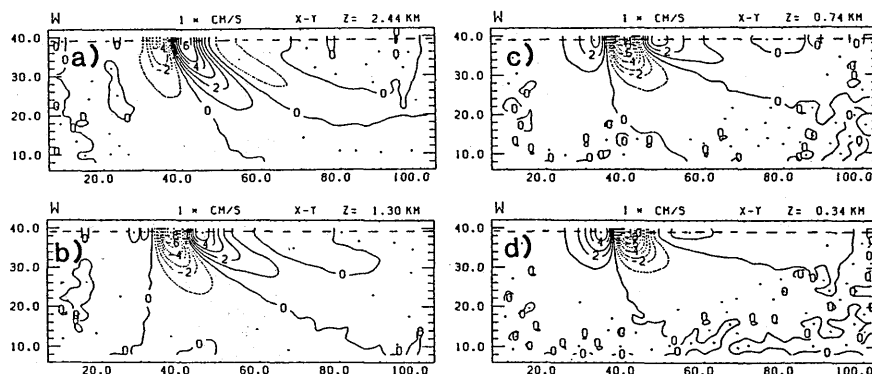


Fig. C-1-4 a) ~ d) As in Figs. C-1-1 e) ~ h) but by the numerical simulation with half domain. Broken line along  $y = 39$  km shows the location of free-slip lateral boundary.

by the nonhydrostatic effect. Fig. C-1-3 f) shows the vertical cross-section of  $w$  through the vicinity of the mountaintop (at  $y = 7.6$ km) obtained by the numerical simulation. The model-simulated flow well agrees with the result of the nonhydrostatic analytic solution shown in Fig. C-1-3 e). The open lateral boundaries located at  $x = 0.2$ km and  $23.2$ km using radiation condition appear to work well.

c) Case with half domain

In the examples of numerical simulation shown in the former sub-sections, a bell-shaped mountain with circular contours was used for the mountain shape. The mountain waves indicated in Figs. C-1-1 and C-1-2 have symmetric patterns with respect to the  $xz$ -plane through the mountaintop. In the case of the simulation of such a symmetric flow, we can save the numerical resources by the use of free-slip rigid wall lateral boundary condition with half domain. In this sub-section, the open lateral boundary condition is used for only  $yz$ -planes at inflow and outflow sides, while the free-slip lateral boundary condition is used for the  $xz$ -planes. A bell-shaped mountain with  $a = 6$ km is given for the mountain shape as in Case a), but the model domain is reduced to half of Case a). The grid number of  $(Nx, Ny, Nz) = (60, 21, 32)$  is used.

Figures C-1-4 a) ~ d) show the vertical velocity  $w$  at various levels obtained by the numerical simulation with half domain ( $t = 120$ min). In these figures, the altitudes of the cross-sectional planes are the same as in Figs. C-1-1 e) ~ h). In this case, the dimensions of the model domain are  $(Lx, Ly) = (118$ km,  $40$ km) and the mountaintop is located at

$x = y = 39\text{km}$ . The rigid wall lateral boundaries are located at the  $xz$ -planes through the mountaintop (along  $y = 39\text{km}$ , shown by broken line) and at  $y = 1\text{km}$ . As shown in these figures, the patterns of  $w$  quite agree with the results of full domain simulation shown in Figs. C-1-1 e)  $\sim$  h).

Generally, the flow obtained by the simulation using half domain with free-slip lateral boundaries agrees with the flow obtained by the simulation using full domain with symmetric orography and periodic lateral boundaries.

## C-2. 3-dimensional simulations of local winds in Japan

In this section, 3-dimensional simulations of local winds in Japan are shown as examples of numerical simulation. Although these are preliminary experiments using simple environmental conditions, these results show us that the model has the potentiality for the future realistic simulation.

### C-2-1. Land-sea breeze in the Kanto district

Originally designed to simulate convective phenomena, our nonhydrostatic model is applicable to such phenomena as the land-sea breeze since the model includes the physical processes. Circulations by the land-sea breeze are generally moderate phenomena and hydrostatic approximation is available in most cases, while simulation of them is a good test of the model's physical processes for the boundary layer. In this sub-section, we will show the results of the 3-dimensional simulation of the land-sea breeze in the Kanto district and

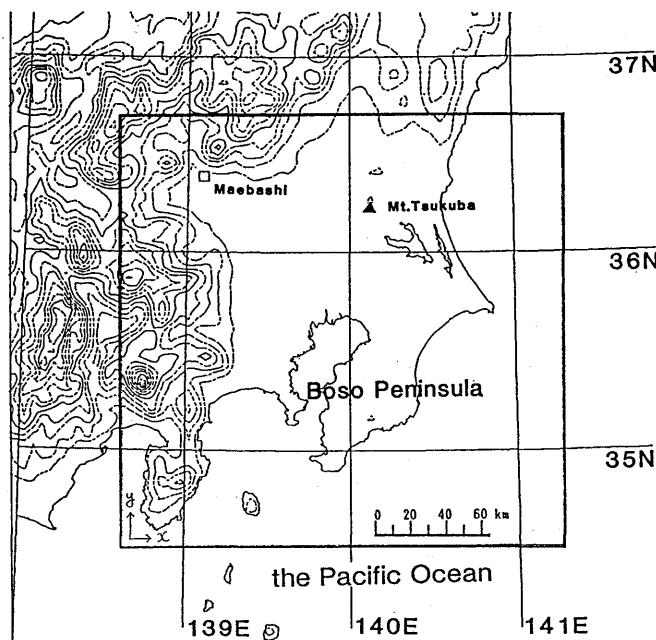


Fig. C-2-1 Geographical map of the Kanto district. The rectangle framed by heavy solid lines shows the area where the simulation is performed. The height contour interval is 200m.

show the performance of the model.

Figure C-2-1 shows a geographical map of the Kanto district. In this figure, the rectangle framed by heavy solid lines shows the area where the simulation is performed. In the simulation, this area is represented by  $(Nx, Ny, Nz) = (50, 50, 22)$  grid points. The horizontal grid interval  $\Delta x = \Delta y = 5\text{km}$  is used, while the variable grid interval  $\Delta z = 40\text{m} \sim 800\text{m}$  is used for the vertical grid interval. The dimensions of the model domain are  $(Lx, Ly, H) = (245\text{km}, 245\text{km}, 8.0\text{km})$ .

In the simulation, anelastic equations are used, while the Boussinesq approximation is not employed. The environmental wind is set to zero, considering that the simulation of a day in which synoptic wind is weak. A constant lapse rate of  $d\theta/dz = 3\text{K/km}$  ( $N = 0.01\text{s}^{-1}$ ) is chosen for the typical atmospheric stability. The sea surface temperature is fixed at  $15^\circ\text{C}$ , while the ground temperature  $Tg$  is given by the following sinusoidal function with an amplitude of  $10^\circ\text{C}$ :

$$Tg = T_{\text{ref}} + 10 \sin\left(\frac{2\pi t}{T}\right), \quad (2-1)$$

where  $T_{\text{ref}}$  is the temperature of the reference atmosphere at the model surface which is calculated using surface height with a constant lapse rate of  $d\theta/dz = 3\text{K/km}$ , and  $T$  is a period of 24hours. The time interval of  $\Delta t = 20\text{sec}$  is used, and the simulation is performed until  $t = 8\text{hours}$  ( $1440\Delta t$ ). The roughness length of the ground surface is assumed to be 10cm. The Coriolis parameter of  $f = 8.57 \times 10^{-5}\text{s}^{-1}$  is used, corresponding to the latitude of the Kanto district ( $36^\circ\text{N}$ ).

Figure C-2-2 a) shows the simulated wind vectors at the lowest level (about 20m above the surface) after  $720\Delta t$  ( $t = 4\text{hrs}$ ). In this time, the ground temperature has risen about  $8.5^\circ\text{C}$  from the initial time. The valley breeze develops in the mountain area. Owing to the difference between the sea surface temperature and the ground temperature, sea breezes occur along the coast line.

Figure C-2-2 b) shows the simulated wind vectors at the lowest level after  $1440\Delta t$  ( $t = 8\text{hrs}$ ). In this time, the sea breeze intrudes into the land area and forms frontal lines in the plain area. In the mountain area, the valley wind further develops, and forms a large-scale circulation.

Figures C-2-3 a) ~ d) show the typical daily change of the surface wind in the Kanto district at every 3hours for a weak synoptic wind case, which was reported by Kawamura (1977). The simulated surface wind shown in Fig. C-2-2 b) well represents the characteristics

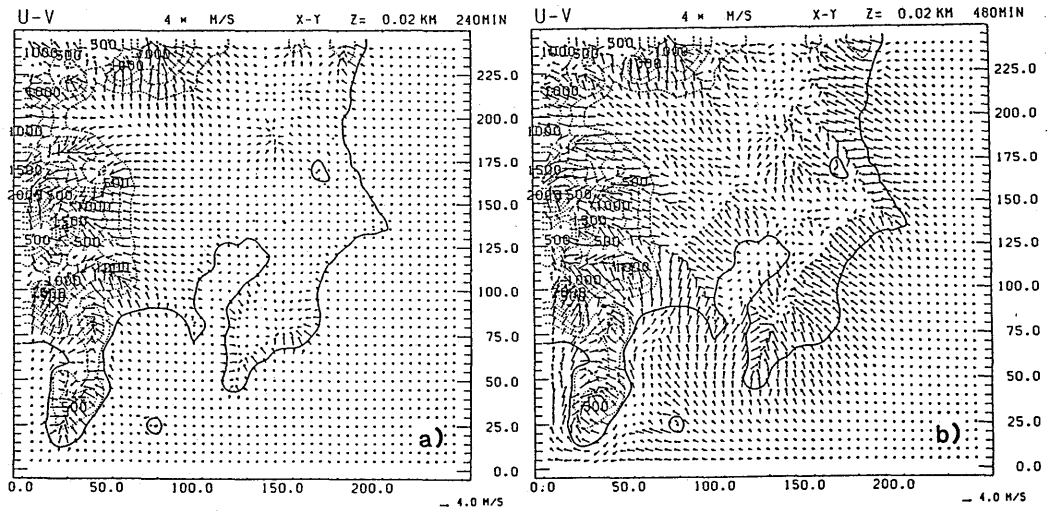


Fig. C-2-2 a) The simulated lowest level (about 20m above the surface) wind vectors at  $t = 4$  hrs. The lower right arrow indicates the scale of 4 m/s. The broken lines mean height contour at every 250m.  
 b) As in a) but for  $t = 8$  hrs.

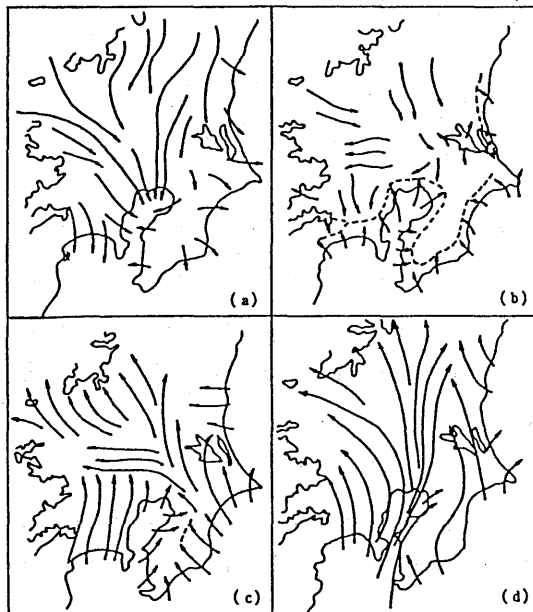


Fig. C-2-3 a) ~ d) The typical daily change of the surface wind in the Kanto District at every 3 hours reported by Kawamura (1977). a) 06LST, b) 09LST, c) 12LST, d) 15LST.

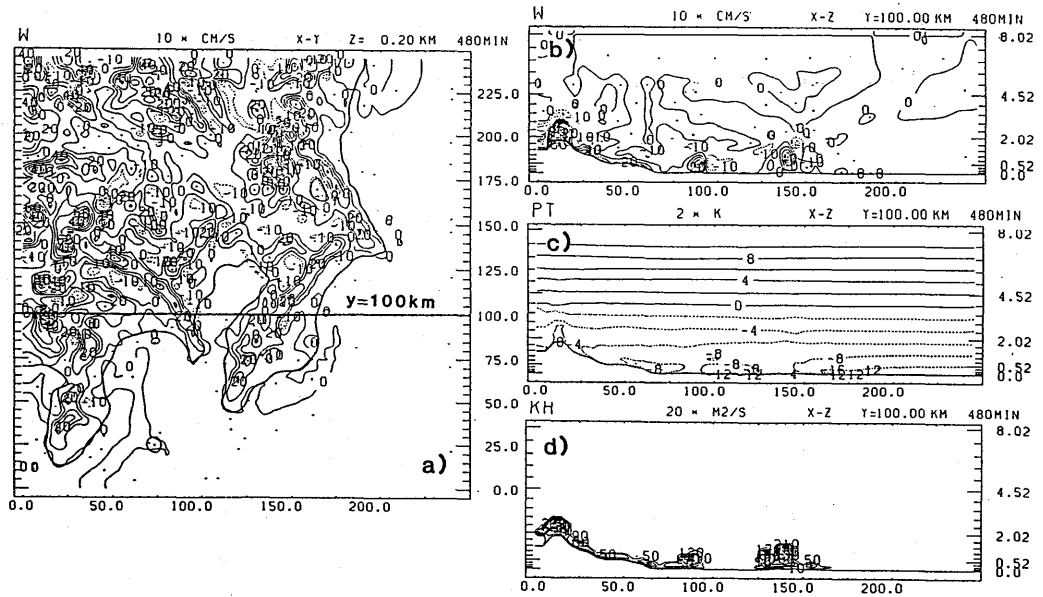


Fig. C-2-4 a) The vertical velocity ( $w$ ) at the 4th level of the model (about 200m above the surface). The contour interval is 10 cm/s. Broken lines show the negative value (downward motion). Heavy line indicates the location of the vertical cross-section shown in Figs. C-2-4 b) ~ d).  
 b) The vertical cross-section of the vertical velocity along  $y = 100$  km (heavy line in Fig. C-2-4 a)). The contour interval is 10 cm/s. The graduations on the vertical axis show the altitudes of the levels of the model corresponding to the variable vertical grid interval.  
 c) As in b) but for the potential temperature. The contour interval is 2K. Deviation from 300K is indicated.  
 d) As in b) but for the diffusion coefficient determined by the turbulent closure model. The contour interval is 20 m<sup>2</sup>/s.

of the typical circulation about 12LST in the Kanto district shown Fig. C-2-3 c).

Figure C-2-4 a) shows the vertical velocity at the 4th level of the model (about 200m above the surface) after 8hrs. The updrafts develop over the mountain area due to the positive buoyancy caused by the difference between the atmospheric temperature over the mountain area and the temperature of the reference atmosphere.

Figures C-2-4 b), c) and d) show the vertical cross-section of the vertical velocity, the potential temperature and the diffusion coefficient determined by the turbulent closure model along  $y = 100$ km (shown by a heavy line in Fig. C-2-4 a)). The top-height of the updrafts is about 1km from the ground surface. On the ground surface, the diffusion coefficient is increased by the production of the turbulent energy due to the positive buoyancy production term.

### C-2-2. Local downslope wind “Yamaji-kaze” in Shikoku Island

The “Yamaji-kaze” is one of the most well-known local winds in Japan. It is a strong downslope wind which occurs over the northern coastal plain of Shikoku Island when the low-level synoptic wind is southerly. Figure C-2-5 shows a geographical map of Shikoku Island, located in western Japan. In its northern central part, the Shikoku Mountains run from east to west. Mt. Ishizuchi (1981m) and Mt. Tsurugi (1955m) are located in the western and eastern part of the Shikoku Mountains, respectively. The central part of the Shikoku Mountains between Mt. Ishizuchi and Mt. Tsurugi is relatively low. The Yamaji-kaze occurs in the narrow northern slope of the Shikoku Mountains facing Hiuchi-nada. The most severe Yamaji-kaze occurs around Doi (○) and Mishima (⊙). Observational studies (Akiyama, 1956; *etc.*) have pointed out the following characteristic features of the Yamaji-kaze.

- a) A northerly wind opposite to the southerly synoptic wind is observed as one of the premonitory symptoms (“Sasoi-kaze”).
- b) In the early stage, the surface wind direction exhibits a sudden variation along a line of discontinuity (“Yamaji-kaze front”).
- c) A northerly wind opposite to the southerly downslope wind prevails over Hiuchi-nada (“Domai”).
- d) Strong winds are seldom observed on the windward side of Shikoku Island such as around

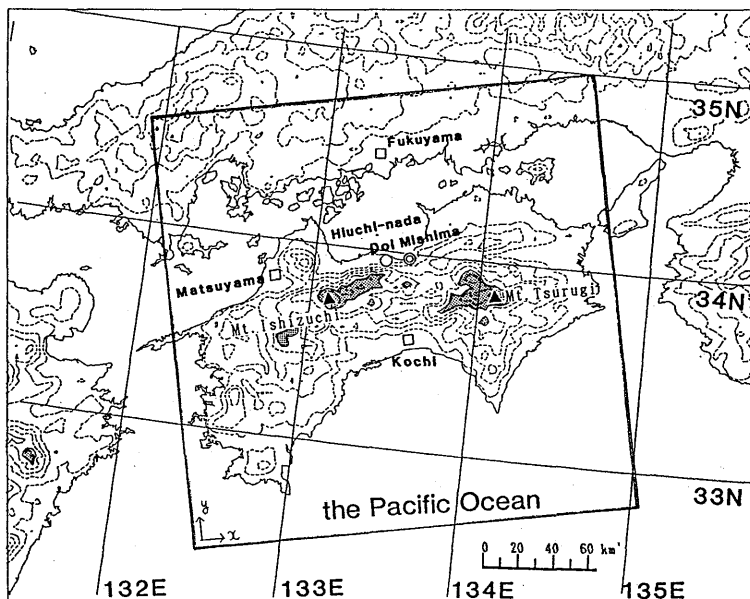


Fig. C-2-5 Geographical map of Shikoku Island, western Japan. The rectangle framed by solid lines shows the area where the simulation is performed. The height contour interval is 200m. The areas above 1000m height are shaded.

Kochi. e) Low surface pressures are observed in the coastal areas facing Hiuchi-nada ("Hiuchi-nada depression").

Saito and Ikawa (1991) made a numerical study of the Yamaji-kaze using a nonhydrostatic model and succeeded in explaining these phenomena in terms of the internal hydraulic jump and the reversed flow just behind it. However, their experiments were performed by 2-dimensional model using an averaged orography and physical processes such as the surface friction were neglected. As will be shown later, the Yamaji-kaze is evidently influenced by the complicated 3-dimensional effect of the actual orography. In this sub-section, we will show some examples of the experiments of 3-dimensional simulation of the Yamaji-kaze. In Fig. C-2-5, the rectangle framed by heavy solid lines shows the area where the simulation is performed. In the simulation, this area is represented by  $(Nx, Ny, Nz) = (50, 50, 32)$  grid points. The horizontal grid interval  $\Delta x = \Delta y = 5\text{km}$  is used, while the variable grid interval  $\Delta z = 40\text{m} \sim 1200\text{m}$  is used for the vertical grid interval. The dimensions of the model domain are  $(Lx, Ly, H) = (245\text{km}, 245\text{km}, 18.0\text{km})$ .

In the simulation, anelastic equations are used, while the Boussinesq approximation is not employed. An absorbing layer is imposed at the highest 10 layers. The lower boundary is assumed to be thermally insulated and heat flux from the surface is neglected. The time interval of  $\Delta t = 30\text{sec}$  is used, and the simulation is performed until  $t = 4\text{hrs}$  ( $480\Delta t$ ). For the smooth start-up, the height of orography is set to zero initially, and is raised linearly to the ordinary height during the first 60 time steps ( $t = 30\text{min}$ ). The environmental wind is set to  $V = 6\text{m/s}$ , assuming a constant SSE-ly wind. A constant lapse rate of  $d\theta/dz = 3\text{K/km}$  ( $N \approx 0.01\text{s}^{-1}$ ) is chosen for the typical atmospheric stability.

Three kinds of experiment, a) no Coriolis force and no surface friction, b) Coriolis force and no surface friction, and c) Coriolis force and surface friction, are performed.

a) No Coriolis force and no surface friction

Firstly, the simulation is performed for the simplest condition with no Coriolis force and no surface friction. Figure C-2-6 a) shows the simulated wind vectors at the lowest level (about 20m above the surface) after  $120\Delta t$  ( $t = 1\text{hrs}$ ). The surface wind becomes weak in the windward side around Kochi by the blocking effect of the Shikoku Mountains, while it increases on their northern slope. The surface wind over Hiuchi-nada is yet southerly as the environmental wind. At  $t = 2\text{hrs}$  (Fig. C-2-6 b)), the surface wind further increases around Doi and Mishima, in the lee of the col of the Shikoku Mountains. Over the western part of

Hiuch-nada, a notable weak wind area develops. This weak wind area is located just behind the hydraulic jump which is generated by the wave breaking. At  $t = 3$  hrs (Fig. C-2-6 c)), the southerly wind around the eastern edge of Hiuchi-nada forms a jet-like area of strong wind. On the other hand, the surface wind over the western part of Hiuchi-nada turns to northerly, opposite to the southerly environmental wind. As shown in Fig. C-2-6 d), this northerly wind extends its area northward as the time elapses, and a cyclonic circulation is formed between this northerly wind and the strong southerly jet-like wind around the eastern edge of Hiuchi-nada. This northerly wind apparently corresponds to the "Domai",

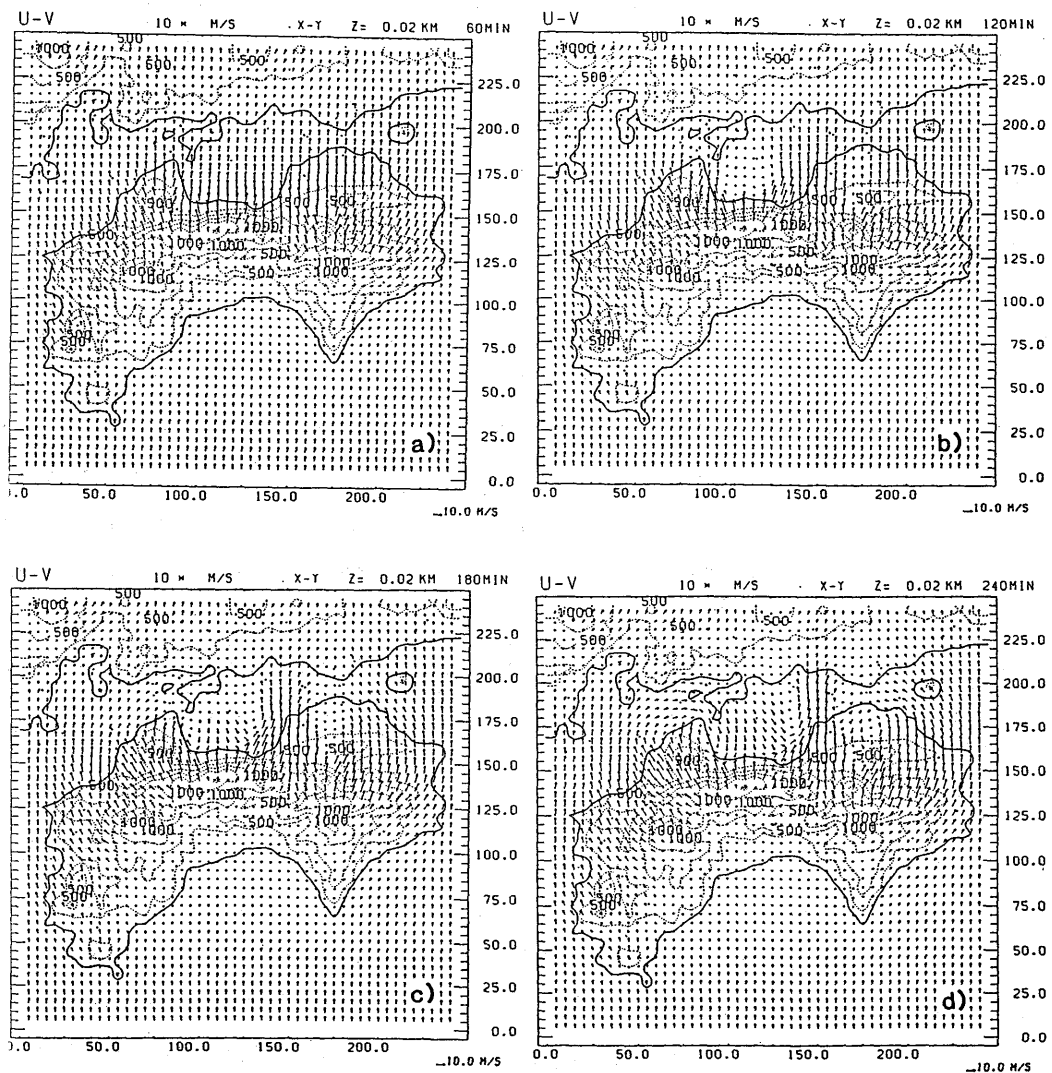


Fig. C-2-6 a) ~ d) The simulated lowest level ( $z^* = 20$  m) wind vectors at every 1 hour. Lower right arrow indicates 10 m/s. The broken lines indicate height contour at every 250m.

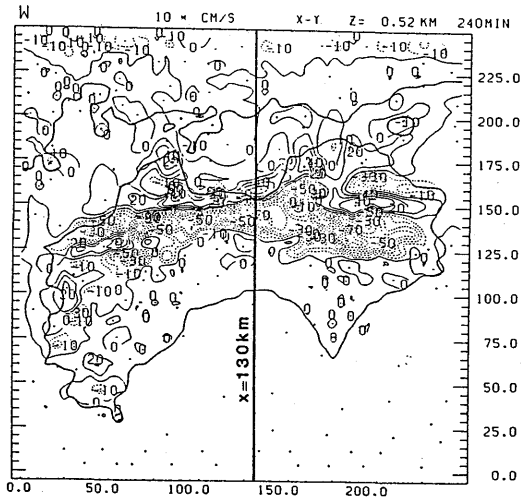


Fig. C-2-7 The vertical velocity ( $w$ ) at the 4th level of the model (about 200m above the surface) and  $t = 4$  hrs. The contour interval is 10 cm/s. Broken lines show the negative value (downward motion). Heavy line indicates the location of the vertical cross-section shown in Figs. C-2-8 a) ~ b).

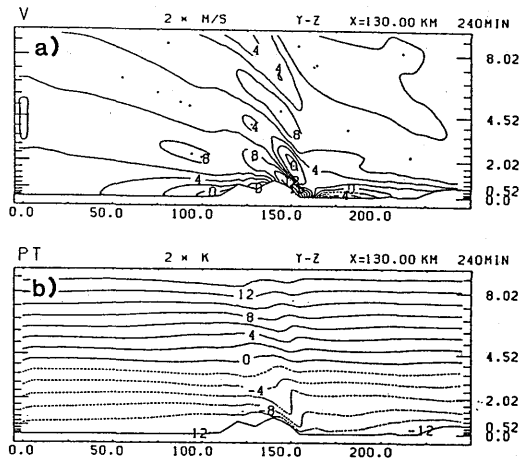


Fig. C-2-8 a) The vertical cross-section of the horizontal wind along  $x = 130$  km (heavy line in Fig. C-2-7) at  $t = 4$  hrs. The contour interval is 2 m/s. b) As in a) but for the potential temperature. The contour interval is 2K. Deviation from 300K is indicated.

one of the characteristic features of the Yamaji-kaze.

Figure C-2-7 shows the vertical velocity at the 4th level of the model (about 200m above the surface) at  $t = 4$  hrs. A strong downdraft region which corresponds to the downslope wind is seen over the northern slope of the Shikoku Mountains, while another long and narrow updraft area is seen along the northern coast line facing Hiuchi-nada. This updraft area is located on the surface convergence between the southerly downslope wind and the northerly wind over Hiuchi-nada, and corresponds to the hydraulic jump.

Figures C-2-8 a), b) show the vertical cross-section of the southerly component of the horizontal wind and the potential temperature along  $x = 130$ km (shown by a heavy line in Fig. C-2-7). In Fig. C-2-8 a), an area of negative horizontal wind which corresponds to the wave over-turning is seen at the level of 2km above the northern slope of the Shikoku Mountains at  $y = 150$ km. A neutral stagnant layer is formed corresponding to this wave breaking, and the isentropes shown in Fig. C-2-8 b) are upright over the northern slope of the Mountains. Below it, the downslope wind greater than 16m/s is seen on their steep northern slope. The surface wind changes suddenly around  $y = 160$ km. This abrupt change

corresponds to the internal hydraulic jump. On the north side of this abrupt change, a northerly wind greater 4m/s is seen over Hiuchi-nada.

b) Coriolis force and no surface friction

Secondly, the simulation is performed with the Coriolis force to check its effect on the Yamaji-kaze. Figure C-2-9 a) shows the simulated wind vectors at the lowest level after 4hrs. In this experiment, the Coriolis parameter of  $f = 8.15 \times 10^{-5} \text{s}^{-1}$  is used, corresponding to the latitude of Shikoku Island (34 N). A geostrophic balanced field is given for the initial condition. On comparing this figure with Fig. C-2-6 d), the surface wind at the stagnant area around Kochi becomes a weak easterly wind. This slight westward component of the surface wind is caused by the westward pressure gradient force which originally balances eastward Coriolis force by the southerly environmental wind. The SE-ly surface wind in the north-western part of Shikoku Island around Matsuyama is enhanced by the effect of this westward pressure gradient force. No notable differences between Fig. C-2-6 d) and Fig. C-2-9 a) are seen in the flow patterns of the downslope wind and the northerly wind over Hiuchi-nada.

c) Coriolis force and surface friction

Next, the simulation is performed not only with the Coriolis force but also with the surface friction, whose effect on the Yamaji-kaze is tested. Over the land, the surface momentum fluxes are calculated from the similarity law, assuming a constant roughness length of 10cm and no heat fluxes. Over the sea, the surface momentum fluxes are determined from the formula by Kondo (1975), depending on the magnitude of the velocity of the surface wind. Figure C-2-9 b) shows the simulated wind vectors at the lowest level after  $t = 4$ hrs. Compared with Fig. C-2-9 a), the surface wind is generally weak. The unnatural strong SE-ly wind around Matsuyama in Fig. C-2-9 a) is no longer seen and the strong southerly jet-like wind along the eastern edge of Hiuchi-nada is also reduced. On the other hand, the downslope wind around Doi is not so weakened, and the northerly wind over the western part of Hiuchi-nada is still obvious.

Figures C-2-10 a) and b) show the vertical cross-section of the southerly component of the horizontal wind and the potential temperature along  $x = 130$ km (shown by a heavy solid line in Fig. C-2-7). Compared with Fig. C-2-8 a), the horizontal wind close to the ground surface is weakened by the effect of the surface friction, while the flow pattern is not

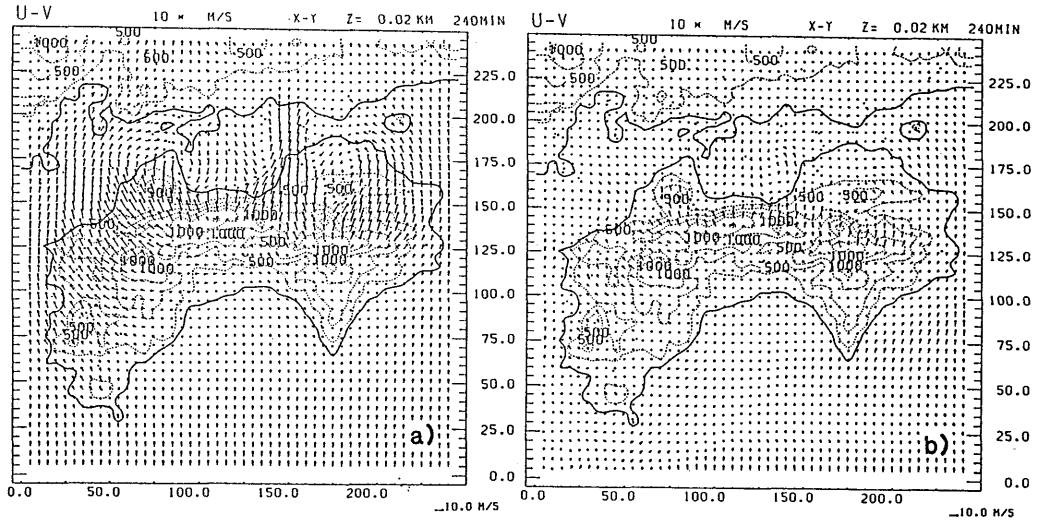


Fig. C-2-9 a) As in Fig. C-2-6 d) but for the case including Coriolis force in the simulation.  
 b) As in a) but for the case including Coriolis force and the surface friction in the simulation.

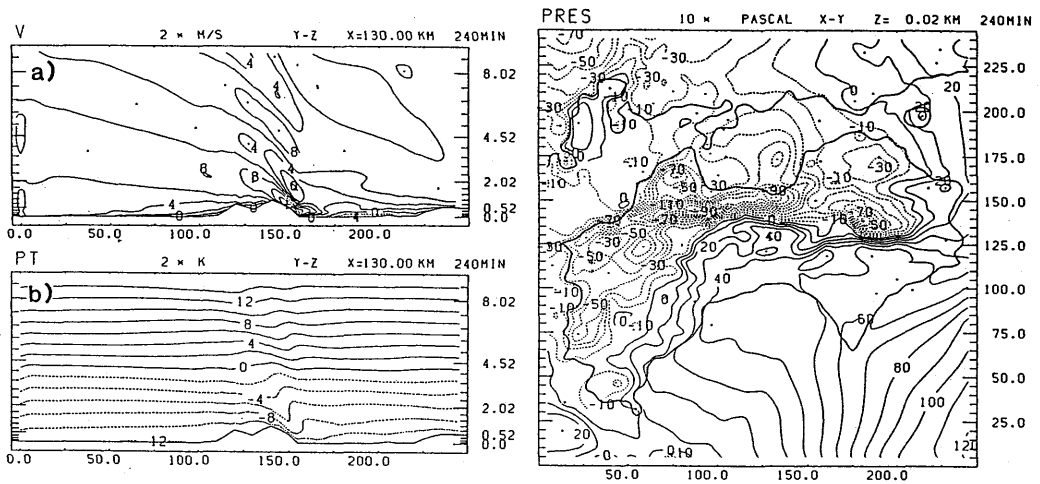


Fig. C-2-10 a), b) As in Figs. C-2-8 a), b) but for the case including Coriolis force and the surface friction in the simulation.

Fig. C-2-11 The simulated surface pressure deviation at  $t = 4$  hrs. The contour interval is 10 hPa.

much different on the whole. An area of negative horizontal wind which corresponds to the wave over-turning is also seen at the level of 2km above the northern slope of the Shikoku Mountains at  $y = 150$ km. Below it, the downslope wind greater than 14m/s is seen on their

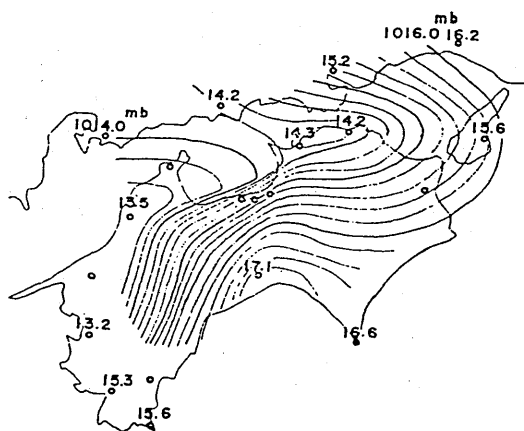


Fig. C-2-12 The averaged surface pressure in 4 hours observed in the Yamaji-kaze on 24 April, 1955. The contour interval is 0.2 mb. Adapted from Furukawa (1966).

northern slope. No notable differences are seen in the pattern of isentropes shown in Fig. C-2-10 b) either.

Figure C-2-11 shows the surface pressure deviation at  $t = 4$  hrs. The surface pressure of the basic state is high on the east side and low on the west, balancing the Coriolis force by the southerly environmental wind, while it is high on the windward side of the Shikoku Mountains and low on the lee side. The magnitude of the minimum depression on the northern slope of the Mountains is about 1hPa. A low pressure area which corresponds to the location of the cyclonic circulation shown in Fig. C-2-9 b) is seen in the eastern part of Hiuchi-nada.

Figure C-2-12 shows the averaged surface pressure in 4 hours observed in the Yamaji-kaze on 24 April, 1955 (Furukawa, 1966). The surface pressure pattern shown in Fig. C-2-11 well expresses the characteristics of the observed surface pressure. The surface pressure deviation in the lee side of the Shikoku Mountains shown in Fig. C-2-12 is almost twice as great as that in Fig. C-2-11. It appears that this difference is caused by the difference of the magnitude of the environmental wind. The southerly synoptic wind in the lower level was greater than 10m/s in the observation of the Yamaji-kaze on 24 April 1955, while it is 6m/s in the simulation.

d) Remarks

The northerly wind over Hiuchi-nada simulated in the former sub-sections is believed to

have some inherent similarities to the reversed flow behind the hydraulic jump which was studied by Saito and Ikawa (1991). However there exists quantitative difference between the occurrence of the two reversed flows. In the 2-dimensional experiments with a homogeneous atmosphere using an averaged orography of Shikoku Island and the Chugoku Mountains by Saito and Ikawa (1991), the reversed flow behind a stationary jump occurred for the case of  $U = 4\text{m/s}$ , but the jump propagated leeward and the occurrence of the reversed flow was obscure for the case of  $U = 6\text{m/s}$ . In the 3-dimensional experiment shown in sub-section C-2-2 a), the hydraulic jump almost stays along the northern coast line facing Hiuchi-nada, and an obvious northerly wind develops on the north side of the jump for the case of  $U = 6\text{m/s}$ . Namely, the northerly wind over Hiuchi-nada occurs more readily for the case of 3-dimensional experiment. This difference appears to be mainly caused by the 3-dimensional effect of the orography of the Island. Considering the fact that the Yamaji-kaze is accompanied by the "Domai" except in extraordinarily strong synoptic wind cases, the easiness of the occurrence of the northerly wind over Hiuchi-nada which was shown in the 3-dimensional experiment appears to be an encouraging result.

It appears that the Yamaji-kaze is not considerably affected by the Coriolis force. However, the Coriolis force is indispensable to obtain the realistic pressure pattern such as is shown in Fig. C-2-11.

The magnitude of the surface wind by the Yamaji-kaze is significantly affected by the surface friction. It appears that the selective effect of the surface friction owing to the difference of the roughness on land and sea makes the flow pattern of the Yamaji-kaze more realistic.

As was stated before, the experiments shown here are preliminary ones using simple conditions. The horizontal resolution employed in the simulation (5km) may not be adequate. More experiments will be required for the further understanding of the effect of the 3-dimensional orography on the Yamaji-kaze and the behavior of its associated hydraulic jump.

#### **Acknowledgement:**

The authors wish to express their thanks to Professor Fujio Kimura of Tohoku University and Shunji Takahashi of the Applied Meteorological Research Division of the MRI for their helpful guidance about geographical data.

## C-3. 3-dimensional simulation of the convective snow cloud observed over the Sea of Japan<sup>†</sup>

### — Sensitivity to ice crystal nucleation rates —

#### C-3-1. Introduction

The coastal region of northern Japan, facing the Sea of Japan, is famous for its heavy snowfall (e.g., Matsumoto *et al.*, 1967). The heavy snowfall is associated with the abundant heat and moisture supply from the warm sea surface (10°C) into the cold air (0°C) blowing from Siberia (e.g., Ninomiya, 1968). The snowfall is brought about by convective snow clouds with the temperature of cloud base and top being  $-5 \sim -10$  and  $-20 \sim -30^\circ\text{C}$ , respectively. However, the cloud microphysical aspects of the heavy snowfall have not been fully investigated yet, observationally or numerically.

Magono and Lee (1973) measured the vertical distribution of the shape, number concentration and mass of snow crystals and mass of cloud droplets at formative, mature and decaying stages of convective snow clouds around Otaru (43.2N, 141.0E) in Hokkaido, northern Japan, utilizing snow crystal sonde. Isono *et al.* (1966) measured the ice nucleus concentration and number precipitation rate of snow and graupel at Wajima (37.4N, 136.9E), and found a correlation between the two. Harimaya and Sato (1989) and Mizuno *et al.* (1990) measured the contribution ratio of riming to the growth of snow flakes and its dependence on meteorological conditions. Their studies suggest that the riming process is a primary process in precipitation formation of convective snow clouds. Recently, Murakami and Matsuo (1990) developed a Hydrometeor Video Sonde (HYVIS) which can measure the vertical distribution of hydrometeors utilizing two types of TV cameras, and Murakami *et al.* (1990) observed convective snow clouds at Tobishima (39.25N, 139.55E) by use of HYVIS. From these observations, it was revealed that few rain drops exist, and they do not play a dominant role in precipitation formation; instead, accretion of cloud droplets by graupel and snow (riming) play a significant role in precipitation formation as well as depositional process; the maximum number concentration of ice crystals amounts to  $10^4$ – $10^5\text{m}^{-3}$ , one or two orders larger than that predicted by Fletcher's formula. These observational studies

---

<sup>†</sup> This is a preliminary report on the research carried out in collaboration with H. Mizuno, T. Matsuo, M. Murakami and Y. Yamada, Physical Meteorology Research Division of the MRI (Ikawa *et al.*, 1991).

provide important and useful information about the cloud microphysical processes taking place in clouds. To supplement these observational studies, numerical and theoretical studies are needed, in addition to better organized intensive and extensive field observations.

Takahashi (1983) conducted numerical simulation of an isolated winter cumulus by use of a 2-dimensional (axisymmetric) model with highly sophisticated cloud microphysics, the so-called bin method, focusing on the electrification. Ikawa *et al.* (1987) and Ikawa (1988a) simulated the convective cloud band observed over the Sea of Japan (Sakakibara *et al.*, 1988) by use of a 2-dimensional model with a bulk parameterization scheme of cloud microphysics where the mixing ratios of water vapor, cloud water, cloud ice, snow and graupel are predicted. Ikawa (1988) demonstrated that the dominant processes in precipitation formation are the condensation of water vapor to form supercooled cloud droplets and accretion of them (riming) by snow and graupel, rather than the depositional growth of ice particles. However, his simulation is 2-dimensional, and the bulk parameterization adopted in his model does not predict the number concentrations of cloud ice (pristine ice crystals), snow (ice crystals greater than pristine ice crystals and snow aggregates) and graupel, and has some ambiguous (or ad-hoc) parts in the parameterization of ice nucleation.

Recently, Cotton *et al.* (1986) and Murakami (1990) developed the bulk parameterization schemes of cloud microphysics in which the number concentrations of ice crystals and snow aggregates are predicted in addition to the mixing ratios of water substances. Cotton *et al.* applied the scheme to the simulation of orographic snowfall from stratiform clouds observed in Colorado in winter. Murakami applied his scheme to the convective cloud observed in Montana in summer. Their schemes appear to be promising for realistic simulation of clouds.

One of the purposes of this paper is to present a bulk parameterization of cloud microphysics which predicts not only the number concentrations of cloud ice and snow but also that of graupel in addition to the mixing ratios of six forms of water substance (water vapor, cloud water, rain, cloud ice, snow and graupel). The parameterization will be applied to a 3-dimensional simulation of the convective snow cloud observed over the Sea of Japan. The results will be compared with observations, and the performance and the insufficient parts of the parameterization scheme will be discussed.

Another purpose of this paper is to examine what the dominant processes are in forming precipitable particles and what the effects of ice nucleation rates are on precipitation formation. There have been many controversies on the disagreement between the number concentrations of ice crystals and ice-forming nuclei. Therefore, sensitivity experiments to

varying ice nucleation rates become necessary. These experiments may shed some light on the mechanism of the high number concentration of the observed ice particles and be useful in the assessment of the effect of seeding over the natural convective snow cloud.

In section C-3-2, observations of the cloud to be simulated are shown. In section C-3-3, the numerical model is described; in section C-3-4, experimental design is given. In section C-3-5, the results of the reference experiment are shown. In section C-3-6, the results of sensitivity experiments are shown and compared with each other. In section C-3-7, numerical results are compared with observations. In section C-3-8, the summary and conclusions are given.

### C-3-2. Observations of the convective cloud

Special observations of convective clouds were conducted in winter from 1989 to 1991 by the joint research group consisting of members of the MRI, the Institute of Low Temperature Science of Hokkaido University, and the National Research Center for Disaster Prevention, by use of dual Doppler radars, HYVIS and other instruments. An isolated convective snow cloud was observed at 1500LST on Feb. 4, 1989 on Tobishima Island (39.25N, 139.55E), 30km north-west off the coast of Sakata, northern Japan. This cloud is the object of the 3-dimensional simulation.

The synoptic chart of surface pressure at 0900LST is shown in Fig. C-3-1. The vertical profiles of wind, temperature and relative humidity are displayed in Fig. C-3-2. A HYVIS was launched into the cloud successfully, and measured the liquid water content, number concentration of cloud droplets and ice crystals in addition to temperature and relative humidity as a function of height, as displayed in Fig. C-3-3 (Murakami *et al.*, 1990). In counting the number of ice particles, those which are of amorphous shape or smaller than  $50\mu\text{m}$  in diameter are excluded. Ice particles of amorphous shape appear to be fragments produced by collision of ice particles with the sampling surface. If they are included, the maximum number of ice particles around  $z = 2.0\text{km}$  is  $2 \times 10^6\text{m}^{-3}$ . From the figure, it is noticed that the number concentration of ice crystals is very large as compared to  $10^3\text{m}^{-3}$  expected from Fletcher's formula for the cloud top temperature of  $-20^\circ\text{C}$ , and in spite of the presence of this large number of ice crystals, there exists cloud water as much as  $0.1\text{g}/\text{m}^3$ . As seen from radar reflectivity patterns shown in Fig. C-3-4 (Yamada *et al.*, 1990), the horizontal and vertical scales of the convective cloud is about 5km and 3km, with the maximum reflectivity less than 30dBZ.

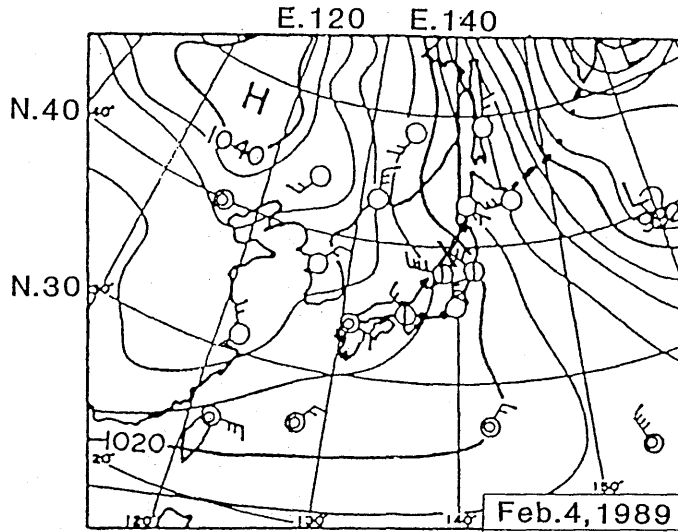


Fig. C-3-1 Surface synoptic pressure chart at 0900LST, Feb. 4, 1989 with the contour interval of 4 hPa. Observation area is indicated by x.

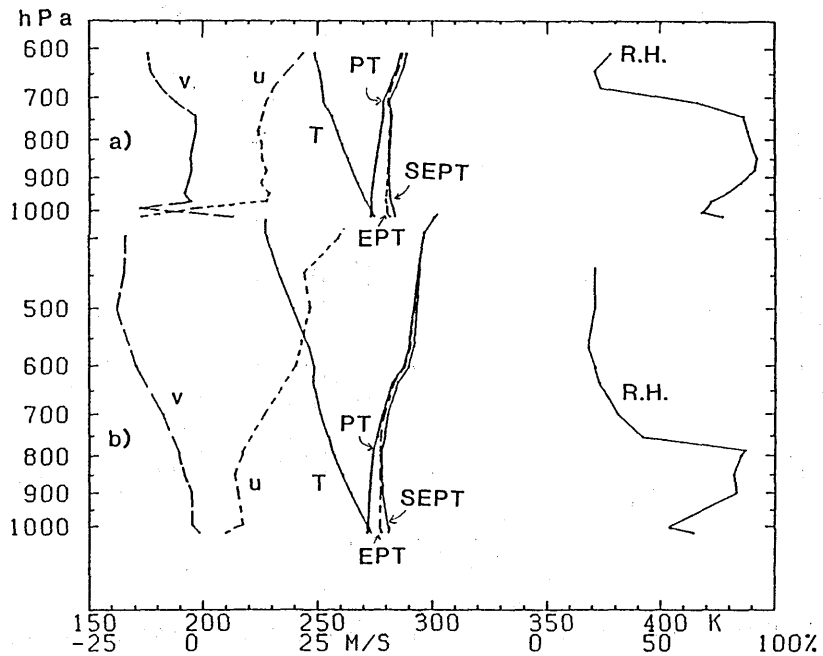


Fig. C-3-2 Vertical profiles of wind (u, west-east component; v, south-north component), temperature (T), potential temperature (PT), equivalent potential temperature (EPT), saturation equivalent potential temperature (SEPT) and relative humidity (R.H.). a) at 1500LST, Feb. 4, 1989 at To-bishima. b) at 0900LST, Feb. 4, at Akita (39.72N, 140.10E).

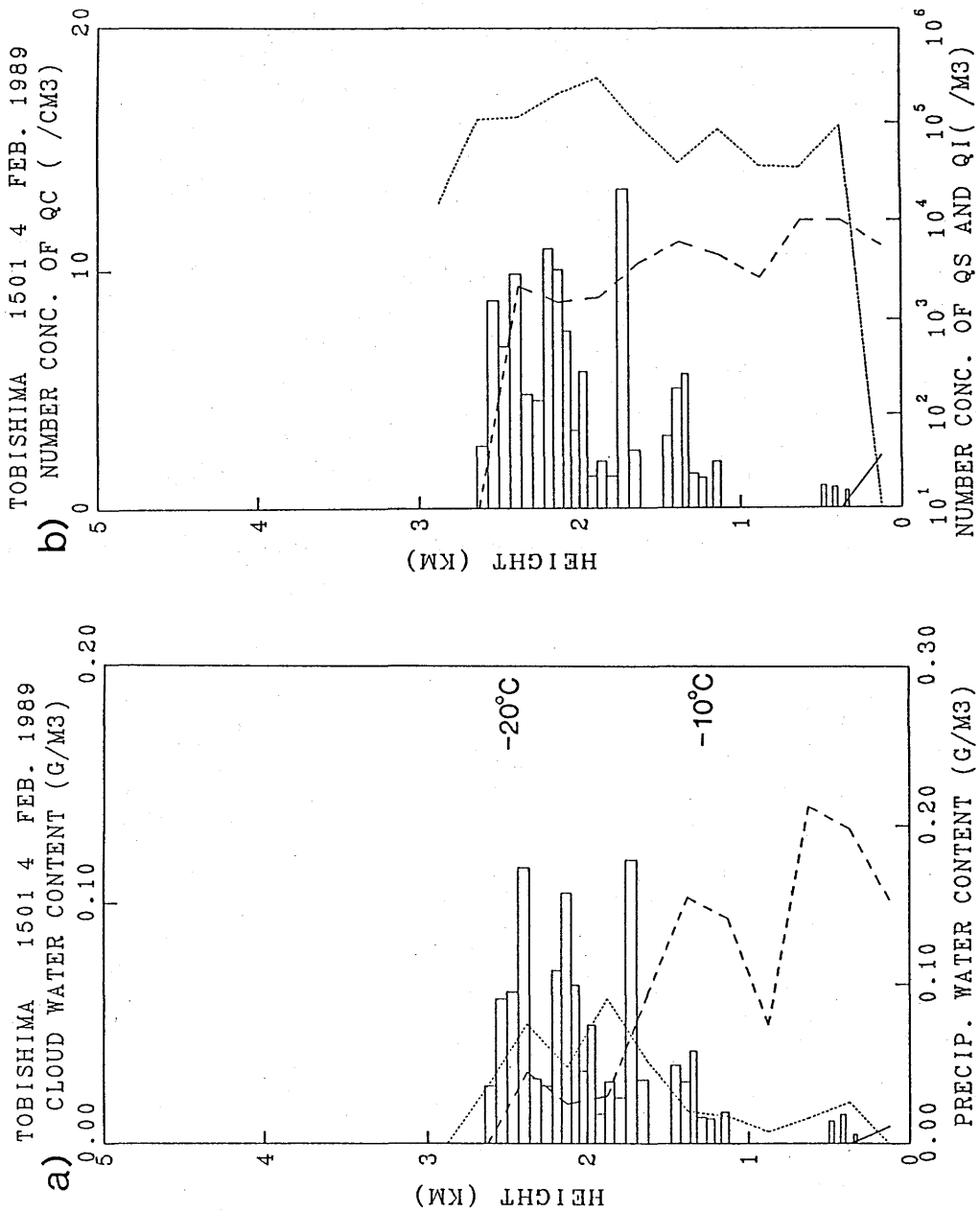
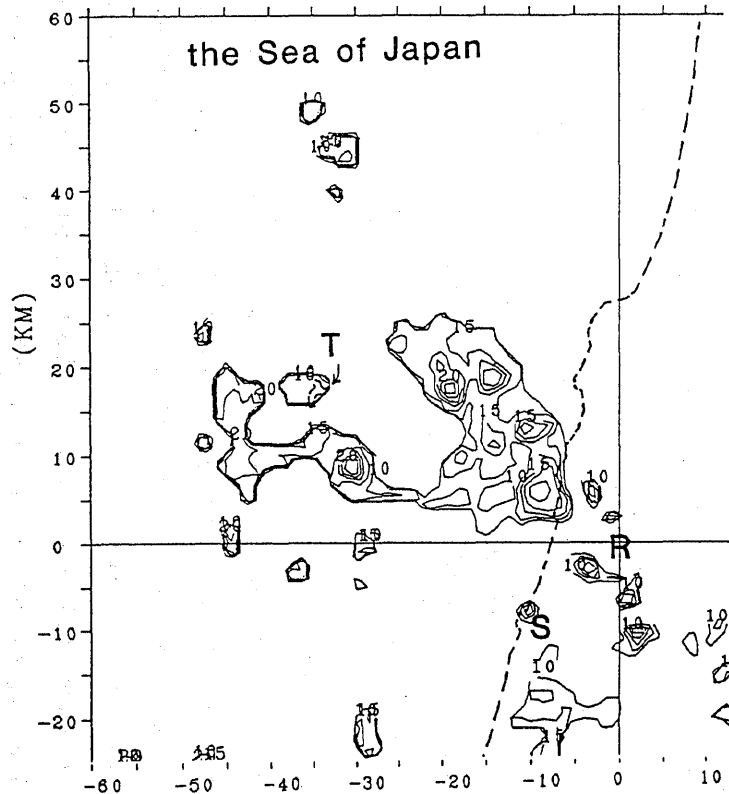


Fig. C-3-3 Vertical distribution of hydrometeors measured by HYVIS, 1500LST, Feb. 4, 1989 (Courtesy to Murakami *et al.*, 1990).

- a) Cloud water contents ( $\text{gm}^{-3}$ ), water contents of ice particles smaller than  $300 \mu\text{m}$  in diameter (dotted line) and of those larger than  $300 \mu\text{m}$  in diameter (broken line).
- b) Number concentrations of cloud droplets ( $\text{cm}^{-3}$ ), ice crystals smaller than  $300 \mu\text{m}$  in diameter (dotted line), and ice particles larger than  $300 \mu\text{m}$  in diameter (broken line).

a) MRI 3CM DOPPLER RADAR  
890204 145828 EL=1.7



b) MRI 3-CM DOPPLER REI  
890204 145959 SAKATA  
AZ=300.1

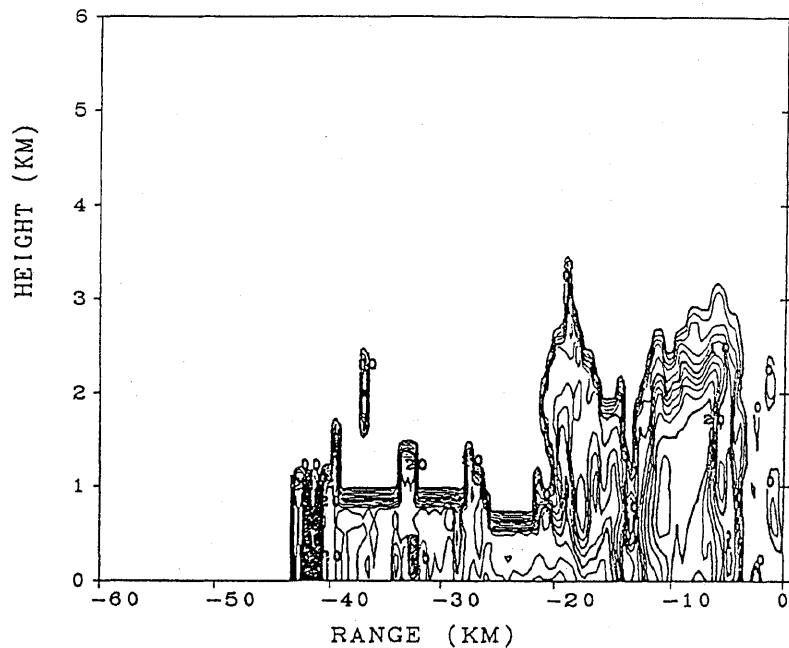


Fig. C-3-4 a) Radar echo patterns (PPI scan) at the elevation angle of  $1.7^\circ$  observed at 1500LST, Feb. 4, 1989. Contour interval is 2.5 dBZ. The locations of the radar site, Tobishima Island and Sakata, are indicated by R, T and S, respectively.  
b) Radar echo patterns (REI scan) at the azimuth angle of  $300^\circ$ . Contour interval is 2.5 dBZ. The location of the radar site is at  $x = 0$  km. (Courtesy to Yamada *et al.*, 1990).

### C-3-3. Numerical model and parameterization of cloud microphysics

The numerical model is basically the same as Ikawa *et al.* (1987) unless specifically mentioned; the dynamical frame is mainly based on Clark (1977); subgrid turbulent mixing terms are parameterized based on Klemp and Wilhelmson (1978) and Deardorff (1980); for the time integration, E-HI-VI scheme (Ikawa, 1988) is used with the time averaging parameter of implicit scheme,  $\alpha < 0.5$  (see Eq. (20) in Ikawa, 1988), the coefficient for the Robert-Asselin time filter,  $\nu = 0.15$ .

Parameterization of cloud microphysics is described in B-11 in this technical report.

The dimensions of the domain are  $(LX, LY, LZ) = (10.0\text{km}, 10.0\text{km}, 4.35\text{km})$ , with the grid number of  $(NX, NY, NZ) = (26, 26, 26)$ . Variable grid mesh is used in the  $z$ -coordinate, whose grid distance varies from 20m (below  $z = 30\text{m}$ ) to 200m (above  $z = 1.2\text{km}$ ). The lowest grid point is placed at  $z = 10\text{m}$ . The leap-frog time integration is used with the time interval of  $\Delta t = 4\text{s}$ . The lateral boundary condition is cyclic. The lower boundary is assumed to be the sea surface with a temperature of  $10^\circ\text{C}$ , and latent and sensible heat fluxes and momentum fluxes from the sea surface are calculated by use of the resistance law based on Kondo's work (see Ikawa *et al.*, 1987).

### C-3-4. Experimental design

There is much uncertainty about ice nucleation. As will be shown later, the observed high number concentration of ice particles is 4 times larger than the maximum number concentration of ice particles simulated by the model where parameterizations for ice nucleation terms are based on three conventional theories, *i.e.*, Fletcher's deposition/sorption nucleation, Bigg's freezing of cloud droplets and Hallet-Mossop rime-splinter ice multiplication. The simulated radar reflectivity is larger by 10dBZ than the observed one (30dBZ). To simulate the cloud more realistically at least in the number concentration of ice crystals, amplification of nucleation rates is necessary.

Sensitivity experiments to varying ice nucleation rates are conducted for three purposes: 1) to simulate the cloud more realistically at least in the number concentration of ice crystals; 2) to see the precipitation formation mechanism in the cloud; 3) to see the effects of changing various kinds of ice nucleation rates on precipitation formation. As shown in Table C-3-1, in these sensitivity experiments, parameters in various kinds of ice nucleation terms are modified to produce more cloud ice in number (EXDS for Fletcher's deposition/sorption nucleation; EXFZ for Bigg's cloud droplet freezing; EXHM for Hallet-Mossop's secondary

Table C-3-1 Kinds of sensitivity experiments to varying ice nucleation terms with  $\alpha\Delta t = 32$  and  $r_0 = 75 \mu\text{m}$  employed. Results are summarized in Table C-3-3.

	deposition /sorption Eq. B-(11-16) Fletcher $a \exp(-bT_c)$ $a = 10^{-2}$ $b = 0.6$	freezing Eq. B-(11-18) Bigg $c \exp(-dT_c)$ $c = 10^2$ $d = 0.66$	ice splinter Eq. B-(11-21) Hallet-Mossop $T_1, T_2, T_3, T_4$ $=(-3, -5, -5, -8)$	seeding	fracturing by collision between snow and graupel particles (Eq. C-(3-1)) $A = 0$
EXN1	normal	normal	normal	no	normal
EXDS1	$a \rightarrow \times 10^3$	normal	normal	no	normal
EXDS2	$a \rightarrow \times 10^6$	normal	normal	no	normal
EXFZ1	normal	$c \rightarrow \times 10^2$	normal	no	normal
EXFZ2	normal	$c \rightarrow \times 10^5$	normal	no	normal
EXHM	normal	normal	$T_1, T_2, T_3, T_4$ $=(-3, -5, -28, -30)$	no	normal
EXS1	normal	normal	normal	0.95–1.75km	normal
EXS2	normal	normal	normal	1.75–3.15km	normal
EXBK1	normal	normal	normal	no	10
EXBK2	normal	normal	normal	no	100

ice nucleation).

EXBK is conducted to see the effects of the secondary ice particle generation by collision between snow and graupel particles (Vardiman, 1978; Griggs and Choulaton, 1986) which is given as below:

$$\text{Nigacs} = A \times \text{Ngacs}, \quad (3-1)$$

where Ngacs is the number of collisions between snow and graupel particles per second and  $A$  is a coefficient. In EXBK1 and EXBK2,  $A$  is assumed to be 10 and 100, respectively.

EXDS1 is regarded as a reference experiment, simply because the number concentration of cloud ice and snow and radar reflectivity are closer to the observed values than EXN1.

To assess the seedability to convective clouds, seeding experiments are conducted by adding the ice nucleation term of

$$100 \times \text{Pidsn}, \quad (3-2)$$

with substitution of  $w = 5\text{m/s}$  and  $T_c = -20^\circ\text{C}$ , during the first 60min at  $0.95 \leq z \leq 1.75\text{km}$  (EXS1) or at  $1.75 \leq z \leq 3.15\text{km}$  (EXS2) all over the horizontal domain. The total number

of added ice nuclei will amount to  $4 \times 10^{17}$  (equivalent to 400kg dry ice) if the seeded area is water-saturated everywhere.

Another kind of sensitivity experiment is conducted to see the effect of the parameters  $\alpha 2\Delta t$  (see Eq. B-(11-43)) and  $r_0$  (see Table B-11-1 and Eq. B-(11-27)) which have a large influence on the conversion term of snow into graupel and that of cloud ice to snow, respectively. Experiments except for those listed in Tables C-3-4 and C-3-5 adopt  $\alpha 2\Delta t = 32$  and  $r_0 = 75\mu\text{m}$ , unless specifically mentioned.

Initial environmental conditions are determined from observations (see Figs. C-3-2 and C-3-5). The initial wind velocity component projected on the  $100^\circ$  azimuth plane,  $u$ , has no vertical shear below  $z = 2.5\text{km}$ , while it has a shear of  $4 \times 10^{-3} \text{ s}^{-1}$  above  $z = 2.5\text{km}$ . The initial wind velocity component projected on the  $10^\circ$  azimuth plane,  $v$ , is set to zero. Time integration is continued up to 213min, during which 3 groups of clouds appears successively. The first cloud is initiated artificially by adding the warm and moist perturbation to the initial field at the central part of the domain. The second and third groups of clouds are excited at the convergence zone that resulted from the collision of the cold outflows.

### C-3-5. Results of reference experiment (EXDS1)

#### a) Overview of the evolution of the convective clouds and the water budget analysis

Figure C-3-5 shows the horizontally averaged values for  $U$  (horizontal wind component in the  $x$ -direction), temperature, mixing ratio of water vapor, potential temperature, equivalent potential temperature, saturation equivalent potential temperature and relative humidity at  $t = 60\text{min}$ . The sea surface temperature is  $10^\circ\text{C}$ . Initially, the potential temperature at  $z = 10\text{m}$  is  $0^\circ\text{C}$ , but it is warmed up to  $2^\circ\text{C}$  at  $t = 60\text{min}$ . Environmental vertical wind shear between  $z = 10\text{m}$  and cloud top ( $z = 2.5\text{km}$ ) has changed from 0 to  $10^{-3}\text{s}^{-1}$  mainly due to the surface friction.

Figure C-3-6 shows the horizontally averaged values for  $Q_c$ ,  $\log(N_i)$ ,  $Q_s$ ,  $\log(N_s)$ ,  $Q_g$  and  $\log(N_g)$  as a function of time and height. The heights of  $0^\circ\text{C}$ ,  $-10^\circ\text{C}$  and  $-20^\circ\text{C}$  are 0.05km, 1.2km and 2.4km respectively. The height of cloud base is about 0.7km and the height of cloud top increases from 2.5km to 3km. The maximum values of  $Q_c$  and  $Q_g$  are seen at the middle level ( $z = 1.5\text{km}$ ), while those of  $N_i$  and  $N_s$  are seen at the upper level ( $z = 2.2\text{km}$ ).

Figure C-3-7a shows the time evolution of the cloud in terms of the maximum values of mixing ratios of water species in air, precipitation rates of snow and graupel, number

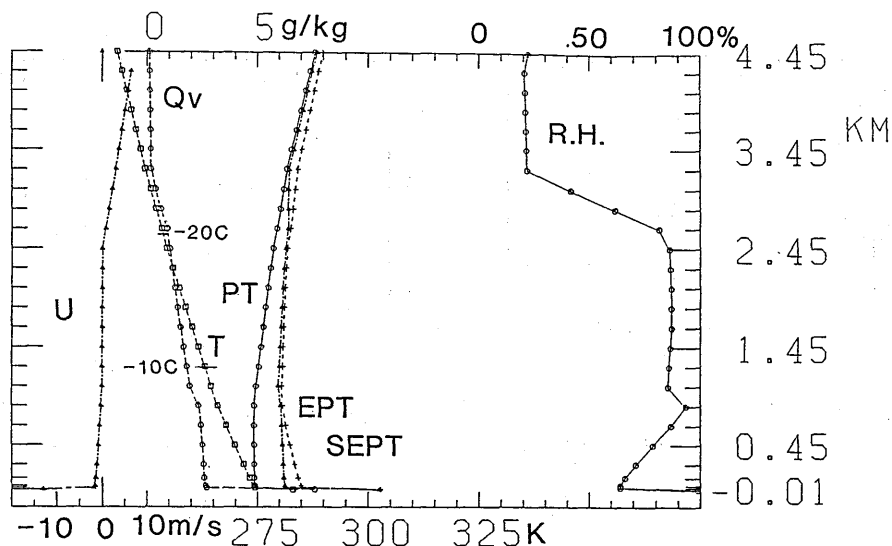


Fig. C-3-5 Horizontally averaged values for  $U$  (horizontal wind component in the  $x$ -direction), temperature,  $T$ , mixing ratio of water vapor,  $Q_v$ , potential temperature,  $PT$ , equivalent potential temperature,  $EPT$ , saturation equivalent potential temperature,  $SEPT$ , and relative humidity  $R.H.$  at  $t = 60$  min by EXDS1.

concentration of cloud ice, snow and graupel and upward velocity,  $w$ , in the domain. Three maxima in upward velocity and cloud water appear at  $t = 60$ min, 127min and 173min. The second and third maxima correspond to the newly generated clouds at the convergence zone where cold outflows from the older clouds collide. A similar initiation of convection by interacting outflows was simulated by Droegemeier and Wilhelmson (1985). About 13 ~ 20min later than the time when cloud water in air becomes maximum, graupel in air reaches its maximum, and about 20 ~ 27min later than the time when cloud water in air reaches its maximum, snow in air reaches its maximum. The life cycle of the simulated clouds is divided into 5 stages as shown in Table C-3-2.

Here, some useful quantities for water budget analysis are defined as follows:

Horizontally averaged and vertically integrated  $Q_x$  in air for the hydrometeor  $x$  ( $v$ , water vapor;  $c$ , cloud water;  $r$ , rain;  $i$ , cloud ice;  $s$ , snow;  $g$ , graupel).

$$TQ_x = \iiint \bar{\rho} Q_x dx dy dz / (LX \times LY) \quad (\text{kgm}^{-2});$$

Horizontally averaged and vertically integrated  $N_x$  in air,

$$TN_x = \iiint N_x dx dy dz / (LX \times LY) \quad (\text{m}^{-2});$$

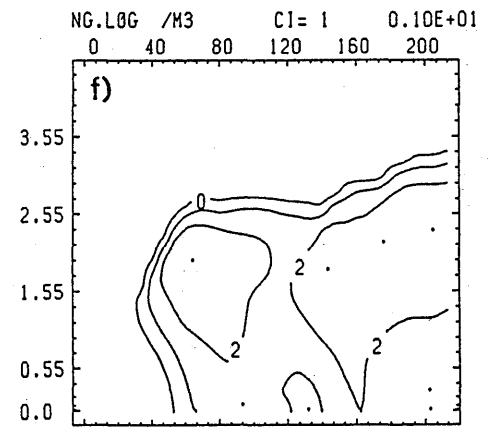
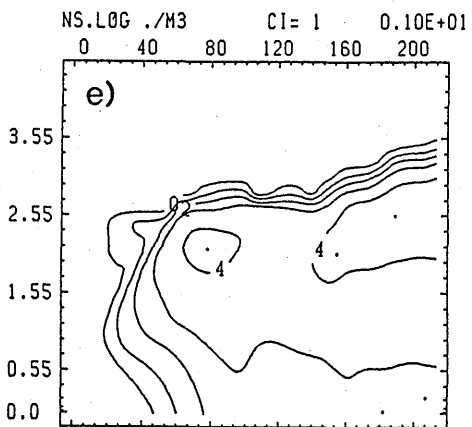
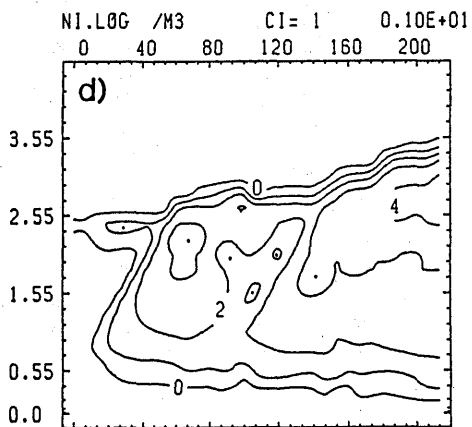
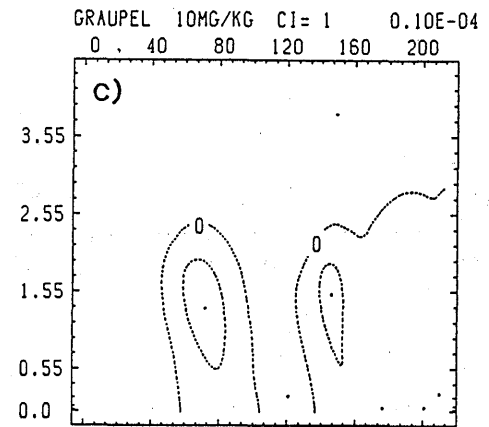
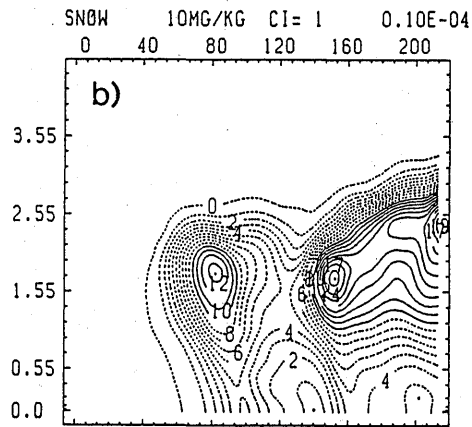
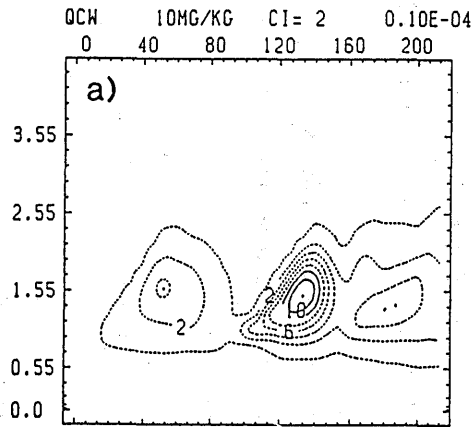


Fig. C-3-6 Horizontally averaged values by EXDS1 for (a)  $Q_c$  ( $10^{-5}$  kg/kg), (b)  $Q_s$  ( $10^{-5}$  kg/kg), (c)  $Q_g$  ( $10^{-5}$  kg/kg), (d)  $\log_{10}(N_i)(N_i : m^{-3})$ , (e)  $\log_{10}(N_s)(N_s : m^{-3})$ , and (f)  $\log_{10}(N_g)(N_g : m^{-3})$  as a function of time and height. Contour intervals are indicated by "CI=nn".

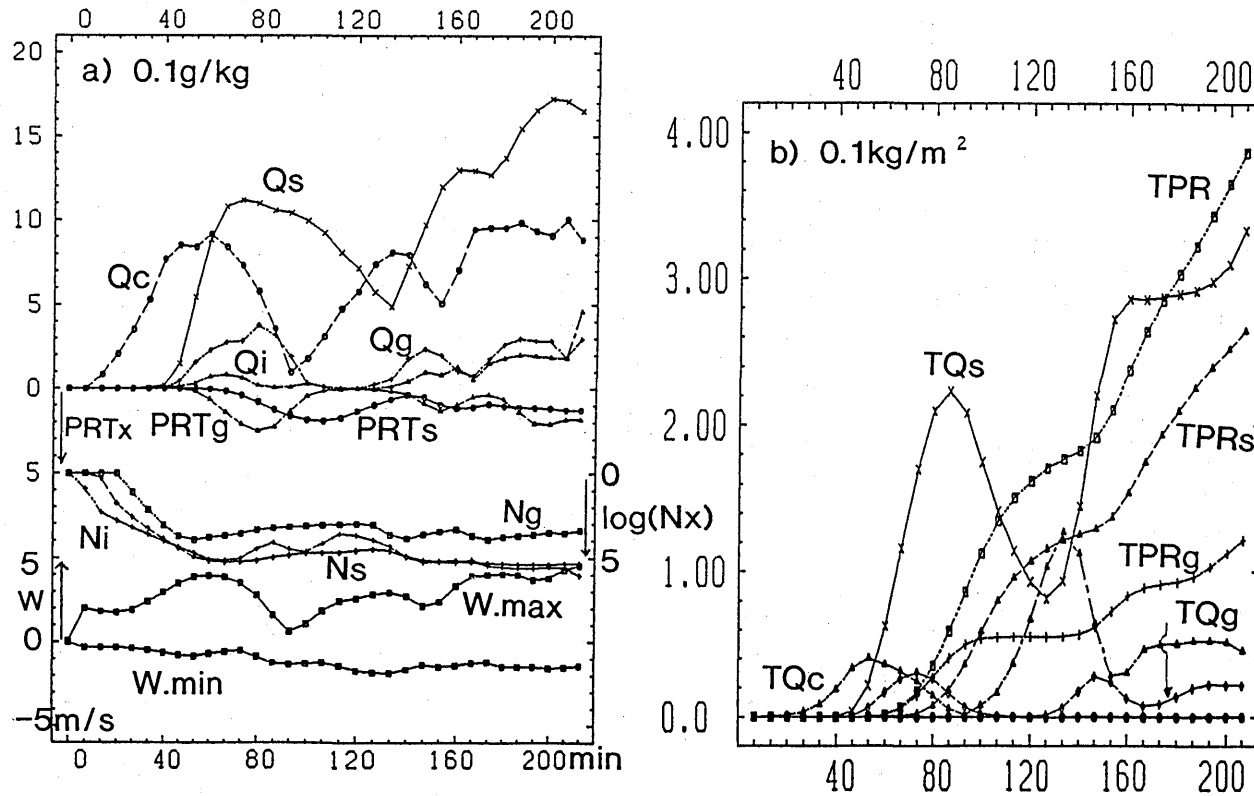


Fig. C-3-7 The results of EXDS1:

- a) The maxima of (upper part)  $Q_c$  (0.1 g/kg),  $Q_i$  (0.01 g/kg),  $Q_s$  (0.1 g/kg),  $Q_g$  (0.1 g/kg), and precipitation intensities (mm/hour) of snow and graupel, (central part)  $\log_{10}(N_i)$ ,  $\log_{10}(N_s)$ ,  $\log_{10}(N_g)$ , and (lower part) the maximum and minimum of the updraft  $w$  (m/s), as a function of time.  $N_i$ ,  $N_s$  and  $N_g$  are the number concentrations of cloud ice, snow and graupel ( $m^{-3}$ ), respectively. Data are sampled every 100 steps (6.67 min).
- b)  $TQ_c$ ,  $TQ_s$ ,  $TQ_g$ ,  $TPR_s$ ,  $TPR_g$  and  $(TPR_s + TPR_g)$  (horizontally averaged vertically integrated quantities of  $Q_c$ ,  $Q_s$ ,  $Q_g$  and the horizontally averaged precipitation amounts of snow, graupel and (snow + graupel)) as a function of time. Unit is 0.1 kg/m<sup>2</sup>.

Table C-3-2 Life cycle of the convective clouds (the first group, 1; the second, 2) that appeared in EXDS1. The symbols  $\uparrow \downarrow$  denote the time tendencies of increase and decrease, respectively. The symbols max and - denote the maximum and minimum values. Stages 1 and 2 might be called formative and developing stages, respectively; stages 3 and 4 mature and decaying stages; stage 5 a decayed stage.

stage	W	Qc	Qg	PRCP.g	Qs	PRCP.s	time (min)	
							1	2
1	$\uparrow$	$\uparrow$	0	0	0 (-)	0 ( $\downarrow$ )	20	107
2	max	max	$\uparrow$	0	$\uparrow$	0 (-)	60	134
3	$\downarrow$	$\downarrow$	max	$\uparrow$	$\uparrow$	$\uparrow$	80	147
4	- $\downarrow$	- $\downarrow$	$\downarrow$	max	max	$\uparrow$	80	160
5	$\uparrow$	$\uparrow$	-	$\downarrow$	$\downarrow$	max	100	167

Horizontally averaged and vertically integrated mass production term for the elementary cloud microphysical process  $Pxqqq$ ,

$$TPxqqq(z_0 < z < z_1) = \int_{z_0}^{z_1} \iint \bar{\rho} Pxqqq \, dx \, dy \, dz / (LX \times LY) \quad (\text{kgm}^{-2}\text{s}^{-1});$$

Horizontally averaged and vertically integrated number production term for the elementary cloud microphysical process  $Nxqqq$ ,

$$TNxqqq(z_0 < z < z_1) = \int_{z_0}^{z_1} \iint Nxqqq \, dx \, dy \, dz / (LX \times LY) \quad (\text{m}^{-2}\text{s}^{-1});$$

Horizontally averaged and vertically integrated total mass production term for the hydrometeor,  $x$ ,

$$TPRD(Q_x) = \int_0^{z_1} \iint \bar{\rho} PRD(x) \, dx \, dy \, dz / (LX \times LY) \quad (\text{kgm}^{-2}\text{s}^{-1});$$

Horizontally averaged and vertically integrated total number production term for the hydrometeor,  $x$ ,

$$TPNx = \int_0^{z_1} \iint NPRD(x) \, dx \, dy \, dz / (LX \times LY) \quad (\text{m}^{-2}\text{s}^{-1});$$

Horizontally averaged precipitation rate of  $x$ ,

$$PRCPx = \int \int \bar{\rho} Qx \bar{U}x \, dx \, dy / (LX \times LY) \quad (\text{kgm}^{-2}\text{s}^{-1});$$

Horizontally averaged accumulated precipitation amount of  $x$ ,

$$TPRx(t_1, t_2) = \int_{t_1}^{t_2} PRCPx \, dt \quad (\text{kgm}^{-2});$$

Horizontally averaged total precipitation amount,

$$TPR(t_1, t_2) = TPRr(t_1, t_2) + TPRs(t_1, t_2) + TPRg(t_1, t_2).$$

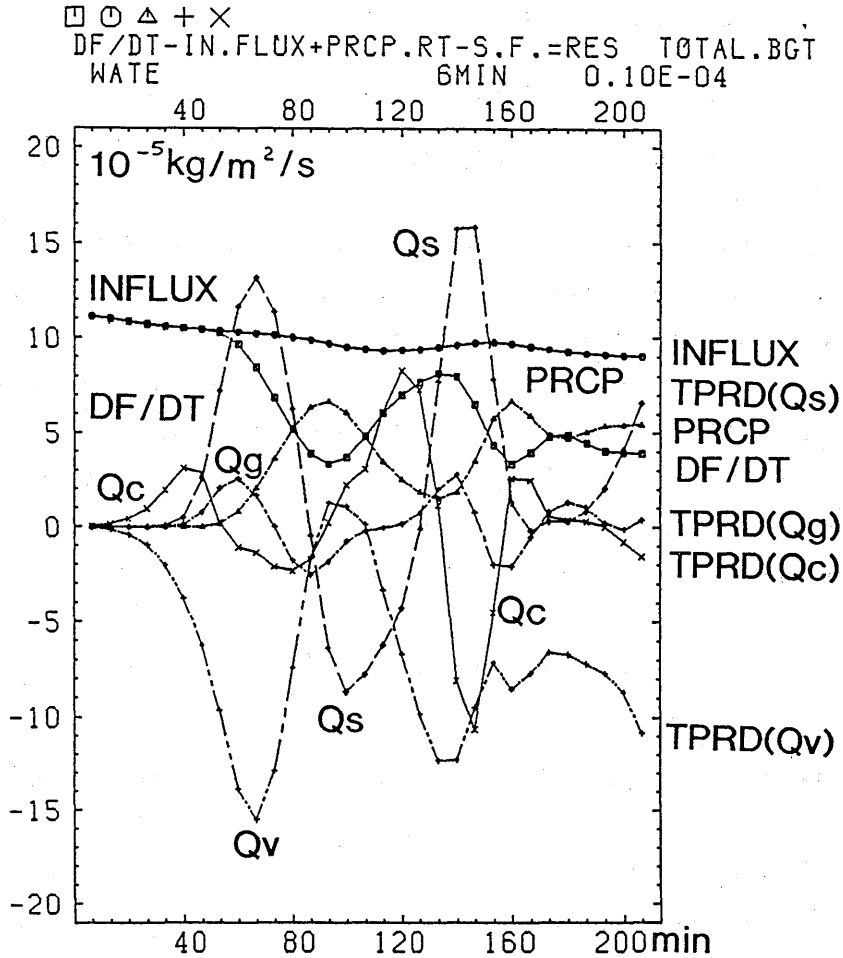


Fig. C-3-8 Water budget analysis for EXDS1.  $DF/DT$ ,  $INFLUX$ ,  $PRCP$  ( $10^{-5} \text{ kg/m}^2/\text{s}$ ) are shown as a function of time, together with  $TPRD(Qv)$ ,  $TPRD(Qs)$ ,  $TPRD(Qg)$ . Data are sampled every 100 steps (6.67 min).

Figure C-3-7b shows the time variations of  $TQc$ ,  $TQs$ ,  $TQg$ ,  $TPRs$ ,  $TPRg$  and  $TPR$ .

Figure C-3-8 shows the water budget of the simulated cloud together with  $TPRD(Qv)$ ,  $TPRD(Qc)$ ,  $TPRD(Qs)$  and  $TPRD(Qg)$ . The water budget equation is given as:

$$\frac{\partial F}{\partial t} - INFLUX + PRCP = RES,$$

where

$$F = TQv + TQc + TQr + TQi + TQs + TQg$$

$$PRCP = PRCP_r + PRCP_s + PRCP_g,$$

$$INFLUX = \iint \overline{\rho Q v'' w''} dx dy / (LX \times LY) \quad (\text{kgm}^{-2}\text{s}^{-1})$$

(the water vapor flux from the sea surface).

RES is a residual term, which should be zero if artificial diffusion terms and computational errors are absent. RES is below  $10^{-6}\text{kgm}^{-2}\text{s}^{-1}$  (not shown in Fig. C-3-8). The water vapor flux from the sea surface is nearly constant ( $1 \times 10^{-4}\text{kgm}^{-2}\text{s}^{-1}$  or  $260\text{Wm}^{-2}$ ). From the heat budget analysis (not shown here), the heating of the air due to the sensible heat supply is about  $175\text{Wm}^{-2}$ ; that due to the cloud microphysical processes varies roughly in accord with  $-Hv \times TPRD(Qv)$  ( $Hv$ , latent heat of vaporization); its maximum is about  $450\text{Wm}^{-2}$  at  $t = 67\text{min}$  and  $140\text{min}$ ; the minimum is about  $-50\text{Wm}^{-2}$  at  $t = 93\text{min}$ .

The precipitation efficiency defined as

$$PRCP.EF(t_1, t_2) = \frac{TPR(t_1, t_2)}{\int_{t_1}^{t_2} INFLUX dt}$$

is about 0.3 for  $(t_1, t_2) = (0\text{min}, 213\text{min})$  and 0.45 for  $(t_1, t_2) = (120\text{min}, 213\text{min})$ .

#### b) Individual fields at various stages of the cloud

Figures C-3-9, C-3-10 and C-3-11 show the cross sections of various fields at the developing to mature stage ( $t = 60\text{min}$ ) of the first cloud, the mature to decaying stage ( $t = 80\text{min}$ ) and the decayed stage of the first cloud and the formative stage of the newly excited cloud ( $t = 120\text{min}$ ). Radar reflectivity is computed by use of Eq. 54 in Murakami (1990). The strong cold outflow at the decayed stage shown in Fig. C-3-11 b) is attributed to cooling by sublimation from snow. Figures C-3-9 k), l), C-3-10 k), l) and C-3-11 j) show the intercept parameter of the inverse exponential size distribution function,  $Nos$  and  $Nog$ . It is noticed that  $Nos$  and  $Nog$  are not constant but increase as the cloud evolves from the developing to the decaying stage.  $Nos$  at the upper and flanking parts tends to be large, suggesting the existence of a large number of small snow particles. The location of the maximum of  $Qs$  near the surface does not coincide with that of the maximum of  $Nos$  at  $t = 80\text{min}$ , while that of  $Qs$  coincides with that of  $Nos$  at  $t = 120\text{min}$ .

Figure C-3-12 shows the accumulated precipitation patterns of snow and graupel at 213min. Precipitation of graupel is more concentrated than that of snow. Precipitation

around  $(x, y) = (4\text{km}, 0\text{km})$  is brought about by the second and third groups of clouds.

c) Cloud microphysical processes and precipitation formation

Figure C-3-13b shows the horizontally averaged values of  $Q_c$ ,  $Q_s$ ,  $Q_g$ ,  $N_i$ ,  $N_s$  and  $N_g$  at  $t = 60\text{min}$  as a function of height. Figures C-3-13 a, c and d show the dominant processes which are horizontally averaged values as a function of height at  $t = 60\text{min}$  relating to the production terms of cloud ice, snow and graupel, respectively. The figures corresponding to Fig. C-3-13 at  $t = 80, 100$  and  $120\text{min}$  are displayed in Fig. C-3-14, C-3-15 and C-3-16, respectively.

Figure C-3-17 shows the dominant mass production terms in forming snow and graupel as a function of time. Figure C-3-18 shows the mass production terms involving cloud ice. Cloud ice (pristine ice crystals) is generated mainly via deposition/sorption nucleation ( $P_{idsn}$ ), and freezing of cloud droplets is  $1/100$  of  $P_{idsn}$ . Cloud ice grows mainly via depositional growth ( $P_{idep}$ ), and finally is turned into snow ( $P_{icns}$ ). Depositional growth of cloud ice ( $P_{idep}$ ) nearly balances the conversion term of cloud ice into snow ( $P_{icns}$ ).

The number generation of snow is via conversion of cloud ice into snow ( $N_{icns}$ ). The number of snow after mature stage decreases via aggregation ( $N_{sag}$ ), precipitation ( $N_{sprc}$ ) and sublimation. The number generation of graupel is via conversion of snow into graupel ( $N_{scng}$ ) which is  $1/100$  of  $N_{icns}$ .

Precipitation formation is summarized as shown in Fig. C-3-19:

- i) At the developing or mature stage (the stage 2-3; Fig. C-3-19a) of the cloud, the water vapor supplied from the warm sea surface condenses to form supercooled cloud water. Cloud ice grows into snow via depositional process. Snow grows via riming and depositional processes. Graupel grows primarily via riming process and secondarily via depositional process.
- ii) At the mature or decaying stage (the stage 3-4; Fig. C-3-19b), cloud water is almost depleted; above the cloud base, depositional growth of ice particles is more dominant than riming growth; the precipitation rate of ice particles is large, and the amount of sublimation below the cloud base is roughly  $1/3 \sim 1/2$  of the amount of deposition above it.
- iii) At the decayed stage (the stage 5; Fig. C-3-19c), cloud water is almost depleted and no graupel particles are found and precipitation of graupel ceases; the amount of snow continues

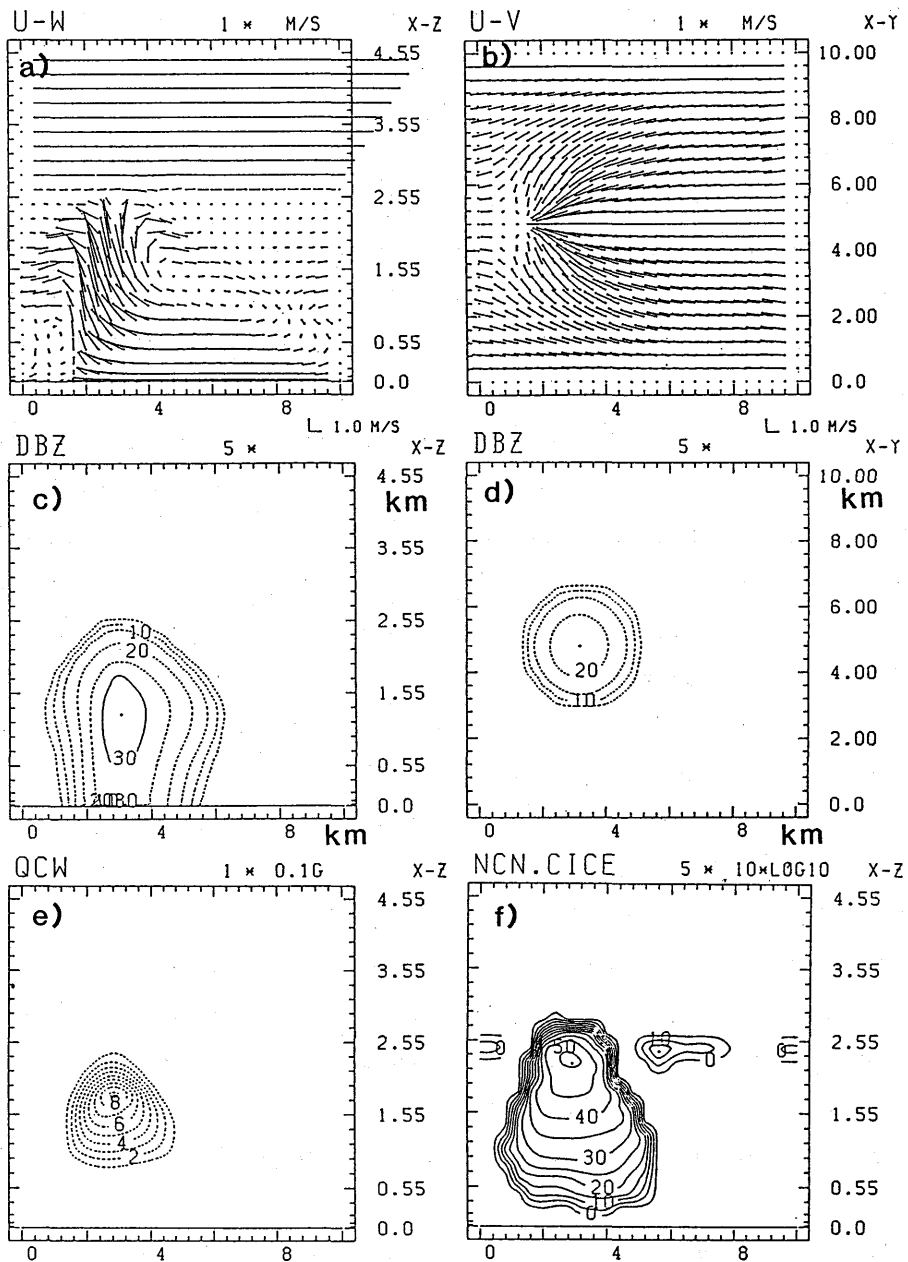


Fig. C-3-9 The cross sections of various fields at  $t = 60$  min (the developing to mature stage of the first cloud) by EXDS1.

- a)  $X$ - $z$  cross section of the  $u$ - $w$  wind vector field at  $y = 4.8$  km.
- b)  $X$ - $y$  cross section of the  $u$ - $v$  wind vector field at  $z = 0.03$  km.
- c)  $X$ - $z$  cross section of the radar reflectivity dBZ at  $y = 4.8$  km with contour intervals of 5 dBZ.
- d)  $X$ - $y$  cross section of the radar reflectivity dBZ at  $z = 2.05$  km with contour intervals of 5 dBZ.
- e)  $X$ - $z$  cross section of  $Q_c$  at  $y = 4.8$  km with contour intervals of 0.1 g/kg.
- f)  $X$ - $z$  cross section of  $10 \times \log_{10}(Ni)$  at  $y = 4.8$  km with contour intervals of 5. The unit of  $Ni$  is  $m^{-3}$ .

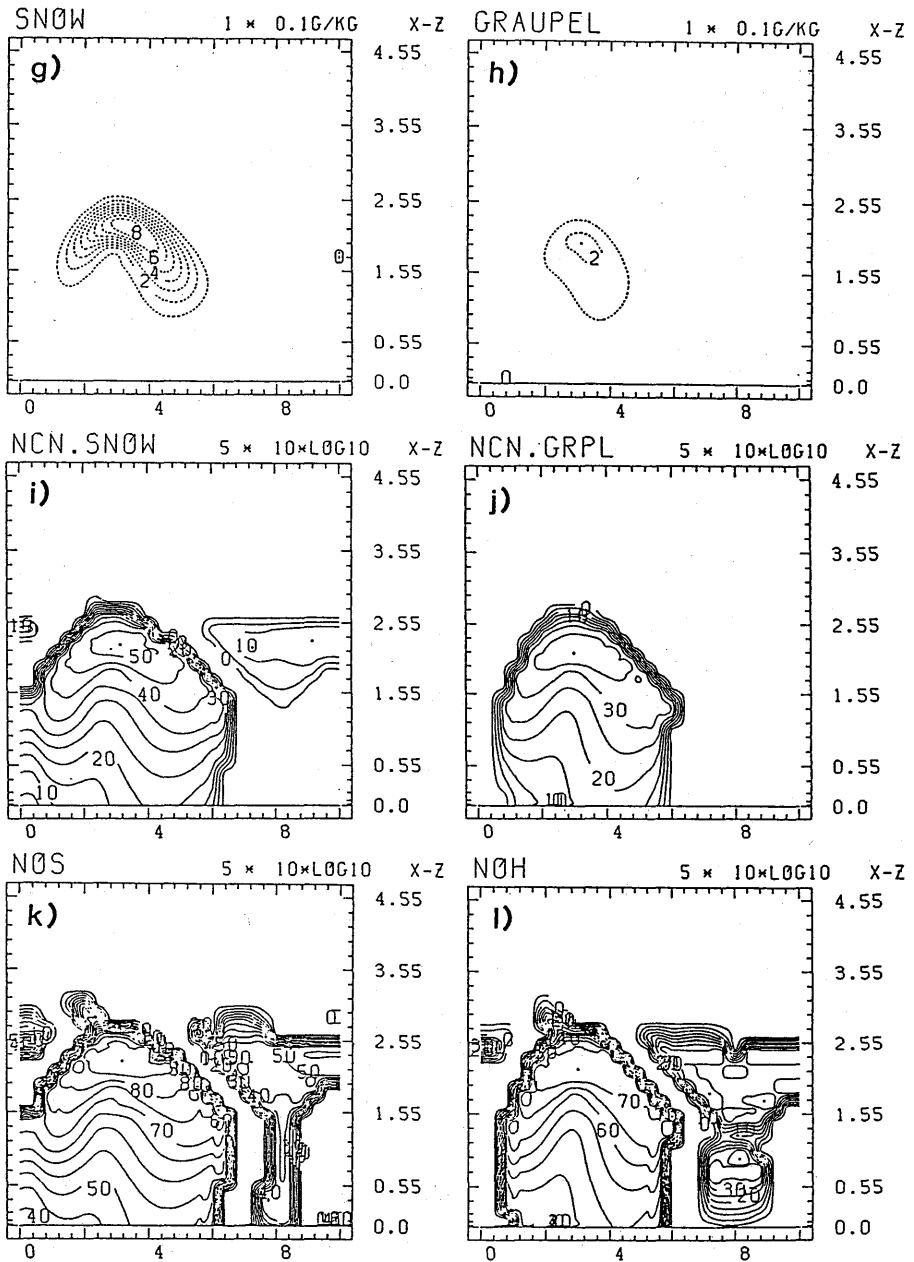


Fig. C-3-9 (Continued.)

- g) The same as e), but for  $Q_s$ .
- h) The same as e), but for  $Q_g$ .
- i) The same as f), but for  $N_s$ .
- j) The same as f), but for  $N_g$ .
- k) X-z cross section of  $10 \times \log_{10}(N_{os})$  at  $y = 4.8$  km with contour intervals of 5. The unit of  $N_{os}$  is  $m^{-4}$ .
- l) The same as k), but for  $N_{og}$ .

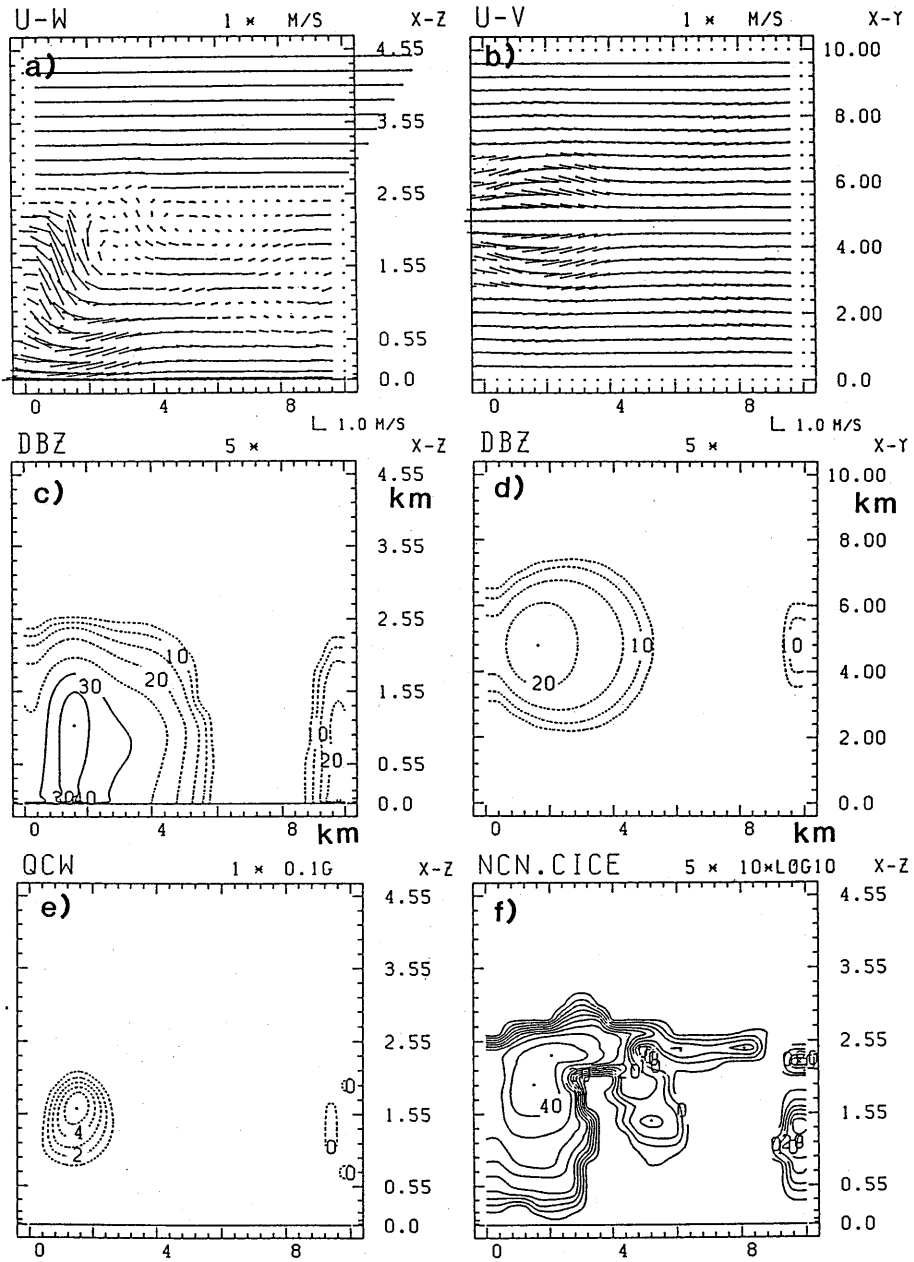


Fig. C-3-10 The same as Fig. C-3-9, but for  $t = 80 \text{ min.}$

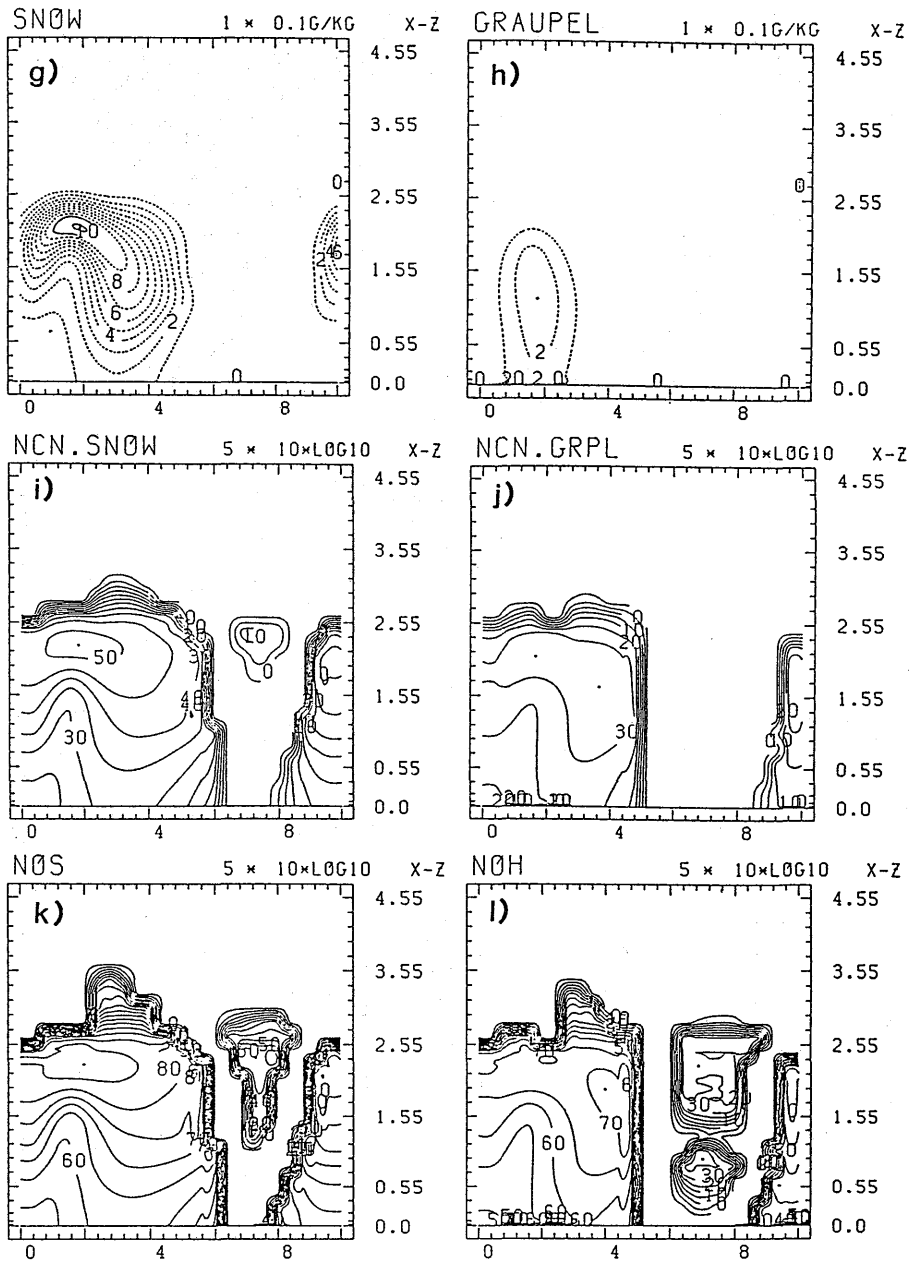


Fig. C-3-10 (Continued.)

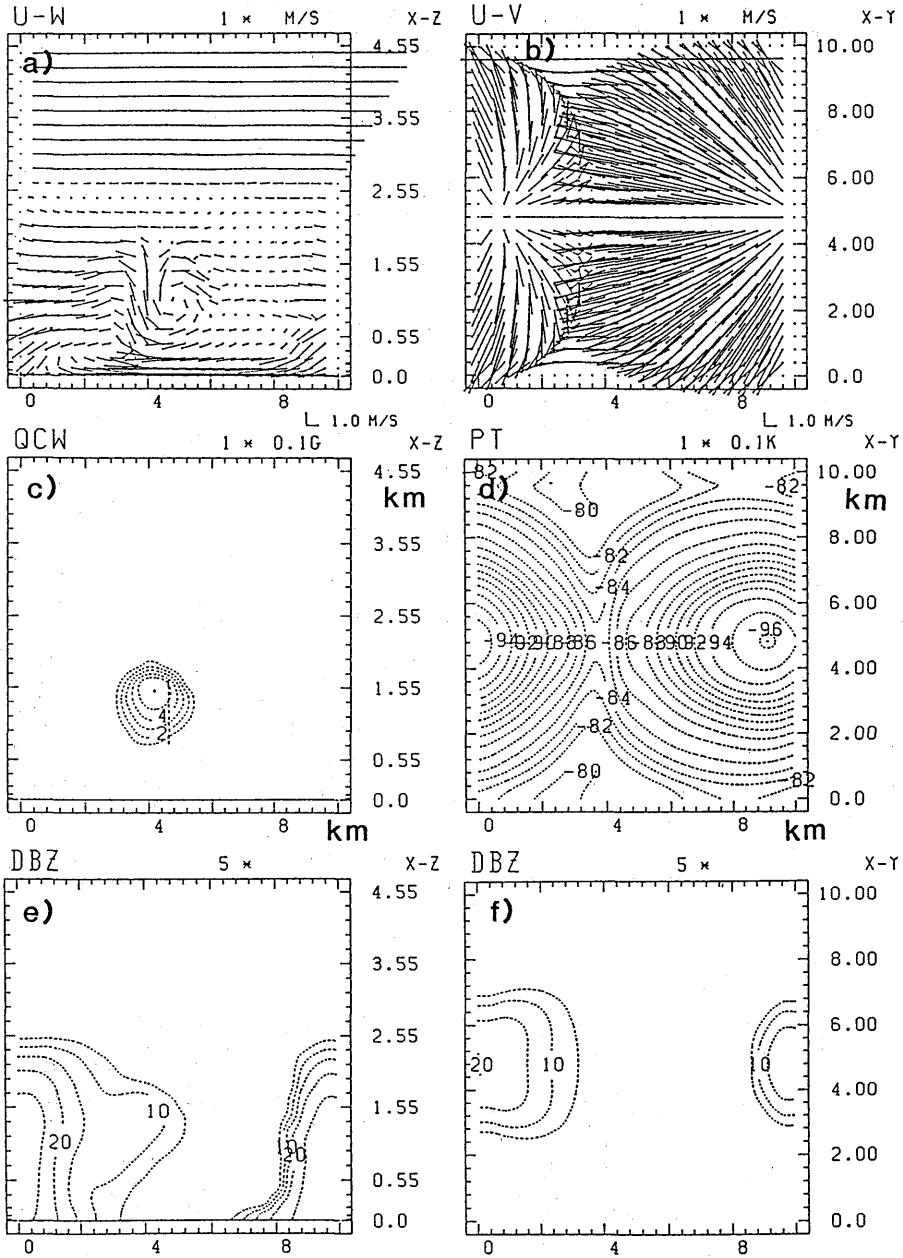


Fig. C-3-11 The cross sections of various fields at  $t = 120$  min (the decayed stage of the first cloud and the formative stage of the newly excited cloud) by EXDS1.

- a) X-z cross section of the  $u-w$  wind vector field at  $y = 4.8$  km.
- b) X-y cross section of the  $u-v$  wind vector field at  $z = 0.03$  km.
- c) X-z cross section of  $Q_c$  at  $y = 4.8$  km with contour intervals of  $0.1$  g/kg.
- d) X-y cross section of the deviation of the potential temperature from its reference field at  $z = 0.03$  km. The unit is  $0.1K$ , with contour intervals of  $0.1K$ .
- e) X-z cross section of the radar reflectivity dBZ at  $y = 4.8$  km with contour intervals of  $5$  dBZ.
- f) X-y cross section of the radar reflectivity dBZ at  $z = 2.05$  with contour intervals of  $5$  dBZ.

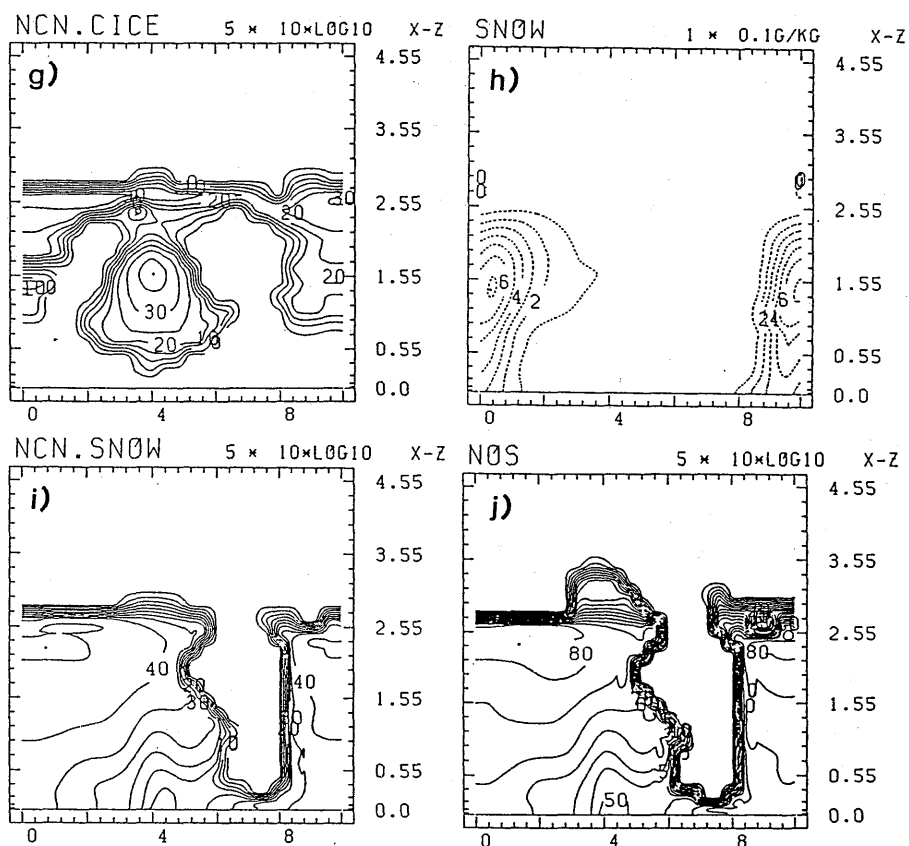


Fig. C-3-11 (Continued.)

- g) X-z cross section of  $10 \times \log_{10}(N_i)$  at  $y = 4.8$  km with contour intervals of 5. The unit of  $N_i$  is  $m^{-3}$ .
- h) The same as c), but for  $Q_s$ .
- i) The same as g), but for  $N_s$ .
- j) X-z cross section of  $10 \times \log_{10}(N_{os})$  at  $y = 4.8$  km with contour intervals of 5. The unit of  $N_{os}$  is  $m^{-4}$ .

to decrease due to the precipitation and sublimation below the cloud base; the amount of sublimation below the cloud base is greater than the amount of deposition above it. The number of snow particles decreases via aggregation, precipitation and sublimation.

### C-3-6. Sensitivity experiments

#### a) Sensitivity to various ice nucleation terms

Results are summarized in Table C-3-3. The figures of EXN1, EXDS2, EXHM, EXBK1, EXBK2, EXS1 corresponding to Fig. C-3-7 of EXDS1 are shown in Figs. C-3-20, C-3-24, C-3-

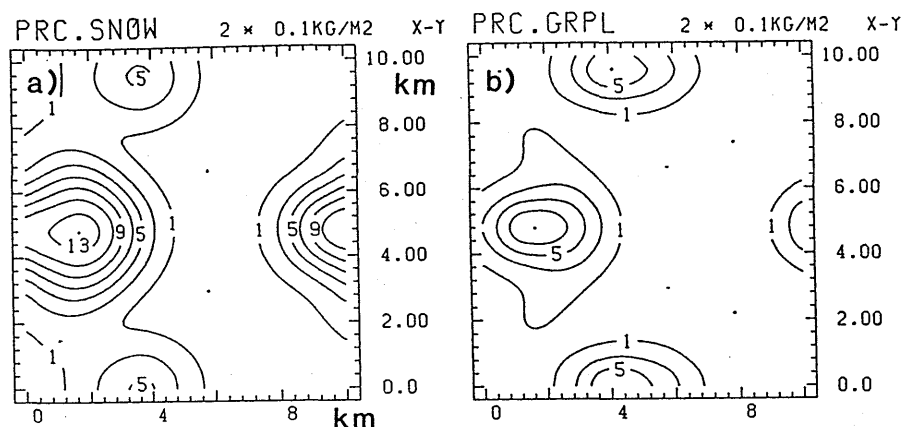


Fig. C-3-12 a) Total accumulated precipitation field of snow at  $t = 213$  min by EXDS1. The unit is  $0.1 \text{ kg/m}^2$ , and the contour interval is  $0.2 \text{ kg/m}^2$ .  
 b) The same as a) but for graupel.

27, C-3-30, C-3-31, C-3-32, respectively. The figures of EXN1, EXDS2, EXHM corresponding to Figs. C-3-17 and C-3-18 of EXDS1 are shown in Figs. C-3-21, C-3-22, C-3-25, C-3-26, C-3-28, C-3-29, respectively.

a-1) EXN1

As shown in Table C-3-3 and Fig. C-3-23, number concentration of ice particles is 1-order smaller than that of EXDS1. The maximum value of number concentration of ice particles is  $1/4$  of the observed counterpart. The dominant generation term of cloud ice is not deposition/sorption nucleation (Pidsn, Nidsn) but freezing of cloud droplets (Pifzc, Nifzc) as shown in Fig. C-3-21b and C-3-22.

It is an interesting discovery that the conventional term of deposition/sorption nucleation by Fletcher is incapable of explaining the high number concentration of ice crystals in the observed cloud, while freezing of cloud droplets can produce fairly large number concentration of ice particles which is still smaller than the observed one but appears to be in a tolerable range.

In Fig. C-3-23,  $x$ - $z$  cross sections of number concentrations of snow and graupel and radar reflectivity at  $t = 80$ min in EXN1 are shown. The maximum of radar reflectivity in EXN1 is about 40dBZ, which is larger by 10dBZ than the observed value.  $Z$  (see Eq. 54 in Murakami, 1990) is approximated as

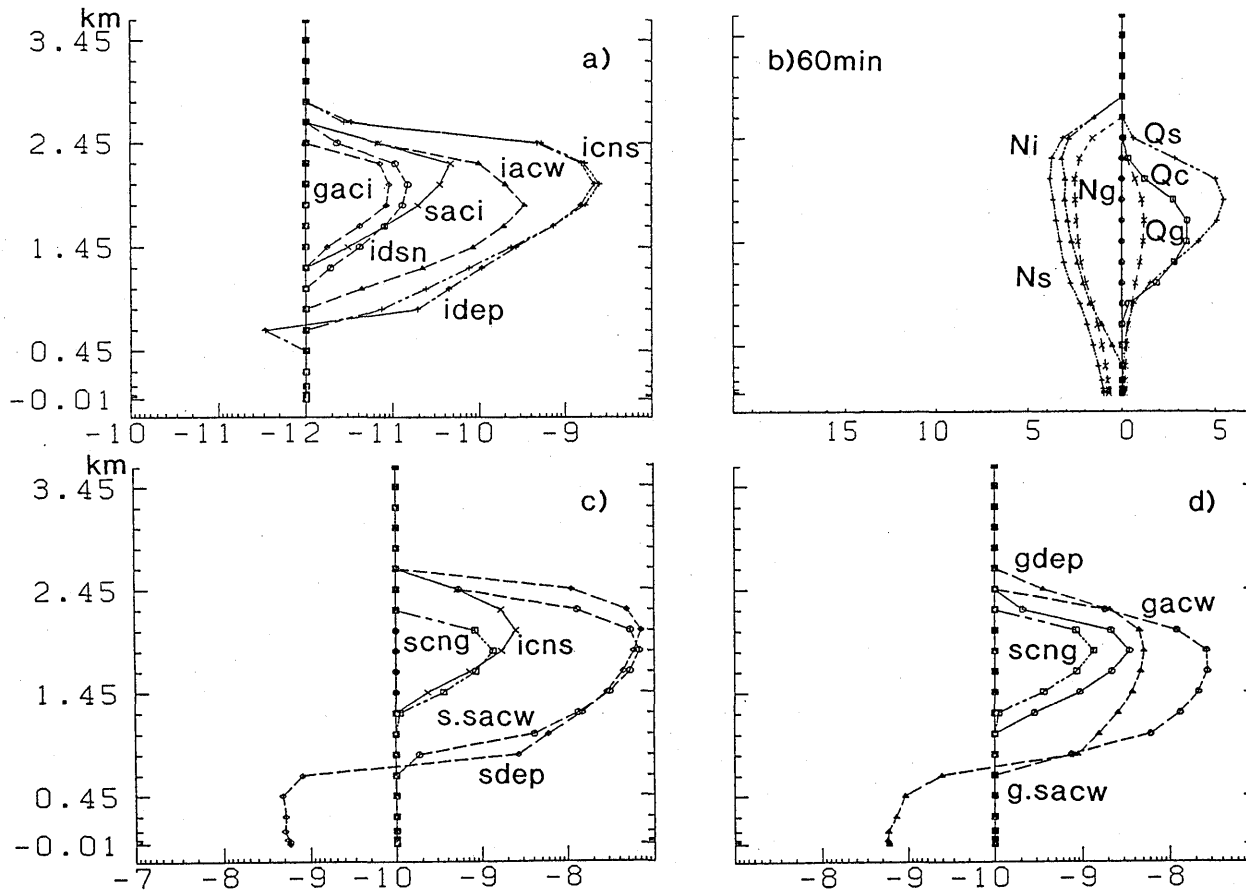


Fig. C-3-13 a) The dominant cloud microphysical processes ( $P_{xqqq}$ ; unit =  $s^{-1}$ ) which are horizontally averaged values as a function of height at  $t = 60$  min relating to cloud ice by EXDS1. For  $P_{xqqq} > p_0 = 10^{-12} s^{-1}$ ,  $\log_{10}(P_{xqqq})$  is plotted in the right side. For  $P_{xqqq} < -p_0$ ,  $\log_{10}(-P_{xqqq})$  is plotted in the left side. b) The horizontally averaged values of  $Q_c$ ,  $Q_s$ ,  $Q_g$  (right side: unit  $10^{-5}$  kg/kg),  $N_i$ ,  $N_s$  and  $N_g$  (left side: unit  $m^{-3}$ , expressed in  $\log_{10}(Nx)$ ) at  $t = 60$  min as a function of height by EXDS1. c) The same as a) but for snow and  $p_0 = 10^{-10} s^{-1}$ . d) The same as a) but for graupel and  $p_0 = 10^{-10} s^{-1}$ .

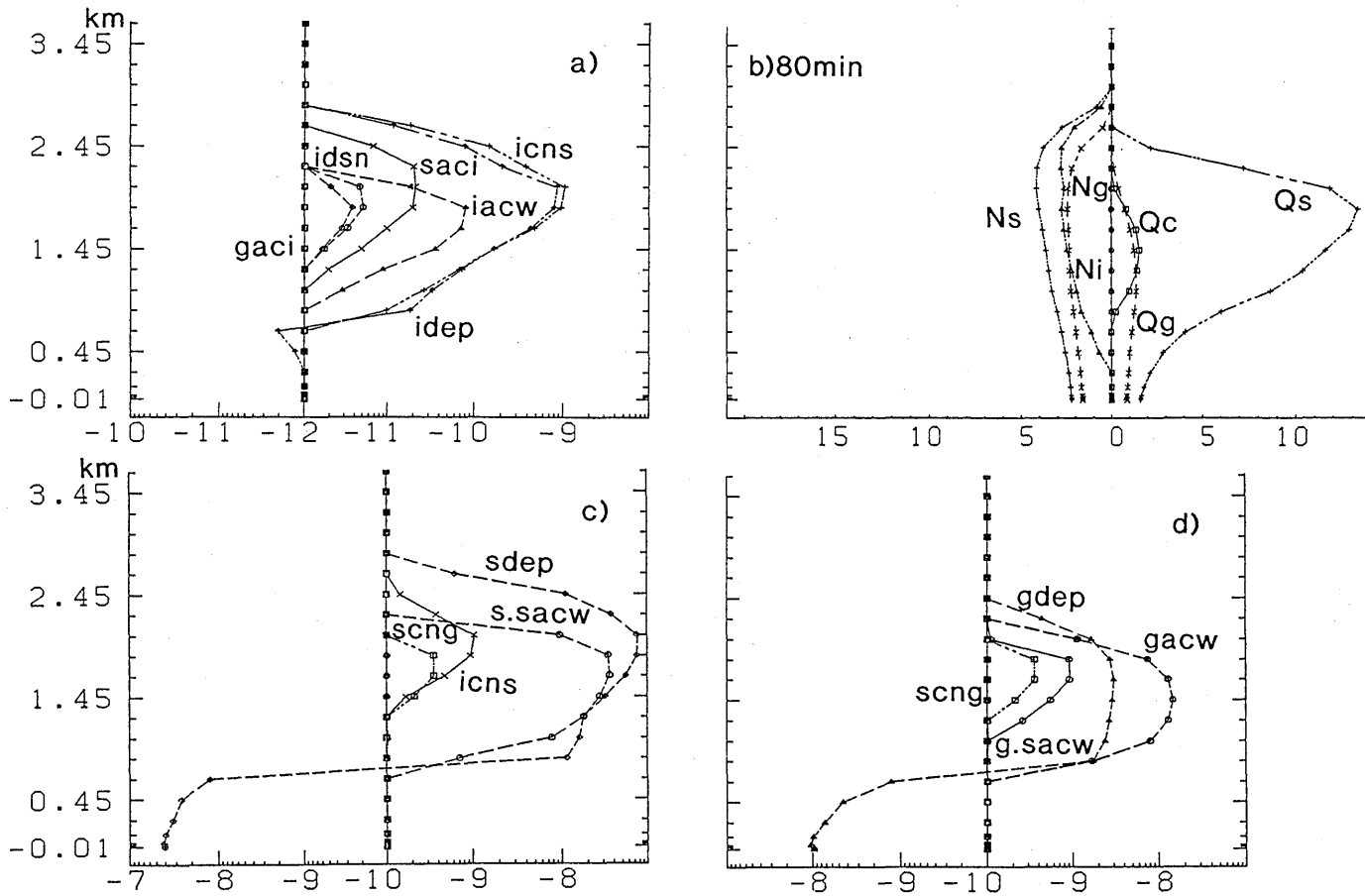


Fig. C-3-14 The same as Fig. C-3-13 but for  $t = 80$  min.

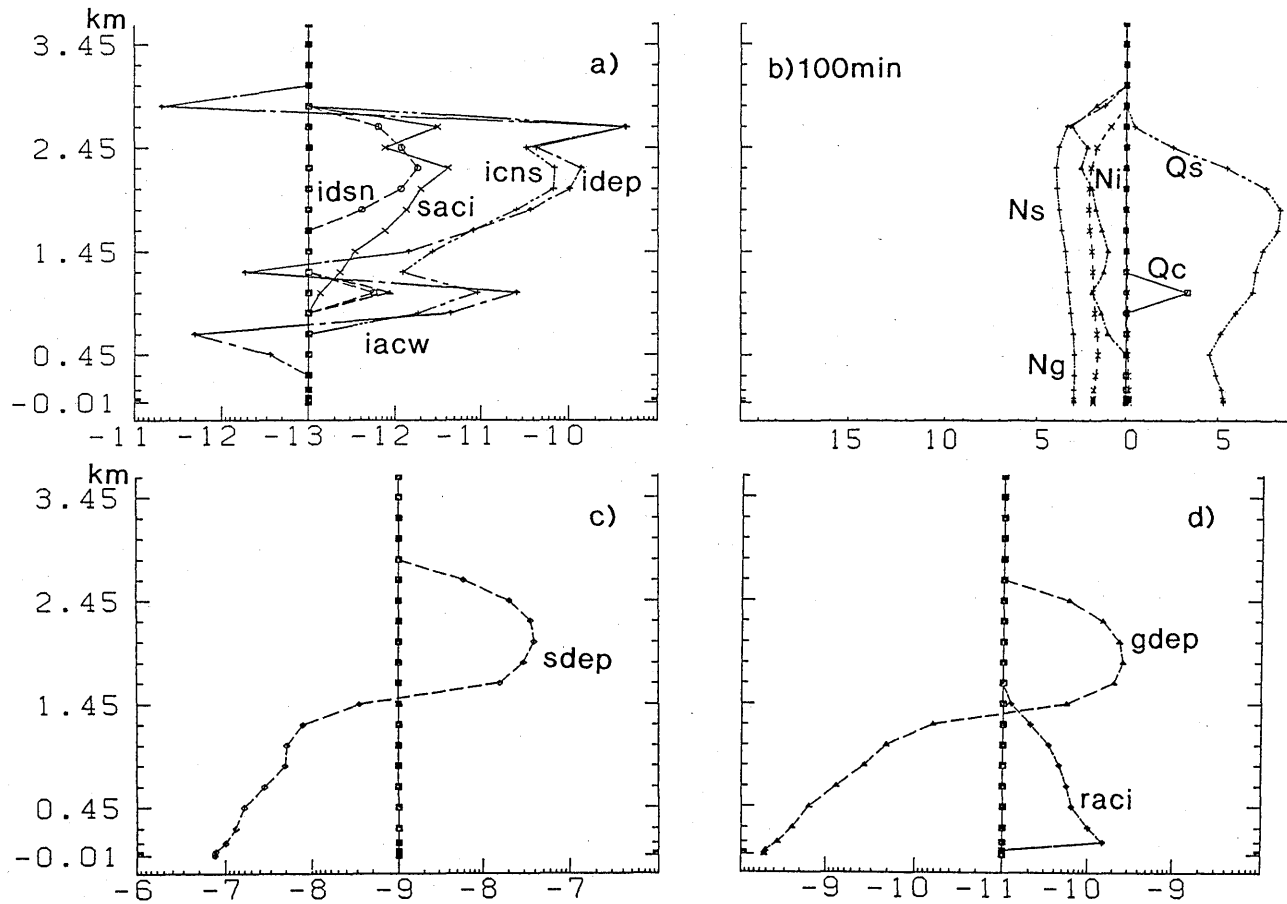


Fig. C-3-15 The same as Fig. C-3-13 but for  $t = 100$  min.  $p_0 = 10^{-13}, 10^{-9}, 10^{-11} s^{-1}$  are used for a), c) and d), respectively.

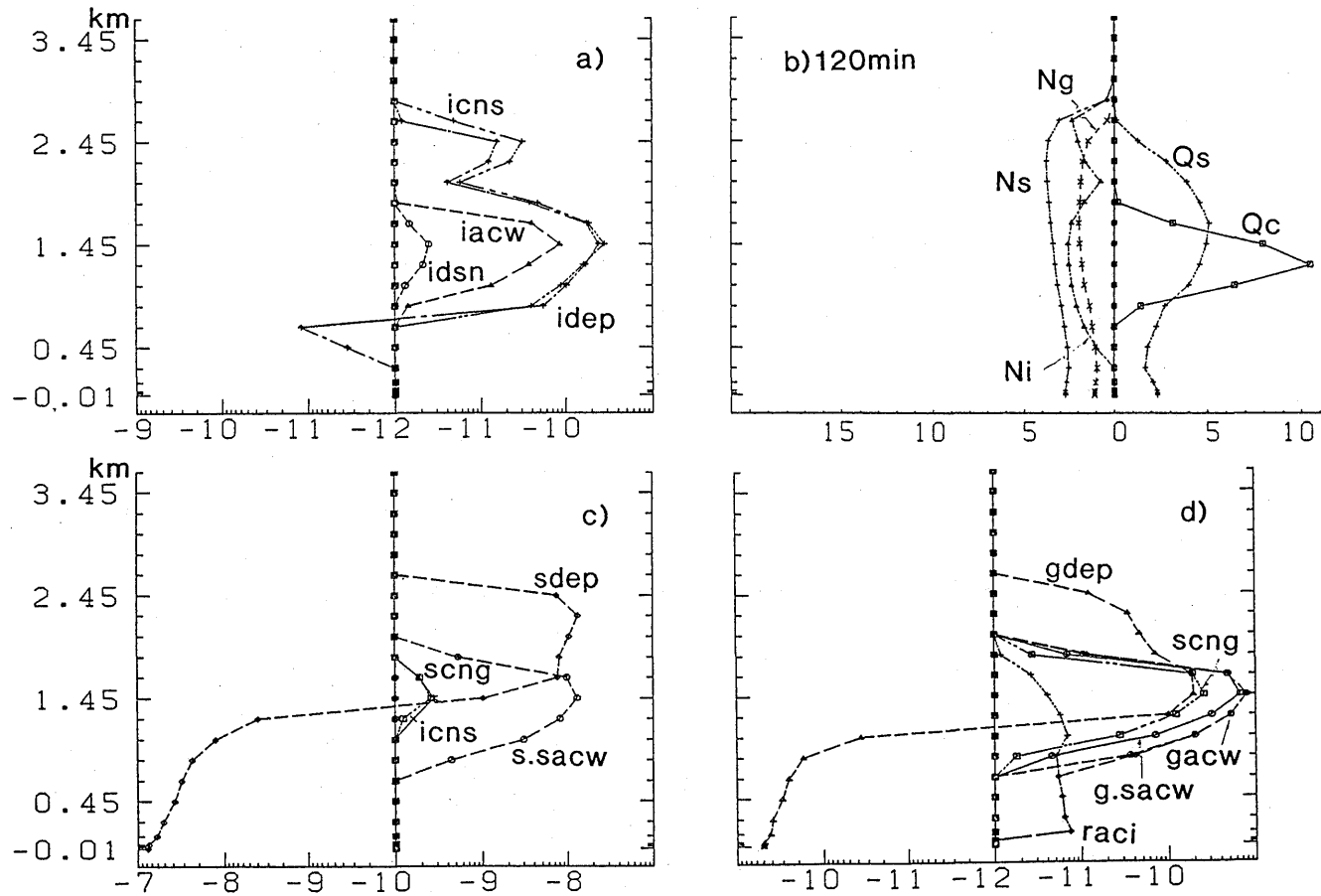


Fig. C-3-16 The same as Fig. C-3-13 but for  $t = 120$  min.  $p_0 = 10^{-12}, 10^{-10}, 10^{-12} \text{ s}^{-1}$  are used for a), c) and d), respectively.

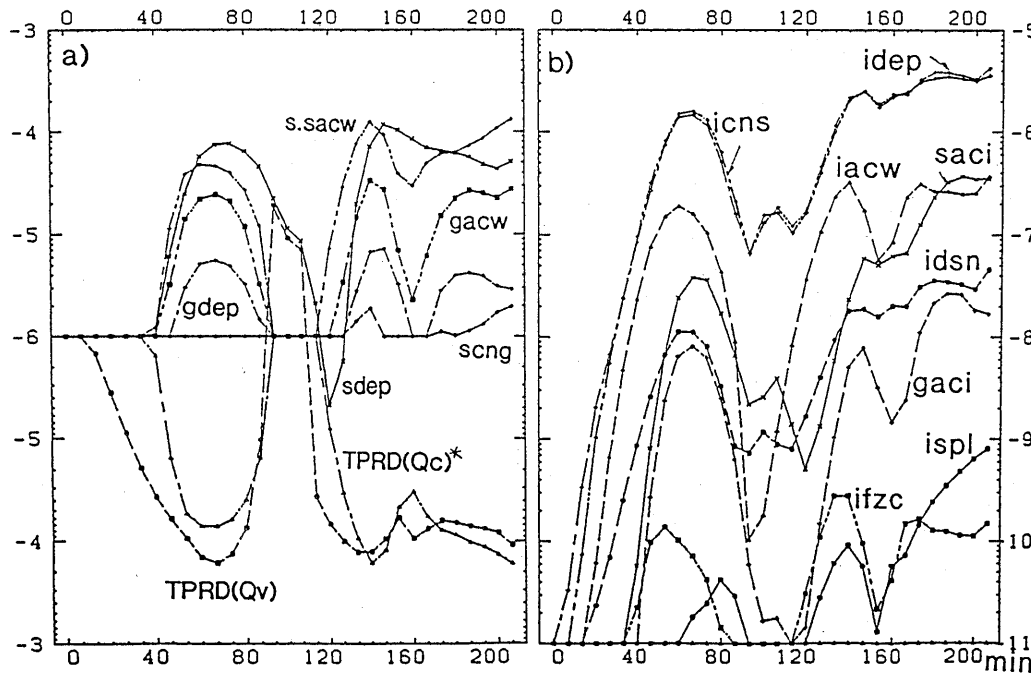


Fig. C-3-17 a) The dominant mass production terms ( $TPxqqq: \text{kgm}^{-2}\text{s}^{-1}$ ) in forming snow and graupel as a function of time by EXDS1.  $TPRD(Qc)* \equiv TPRD(Qc) - TPccnd$ . For positive value  $TPxqqq > 10^{-6}$ ,  $\log_{10}(TPxqqq)$  is drawn in the upper part of the figure. For negative values  $TPxqqq < -10^{-6}$ ,  $-\log_{10}(-TPxqqq)$  is drawn in the lower part of the figure. For  $-10^{-6} < TPxqqq < 10^{-6}$ , values are plotted on the horizontal line indicated by  $-6$  on the ordinate.  
 b) The dominant mass production terms ( $TPxqqq: \text{kgm}^{-2}\text{s}^{-1}$ ; expressed in  $\log_{10}(TPxqqq)$ ) involving cloud ice as a function of time by EXDS1.

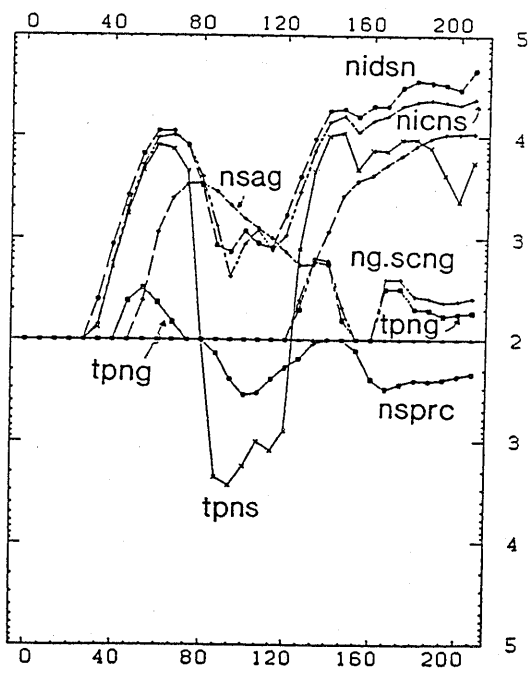


Fig. C-3-18 The dominant number production terms ( $TNxqqq: \text{m}^{-2}\text{s}^{-1}$ ) in forming cloud ice, snow and graupel as a function of time by EXDS1. For positive values  $TNxqqq > p_0 = 10^2$ ,  $\log_{10}(TNxqqq)$  is drawn in the upper part of the figure. For negative values  $TNxqqq < -p_0$ ,  $-\log_{10}(-TNxqqq)$  is drawn in the lower part of the figure. For  $-p_0 < TNxqqq < p_0$ , values are plotted on the horizontal line indicated by  $2$  on the ordinate.

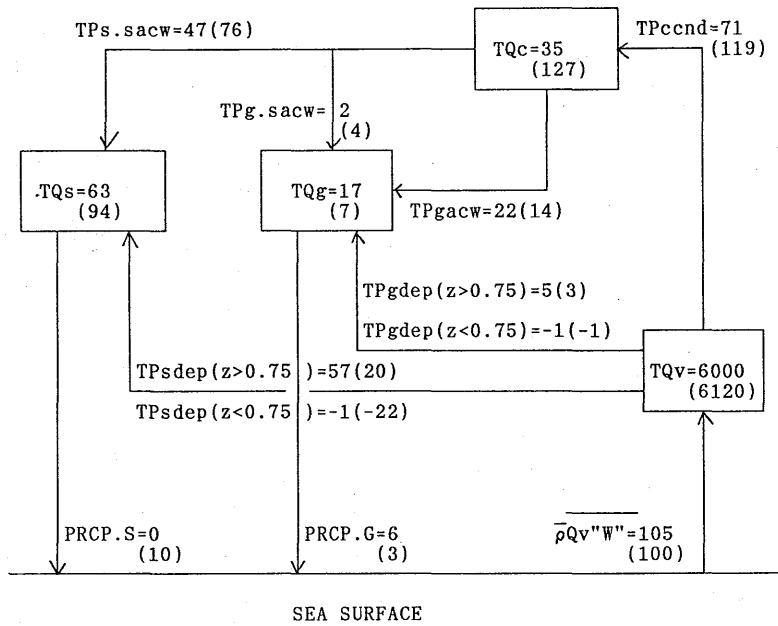


Fig. C-3-19a Dominant mass production terms in precipitation formation by EXDS1 at  $t = 60$  min and  $t = 133$  min (denoted by bracket)(a developing or mature stage). The unit for  $TQv$ ,  $TQc$ ,  $TQs$  and  $TQg$  is  $g/m^2$ , and the unit for  $TPccond$ ,  $TPs.sacw$ .... $PRCP.s$  is  $10^{-3} g/m^2/s$ .

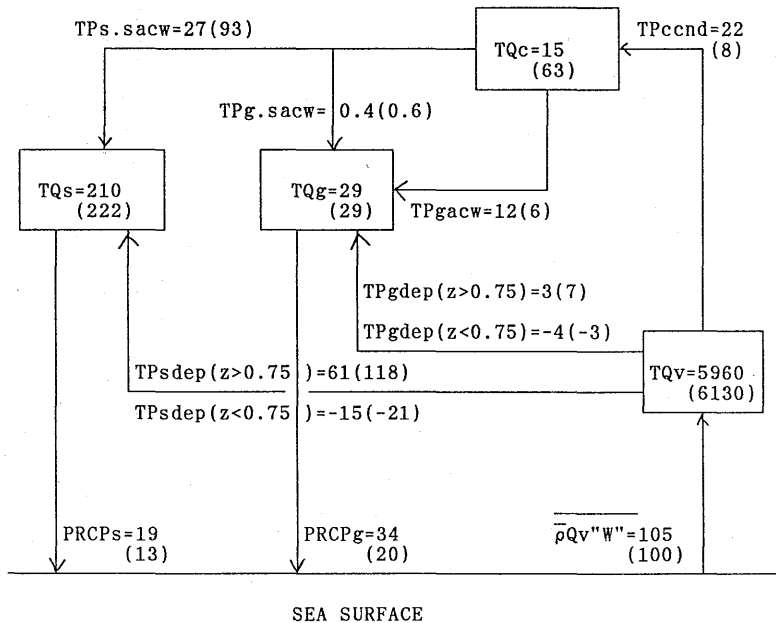


Fig. C-3-19b The same as Fig. C-3-19a, but for  $t = 80$  min and  $t = 147$  min (denoted by bracket)(a mature or decaying stage).

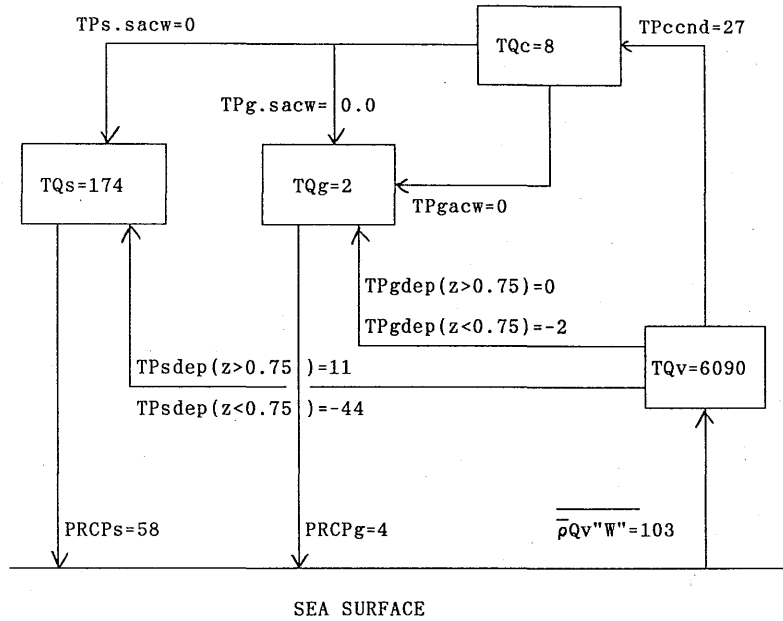


Fig. C-3-19c The same as Fig. C-3-19a, but for  $t = 100$  min (a decayed stage).

$$Z = \sum D^6 \simeq N \left( \frac{\rho Q}{N} \right)^2 \propto N^{-1}$$

Therefore, this difference is partly attributable to the low ice nucleation rates and resultant low number concentrations of cloud ice and snow in EXN1.

In EXN1,  $Q_c$  exceeds the threshold value ( $Q_{co} = 10^{-3}$ ) for the conversion of cloud water into rain which is given as

$$P_{ccnr} = 10^{-3}(Q_c - Q_{co}),$$

and rain is generated. However, the amount of rain is small; the generation term of graupel via collision between ice particles and rain ( $P_{iacr}$ ,  $P_{g.sacr}$ ) and freezing of rain ( $P_{gfzr}$ ) is smaller than  $P_{scng}$  (at most 1/4 of  $P_{scng}$ ); the most dominant term of graupel generation is still  $P_{scng}$ ; the growth of snow and graupel by accretion of rain is still less than  $P_{sacw}$  and  $P_{gacw}$ . Therefore, rain does not play a dominant role in precipitation formation.

The differences between EXN1 and EXDS1 are summarized as follows: 1) The maximum of  $N_i$  and  $N_s$  is  $3 \times 10^4 \text{m}^{-3}$ , 1-order smaller than those by EXDS1. 2) In EXN1, freezing of

Table C-3-3 Results of the sensitivity experiments (Table C-3-1) to ice nucleation rates. The suffix "max" to  $Nx$  means the maximum value in the domain during  $0 < t < 213$  min. In the row of  $TQc$ .max, the time when  $TQc$  takes its maximum is shown in the bracket, which reflects the onset time of glaciation. In the columns of EXS1 and EXS2, values left to the arrow symbol denote the maxima during  $0 < t < 120$ min, and values right to the arrow symbol denote the maxima during  $120 < t < 213$ min.

	EXN1	EXDS1 ds × 10 <sup>3</sup>	EXDS2 ds × 10 <sup>6</sup>	EXHM -3 ~ -30	EXFZ1 Bigg × 10 <sup>2</sup>	EXFZ2 Bigg × 10 <sup>5</sup>	EXBK1 A=10	EXBK2 A=100	EXS1 0.95-1.75	EXS2 1.75-3.15
$Ni$ .max(m <sup>-3</sup> )	3 × 10 <sup>4</sup>	3 × 10 <sup>5</sup>	10 <sup>7</sup>	2 × 10 <sup>5</sup>	4 × 10 <sup>5</sup>	3 × 10 <sup>8</sup>	10 <sup>5</sup>	3 × 10 <sup>7</sup>	10 <sup>6</sup> → 3 × 10 <sup>4</sup>	4 × 10 <sup>5</sup> → 2 × 10 <sup>4</sup>
$TNi$ .max(m <sup>-2</sup> )	8 × 10 <sup>5</sup>	10 <sup>7</sup>	6 × 10 <sup>8</sup>	8 × 10 <sup>6</sup>	8 × 10 <sup>5</sup>	4 × 10 <sup>7</sup>	2 × 10 <sup>6</sup>	6 × 10 <sup>9</sup>	5 × 10 <sup>7</sup> → 10 <sup>6</sup>	10 <sup>7</sup> → 3 × 10 <sup>5</sup>
$TQi$ .max(0.1kg/m <sup>2</sup> )	6 × 10 <sup>-5</sup>	6 × 10 <sup>-4</sup>	3 × 10 <sup>-2</sup>	5 × 10 <sup>-4</sup>	4 × 10 <sup>-4</sup>	2 × 10 <sup>-5</sup>	10 <sup>-4</sup>	8 × 10 <sup>-2</sup>	10 <sup>-3</sup> → 5 × 10 <sup>-5</sup>	4 × 10 <sup>-4</sup> → 7 × 10 <sup>-5</sup>
$Ns$ .max(m <sup>-3</sup> )	2 × 10 <sup>4</sup>	2 × 10 <sup>5</sup>	10 <sup>6</sup>	2 × 10 <sup>5</sup>	10 <sup>5</sup>	10 <sup>6</sup>	2 × 10 <sup>5</sup>	10 <sup>6</sup>	10 <sup>6</sup> → 3 × 10 <sup>4</sup>	6 × 10 <sup>5</sup> → 10 <sup>4</sup>
$TNs$ .max(m <sup>-2</sup> )	3 × 10 <sup>6</sup>	3 × 10 <sup>7</sup>	3 × 10 <sup>8</sup>	5 × 10 <sup>7</sup>	10 <sup>7</sup>	10 <sup>8</sup>	8 × 10 <sup>6</sup>	2 × 10 <sup>8</sup>	10 <sup>8</sup> → 2 × 10 <sup>6</sup>	4 × 10 <sup>7</sup> → 3 × 10 <sup>6</sup>
$Ng$ .max(m <sup>-3</sup> )	3 × 10 <sup>3</sup>	10 <sup>4</sup>	10 <sup>4</sup>	2 × 10 <sup>4</sup>	10 <sup>4</sup>	3 × 10 <sup>4</sup>	2 × 10 <sup>3</sup>	5 × 10 <sup>4</sup>	10 <sup>4</sup> → 3 × 10 <sup>3</sup>	2 × 10 <sup>4</sup> → 10 <sup>3</sup>
$TNg$ .max(m <sup>-2</sup> )	2 × 10 <sup>5</sup>	7 × 10 <sup>7</sup>	10 <sup>6</sup>	2 × 10 <sup>6</sup>	8 × 10 <sup>5</sup>	10 <sup>6</sup>	10 <sup>5</sup>	2 × 10 <sup>6</sup>	6 × 10 <sup>5</sup> → 10 <sup>5</sup>	6 × 10 <sup>6</sup> → 10 <sup>5</sup>
$TQc$ .max	1.2	0.4	0.1	0.8	0.5	0.1	1.1	1.1	< 0.1	0.3
(0.1kg/m <sup>2</sup> )	(67min)	(53min)	(80min)	(60min)	(53min)	(53min)	(67min)	(67min)	(47min)	(53min)
	1.5	1.3		1.6	1.3		2.0	1.4	2.7	1.5
	(147min)	(133min)		(140min)	(140min)		(147min)	(140min)	(113min)	(127min)
at t=213min										
$TQs$ (0.1kg/m <sup>2</sup> )	1.2	3.4	4.6	3.7	3.2	4.2	1.7	4.8	2.1	2.0
$TPRs$ (0.1kg/m <sup>2</sup> )	2.6	2.6	1.2	1.6	2.8	1.8	1.8	0.5	2.0	2.8
$TQs + TPRs$ (0.1kg/m <sup>2</sup> )	3.8	6.0	5.8	5.3	6.0	6.0	3.5	5.3	4.1	2.8
$TQg$ (0.1kg/m <sup>2</sup> )	0.9	0.2	<0.1	0.2	0.3	0.2	0.0	0.2	0.6	0.1
$TPRg$ (0.1kg/m <sup>2</sup> )	1.6	1.2	0.1	2.1	1.3	0.5	1.2	1.0	2.4	1.3
$TQg + TPRg$ (0.1kg/m <sup>2</sup> )	2.5	1.4	0.1	2.3	1.6	0.7	1.2	1.2	3.0	1.4
$TPRs + TPRg$ (0.1kg/m <sup>2</sup> )	4.2	3.9	1.2	3.7	4.1	2.3	3.0	1.5	4.4	4.1
$'' + TQs + TQg$ (0.1kg/m <sup>2</sup> )	6.3	7.4	5.9	7.6	7.6	6.7	4.7	6.5	7.1	6.2

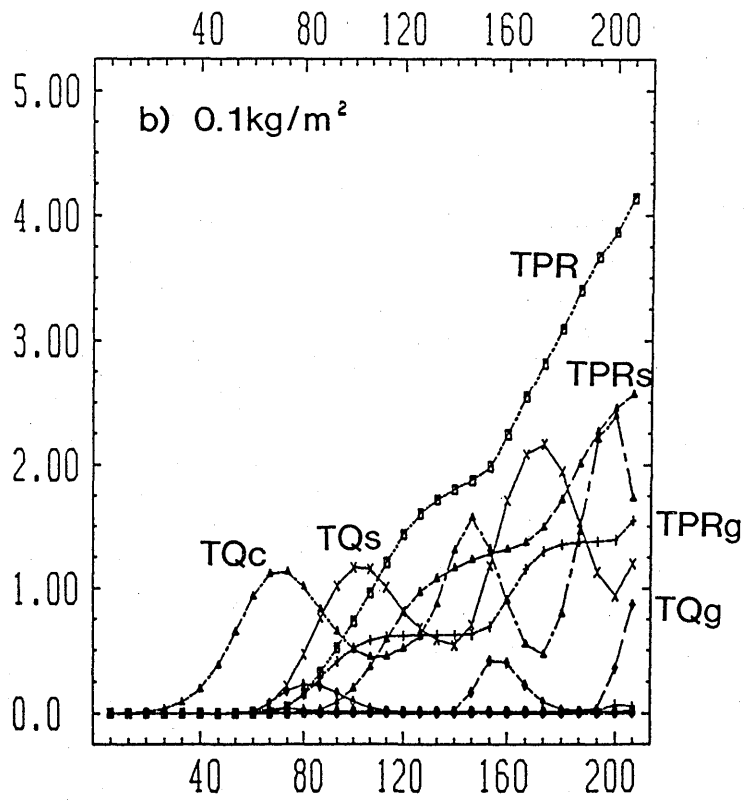
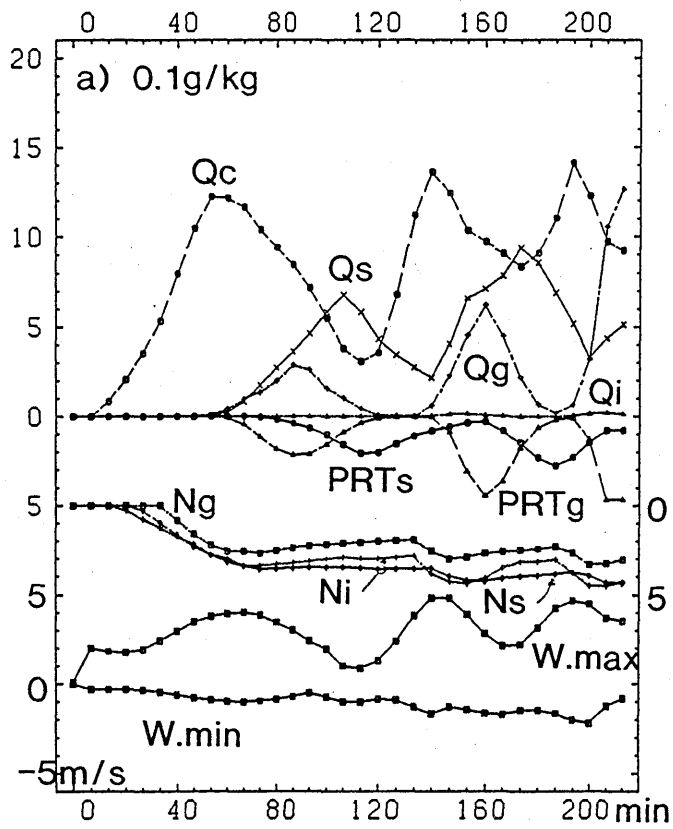


Fig. C-3-20 The same as Fig. C-3-7 but for EXN1.

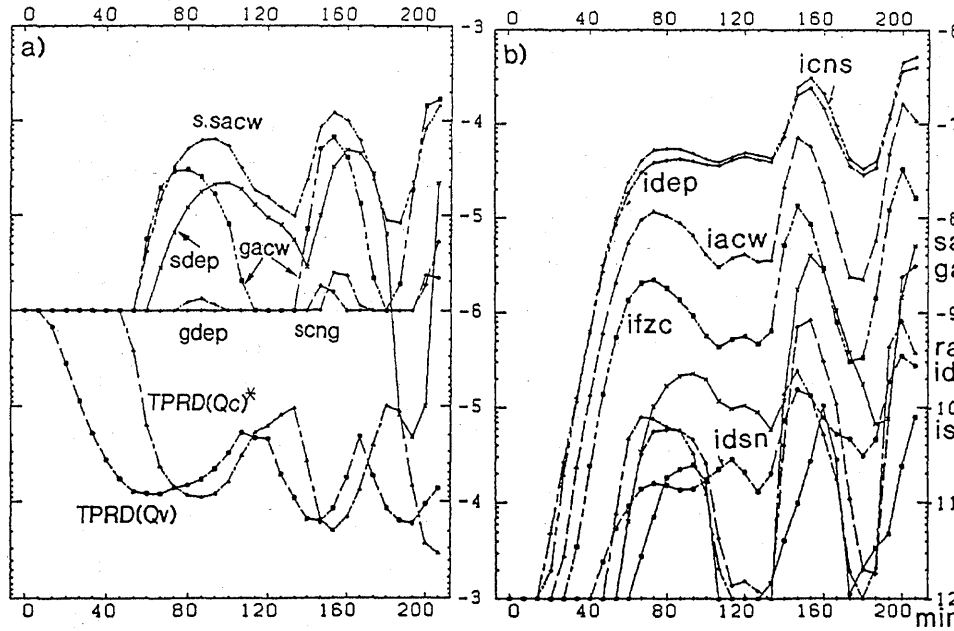


Fig. C-3-21 The same as Fig. C-3-17 but for EXN1.

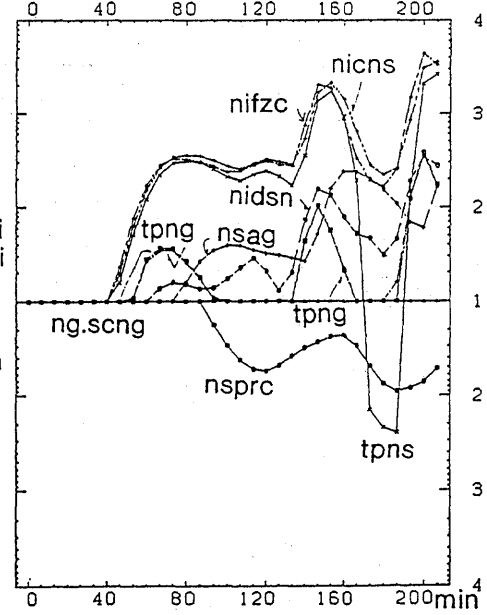


Fig. C-3-22 The same as Fig. C-3-18 but for EXN1 and  $p_0 = 10$ .

cloud droplets ( $P_{ifzc}$ ) is the dominant generation term of cloud ice which is 10 times larger than deposition/sorption nucleation ( $P_{idsn}$ ) but 1/10 of enhanced  $P_{idsn}$  in EXDS1. 3)  $TQ_c$  by EXN1 is larger than EXDS1 and  $TQ_s$  is by a factor of 0.3 ~ 0.5 smaller than that of EXDS1. 4) Glaciation in EXN1 occurs 13min later than EXDS1. As for 3), a qualitatively similar result was obtained by Rutledge and Hobbs (1984).

a-2) *EXDS2*

The differences between EXDS2 and EXDS1 are as follows: 1)  $TQ_c$  by EXDS2 is almost zero, much smaller than EXDS1. 2) The maxima of  $N_i$  and  $N_s$  are  $10^7 m^{-3}$  and  $10^6 m^{-3}$ , respectively, much larger than those by EXDS1. 3) The cloud in EXDS2 is glaciated from the beginning of time, and main precipitation formation is depositional growth of cloud ice and snow rather than riming process. 4) Little precipitation occurs because of the small fall velocity of small snow particles.

a-3) *EXHM*

The differences between EXHM and EXDS1 are as follows: 1)  $TQ_c$  by EXHM is larger than EXDS1, although the maximum values of  $N_i$  and  $N_s$  are nearly the same as those by EXDS1. 2) The cloud in EXHM is glaciated 13min later than EXDS1, similar to EXN1. 3) The precipitation amount of graupel is much larger than that of EXDS1, while that of snow is much smaller than that of EXDS1. These characteristics are attributable to the timing of Hallet-Mossop rime-splinter production of ice nuclei. The number of ice crystals are almost the same as EXN1 until cloud water accumulates in air and riming occurs. Therefore, the beginning of glaciation is almost the same as EXN1. However, once riming takes place, the number of cloud ice particles rapidly increases, resulting in sharp glaciation.

a-4) *EXFZ1 and EXFZ2*

As shown in Table C-3-3, the results of EXFZ1 are similar to those of EXDS1, and those of EXFZ2 are between those of EXFZ1 and EXDS2.

a-5) *EXBK1 and EXBK2*

The characteristic features of EXBK1 are as follows: 1) During  $0 < t < 80$ min when production and growth of graupel and snow are small, the results of EXBK1 are similar to EXN1. The beginning of glaciation is almost the same as EXN1. 2)  $TQ_s$  is larger than that

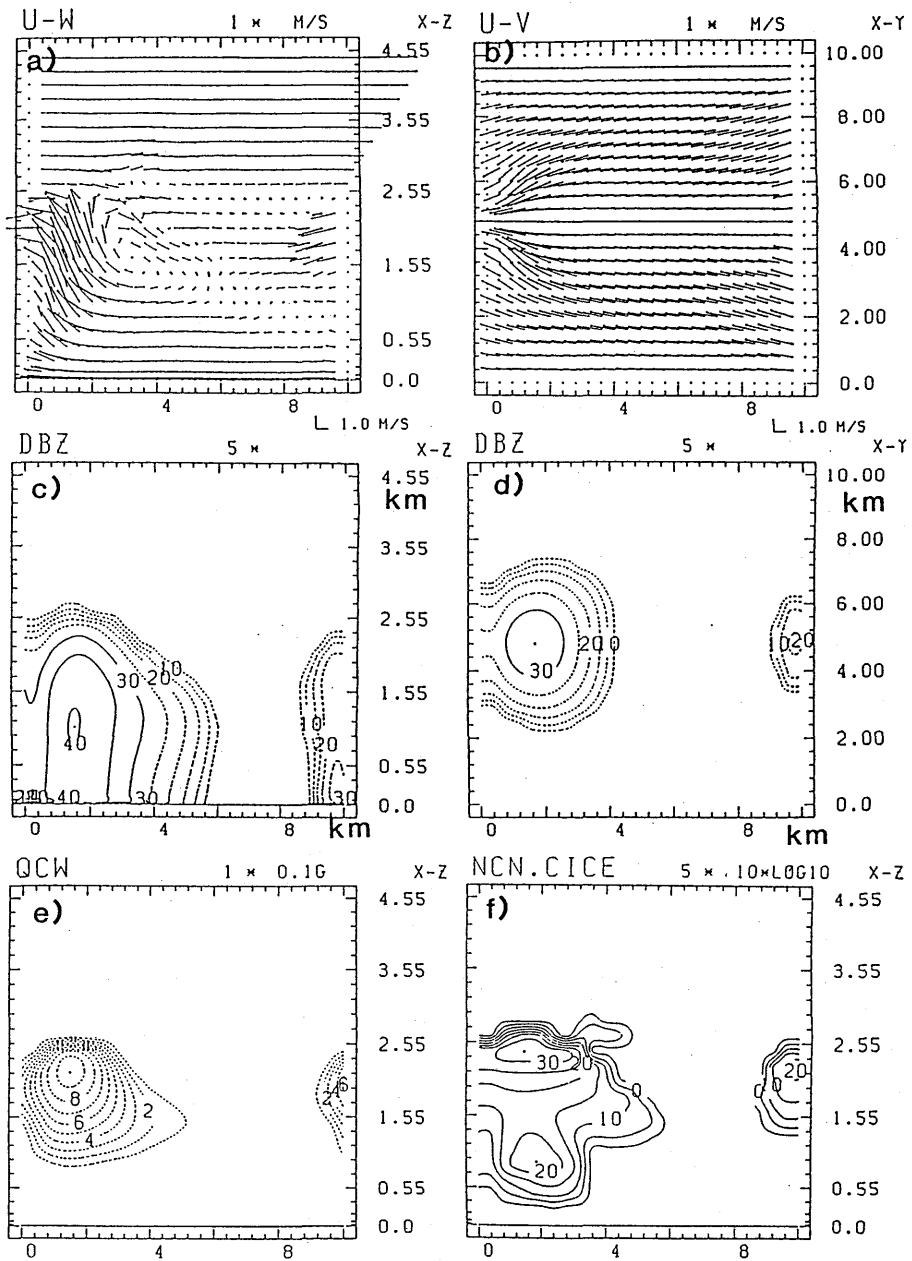
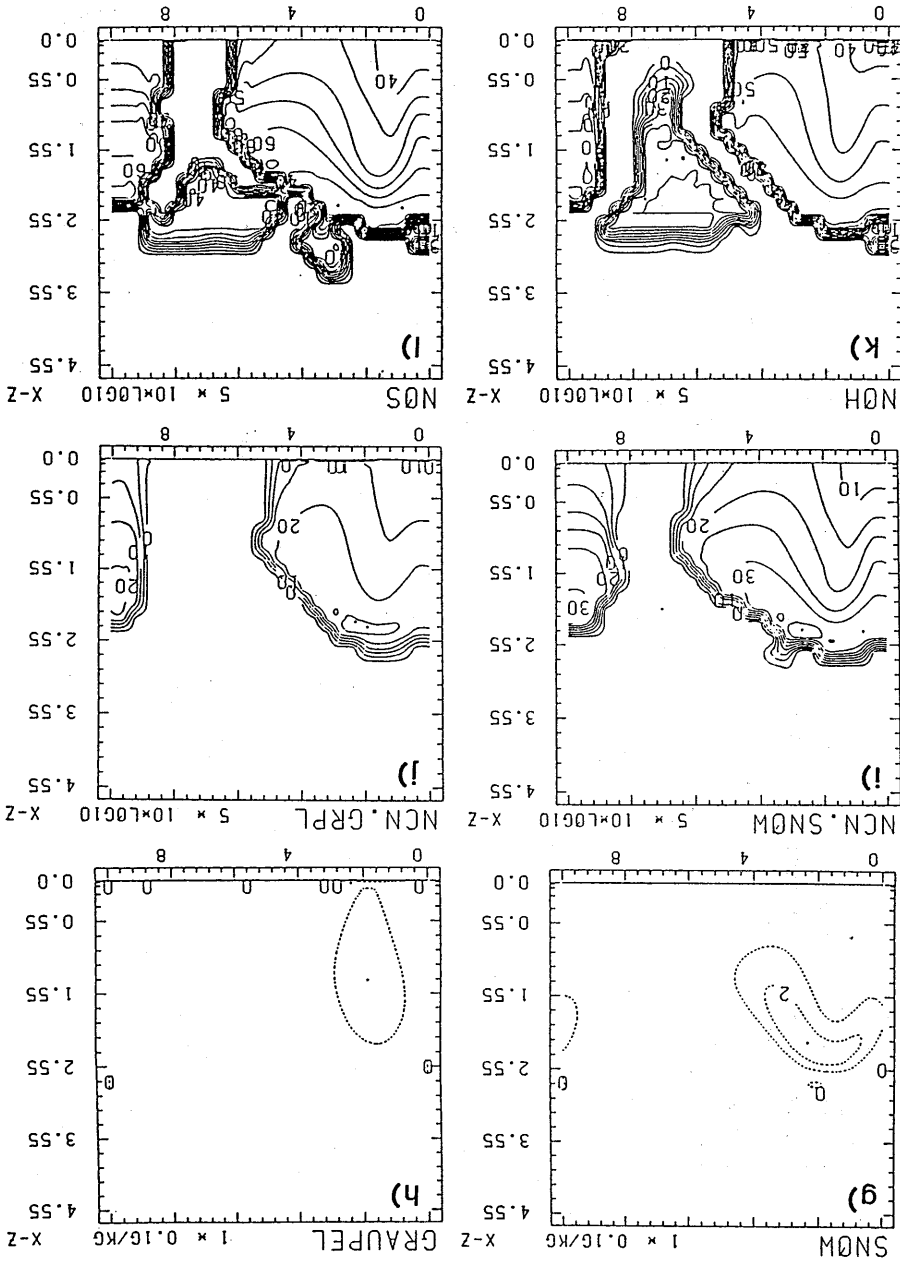


Fig. C-3-23 The same as Fig. C-3-10 but for EXN1.

Fig. C-3-23 (Continued.)



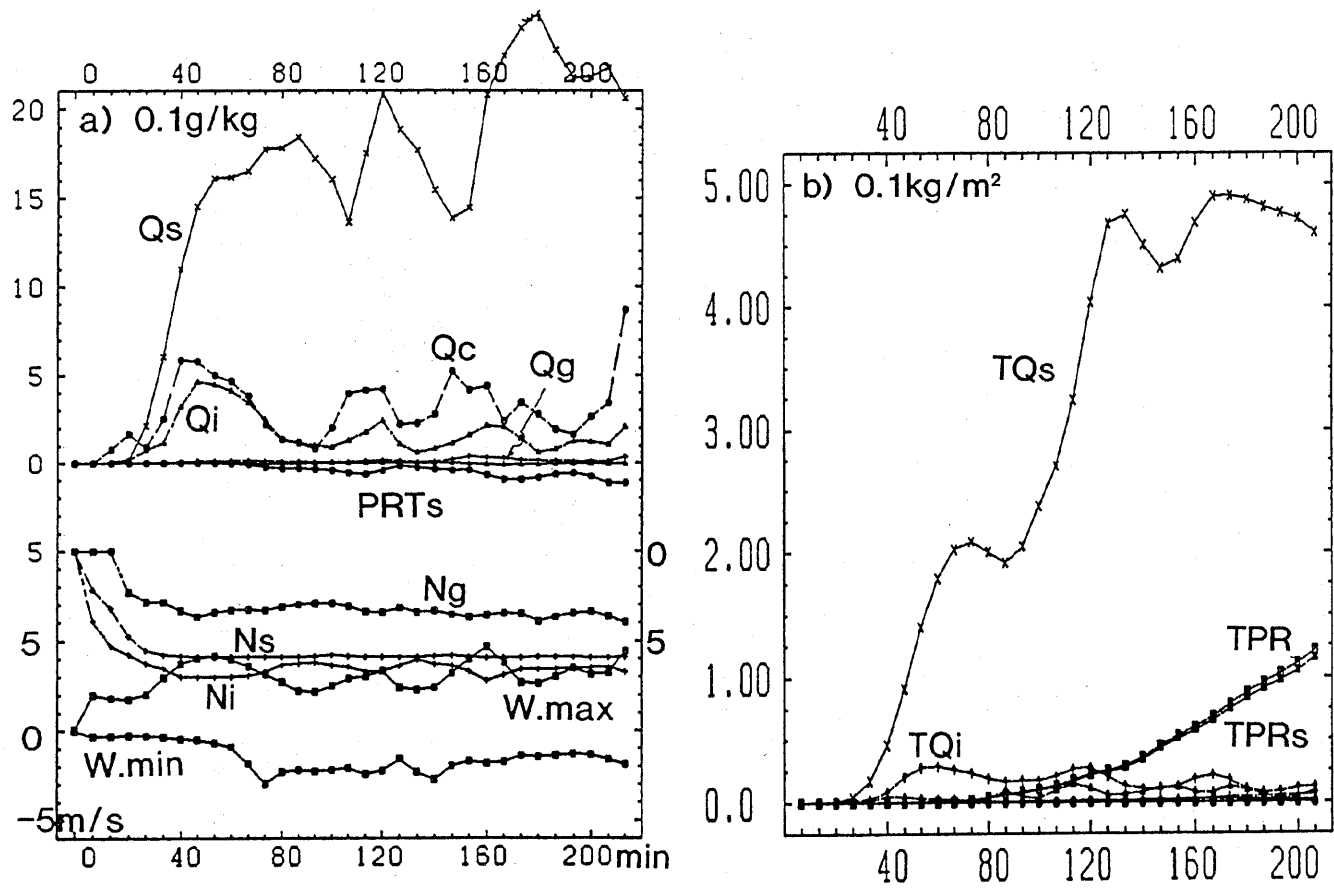


Fig. C-3-24 The same as Fig. C-3-7 but for EXDS2. The unit of  $Q_i$  in a) is 0.1 g/kg.

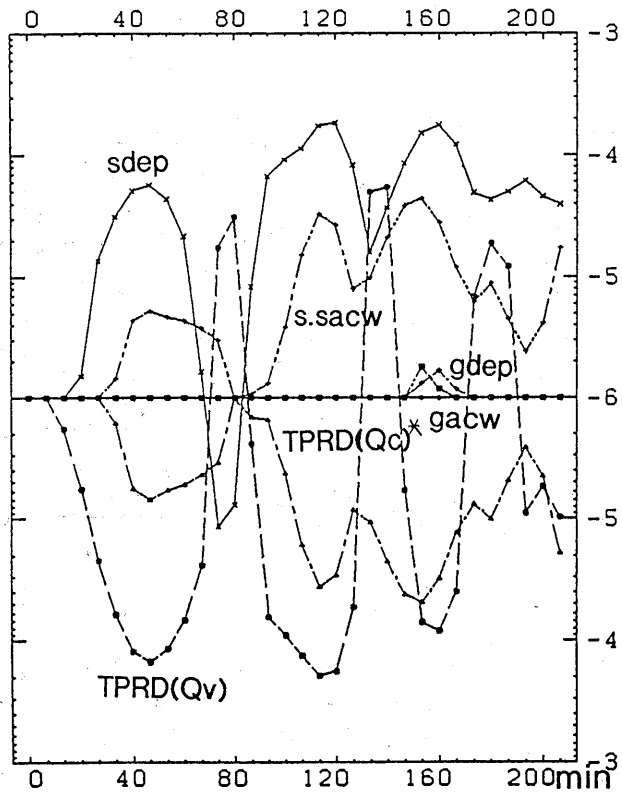


Fig. C-3-25 The same as Fig. C-3-17 but for EXDS2.

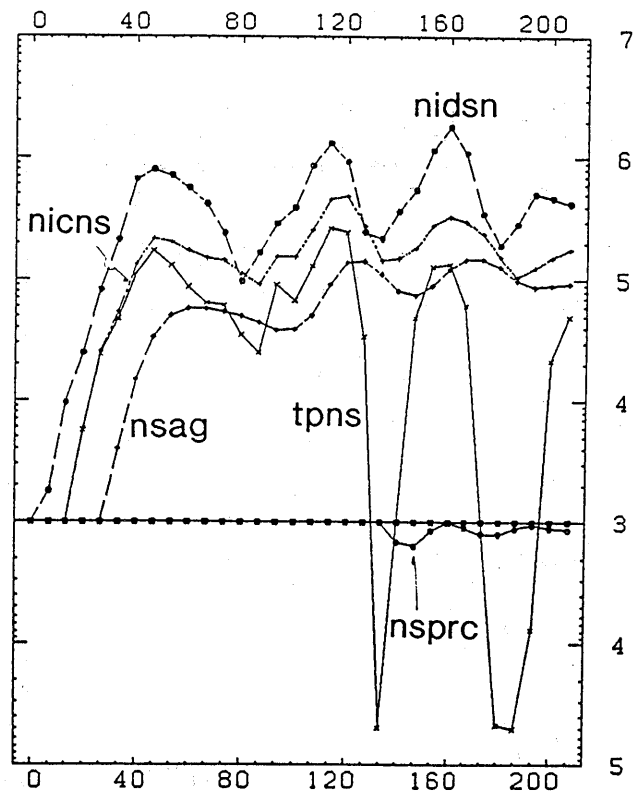


Fig. C-3-26 The same as Fig. C-3-18 but for EXDS2 and  $p_0 = 10^3$ .

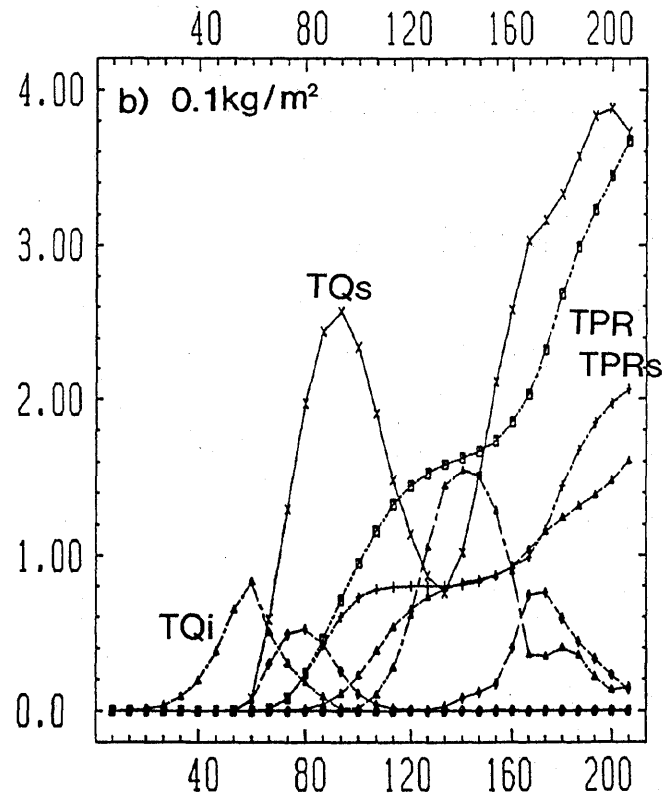
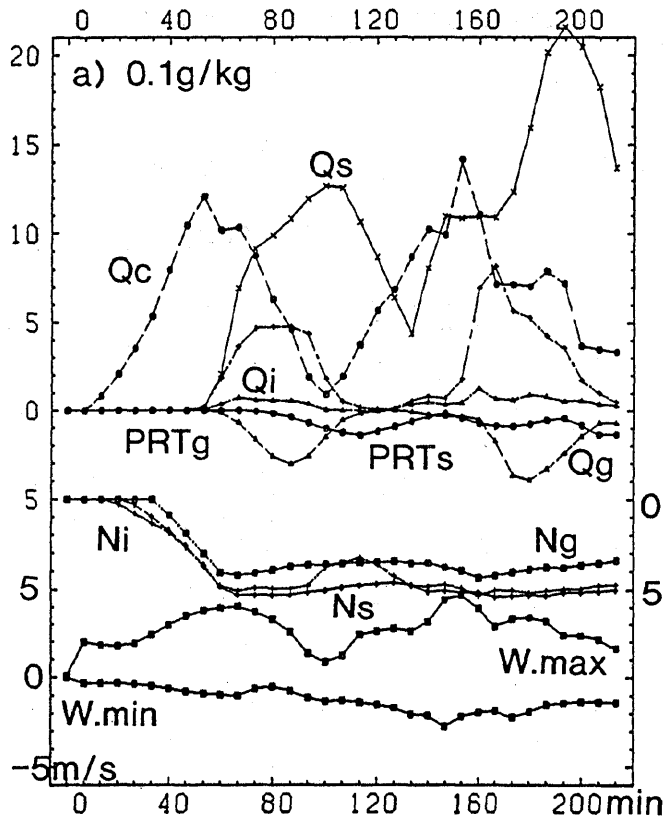


Fig. C-3-27 The same as Fig. C-3-7 but for EXHM.

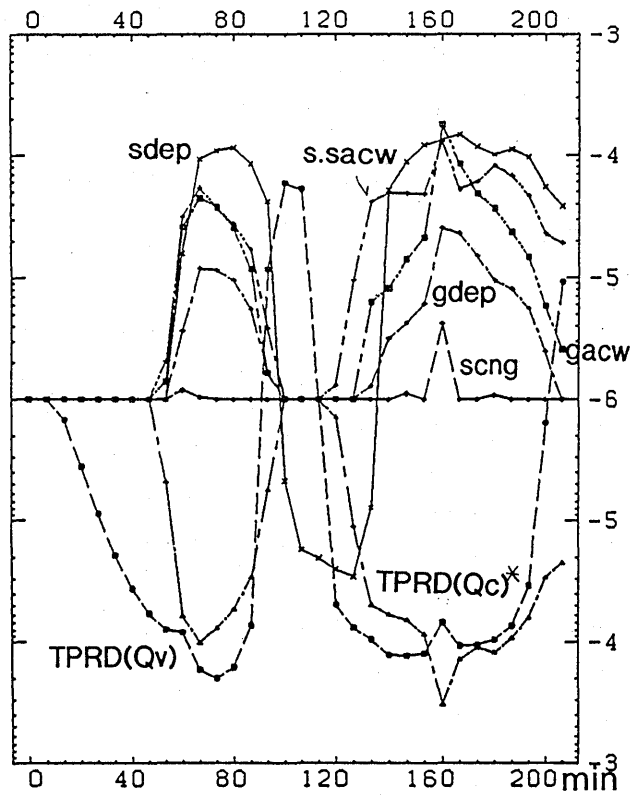


Fig. C-3-28 The same as Fig. C-3-17 but for EXHM.

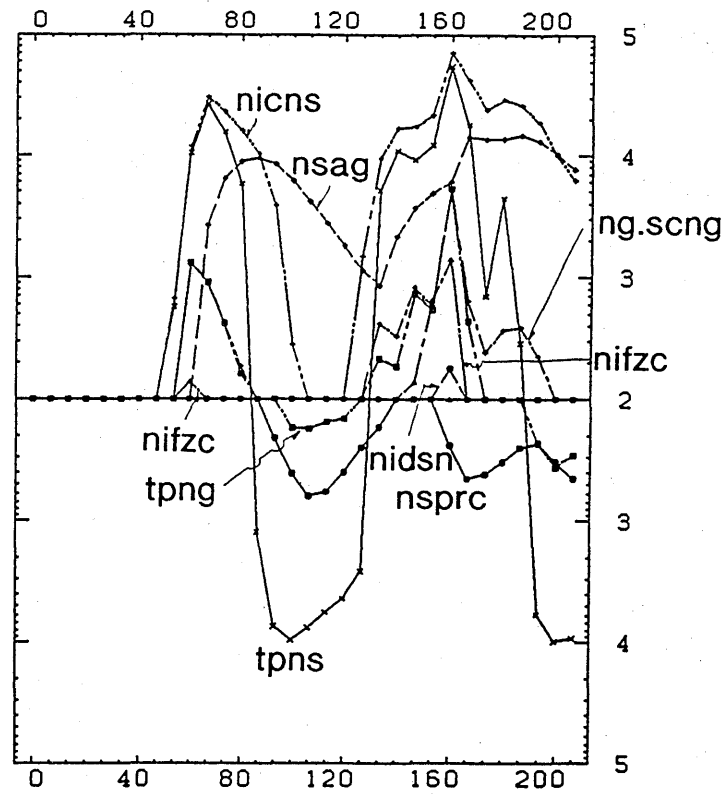


Fig. C-3-29 The same as Fig. C-3-18 but for EXHM and  $p_0 = 10^2$ .

of EXN1. 3)  $TNi$  and  $TNs$  are 2 ~ 3 times larger than those of EXN1 and almost the same as those of EXDS1.

The characteristic features of EXBK2 are as follows: 1) The maximum value of  $TQc$  is similar to that of EXN1. 2)  $TNi$  and  $TNs$  are  $10^3$  times larger than those of EXN1. 3) The precipitation amount is 1/3 of EXN1. Remarkable increase of  $Ni$  and  $Ns$  is attributable to that the number of collisions between snow and graupel is proportional to the product of  $Ns$  and  $Ng$ .

#### a-6) EXS1 and EXS2

The characteristic features of EXS1 are as follows: 1) During  $0 < t < 60$ min, the results of EXS1 are similar to those of EXDS2 in large  $Ni$ ,  $Ns$  and  $Qs$ , and very small  $Qc$ ,  $Qg$  and little precipitation. 2) During  $120 < t < 213$ min, the results of EXS1 are similar to those of EXN1 in large  $Qc$ ,  $Qg$ , large precipitation rate and small  $Ni$  and  $Ns$ . Seeding effect in suppressing precipitation is remarkable (overseeding) until  $t = 100$ min. However, this effect does not continue long. The seeding effect of EXS2 is not so remarkable as that of EXS1, indicating that seeding at the lower part is more effective.

#### a-7) Summary

In EXN1, the maximum value of number concentration of ice particles is 1/4 of the observed counterpart. The dominant generation term of cloud ice is not deposition/sorption nucleation ( $Pidsn$ ,  $Nidsn$ ) but freezing of cloud droplets ( $Pifzc$ ,  $Nifzc$ ). Freezing of cloud droplets can produce fairly large number concentration of ice particles which is still smaller than the observed one but appears to be in a tolerable range. The number concentration of ice particles is 1-order smaller than that of EXDS1. The radar reflectivity is the largest among all experiments, yielding a difference of 10dBZ from the observed value.

The increase in the number concentration of ice crystals to the observed value ( $2 \times 10^5/m^3$ ) by enhancing Fletcher's deposition/sorption nucleation results in rapid glaciation (13min earlier), the decrease of cloud water, the increase of deposition, the decrease of riming, the increase of the number concentration of graupel, the increase of snow in mass and number, the decrease of the precipitation intensity of snow and the decrease of radar reflectivity to 37dBZ.

A further increase in the number concentration of ice crystals to the value ( $10^7/m^3$ ) results in suppression of precipitation and glaciation of cloud with little cloud water, little

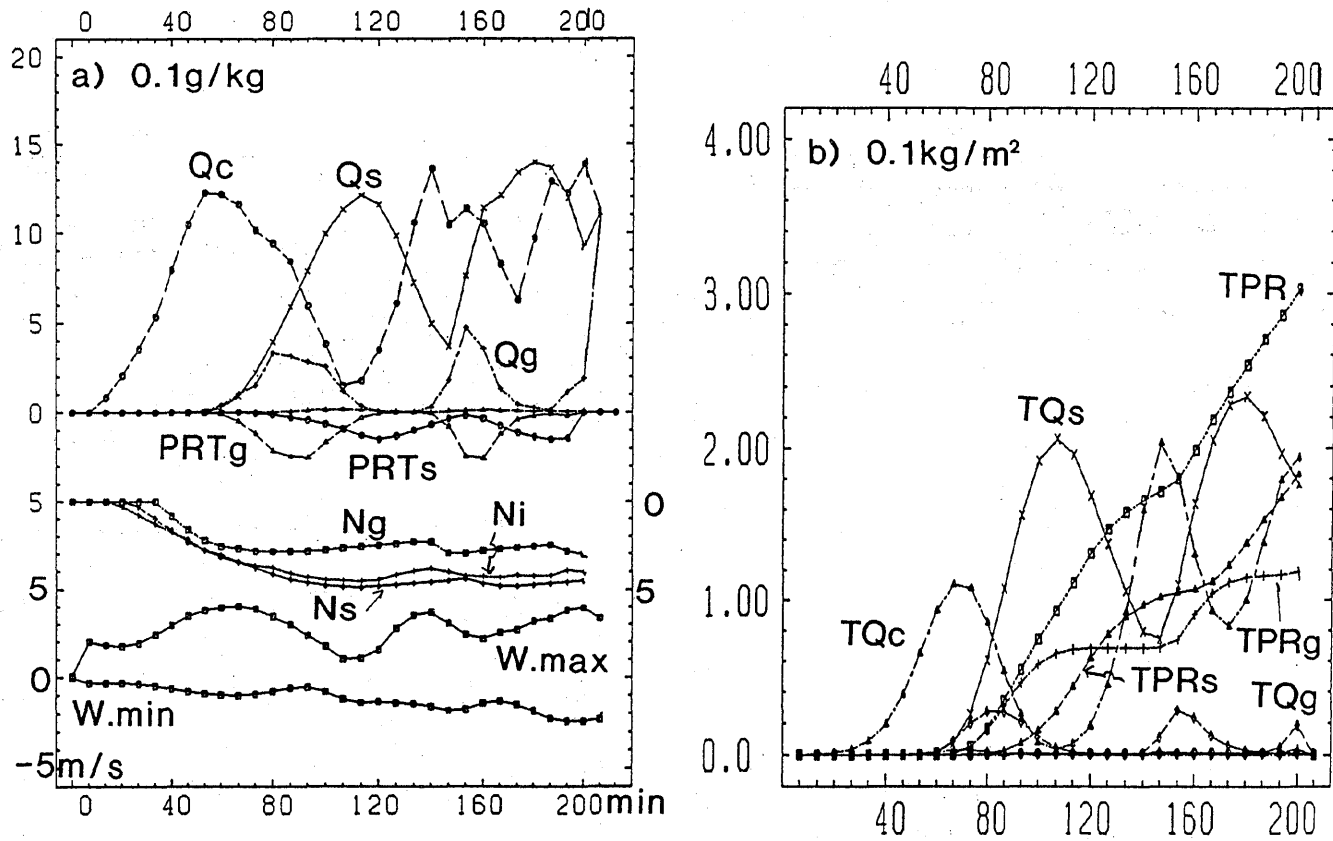


Fig. C-3-30 The same as Fig. C-3-7 but for EXBK1.

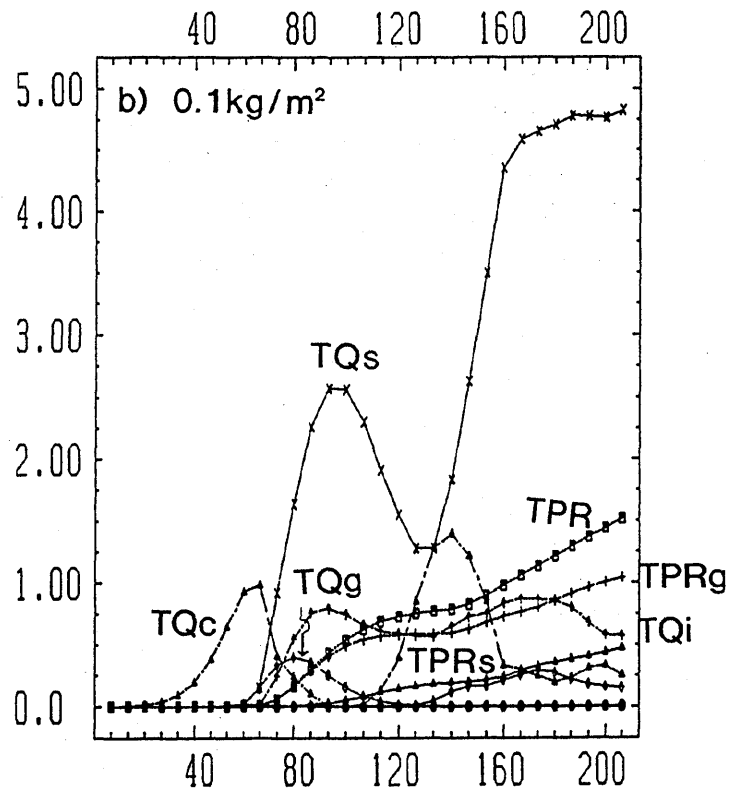
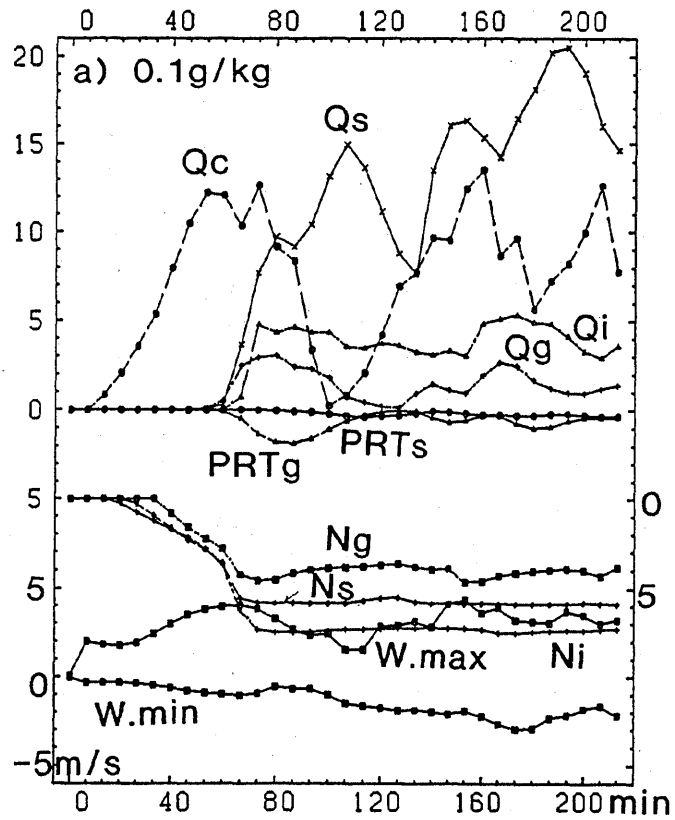


Fig. C-3-31 The same as Fig. C-3-7 but for EXBK2.

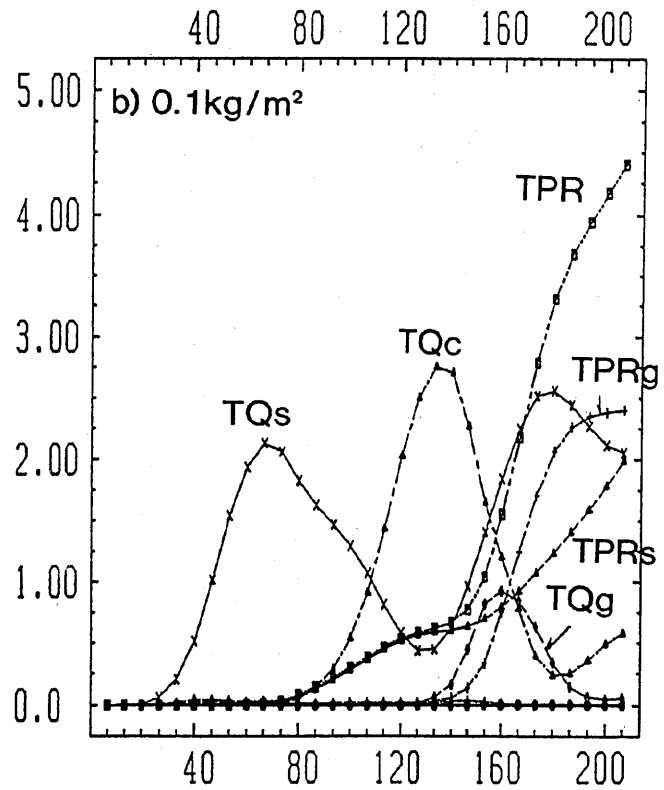
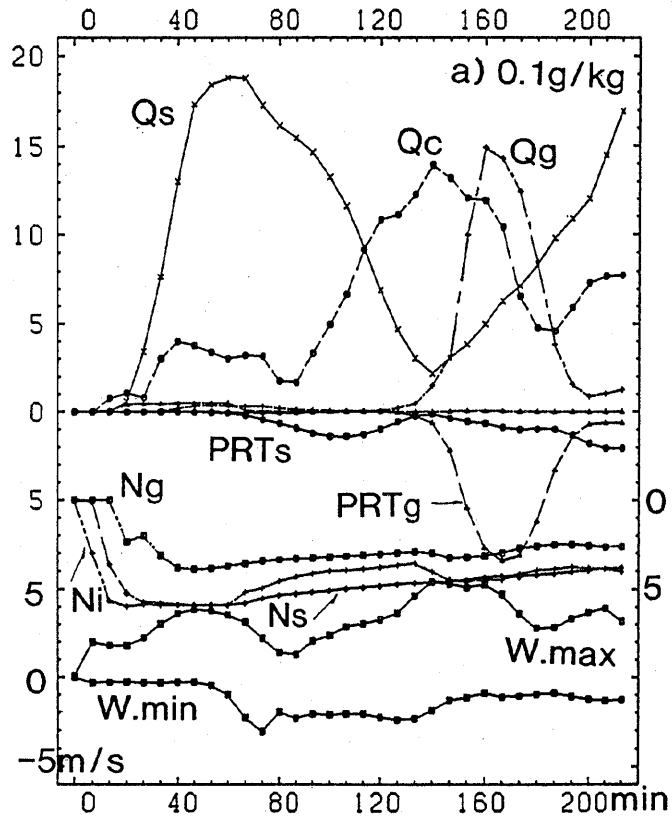


Fig. C-3-32 The same as Fig. C-3-7 but for EXS1.

graupel and abundant snow.

Based on these experiments including seeding experiments EXS1 and EXS2, it can be said that there is the possibility of suppressing precipitation or changing the location of precipitation leeward by overseeding.

The maximum of the number concentrations of cloud ice and snow obtained from EXN1, EXDS1, EXFZ1, EXHM and EXBK1 lies within a tolerable range, *i.e.*, within one order different from the observed counterpart. There are differences among these experiments in the amount of cloud water ( $TQc$ ) and the onset time of glaciation. In EXHM and EXBK1, the amount of cloud water and onset time of glaciation are nearly the same with EXN1, while, in EXDS1,  $TQc$  is smaller and the onset time is earlier than that in EXN1. In most experiments, the level of the maximum  $Ni$  is higher than that of the maximum  $Qc$  by 0.5 ~ 1.0km. However, EXHM shows the proximity of both levels. In addition to these numerical sensitivity experiments, more observations are needed, especially on the developing stage of the cloud, for more understanding of the ice nucleation processes.

b) Sensitivity to  $r_0$

The parameter  $r_0$  (Eq. B-(11-27), Table B-11-1) is assumed to be the minimum radius of snow and graupel particles which determines the minimum weight of snow and graupel particles as follows:

$$m_{s0} = \frac{4\pi}{3} \rho_s r_0^3, \quad m_{g0} = \frac{4\pi}{3} \rho_g r_0^3.$$

The conversion term from cloud ice to snow (Picns: Eq. B-(11-30)) is highly dependent on  $m_{s0}$ . The conversion term from cloud ice to graupel via riming (Picng: Eq. B-(11-36)); Pgiacw: Eq. B-(11-38)) is also highly dependent on  $m_{g0}$ . However, in the present case, Pgiacw is less than Pidep, and Picng is not effective. Picns almost balances Pidep. As shown in Table C-3-4, the number and mass of cloud ice are highly dependent on the parameter  $r_0$ , while the number of snow particles is not so sensitive to it from a global point of view. The total precipitation is not dependent on  $r_0$  as shown in Table C-3-4. However, locally speaking, the parameter brings about some differences in the snow field. Around the region where updraft is strong and snow and graupel particles are vigorously generated, the number of snow particles in the case of small  $r_0$  is larger than that for large  $r_0$ , as shown in Fig. C-3-33. As a consequence, radar reflectivity for  $r_0 = 50\mu\text{m}$  attains 33dBZ at this region, smaller than 37dBZ in the case of  $r_0 = 75\mu\text{m}$  (see Fig. C-3-11e). Smaller  $r_0$  gives rise to more realistic

Table C-3-4 Sensitivity to the parameter  $r_0$ . "rnn" denotes the experiment which adopts the value "nn"  $\mu\text{m}$  for  $r_0$ . In the experiments in the table, the value 32 is used for  $\alpha 2\Delta t$ . The unit of  $Ni.\text{max}$  and  $Ns.\text{max}$  is  $\text{m}^{-3}$ ; "max" denotes the maximum value during  $0 < t < 213$  min; the unit of  $TQi$ , ... $TPR.g$  is  $\text{kg}/\text{m}^2$ .

	$Ni.\text{max}$	$TQi$	$Ns.\text{max}$	$TQs$	$TPR.s$	$TQg$	$TPR.g$	$dBZ.\text{max}$
EXDS1.r50	$10^{5.0}$	$2.8 \times 10^{-5}$	$10^{5.3}$	0.34	0.25	0.01	0.11	33
EXDS1.r75	$10^{5.3}$	$6.0 \times 10^{-4}$	$10^{5.3}$	0.34	0.26	0.02	0.12	36-37
EXDS1.r100	$10^{5.8}$	$1.2 \times 10^{-3}$	$10^{5.4}$	0.31	0.24	0.02	0.13	40

Table C-3-5 Sensitivity to the parameter  $\alpha 2\Delta t$ . "ann" denotes the experiment which adopts the value "nn" for  $\alpha 2\Delta t$ .  $SUM.x \equiv TPR.x + TQx$  ( $x = s$  or  $g$ ). Values at  $t = 213$  min are listed. The unit of  $TQx$  and  $TPRx$  is  $\text{kg}/\text{m}^2$ .

	$TQs$	$TPR.s$	$SUM.s$	$TQg$	$TPR.g$	$SUM.g$	$TPR.g/TPR.s$	$SUM.g/SUM.s$
EXN.a10	0.18	0.32	0.50	0.06	0.09	0.15	0.28	0.30
EXN.a32	0.12	0.26	0.38	0.09	0.15	0.24	0.58	0.63
EXN.a80	0.06	0.16	0.22	0.11	0.26	0.37	1.6	1.7

dBZ, but more unrealistic  $Ni$ .

### c) Sensitivity to $\alpha 2\Delta t$

The parameter  $\alpha 2\Delta t$  (see Eq. B-(11-43)) has a large influence on the conversion term of snow into graupel via riming (Pscng). Results of sensitivity experiments to  $\alpha 2\Delta t$  are summarized in Table C-3-5. As  $\alpha 2\Delta t$  becomes large, more graupel is generated and snow is suppressed. From observational studies, the ratio of the precipitation amount of graupel over that of snow is about 0.1 ~ 1.3 (Konishi *et al.*, 1989; Mizuno, 1989). An appropriate value for  $\alpha 2\Delta t$  is considered to be 10 ~ 40.

## C-3-7 Comparison with observations

Comparison with observations is summarized in Table C-3-6. Main discrepancy is in radar reflectivity. As for the maximum of the number concentrations of cloud ice and snow, EXN1, EXDS1, EXFZ1, EXHM and EXBK1 reproduce it within a tolerable range.

### a) Contribution ratio of riming over deposition to the growth of ice particles

Harimaya and Sato (1989) measured the contribution ratio of riming over deposition to the growth of snow aggregates around Sapporo. They reported as follows: When a strong

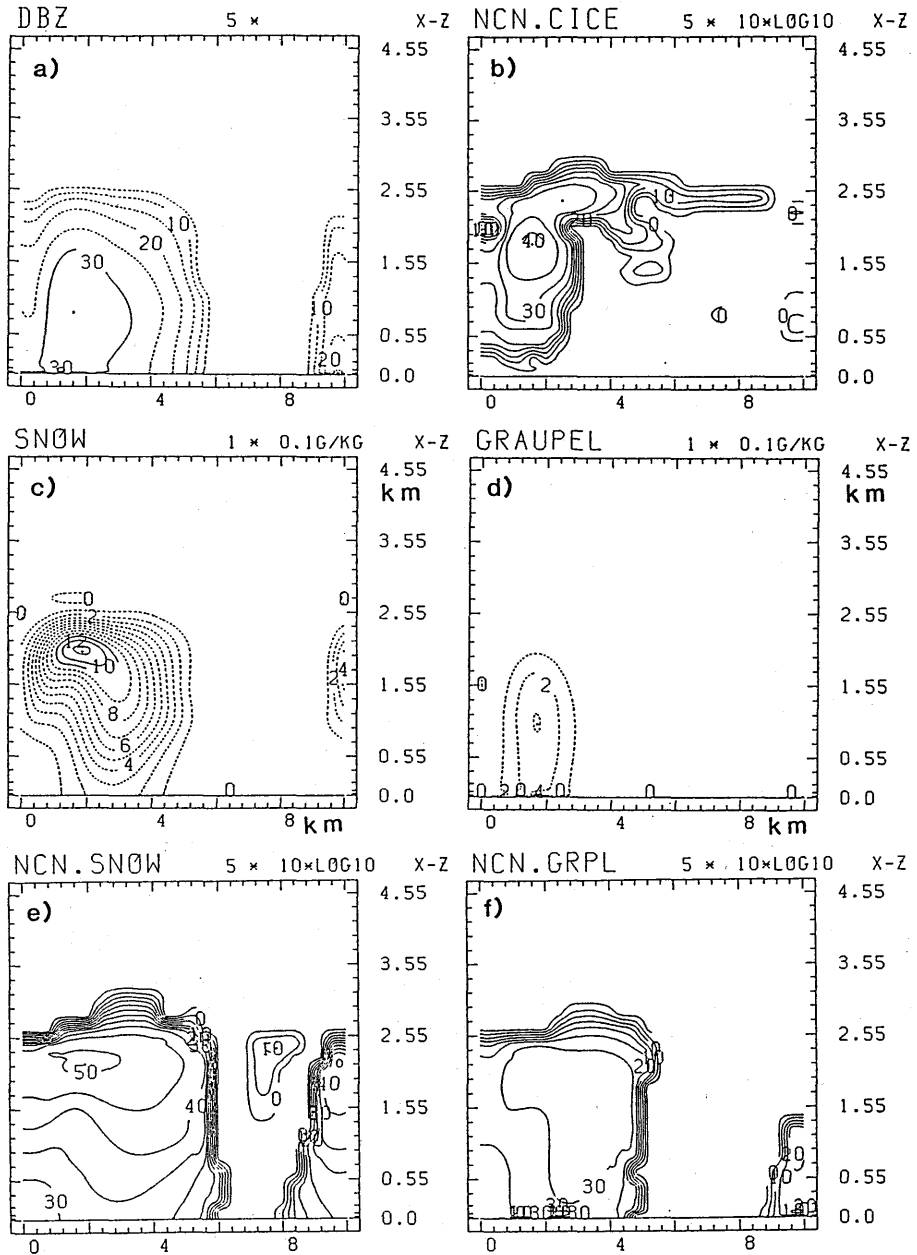


Fig. C-3-33 X-z cross sections at  $t = 80$  min by EXDS1.r50.  
 a) The same as Fig. C-3-10c but for  $r_0 = 50\mu\text{m}$ .  
 b) The same as Fig. C-3-10f but for  $r_0 = 50\mu\text{m}$ .  
 c) The same as Fig. C-3-10g but for  $r_0 = 50\mu\text{m}$ .  
 d) The same as Fig. C-3-10h but for  $r_0 = 50\mu\text{m}$ .  
 e) The same as Fig. C-3-10i but for  $r_0 = 50\mu\text{m}$ .  
 f) The same as Fig. C-3-10j but for  $r_0 = 50\mu\text{m}$ .

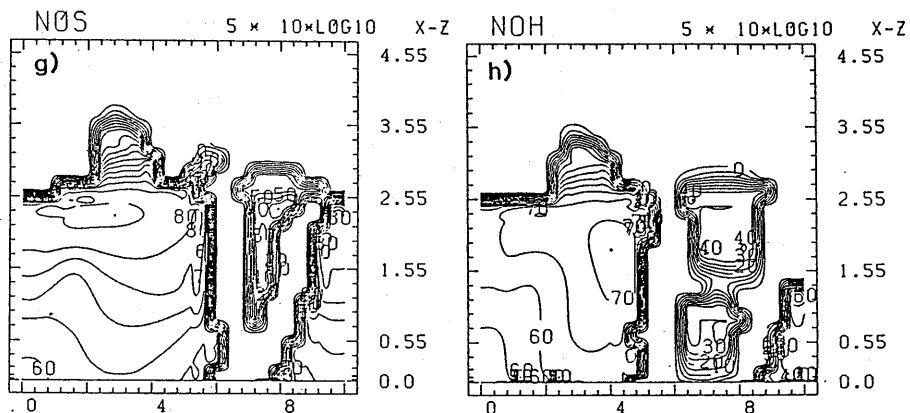


Fig. C-3-33 (Continued.)

- g) The same as Fig. C-3-10k but for  $r_0 = 50\mu\text{m}$ .  
 h) The same as Fig. C-3-10l but for  $r_0 = 50\mu\text{m}$ .

Table C-3-6 Comparison between results of EXN1 and EXDS1 and observations at Tobishima (Murakami *et al.*, 1990) and Otaru (Magono and Lee, 1973).

	Tobishima (1989) Feb.			Otaru (1970) Jan.
	EXN1	sim. EXDS1	obs.	obs.
cloud top(km)	3.0	3.0	3.0	1.5 ~ 2.5
temp.(°C)	-20	-20		-15 ~ -22
cloud base	0.7	0.7	1.0	0.5 ~ 1.5
temp.(°C)	-8	-8		-9 ~ -15
horizontal scale (km)	5	5	5	
max.w(m/s)	4	4		
max dBZ	40	37	30	
max.Qc(g/kg)	1.4	1.0	0.12	1.0
max.(Ni + Ns)(m <sup>-3</sup> )	$5 \times 10^4$	$5 \times 10^5$	$2 \times 10^5$	$5 \times 10^4$
max.Qs(g/kg)	0.7	1.2	0.25	0.1

snow cloud passed over the observation site, first, graupel particles fell and riming proportion increased (80–100%). Then the snowfall intensity continues to increase gradually. By contrast, the riming proportion decreased from 80–100% to 60%. In the later stage, both the snowfall intensity and riming proportion become small (40–60%). Mizuno *et al.* (1990) also observed snow clouds around Sakata. From their observation, at the first stage, graupel and heavily rimed snow particles fell with the riming proportion greater than 70%. At a later stage, rimed snow particles with the riming proportion of about 50% fell.

Table C-3-7 Riming proportion ratio in EXDS1 and EXN1.

	EXDS1		EXN1			
	developing to mature	mature to decay	developing to mature	mature to decay		
<i>t</i> (min)	60	133	80	80	147	100
<i>Rrim</i>	0.54	0.76	0.41	0.85	0.80	0.56

These characteristic features are well reproduced by the model. The riming proportion ratio defined as

$$Rrim = \frac{TPs.sacw + TPg.sacw + TPgacw}{TPs.sacw + TPg.sacw + TPpdep + TPgacw + TPgdep}$$

is listed in Table C-3-7. This ratio does not directly correspond to the observed ones by Harimaya and Sato (1989) and Mizuno *et al.* (1990). However, it can be said that, at least qualitatively, the model reproduces the riming proportion ratio successfully.

b) Comparison of  $Nos$  and  $Nog$  with observations

Harimaya (1978) observed size distributions of snow and graupel around Sapporo (43.08N, 141.35E). Yagi *et al.* (1979) did the same at Nagaoka (37.45N, 138.80E). Kajikawa and Kiba (1878) observed that of graupel around Akita (39.75N, 140.10E). These observed  $Nos$  and  $Nog$  as a function of precipitation rate  $R$  (mm/hr) are plotted in Fig. C-3-34, together with  $Nos$  obtained by Gunn and Marshall (1958). Sapporo and Nagaoka are located about 15km distant from the sea coast. Moreover, a range of hills as high as 400m lies between Nagaoka and the sea coast. Therefore, the clouds observed by Harimaya and Yagi *et al.* are not considered to be representative convective clouds over the warm Sea of Japan. The dependency of  $Nos$  and  $Nog$  on precipitation rate,  $R$ , show a lot of variation, suggesting the complex influence of meteorological and geographical conditions on  $Nos$  and  $Nog$ . This dependency of  $Nos$  on  $R$  is different from Gunn-Marshall's which is considered to fit well with the stratiform cloud where aggregational growth is dominant.

For the observed case of Feb. 4, 1989 at Tobishima (see Fig. C-3-4),  $Nos$  estimated by extrapolating the size distribution curve to  $D = 0$  is  $10^6 \sim 8 \times 10^7 m^{-4}$ , showing a large variation with height. On the other hand, that estimated by the formula based on the inverse exponential size distribution function,

$$Nos = N_s \left( \frac{\pi \rho_s N_s}{\rho Q_s} \right)^{1/3}$$

Table C-3-8  $N_{os}$  and  $N_{og}$  ( $m^{-4}$ ) simulated in EXDS1 and EXN1 as a function of the cloud stage and precipitation rate,  $R$  (mm/hr). These are shown in Fig. C-3-34 (EXDS1,  $\Delta$ ; EXN1,  $\times$ ).

	EXDS1			EXN1		
time(min)	80	100	120	100	113	127
PRCP.s(mm/hr)	1.0	2.0	1.0	1	2.5	1
$N_{os}(m^{-4})$	$2 \times 10^6$	$2 \times 10^7$	$5 \times 10^7$	$1 \times 10^5$	$3 \times 10^5$	$5 \times 10^5$

	EXDS1			EXN1		
time(min)	73	80	87	80	87	93
PRCP.g(mm/hr)	1	2.5	1	1	2.5	1
$N_{og}(m^{-4})$	$1 \times 10^6$	$2 \times 10^6$	$3 \times 10^6$	$3 \times 10^4$	$6 \times 10^4$	$2 \times 10^5$

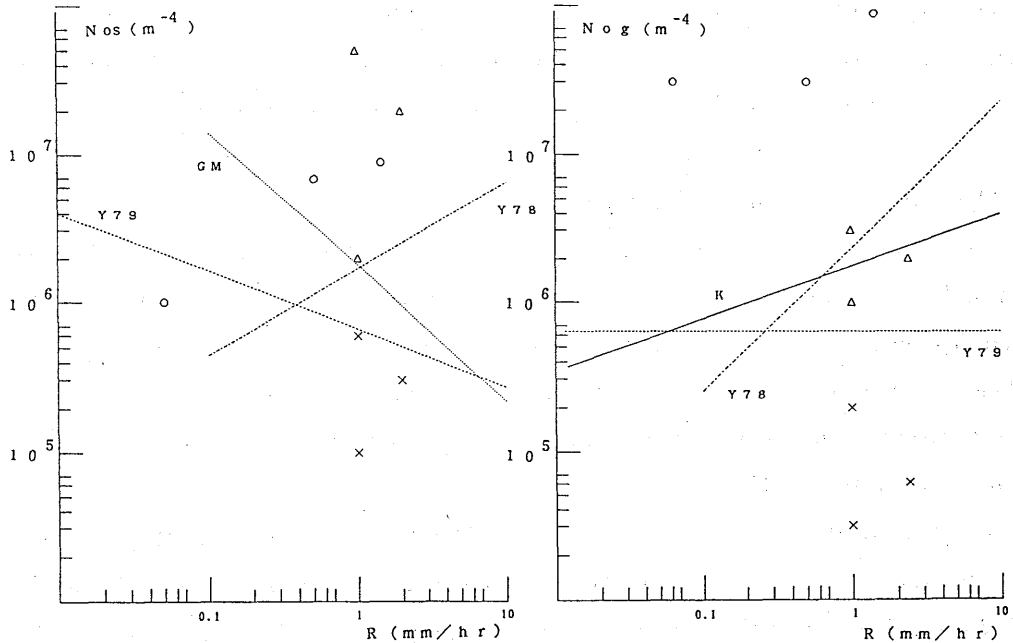


Fig. C-3-34  $N_{os}$  and  $N_{og}$  ( $m^{-4}$ ) simulated in EXDS1 ( $\Delta$ ) and EXN1 ( $\times$ ) as a function of precipitation rate,  $R$  (mm/hr). Empirical formula of Yagi *et al.* between  $N_{os}$  and  $R$  based on observational studies for the cases of 1978 and 1979 are indicated by Y78, and Y79; that of Kajikawa by K; that of Gunn and Marshall by GM. Harimaya's data are indicated by  $\circ$ .

with substitution of  $N_s = 10^5 m^{-3}$  and  $\rho Q_s = 0.13 g/m^3$ , is  $6 \times 10^8 m^{-4}$ . This large difference means the inadequacy of the assumed inverse exponential size distribution. Precipitation rate for this case is about  $R = 0.5 mm/hr$ .

$N_{os}$  and  $N_{og}$  in the simulated clouds are listed in Table C-3-8, and also added in Fig. C-3-34.  $N_{os}$  and  $N_{og}$  obtained in the simulation show remarkable dependency on the stage

of the cloud rather than the precipitation rate.  $Nog$  increases monotonically as the cloud evolves from stage 3 to 5;  $Nog$  at the stage 5 is larger than that at stage 3, even for the same precipitation rate. The same can be said about  $Nos$ . The examples of  $Nos$  in EXN1 are shown in Fig. C-3-35. These results simply reflect the fact that relatively large particles fall down to the ground faster than smaller ones and that large particles are more abundant at the developing or mature stage of cloud than small ones at the decaying stage.

A direct comparison between the observed and simulated  $Nos$  and  $Nog$  is not fruitful because of neglecting the stage of the cloud in observations and the long distance of Sapporo and Nagaoka from the sea coast. With these reservations, the following might be said:  $Nos$  of EXDS1 is larger than the observed counterpart, while  $Nos$  of EXN1 is smaller;  $Nog$  of EXDS1 is close to the observed counterpart, while  $Nog$  of EXN1 is smaller. These discrepancies are partly related to the essential unknowns about ice nucleation terms, and partly to the insufficiency of the bulk parameterization adopted in the model.

### C-3-8. Summary and conclusion

We have developed a bulk parameterization scheme of cloud microphysics which predicts not only the number concentrations of cloud ice and snow but also that of graupel ( $Ni$ ,  $Ns$  and  $Ng$ ) in addition to the mixing ratios of six water species (water vapor, cloud water, cloud ice, snow and graupel), and this scheme is applied to the 3-dimensional simulation of the convective snow cloud observed over the Sea of Japan on Feb. 4, 1989, with the cloud top temperature at  $-20^{\circ}\text{C}$ .

Sensitivity experiments are conducted for three kinds of generation terms, *i.e.*, ice nucleation rates (C-3-6 a)), the conversion term of cloud ice into snow via depositional growth (C-3-6 b);  $Picns$ ), and the conversion term of snow into graupel via riming growth (C-3-6 c);  $Pscng$ ).

Ice nucleation terms exert a large influence on the number concentrations of cloud ice, snow and graupel, the amount of supercooled cloud water, the amounts of riming and deposition and the timing of glaciation. When conventional parameters for Fletcher's deposition/sorption nucleation, Bigg's freezing of supercooled droplets and Hallet-Mossop rime splinter nucleation are used, the maximum number of ice particles reproduced by the model is 1/4 of the observed counterpart. Radar reflectivity is larger by 10dBZ than the observed one, and  $Nos$  and  $Nog$  are smaller than the observed ones. In this case, freezing of cloud droplets plays a dominant role in ice crystal generation rather than Fletcher's deposition/sorption

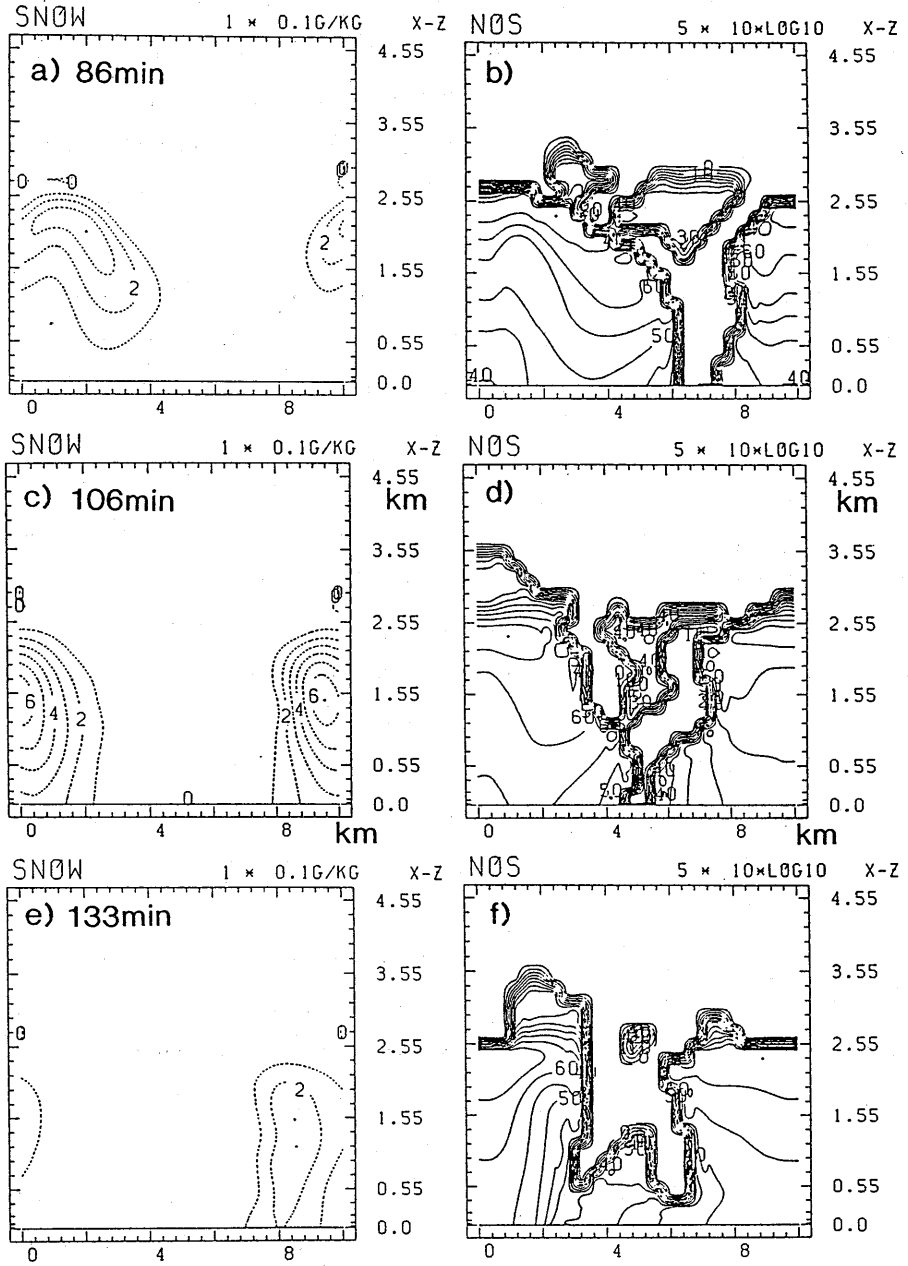


Fig. C-3-35  $Q_s$  and  $N_{os}$  fields by EXN1.

- a) X-z cross section of  $Q_s$  at  $t = 87$  min with contour intervals of 0.1 g/kg.
- b) X-z cross section of  $\log_{10}(N_{os})$  at  $t = 87$  min with contour intervals of 5. The unit of  $N_{os}$  is  $\text{m}^{-4}$ .
- c) The same as a) but for  $t = 107$  min.
- d) The same as b) but for  $t = 107$  min.
- e) The same as a) but for  $t = 133$  min.
- f) The same as b) but for  $t = 133$  min.

nucleation. When ice nucleation terms are enhanced to reproduce the number concentration of  $10^5$ – $10^6$   $\text{m}^{-3}$ , the amount of supercooled cloud water decreases, the amount of snow increases in mass and number, and radar reflectivity decreases. Further enhancement of the number concentration of ice particles to  $10^6$ – $10^7$   $\text{m}^{-3}$  leads to the suppression of precipitation with abundant snow in air. This gives some support to the possibility of suppression of precipitation by overseeding.

Sensitivity experiments to the parameter  $r_0$  which has a large influence on the conversion term of cloud ice into snow (Picns) reveals that the parameter  $r_0$  have a large influence on the mass and number of cloud ice particles, but not on the mass and number of snow and graupel particles.

Sensitivity experiments to the parameter  $\alpha 2\Delta t$  which has a large influence on the conversion term of snow into graupel (Pscng) reveals that the parameter  $\alpha 2\Delta t$  has a large influence on the mass and number of snow and graupel particles and their precipitation amount.  $\alpha 2\Delta t$  is tuned so as to reproduce the observed ratio of precipitation amount of graupel to that of snow, and  $10 \leq \alpha 2\Delta t \leq 40$  is found to be appropriate for the present case. Such a tuning appears to be inevitable to some extent in a bulk parameterization.

Precipitation formation in the simulated cloud is as follows (C-3-5 c)): The water vapor supplied from the warm sea surface is lifted upward by convection and condenses to form supercooled cloud droplets. At the developing and mature stages of the cloud, these supercooled droplets are accreted on snow and graupel particles, and this riming process is more dominant than the depositional process in precipitation formation. At the dissipation stage, almost all of the supercooled cloud droplets are depleted, and graupel particles are absent; depositional growth is the dominant process for the growth of snow above the cloud base; below it, sublimation from snow particles is active enough to be almost equal to deposition above the cloud base. Aggregation of snow becomes active after the mature stage. The net decrease in the number of snow at the decayed stage is due to aggregation, precipitation and sublimation. These features are consistent with observational studies of Harimaya and Sato (1989) and Mizuno *et al.* (1990).

In this simulation,  $N_{os}$  and  $N_{og}$  are found to be more dependent on the stage of the cloud than the precipitation rate. Even for the two cases of the same precipitation rate,  $N_{os}$  at the developing stage is smaller than that at the dissipating stage. This point should be confirmed in future field experiments.

The merits of predicting number concentrations of cloud ice, snow and graupel are as

follows:

- i) No need of the prescription of  $N_{os}$  and  $N_{og}$ .
- ii) Capability of simulating the separation between heavy large particles and light small particles via precipitation.
- iii) Capability of simulating aggregational growth.
- iv) Applicability to seeding experiments.

However, for predicting number concentrations of ice particles realistically, more reliable knowledge about ice nucleation is needed, because they are so sensitive to ice nucleation terms as they are demonstrated in this study.

## **D. Guide to running the model**

## D-1. Flow charts of the program

### D-1-1. Job step

Job is divided into 3 job steps currently.

#### Job Step 1

Preparation of eigen-vectors and values which are used in pressure equation solver is made in disk by sub. CVEVSI. The grid structure and lateral boundary conditions must be specified in the same way as those specified in the running model.

#### Job Step 2

Running the model (time integration of the equations).

See the main program SIMAIN in mem. SFXMAIN2.

#### Job Step 3

Plotting the results of the model. See the main program PLCONV in mem. PLPMN.

### D-1-2. Flow chart of the main program "SIMAIN" for the job step 2

initial set-up procedures

VRGDIS --- generates variable grids in arrays VRDX, VRDX2.....  
INIFLD --- set environmental initial fields  
ORGIN0 --- generate system constants such as mountain shape  $Z_s$ , metric tensors  $G^{1/2}$ ,  $G^{12}$ ,  $G^{13}$  and reference atmosphere.  
SETEXT --- set external environmental fields which are currently the same as the initial environmental fields in arrays EXTU, EXTV, ,,EXTQV.

if (itst=0) then initial start-up; store system constants in disk sub. STMTC1.

else if (itst>0) then restart the model; load the results of the previous model run by sub. LADMTS.

load eigen-vector and eigen-values in array EIGVCX, EIGVLX,,, from magnetic tape

start the time integration from it=itst to itend.

CADVC3 --- compute advection term of  $u$ ,  $v$  and  $w$ .

- CRSTUV --- compute Reynolds stress of  $u$ ,  $v$  and  $w$  in the free atmosphere and at the lower boundary. Sensible and latent heat fluxes at the lower boundary are also computed. (see B-10)
- CETUR5 --- time integration of the subgrid scale turbulent kinetic energy. (See Eq.B-(10-1))
- CPTQUVS--- time integration of  $\Theta$ ,  $Qv$ ,  $Qc$ ,  $Qr$ ,  $Qi$ ,  $Qs$ ,  $Qg$ , including all cloud microphysical processes.
- CBUOYC --- buoyancy term is set in array BUOY.  $\partial\text{BUOY}/\partial t$  is set in array DBUYDT.
- SUVPBD --- set the time tendency of  $u$  and  $v$  at the open lateral boundaries in array DUDTBC and calculate some data necessary for the specification of the lateral boundary condition of the pressure equation. (see B-7-2 c) and B-7-3).

time integration of  $u$ ,  $v$ ,  $w$ , and puressure

if (swcmp=0) then anelastic scheme, iteration for pressure equation

do 10 i=1, itrnx (i: iteration counter)

MODADV --- modify advection term to provide forcing terms for pressure eq.

10 SCPI --- Poisson equation solver

SVELC --- time integration of  $u$ ,  $v$  and  $w$ .

else if (swcmp=1) then E-HI-VI scheme

MODADV --- compute Eqs. B-(3-31), (3-33), (3-35).

SCPI --- Helmholtz eq. solver

SVELC

else if (swcmp=2) then E-HE-VI scheme

MODADV ---

FTVELC --- repeat small time step integration of  $u$ ,  $v$ ,  $w$ ,  $p$

end if

CNVED3 --- the eddy diffusion coefficients  $K_m$  are dianostically determined from the turbulent kinetic energy computed by sub. CETUR5.

if (mod(it, istrmt)=0) store the numerical results into disk by sub. STRMTS.

it ← it+1

if (it<itend) then repeat time integration  
else stop

### D-1-3. Flow chart of the subroutine CADVC3

CADVC3 --- compute advection term in flux form

compute ADVW:

compute flux  $Uw$ , and  $ADVW \leftarrow \partial x Uw$

compute flux  $Vw$ , and  $ADVW \leftarrow ADVW + \partial x Vw$

compute flux  $W^*w$ , and  $ADVW \leftarrow ADVW + \partial z W^*w$

artificial diffusion DMP2DN (see B-12-2) DUMPNL (see B-12-1)

LTRLB2 --- adjust the values at the lateral boundary taking into account the  
cyclic or open lateral conditions

end of computation of ADVW

compute ADVV in a similar way as ADVW

compute ADVU in a similar way as ADVW

return

### D-1-4. Flow chart of the subroutine SVELC

SVELC --- time integration of  $U, V, W$  for AE (plus  $P$  for E-HI-VI)

UADVB ( $V, \cdot$ ) set array FUBD1 for  $V$ . At the inflow boundary of  $u$ , FUBD1 is  
set to be zero. At the outflow boundary of  $u$ , FUBD1 is set to be  
non-zero.

UADVB1 ( $W, \cdot$ ) set array FUBD1 for  $W$ .

VADVB1 ( $U, \cdot$ ) set array FVBD1 for  $U$ .

VADVB1 ( $W, 0$ ) set array FVBD1 for  $W$ .

time integration of  $U$  inside the domain

if (swcmp=0) then (AE)

$U^{it+1} \leftarrow P^{it}, ADVU$

else if (swcmp=1) then (E-HI-VI-PI)

$U^{it+1} \leftarrow \Delta^2 P, ADVU$

end if

time smoothing of  $U$  by applying Assellin's time filter.

ORUCPH --- estimate the phase speed of  $U$  at the open boundary following  
Orlanski (see B-7-2 b))

input:  $U^{it-1}, U^{it}, U^{it+1}$

output: array CPHU

EXTNRU --- time integration of  $U$  outside the boundary plane normal to  
 $U$ -component (see B-7-2 b)).

input: DUDTBC,  $U^{it}, U^{it-1}, EXTU$

output:  $U^{it+1}(1, j, k), U^{it+1}(2, j, k), U^{it+1}(nx, i, j)$

EXTRX1A --- time integration of  $U$  outside the boundary plane parallel to  
 $U$ -component (see B-7-2 a)).

input: FVBD1( $u$ ),  $U^{it}, U^{it-1}, EXTU$

output:  $U^{it+1}(i, 1, k), U^{it+1}(i, ny, k),$

set  $U^{it+1}$  outside the upper and lower boundary

output:  $U^{it+1}(i, j, 1), U^{it+1}(i, j, nz),$

ADJ2DM --- adjust the values of  $U$  outside the lateral boundary taking  
account of the cyclic or open lateral boundary conditions

time integration of  $V$  in the similar way to  $U$  except that EXTNRV is called instead of  
EXTNRU.

time integration of  $W$  in the similar way to  $U$ , except that EXTNRU is not called, and  
upper and lower boundary conditions are kinematical conditions, i.e., always  $W^{it+1} =$   
 $-G^{1/2}G^{13}U^{it+1}$

if (swcmp=1) then (E-HI-VI)

time integration of  $P$ ; obtain  $P^{it+1}$  from  $\Delta^2 P$ ; time smoothing

ADJ2DM

end if

return

**D-1-5. Flow chart of sub.SCPI**

Sub.SPAI in mem.SFXHEL is the pressure equation solver.

SCPI

```

SPFORI  --- prepare forcing term  $F$  in Eq. B-(6-1)
SFPBD   --- prepare boundary forcing  $B_x$ ,  $B_y$  and  $B_z$  in Eqs. B-(6-3)—(6-5).
SPAI    --- forward transformation in the  $x$ -direction (operate  $I \otimes P^{-1}$  from
        left)
        --- VHELMX
        --- forward transformation in the  $y$ -direction (operate  $Q^{-1} \otimes I$ 
        from left)
        --- TRIDIG: solve vertical structure Eq. B-(6-24),
                 $C S_{i,j}; = R_{i,j};$ 
                 $C$  is tridiagonal matrix.
        --- backward transformation in the  $y$ -direction.
        (operate  $Q \otimes I$  from left)
        return
        --- backward transformation in the  $x$ -direction (operate  $I \otimes P$  from
        left)
        return
return
    
```

**D-1-6. Flow chart of the subroutine FTVELC**

FTVELC: time integration of  $U$ ,  $V$ ,  $W$  and PRS by E-HE-VI scheme

set arrays PRSF,UF,,WF used for small time step integration

PRSF ← PRS(,,it-1)

UF ← U(,,it-1)

VF ← V(,,it-1)

WF ← W(,,it-1)

PPFORI --- forcing terms on the pressure equation invariant during small time  
 step integration (FP.HE.INV and FPB.HE.INV; see Eqs.B-(4-8)  
 and B-(4-11)) are stored in array PFORCI

small time integration start

do its=1, MSW(9)

small time step integration of  $UF^{\tau+1}$  and  $VF^{\tau+1}$

at the open lateral boundary.

$$\frac{\partial UF}{\partial x} = \frac{\partial VF}{\partial x} = 0 \text{ is imposed, currently.}$$

FPFORV --- forcing terms on the pressure equation variant during small time step integration (FP.HE.VAR and FPB.HE.VAR; see Eqs. B-(4-9) and B-(4-12)) are stored in array PFORCV

VRPOIS --- solve 1-dimensional pressure equation for  $\bar{P}^{\tau\beta}$ .

small time integration of  $WF^{\tau+1}$  and  $PRSF^{\tau+1}$  from  $\bar{P}^{\tau\beta}$ .

WF outside the upper and lower boundaries are set.

end doloop

small time integration end

set arrays PRS,  $U$ ,  $V$ ,  $W$  at  $it + 1$  large time step using PRSF,UF,,WF obtained from small time step integration

PRSF ———→ PRS(,,it+1)

UF ———→ U(,,it+1)

VF ———→ V(,,it+1)

WF ———→ W(,,it+1)

time smoothing of  $U$ ,  $V$ ,  $W$ , PRS

set values of  $U$ ,  $V$  and  $W$  outside the lateral boundary in the same way as AE or E-HI-VI schemes

UADVb1(V,,) set array FUBD1 for  $V$ . At the inflow boundary of  $u$ , FUBD1 is set to be zero.

At the outflow boundary of  $u$ , FUBD1 is set to be non-zero. (see B-7-2 a))

UADVb1(W,,) set array FUBD1 for  $W$ .

VADVb1(U,,) set array FVBD1 for  $U$ .

VADVb1(W,,) set array FVBD1 for  $W$ .

ORUCPH --- estimate the phase speed of  $U$  at the open boundary following Orlandi.

input:  $U^{it-1}$ ,  $U^{it}$ ,  $U^{it+1}$

output: array CPHU (see B-7-2 b))

EXTNRU --- time integration of  $U$  outside the boundary plane normal to  $U$ -  
component.  
input: DUDTBC,  $U^{it}$ ,  $U^{it-1}$ , EXTU  
output:  $U^{it+1}(1, j, k)$ ,  $U^{it+1}(2, j, k)$ ,  $U^{it+1}(nx, i, j)$  (see B-7-2 b))

EXTRX1 --- time integration of  $U$  outside the boundary plane parallel to  $U$ -  
component.  
input: FVBD1( $u$ ),  $U^{it}$ ,  $U^{it-1}$ , EXTU  
output:  $U^{it+1}(i, 1, k)$ ,  $U^{it+1}(i, ny, k)$ , (see B-7-2 a))

ADJ2DM adjust the values of  $U$ ,  $V$ ,  $W$  outside the lateral boundary taking account  
of the cyclic or open lateral boundary conditions

return

#### D-1-7. Flow chart of sub.CPTQVS

##### CPTQVS

if (msw(18)=3) then (dry case)  
    time integration of  $\Theta$  by sub.CPT5

if (msw(18)< 2) then (warm rain and cold rain)  
    CLDPHY: compute all source terms for  $\Theta$ ,  $Q_v, \dots, Q_g$  due to cloud micro-  
    physical processes and store them in array PPT, PQV, ..., PQG.  
    (see B-11)

    time integration of  $Q_v$  by sub.CQS3  
    time integration of  $Q_c$  by sub.CQS3  
    time integration of  $Q_r$  by sub.CQS3

if (msw(18)< 1) then (cold rain)  
    time integration of  $Q_i$  by sub.CQS3  
    time integration of  $Q_s$  by sub.CQS3  
    time integration of  $Q_g$  by sub.CQS3  
    time integration of  $N_i$  by sub.CQS3

if (msw(18)  $\leq$  - 1) then  
    time integration of  $N_s$  by sub.CQS3

if (msw(18)  $\leq$  - 2) then

time integration of  $N_g$  by sub.CQS3

end if

if (msw(18) < 2) then

ADJQV4 --- instantaneous adjustment on  $Qv^{it+1}$ ,  $Qc^{it+1}$ ,  $\Theta^{it+1}$ , condensation of water vapour into cloud water and warming (see B-11-5 a))

time smoothing to  $Qv^{it}$ ,  $Qv^{it}$ ,  $Qcw^{it}$

ADJQV4 --- instantaneous adjustment on  $Qv^{it}$ ,  $Qc^{it}$ ,  $\Theta^{it}$ ; condensation of water vapour into cloud water and warming

set lower and upper boundary values for  $\Theta$  and  $Qv$ .

(MSW(13)=0) no flux of  $\Theta$  and  $Qv$  from the lower boundary

(MSW(13)=1) flux for  $\Theta$  and  $Qv$  from the lower boundary

end if

if (msw(18)  $\leq$  0) then

ADJNUM --- adjustment on  $N_i$  for the fixed  $Q_i$  (see B-11-7)

if (msw(18)  $\leq$  - 2) then

ADJNUM --- adjustment on  $N_s$  for the fixed  $Q_s$

if (msw(18)  $\leq$  - 2) then

ADJNUM --- adjustment on  $N_g$  for the fixed  $Q_g$

end if

return

#### D-1-8. Flow chart of sub.CQS3

CQS3 --- time integration of  $QQ$  with the given production term  $PQQ$  ( $QQ = QV, Qcw \dots Qg > 0$ )

CADVET compute advection term of the flux form

CDIFE3 compute diffusional term (subgrid eddy) (see B-10)

DMPNL compute non-linear damping and 4-th order linear damping (see B-12-1 and B-12-2)

RLDUMP compute Rayleigh friction near the lateral boundary and the upper boundary is not active (see B-12-3 and B-12-4)

time integration of  $QQ$  ( $QQ^{it+1} \leftarrow QQ^{it}, QQ^{it-1}, PQQ$ )

UADVB1(QQ,,) set array FUBD1 for  $QQ$ . At the inflow boundary of  $u$ , FUBD1 is set to be zero.  
At the outflow boundary of  $u$ , FUBD1 is set to be non-zero. (see B-7-2 a))

VADVB1(QQ,,) set array FVBD1 for  $QQ$ . At the inflow boundary of  $u$ , FVBD1 is set to be zero.  
At the outflow boundary of  $u$ , FVBD1 is set to be non-zero, (see B-7-2 a))

EXTRX1 time integration of  $QQ$  at the lateral boundary plane normal to the  $u$ -component using array FUBD1 which is set by sub.UADVB1

EXTRY1 time integration of  $QQ$  at the lateral boundary plane normal to the  $v$ -component, using array FVBD1 which is set by sub.VADVB1.

CHKMN2 check whether  $QQ$  is negative or not, and if positive,  $QQ$  is adjusted to become zero, transferring positive  $QQ$  from adjacent grid points, under the constraint of conservation of  $QQ$ .

TSMOTH apply Asselin's time filter

ADJ2DM adjust the values of  $QQ$  outside the lateral boundary taking account of the cyclic or open lateral boundary conditions

return

## D-2. Specification of system parameters

They are divided into 4 classes, namely, P1, P2, P3 and P4 as below. An example of the parameter list P3 and P4 is shown in Table D-1.

### D-2-1. P1

Specification is made in the usual program. Load module must be renewed for changing these parameters.

ex.  $NX$ ,  $NY$ ,  $NZ$  (The dimension of arrays in the program)

### D-2-2. P2

Specification is made in MAIN.MAIN program which calls the main program SIMAIN.

SWCMP	0	for AE:	PRCMP . . . dummy
	1	for E-HI-VI;	PRCMP1=1 (no other choice)
	2	for E-HE-VI	PRCMP= $\beta$
MSW(1)	0	---	no flux (free-slip) condition of $u$ and $v$ at the lower boundary
	1	---	flux (non-slip) condition of $u$ and $v$ at the lower boundary
MSW(2)	1	---	no other choice
MSW(3)	0	---	no other choice
MSW(4)	2	---	no other choice (related to open outflow condition for non-normal $u, v, w$ )
MSW(5)	2	---	no other choice (related to open outflow condition for $\Theta, QV..$ )
MSW(6)	0	---	dummy
MSW(7)	1	---	no other choice
MSW(8)	0	---	dummy
MSW(9)	$N$	---	$N$ is the number of iteration in solving pressure equation for AE and E-HI-VI schemes. 3 is sufficient for most cases. For E-HE-VI, the number of small time integration during one large time integration, $\Delta\tau = (2\Delta t)/N$
MSW(10)	0	---	3-dimensional mode ( $NY > 1$ is additionally needed)

- MSW(11) 1 --- 2-dimensional mode ( $NY = 1$  is additionally needed)  
 0 --- no other choice
- MSW(12) 0 --- in the presence of a mountain, mountain growing method is activated to reduce the initial shock (see B-13-4 a))  
 1 --- in the presence of a mountain, wind growing method is activated to reduce the initial shock (see B-13-4 b))
- MSW(13) 0 --- no flux condition of  $\Theta$  and  $Qv$  at the lower boundary  
 1 --- flux condition of  $\Theta$  and  $Qv$  at the lower boundary together with MSW(1)=1 (see B-8 and B-10-2)
- MSW(14) -1 --- open in  $x$ -direction and wall in  $y$ -direction; only effective for the 3-dim mode (MSW(10)=0,  $NY > 1$ )  
 0 --- open in both  $x$  and  $y$ -directions; only effective for the 3-dim mode (MSW(10)=0,  $NY > 1$ )  
 1 --- non-cyclic in  $x$ -direction, but cyclic in  $y$ -direction  
 2 --- cyclic in both  $x$  and  $y$ -directions
- MSW(15) 0 --- no other choice
- MSW(16) 0 --- no other choice
- MSW(17) 0 --- dummy
- MSW(18) 2 --- no cloud microphysics . . . dry model  
 1 --- cloud microphysics . . . no ice phase is included; warm rain parameterization  
 0 --- cloud microphysics . . . ice phase is included.  
 --- ( $Qc, Qr; Qi, Qs, Qg; Ni$ ) are predicted.  
 -1 --- cloud microphysics . . . ice phase is included.  
 --- ( $Qc, Qr; Qi, Qs, Qg; Ni, Ns$ ) are predicted.  
 -2 --- cloud microphysics . . . ice phase is included (see B-11).  
 --- ( $Qc, Qr; Qi, Qs, Qg; Ni, Ns, Ng$ ) are predicted.
- MSW(19) 0 --- no other choice

**D-2-3. P3**

Specification is made in the input parameter list, VALINO:

- ITST start time step "it"; for initial start ITST=0  
 ITEND end time step. time integration from it=ITST to ITEND

Table D-1 An example of input parameter list for job step 2 (running the model).

```

I SET NAME E01MI04.JCL.CNTL
IER NAME SNGPLG
//GO.SYABEND DD SYSOUT=A
//GO.SYSIN DD *
S33,4:PG.CNS(*4.0) BIGG=E+5:IACW->G(A=0.2):RS=75
:NCW***8.NO SEED(*100.-8):IDSN*10**0(0.6):H-M(-8C):CTR:MOD
2-DIM.CYCLIC NEW ( 1.0*E-11)
      IIST      ITEND      ITMATU      ISTRMT      ITOUT      ITCHK
      2600      3200      80021      100      1200      1200
valin(1,1) -> DT 4.0 DX 400.0 DY 400.0 DZ 200.0 **ECTURB..CHKMNS.THRESH 0.0
      PTRF      UGRF      PTDIS      PRESRF(MB)** 0.1 10 PERCENT MOIST
      283.15      0.0      1.5      1000.0
      EKMHRF      EKMZRF      EKTHRF      EKEZRF      EKBACK 200
      50.0      50.0      50.0      50.0      10.00
      U TOBISIMA 1989.2.04 15JST
valin(1,1) -> 1 2 4 16 LATERAL BD.DIFFUSION 11
      -13.0 20 30 39 0.0 0.000 1.0
      3.0 21 10.0 10.0 10.0 60 UVWEXT(1) MEAN(O)
      15.0 21 50 60 12.0 0.0 1.0
      13 14 15 16 PTQEXT(1) INFLOW
      0.0
      17 18 19 20 16 NRM,U,V EXT V+(1-RATIO)*VOLD
      0.0
      21 22 23 24 20 RATIOW MSWBW
      5.0
      21 22 23 24 24 SWCMP PRCMP valin(36,1)
      V
valin(1,2) -> 1 2 4 9 VARIABLE DIFFUSION CONST.
      -2.0 14 18 24 0.0 9 NON-L.DIF 20 ASTFC
      0.0 36 60 11 0.0 100.0 0.3
      0.0 13 14 15 16 12 EOVER(CHI-VI)
      0.5
      17 18 19 20 16 EKMHU EKMZU UPPER B.C.
      100.0 100.0
      17 18 19 20 60 EKMHW EKMZW LARGE DIFF.
      100.0 100.0
      21 22 23 24 24 EKMHT EKMZT PREVENT REFLECTIO
      100.0 100.0
      PT
valin(1,3) -> 1 2 4 5 VARIABLE GRID
      -10.15 9 10 16 -9.84 17 INITIAL THERMAL BUBBLE
      0.00 -0.3
      -8.80 20 30 39 -3.60 60 DXL DXL VARIABLE GRID
      400.0 400.0
      -1.35 13 14 15 16 20.0 180.0
      400.0 400.0
      17 18 19 20 60 DYL DYR
      400.0 400.0
      21 22 23 24 60 IY1 IY2
      3.0 133.0
      000.0 21 22 23 24 60 COOLING FOR INITIATING CONV
      -0.0008 4.0
      DRNGRAPHY
valin(1,4) -> 1 2 4 5 CIN valin(36,3)
      1.0000 9 10 16 17 1.0 -1.0
      0.8900 20 30 39 60 IXTST IXTEN
      200.0
      0.22 9 10 11 12 JYTST JYTEN
      4.0
      13 14 15 16 12 XCENT YCENT
      120.0 4.0
      17 18 19 20 60 PWX PWY
      10.00 10.00
      0.0 ZTOP PWDI
      1.0
      QC
valin(1,5) -> 1 2 3 4 8 VARIABLE GRID Z
      5 6 7 8 20.0 200.0
      9 10 11 12 IZL IZU
      5.0 15.0
      13 14 15 16 RLDUMP.IZL RLDUMP.IZU
  
```

```

17      18      19      15.0      35.0
      80RLDUMP X      RLDUMP Z
21      34      36      45      80.0
      50000.0000
      PTGRD      EXP( *R2)
QR      1      2      3      4
valin(1,b) → 5      6      7      10.0      -0.00
      8PTGRD.RAND      PT.RANDOM
      9      10      11      12      WMAX      Z1 INITIAL CONVERGE
      13      14      15      16      X1      X2
      17      18      19      80      PTDIF.LAND      IXB.LS
      21      34      36      45      U.BIAS      V.BIAS
      13.0      -0.0
/*
//
valin(36,b)

```

- 
- ISRTMT results are stored in magnetic tape at the time step 'it' which fulfills  $\text{mod}(\text{it}, \text{ISTRMT})=0$
  - ITOUT results are printed out by line printer at the time step 'it' which fulfills  $\text{mod}(\text{it}, \text{ITOUT})=0$ ; for quick look.
  - DT time step  $\Delta t(\text{sec})$
  - DX grid distance at the central part of the domain in the  $x$ -direction, the unit of which is meter (see D-4).
  - DY grid distance at the central part of the domain in the  $y$ -direction, the unit of which is meter.
  - DZ grid distance at the central part of the domain in the  $z$ -direction, the unit of which is meter.
  - PTBIAS  $\text{PTBIAS}=\Theta_{\text{bias}}$ ;  $\Theta = \theta + \Theta_{\text{bias}}$ ;  $\theta$  is the potential temperature deviation stored in array PT which is actually predicted in the model.
  - PTDIS a parameter which specifies the amplitude of the potential temperature for thermal bubble initiation (see D-7-1).
  - EKBACK the parameter associated with the coefficient for the 4-th order artificial diffusion for damping small scale noises (2 grid noises) (see D-9-2).

#### D-2-4. P4

Specification is made in the input parameter list, VALIN and KZIN. Initial environmental fields and system parameters, such as coefficients of Rayleigh friction are given in the input parameter list as shown in Table D-1.

### D-3. Scheme selection among AE, E-HI-VI and E-HE-VI

The parameter SWCMP=0 --- AE

The parameter SWCMP=1 --- E-HI-VI

The parameter SWCMP=2 --- E-HE-VI

Parameter SWCMP is set in MAIN.MAIN program which calls main program SIMAIN.

## D-4. Size of the domain, grid indexing and variable grid generation

The array size ( $NX, NY, NZ$ ) must be set in the parameter statement of the main program SIMAIN. For the 2-dimensional simulation,  $NY = 1$  must be specified in addition to MSW(10)=1. For the 3-dimensional simulation,  $NY > 1$  must be specified in addition to MSW(10)=0.

In the program, the array index ( $IX, JY, KZ$ ) is used instead of the logical index, such as  $(i, j + 1/2, k)$ . The model adopts the staggered grid system shown in Figs. B-5-1, B-5-2 and B-5-3. Table D-2 shows the correspondence between the logical index and the array index in the program code for various kinds of field variables. The dimension of the array in program is  $(NX, NY, NZ) = (nx, ny, nz)$ . Table D-3 shows the inner grid points and their indexing for various kinds of field variables.

Variable Grid is generated as follows. Let us take the case of  $\Delta x_{i+1/2}$ . As shown in Fig. D-1, the grid distance  $\Delta x_{i+1/2}$ , which is the distance between the grid points  $(i, j, k)$  and  $(i + 1, j, k)$ , is the constant value of  $DX$  at the central part of the domain, *i.e.*,  $\Delta x$  for  $i_l < i < i_r$ .  $\Delta x$  for the two leftmost grid distances, *i.e.*, for  $i = 1/2$  and  $i = 1 + 1/2$  is

Table D-2 Correspondence between the logical index  $(i, j, k)$  and the array index  $(IX, JY, KZ)$  in the program code.

logical index	array index in the program code
$\Theta_{i,j,k}; (P; Qv\dots)$	PT(IX,JY,KZ);
$U_{i+1/2,j,k}$	U(IX+1,JY,KZ);
$V_{i,j+1/2,k}$	V(IX,JY+1,KZ)
$W_{i,j,k+1/2}$	W(IX,JY,KZ)
$W_{i,j,k+1/2}^*$	OMW(IX,JY,KZ)
$\bar{\rho}_{i,j,k}$	DNSRFT(IX,JY,KZ)
$G_{i,j}^{1/2}$	G2(IX,JY)
$1/G_{i,j}^{1/2}$	G2INV(IX,JY)
$\bar{\rho}G_{i,j,k}^{1/2}$	DNSG2(IX,JY,KZ)
$G_{i+1/2,j,k+1/2}^{12}$	G12(IX+1,JY,KZ)
$G_{i,j+1/2,k+1/2}^{13}$	G13(IX,JY+1,KZ)
BUOY $_{i,j,k+1/2}$	BUOY(IX,JY,KZ)
$g/Cs_{k+1/2}^2$	RGRTMN(KZ)

Table D-3 Inner grid points (outer grid points are dummy grids) and their indexing. Array size is indicated by (NX, NY, NZ) in the program code. (see Figs. B-5-2 and B-5-3)

for $P, Qv$ ....	$IXST=2 \leq IX \leq IXEN=NX-1;$ $2 \leq i \leq nx-1;$ $KZST=2 \leq KZ \leq KZEN=NZ-1$ $2 \leq k \leq nz-1$	$JYST=2 \leq JY \leq JYEN=NY-1$ $2 \leq j \leq ny-1$
for $U$ ....	$IXST=2 \leq IX \leq NX;$ $1+1/2 \leq i \leq nx - 1/2$ $KZST=2 \leq KZ \leq KZEN=NZ - 1$ $2 \leq k \leq nz - 1$	$JYST=2 \leq JY \leq JYEN=NY-1$ $2 \leq j \leq ny - 1$
for $V$ ....	$IXST=2 \leq IX \leq IXEN=NX - 1;$ $2 \leq i \leq nx - 1;$ $KZST=2 \leq KZ \leq KZEN=NZ - 1$ $2 \leq k \leq nz - 1$	$JYST=2 \leq JY \leq NY$ $1+1/2 \leq j \leq ny - 1/2$
for $W$ ....	$IXST=2 \leq IX \leq IXEN=NX - 1;$ $2 \leq i \leq nx - 1;$ $1 \leq KZ \leq KZEN=NZ - 1$ $1+1/2 \leq k \leq nz - 1/2$	$JYST=2 \leq JY \leq JYEN=NY - 1$ $2 \leq j \leq ny - 1$

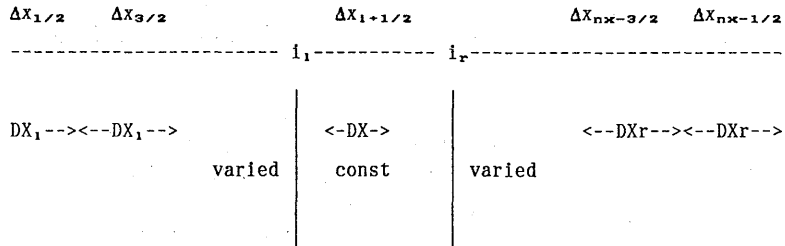


Fig. D-1 Generation of variable grid.

$DX_\ell$ ;  $\Delta x$  for rightmost grid distances, i.e., for  $i = nx - 1/2$  and  $nx - 2/1/2$  is  $DX_r$ . Grid distances  $\Delta x$  for  $3/2 < i + 1/2 < i_\ell$  are linearly dependent on  $i + 1/2$  and between  $DX$  and  $DX_\ell$ . Grid distances  $\Delta x$  for  $i_r < i + 1/2 < nx - 3/2$  are linearly dependent on  $i + 1/2$  and between  $DX$  and  $DX_r$ .

$$\Delta x_{i+1/2} = \frac{DX_\ell - DX}{3/2 - i_\ell} (i + 1/2 - i_\ell) + DX \quad \text{for } 3/2 < i + 1/2 < i_\ell \quad (4-1)$$

$$\Delta x_{i+1/2} = DX \quad \text{for } i_\ell < i + 1/2 < i_r, \quad (4-2)$$

$$\Delta x_{i+1/2} = \frac{DX_r - DX}{nx - 3/2 - i_r} (i + 1/2 - i_r) + DX \quad \text{for } i_r < i + 1/2 < nx - 3/2. \quad (4-3)$$

The grid distance  $\Delta x_i$ , which is the distance between the grid points  $(i - 1/2, j, k)$  and  $(i + 1/2, j, k)$ , is given as

$$\Delta x_1 = 0.5(\Delta x_{1+1/2} + \Delta x_{i-1/2}) \quad (4-4)$$

$\Delta y$  and  $\Delta z$  are determined in a similar way.

Variable grids are generated by sub.VRGDIS. Calling sequence is as follows:

```

sub.VRGDIS ←———— sub.INIVG1      ←———— sub.CVEVSI
              ←———— sub.SFXMAIN2.
    
```

$DX_\ell, DX_r, i_\ell, j_r$  are given in array VALIN (11,3)(12,3)(17,3), (18,3)

$DY_\ell, DY_r, i_\ell, j_r$  are given in array VALIN (23,3)(24,3)(29,3), (30,3)

$DZ_\ell, DZ_r, k_\ell, k_r$  are given in array VALIN (11,5)(12,5)(17,5), (185)

$DX, DY, DZ$  are given in the input parameter list VALINO.

## D-5. Specification of the boundary conditions

### D-5-1. Lateral boundary conditions

First, open or cyclic or wall conditions must be selected.

MSW(14)	-1	----	open in the $x$ -direction and wall in the $y$ -direction
	0	----	open in both the $x$ - and $y$ -directions
	1	----	open in the $x$ -direction, but cyclic in the $y$ -direction
	2	----	cyclic in both $x$ - and $y$ -directions

For the case of open boundary conditions, several parameters must be specified. Near the lateral boundary, a sponge layer can be imposed.

#### a) Open boundary conditions

a-1) For  $\Theta$ ,  $Qv$ ,  $Qc$  .... and velocity components non-normal to the boundary plane (see Fig. B-7-1)

#### i) At the inflow boundary

Boundary values are specified as below.

$$Fb^{it+1} = \mu F.\text{ext} + (1 + \mu) Fb^{it-1} \quad \text{B-(7-1)}$$

$Fb$ : the value just outside the boundary

$F.\text{ext}$ : external value specified from outside

$\mu$  for  $U$ ,  $V$  or  $W$  is set in array VALIN(11,1).

$\mu$  for  $\Theta$ ,  $Qv$  is set in array VALIN(17,1).

The array FUBD is set to be zero by sub.UADVBI at the inflow boundary.

$F.\text{ext}$  is set in arrays EXTU, EXTV, EXT $\Theta$ , EXTQV.

#### ii) At the outflow boundary

If the left boundary ( $i = 3/2$ ) is the outflow boundary, boundary values are extrapolated from the values of the inner domain as below:

$$F_b^{it+1} = 2F_{b+1}^{it} - F_{b+2}^{it-1} \quad \text{B-(7-2)}$$

For the right boundary case, boundary values are extrapolated in a similar way.

The array FUBD is set to be non-zero by sub.UADVBI at the outflow boundary.

$F_b$  is computed subs. EXTRX1, EXTRY1 with input array FUBD.

a-2) Velocity components normal to the boundary plane

For simplicity, one dimensional case shown in Fig. B-7-2 is considered. First, the phase speed,  $Cp^*$  of waves at the boundary is estimated. Next, it is determined whether the waves are outgoing or incoming from the sign of the phase speed.

In the case of an incoming case, *i.e.*,

at the left boundary (at  $i = JS$ ),  $Cp^* \geq 0$  or

at the right boundary (at  $i = JM$ ),  $Cp^* \leq 0$ ,

the time tendency of  $U$  at the boundary, DUDTBC, is computed in order to restore the boundary value to the external value,  $U.ext$ , to a certain degree as follows:

$$DUDTB \equiv \left( \frac{\partial U}{\partial t} \right) = [\mu U.ext + (1 - \mu)U^{it-1} - U^{it-1}] / 2\Delta t. \quad B-(7-11c)$$

Note that  $\mu = 1$  makes  $U^{it+1}$  at the boundary equal to  $U.ext$ .  $\mu$  is specified in the input parameter list VALIN(23,1).

b) Sponge layer

Rayleigh damping near the lateral boundary is imposed to prevent the false reflection of internal gravity waves from the lateral boundary, enforce the environmental external conditions (designated by  $f.exp$  below) and suppress the noises.

$$D_{r\ell}(f) = -\frac{1}{2m_{r\ell}\Delta t} \left( 1 + \cos \left( \frac{\pi(LX - x)}{x_d} \right) \right) (f - f.ext) \quad \left. \vphantom{D_{r\ell}(f)} \right\} \quad B-(7-23)$$

for  $x > LX - x_d$ .

$$D_{r\ell}(f) = -\frac{1}{2m_{r\ell}\Delta t} \left( 1 + \cos \left( \frac{\pi x}{x_d} \right) \right) (f - f.ext) \quad \left. \vphantom{D_{r\ell}(f)} \right\} \quad B-(7-24)$$

for  $x < x_d$ .

See sub.RLDMP1 in mem.CVTDIF1 for more detail.  $x_d$  is set in array VALIN(6,1). Relaxation time constant  $m_{r\ell}$  is set in array VALIN(29,5).

**D-5-2. Lower boundary conditions**

No-flux or lux conditions must be selected.

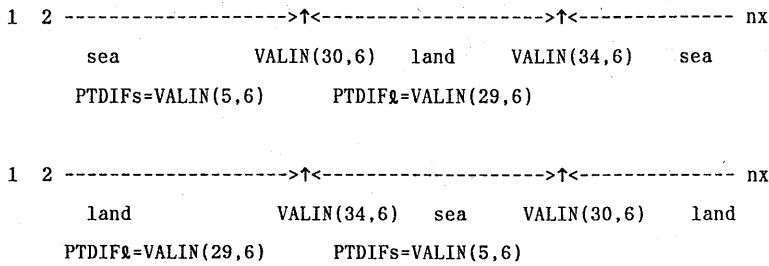


Fig. D-2 Specification of the sea or land surface.

MSW(13) 0 --- no flux condition of  $\Theta$  and  $Qv$  at the lower boundary

MSW(13) 1 --- flux condition of  $\Theta$  and  $Qv$  at the lower boundary together with  
MSW(1)=1

For the surface condition, land surface or sea surface can be specified as shown in Fig.D-2. If  $VALIN(34, 6) > VALIN(30, 6)$ , the region  $VALIN(30, 6) < IX < VALIN(34, 6)$  is assumed to be the land surface, and the remaining region is assumed to be the sea surface. If  $VALIN(34,6) < VALIN(30,6)$ , the region  $VALIN(34,6) < IX < VALIN(30, 6)$  is assumed to be the sea surface, and the remaining region is assumed to be the land surface.

Land surface potential temperature =  $\Theta_{bias} + \Theta_{init}(KZ = 1) + VALIN(5, 6)$

Sea surface potential temperature =  $\Theta_{bias} + \Theta_{init}(KZ = 1) + VALIN(29, 6)$

The surface mixing ratio of water vapour is given by the saturation mixing ratio corresponding to the surface temperature.

$QVGRD(IX, JY) = QVSATU(IX, JY) \dots$ saturation mixing ratio

In case of the land surface, surface friction  $z^*$  must be specified in the program, sub.CRSTUV in mem.CVTURBXXZ. The relative translation speed of the numerical model frame to the earth surface (Galilean transformation) is specified as

$$U^* = UGRND = \bar{p} \times VALIN(35, 6),$$

$$V^* = VGRND = \bar{p} \times VALIN(36, 6),$$

In the program, the velocity component of air relative to the model frame in the  $x$  direction,  $U = U - U^*$ , is stored in the array  $U$ , and this is predicted. The velocity component of air relative to the model frame in the  $y$  direction,  $V' = V - V^*$ , is stored in the array  $V$ , and this is predicted.

See sub.GENPTD in mem.CVTINIT for more detail.

### D-5-3. Upper boundary conditions

The parameters for the upper absorption layer must be specified. Rayleigh damping near the upper boundary is imposed in order to prevent the false reflection of internal gravity waves from the upper rigid wall.

$$D_{ru}(f) = -\frac{1}{m_{ru}\Delta t} \left( 1 - \cos \left( \frac{\pi(LZ - z)}{LZ - z_d} \right) \right) (f - f.\text{ext}) \quad \text{B-(9-6)}$$

for  $z > z_d$ ,

where  $LZ$  is the height of the domain.

See sub.RLDMP1 in mem.CVTDIF1 for more detail.  $z_d$  is set in array VALIN(23, 5). Relaxation constant  $m_{ru}$  is set in array VALIN(30, 5).

## D-6. Specification of initial environmental fields

They are specified by the pair of arrays, KZIN and VALIN for  $U$ ,  $V$ ,  $\Theta$ , and  $Qv$ .

KZIN( $m+4(n-1)$ , kind) . . . integer indicates  $k$ , the vertical location, for the  
 ( $m \leq 4$ ) variable denoted by "kind".

VALIN( $m+6(n-1)$ , kind) . . . real number indicates the initial value at the vertical  
 ( $m \leq 4$ ) grid point denoted by KZIN ( $m+4(n-1)$ , kind), for  
 the variable denoted by kind

kind=1 ....  $u$  (m/s) not  $\bar{\rho}G^{1/2}u$

kind=2 ....  $v$  (m/s) not  $\bar{\rho}G^{1/2}v$

kind=3 ....  $\Theta - \Theta_{\text{bias}}$

kind=4 .... relative humidity  $Qv/Qvsw$

The values between the two vertical grid points in KZIN are obtained by linear interpolation as

$$F(., k) = \frac{\text{VALIN}(m+1,.) - \text{VALIN}(m,.)}{\text{KZIN}(m+1,.) - \text{KZIN}(m,.)} (k - \text{KZIN}(m,.) + \text{VALIN}(m,.) \quad (6-1)$$

Horizontal wind velocity components  $u$  and  $v$  specified in the input list are the speed of air relative to the numerical model frame, and not relative to the ground surface. The translation speed of the model frame to the ground surface can be specified by VALIN(35, 6) in the  $x$ -direction and by VALIN(36, 6) in the  $y$  direction. Horizontal velocity components  $u$  and  $v$  are converted to  $\bar{\rho}G^{1/2}u$  and  $\bar{\rho}G^{1/2}v$  by sub.UCVDNU and stored in arrays U and V, respectively.

The mixing ratio of water vapor is computed from relative humidity and stored in the array QV.

See sub.INIFLD, INIVAL in mem.CVTINIT.

## D-7. Initiation method of convection

Currently, two kinds of initiation methods are implemented. One, thermal bubble initiation, and the other, cold dome initiation.

### D-7-1. Thermal bubble initiation

Warm perturbation in the  $\Theta$  field is given at the initial time such as:

$$\Theta = \text{PTDIS} \sin(f(k)) \exp(\text{VALIN}(6, 3) \times R^2) \quad (7-1)$$

$$R^2 = (i - i_c)^2 + (j + j_c)^2,$$

where  $i_c$  and  $j_c$  (integer index) are the center position of the horizontal domain. PTDIS is given in the input parameter list VALIN0. Functional form of  $f(k)$  is given in sub.GENPTD in mem.CVTINIT.

### D-7-2. Cold dome initiation

Artificial cooling, SRC. $\Theta$ , is added to form a cold dome in the lower part of the atmosphere in sub.CPTQV.

$$\text{SRC}.\Theta(\text{cooling}) = \exp(-(k-3)) \text{VALIN}(32, 3) \exp\left(-\left(\frac{i - \text{VALIN}(33, 3)}{\text{VALIN}(34, 3)}\right)^2\right) \quad (7-2)$$

for  $k < 7$  and  $0 \leq i \leq \text{VALIN}(31, 3)$ .

## D-8. Generation of mountain shape and metric tensors

Mountain shape is specified by input parameters. After mountain shape is determined, metric tensors such as  $G^{1/2}$ ,  $G^{12}$ ,  $G^{13}$  are computed. As an initial start-up procedure in the presence of mountains, two methods, *i.e.*, mountain growing method (with specification of MSW(12)=0) and wind growing method (with specification of MSW(12)=1) are implemented to reduce the initial noises (see B-13-4).

Mountain shape function is stored in array ZS which is generated by sub.SETZS which is called from sub.ORGIN0. Input parameters for the specification of the bell shaped mountain is as follows:

$$Z_s(i, j) = \frac{a^2 b^2 h}{(a^2 + (i - i_m)^2)(b^2 + (j - j_m)^2)} \quad (8-1)$$

$h$ . . .	mountain height (meter).....	VALIN(35, 4)
$i_m$ . .	integer indexing grid point in the $x$ -direction	VALIN(23, 4)
$j_m$ . .	integer indexing grid point in the $y$ -direction	VALIN(24, 4)
$a$ . . .	half width in the $x$ -direction; integer	VALIN(29, 4)
$b$ . . .	half width in the $x$ -direction; integer	VALIN(30, 4)

Metric tensors such as  $G^{1/2}$ ,  $G^{12}$ ,  $G^{13}$  are generated after  $Z_s$  is generated in sub.ORGIN0.

## D-9. Specification of computational diffusion

Artificial computational diffusion is added to suppress computational noises and to overcome some problems near the upper and lateral boundaries.

### D-9-1. Nonlinear damping $Dn$

$$Dn(f) = \frac{DX^3}{8m_n\Delta t|\Delta f|} \frac{\partial}{\partial x} \left( \left| \frac{\partial}{\partial x} \right| \frac{\partial}{\partial x} \right) + \frac{DZ^3}{8m_n\Delta t|\Delta f|} \frac{\partial}{\partial z} \left( \left| \frac{\partial(f-f.ext)}{\partial z} \right| \frac{\partial(f-f.ext)}{\partial z} \right), \quad B-(12-1)$$

where  $f.ext$  denotes the horizontally averaged value of initial  $f$ .

See. sub.DMPCN in mem.CVTDFIH for more detail. Relation time constant,  $m_n$ , is set in VALIN(5, 2).  $\Delta f$  must be set in the program (e.g., 2m/s for  $U$ ,  $V$  and  $W$ ; 1K for  $\Theta$ , 0.001kg/kg for  $Qv$ ,  $Qc$ ,  $Qs...$ )

### D-9-2. Fourth-order linear damping

For suppressing mainly 2 grid noises, the damping is given as

$$D_{4\ell}(f) = \frac{DX^4EKH(k)EKMXF(i)}{16m_{4\ell}\Delta t} \frac{\partial^4 f}{\partial x^4} \quad B-(12-2)$$

See DMPCN in mem.CVTDFIH for more detail. The relaxation coefficient,  $m_{4\ell}$ , is given in VALINO.EKBACK in the input parameter list.

- a)  $EKH(KZ)$  is determined from VALINO.EKMZ and VALIN(17, 2) in the input parameter list as follows:

$$\left. \begin{array}{l} \text{for } KZ < 0.7NZ \\ EKH(KZ) = EKMZ \\ \\ \text{for } KZ > 0.7NZ \\ EKH(KZ) = \frac{(KZ - 0.72NZ)(EKMHU - EKMZ)}{0.3NZ} + EKMZ \end{array} \right\} \quad (9-1)$$

b) EKMXF(IX) is specified from the input parameter list VALIN as follows:

for  $IX < VALIN(6, 1)$

$$EKMXF(IX) = (1 + VALIN(5, 1) * VALIN(6, 1)) \frac{VALIN(6, 1) - IX}{VALIN(6, 1)} + 1$$

for  $IX > NX + 1 - VALIN(6, 1)$

$$EKMXF(IX) = (1 + VALIN(5, 1) * VALIN(6, 1)) \frac{VALIN(6, 1) - NX + IX - 1}{VALIN(6, 1) - 1} + 1$$

(9-2)

### D-9-3. Rayleigh damping near the upper boundary

This dampint is imposed in order to prevent the false reflection of internal gravity waves from the upper rigid wall.

$$D_{ru}(f) = -\frac{1}{2m_{ru}\Delta t} \left( 1 + \cos \left( \frac{\pi(LZ - z)}{Lx - z_d} \right) \right) (f - f.ext) \quad B-(12-3)$$

for  $z > z_d$ .

Here,  $LZ$  is the height of the model domain.

See sub.RLDMP1 in mem.CVTDIF1.  $z_d$  is set in the input parameter list VALIn(23,5). Relaxation constant  $m_{ru}$  is set in the input parameter list VALIN(30, 5).

### D-9-4. Rayleigh damping near the lateral boundary

This damping is imposed in order to prevent the false reflection of internal gravity waves from the lateral boundry, enforce the environmental external conditions and suppress the noises.

$$D_{r1}(f) = -\frac{1}{2m_{r1}\Delta t} \left( + \cos \left( \frac{\pi(LX - x)}{x_d} \right) \right) (f - f.ext) \quad B-(12-4)$$

for  $x > LX - x_d$ .

$$D_{r1}(f) = -\frac{1}{2m_{r1}\Delta t} \left( 1 + \cos \left( \frac{\pi x}{x_d} \right) \right) (f - f.ext)$$

for  $x < x_d$ .

Here,  $LX$  is the width of the model domain.

See sub.RLDMPPI in mem.CVTDFIH for more detail.  $x_d$  is set in the input parameter list VALIN(6, 1). Relaxation constant  $m_{r\ell}$  is set in the input parameter list VALIN(29, 5).

#### D-9-5. Damping in the time integration schemes

i) Asselin's time filter

$$f(it) = f^*(it) + 0.5\nu(f^*(it+1) - 2f^*(it) + f(it-1)) \quad \text{B-(12-5)}$$

$\nu$  is given in the input parameter list VALIN(6, 2).

ii)  $\alpha$  parameter used in E-HI-VI scheme (Eq. B-(3-4))

$\alpha$  is set in the input parameter list VALIN(17, 2).

iii)  $\beta$  and  $\gamma$  parameters used in E-HE-VI scheme (Eqs. B-(4-4) and B-(4-5))

$\beta$  and  $\gamma$  are set by  $\beta=\text{PRCMP}$  in MAIN.MAIN and  $\gamma=\text{VALIN}(18, 2)$ .

## D-10. Store of the results and restart

ITST        start time step 'it'; for initial start ITST=0  
ITEND       end time step (time integration from it=ITST to it=ITEND)  
ISTRMT      results are stored in magnetic tape at 'it' which fulfills mod(it,  
              ISTRMT)=0.

## **E. Plot of the model results**

## E-1. Format of the stored results in magnetic tape

i) First record.

System constants, such as NX, NY, NZ, DX,, VALIN,KZIN are stored. For the detailed format, see sub.STMTC1 in mem.CVTIOS (see Table E-1).

Table E-1 Program list of sub "STMTC1".

```

          STMTC1          SOURCE LISTING          90-11-02   08:44:15
ISN  SOURCE STATEMENT
C
C
1      SUBROUTINE STMTC1( MT, JTIME,MES)
2      COMMON /CON1/ CP, RDVCP, CV, RD, RV, CVDVCP, HLATNT,
1      TKELVN
3      COMMON /CON2/ REARTH, G , OMEGA, FCORI
4      COMMON /CON3/ PAI1, PAI2
5      COMMON /CONGRD/ NX,NY,NZ, IXMAX, IXST, IXEN, JYMAX, JYST, JYEN, KZMAX,
1      KZST, KZEN, NKX, NKY
6      COMMON /PAR2/ CSTBL(64)
7      COMMON /PAR4/ IT, RDX, RDY, RDZ, RDX2, RDY2, RDZ2, EKBACK, RKMKH
8      COMMON /PAR1/ DT,DX,DY,DZ, PTRF , PRESRF,
1      EKMHRF, EKMZRF, EKTHRF, EKTZRF, UGRF , PTDIS
C
9      COMMON /PAR6/ KZIN(24,6), VALIN(36,6)
10     COMMON /PAR7/VRDX(514),VRDX2(514),VRDY(514),VRDY2(514),VRDZ(514),
1      VRDZ2(514),MSWSYS(20)
11     COMMON /PAR1N/ RESERV(26)
12     DIMENSION DTC(12),ICON(14)
13     EQUIVALENCE( DTC(1),DT),(ICON(1),NX)
14     DIMENSION MES(20,3)
C
15 8000 CONTINUE
16     REWIND MT
17     WRITE(MT) JTIME,
1      DT,DX,DY,DZ, PTRF , PRESRF,
2      EKMHRF, EKMZRF, EKTHRF, EKTZRF, UGRF , PTDIS
3      , NX,NY,NZ, IXMAX, IXST, IXEN, JYMAX, JYST, JYEN, KZMAX,
4      KZST, KZEN, NKX, NKY ,
5      RDX, RDY, RDZ, RDX2, RDY2, RDZ2, EKBACK, RKMKH
6      ,KZIN , VALIN, MES
7      , VRDX , VRDX2 , VRDY , VRDY2 , VRDZ ,
8      VRDZ2 , MSWSYS, ISTRMT, ICHMT, RESERV
18     RETURN
C
19     ENTRY STMTC2( MT, JTIME, MES, ISTRMT, ICHMT)
20     GO TO 8000
C
21     ENTRY LOADC2( MT ,MES, ISTRMT, ICHMT)
22     REWIND MT
23     READ(MT) JTIME,
1      DT,DX,DY,DZ, PTRF , PRESRF,
2      EKMHRF, EKMZRF, EKTHRF, EKTZRF, UGRF , PTDIS
3      , NX,NY,NZ, IXMAX, IXST, IXEN, JYMAX, JYST, JYEN, KZMAX,
4      KZST, KZEN, NKX, NKY ,
5      RDX, RDY, RDZ, RDX2, RDY2, RDZ2, EKBACK, RKMKH
6      ,KZIN , VALIN, MES

```

```

7      , VRDX      , VRDX2      , VRDY      , VRDY2      , VRDZ      ,
8      VRDZ2      , MSWSYS, ISTRMT, ICHMT, RESERV
24     RETURN
      END

```

ii) Second, Third... and N-th record

Results of numerical simulation at the time step of  $(N-1) \times \text{ISTRMT}$  are stored. For the detailed format, see sub.STRMNG in mem.CVTIONG. (see Table E-2).

Table E-2 Program list of sub "STRMNG".

```

          STRMNG          SOURCE LISTING          90-11-02   08:44:15
ISN  SOURCE STATEMENT
C-----
C-----
1     SUBROUTINE STRMNG( U, V, W, PT, PAI,PRECIP,SMQS,SMQH,
      1         QV, QC, QR, ETURB,EDDYCO,
CCI  2     VPCOND,RNEVAP,QCI,QS,QH,RSTVW ,
      2     QCI,QS,QH, PQV,PQCW,PQR,PQCI,PQS,PQH,
      3     ZS, G2, PPT, G23, DNSG2,
      3     QNCI,QNS,QNH,PQNCI,PQNS,PQNH,
      4     AS,LAS,BS,LBS, A1,LA1,AW1,LAW1, B1,LB1, TLDATA,TLDTPR,TLDTPC,
      5     IDLIST, ITDT,MT ,ITSTR )
2     COMMON/CONGR1/JYSTM1,JYENP1,JYMPX1,JYMPX2,JYTD,JYTST,JYTEN,
      1     JCMAX,NYNY,NYNM2,NYNYP2,JYSTM2,JYENP2,JYTSM1,JYTEP1,
      2     JYTSM2,JYTEP2,JA(8)
3     COMMON /CONGRD/ NX,NY,NZ, IXMAX,IXST,IXEN,JYMAX,JYST,JYEN,KZMAX,
      1     KZST,KZEN,NKX,NKY
4     COMMON /PAR7/VRDX(514),VRDX2(514),VRDY(514),VRDY2(514),VRDZ(514),
      1     VRDZ2(514),MSWSYS(20)
5     DIMENSION TLDATA(NX,NY,NZ,2),TLDTPR(NX,NY,NZ),TLDTPC(NX,NY,NY)
6     DIMENSION KD(28),IDLIST(28)
7     DATA KD/1,2,3,4,5,6,7,8,9,10, 11,12,13,14,15,16,17,18,19,20,
      1     21,22,23,24,25,26,27,28 /
8     DATA KDU,KDV,KDW,KDOMW,KDPT,KDQV,KDQC,KDQR,KDETU,KDEDY,KDPRS,
      1     KD SMRN,KDPREC,KDDNS,KDZS /
      2     201,202,203,204,205,206,207,208,209,210,211,601,602,104,501/
9     DIMENSION U(NX,NY,NZ,2),V(NX,NY,NZ,2),W(NX,NY,NZ,2),
      2     PT(NX,NY,NZ,2),PRECIP(NX,NY),PAI(NX,NY,NZ),QV(NX,NY,NZ,2),
      3     QC(NX,NY,NZ,2), QR(NX,NY,NZ,2),EDDYCO(NX,NY,NZ,2),
      4     QCI(NX,NY,NZ,2),QS(NX,NY,NZ,2),QH(NX,NY,NZ,2),
      5     SMQS(NX,NY),SMQH(NX,NY),
C     6     RSTUV(NX,NY,NZ,2)
      4     ETURB(NX,NY,NZ,2),PQV(NX,NY,NZ),PQCW(NX,NY,NZ),PQR(NX,NY,NZ),
      5     PQCI(NX,NY,NZ),PQS(NX,NY,NZ),PQH(NX,NY,NZ)
10    DIMENSION QNCI(NX,NY,NZ,2),QNS(NX,NY,NZ,2),
      1     PQNCI(NX,NY,NZ),PQNS(NX,NY,NZ ),
      2     QNH(NX,NY,NZ,2),PQNH(NX,NY,NZ )
11    DIMENSION ZS(NX,NY), G2(NX,NY), PPT(NX,NY,NZ),
      1     G23(NX,NY,NZ), DNSG2(NX,NY,NZ)
12    DIMENSION AS(NX,NY,NZ,LAS),BS(NX,NY,LBS),A1(NX,NY,NZ,2,LA1),
      1     B1(NX,NY,LB1)
13    DIMENSION MESD( 8 )
14    DATA MESD / '*I S', 'TRMT', 'I M', 'T=', 'I', 'T= ' /
15    DATA NT /2 /
C

```

```

16      WRITE(6,200) ITDT
17      200 FORMAT( ' *I  STRMT ', I12 )
18      MTOUT=MT
19      IF (ITDT.GT.600) MTOUT=MT+1
20      WRITE(6,100)
21      100 FORMAT( ' *I  STRMTI  ' )
-----
C
C      REWIND MT
22      150 CONTINUE
23      IF (NY.EQ.NYNY) THEN
24      WRITE( MTOUT )ITDT,KD(1), U
25      WRITE( MTOUT )ITDT,KD(2), V
26      WRITE( MTOUT )ITDT,KD(3), W
27      WRITE( MTOUT )ITDT,KD(4), PT
28      WRITE( MTOUT )ITDT,KD(5), QV
29      WRITE( MTOUT )ITDT,KD(6), QC
30      WRITE( MTOUT )ITDT,KD(7), QR
31      WRITE( MTOUT )ITDT,KD(8), ETURB
32      WRITE( MTOUT )ITDT,KD(9), EDDYCO
33      WRITE( MTOUT )ITDT,KD(10), PAI,PRECIP,SMQS,SMQH
CI     WRITE( MTOUT )ITDT,KD(11), RSTUU
34      CI     WRITE( MTOUT )ITDT,KD(11), PQV,PQCW,PPT
CI     WRITE( MTOUT )ITDT,KD(12), RSTVV
35      WRITE( MTOUT )ITDT,KD(12), PQR,PQCI
36      WRITE( MTOUT )ITDT,KD(13), QCI
37      WRITE( MTOUT )ITDT,KD(14), QS
38      WRITE( MTOUT )ITDT,KD(15), QH
39      WRITE( MTOUT )ITDT,KD(16), PQS,PQH
40      WRITE( MTOUT )ITDT,KD(17), DNSG2,ZS
41      WRITE( MTOUT )ITDT,KD(18), QNCI
42      WRITE( MTOUT )ITDT,KD(19), QNS
43      WRITE( MTOUT )ITDT,KD(20), PQNCI,PQNS
44      WRITE( MTOUT )ITDT,KD(21), QNH
45      WRITE( MTOUT )ITDT,KD(22), PQNH,PQNS
C      WRITE( MTOUT )IT, U, V, W, PT, PAI, QV, QC, QR, ETURB,EDDYCO,
C      1 RSTUU,RSTVV,RSTWW,RSTUV,RSTUW,RSTVW
46      ELSE
C      X-Z SLICING MODE
47      KT=1
48      KTN=2
49      CALL TLDRED(TLDATA,NX,NYNY,NZ,NT,1 ,2,1 ,IDLIST,KDU)
C      WRITE( MTOUT )ITDT,KD(17), DNSG2,ZS
50      END IF
51      WRITE(6,951) ITDT,MTOUT
52      951 FORMAT(1H , '*I  STRMTS: DATA ARE STORED. IT,MT==',2I10)
53      ENCODE(12, 955, MESD(6 ) ) MT, ITDT
54      955 FORMAT( I4,I8 )
CCI     CALL DISPLY( 1, 32, MESD )
55      IF (ITDT.LT.600) RETURN
56      IF (ITDT.GT.600) RETURN
57      ENDFILE MTOUT
58      RETURN
END

```

In the magnetic tape designated by FT12.000, the first record and the results whose time step is less than or equal to 600 is stored. To the magnetic tape designated by FT13.000, the results whose time step is greater than 600 are stored.

## E-2. Plot of the ( $x-z$ ; $y-z$ ; $x-y$ ) cross sections at the fixed time

- i) Set (NX, NY, NZ) in the parameter statement of the main program PLPMN to be the same as those of the numerical model whose results you want to plot.
- ii) Determine the size of the plotted picture. Set the parameters which relate the real canvas to virtual canvas.
- iii) Designate the time step, kind of data, contour interval of the plot (integer), cross section, the portion of area.

$x-y$ cross section	1
$x-z$ cross section	2
$y-z$ cross section	3

### Data kind

1 . . u-v	m/s	in vector arrow representation
2 . . u-w	m/s	in vector arrow representation
3 . . v-w	m/s	in vector arrow representation
4 . . PT	0.1K	potential temperature
5 . . QV	0.1g/kg	mixing ratio of water vapor
6 . . QCW	0.1g/kg	mixing ratio of cloud water
7 . . QR	0.1g/kg	mixing ratio of rain
8 . . E.T	joul/m <sup>3</sup>	eddy kinetic energy
9 . . E.C	m <sup>2</sup> /s	eddy diffusional coefficient
10 . . TOT.PRCP	0.1kg/m <sup>3</sup>	total precipitation
11 . . W	cm/s	vertical velocity
12 . . DIV	10 <sup>-4</sup> /s	divergence
13 . . VOR	10 <sup>-4</sup> /s	vorticity
14 . . TILT	10 <sup>-6</sup> /s <sup>2</sup>	tilting term in vorticity equation
15 . . STRC	10 <sup>-6</sup> /s <sup>2</sup>	stretching term in vorticity equation
16 . . PRES	Pascal	pressure
17 . . DPDZ	cm/s <sup>2</sup>	$\partial p / \partial z$
18 . . TQ.BUOY	cm/s <sup>2</sup>	total buoyancy

19 .. DRAG	$10^{-3}\text{m/s}^2$	buoyancy component due to water loading
20 .. DWDT	$\text{cm/s}^2$	$\partial w/\partial t$
21 .. LWC	$0.1\text{g/kg}$	$Qc + Qr$
22 .. EQPT	K	equivalent potential temperature
23 .. EMAGRAM		vertical profiles of horizontally averaged quantities
24 .. EMAG		
25 .. ANU	$\text{m/s}$	$u$ of analytic linear mountain waves
26 .. ANW	$\text{m/s}$	$w$ of analytic linear mountain waves
27 .. ANPT	K	$\Theta$ of analytic linear mountain waves
28 .. ANUW	$\text{m/s}$	$u - w$ of analytic linear mountain waves
29 .. ANP. RESS	Pascal	pressure of analytic linear mountain waves
30 ..		
31 .. PQV	$0.1\text{mg/kg/s}$	total production rate of $Qv$ due to cloud micro-physical processes
32 .. PQR	$0.1\text{mg/kg/s}$	total production rate of $Qr$ due to cloud micro-physical processes
33 .. U	$\text{m/s}$	velocity component in the $x$ -direction
34 .. V	$\text{ms/}$	velocity component in the $y$ -direction
35 .. PRS.BUOY	$\text{cm/s}^2$	
36 .. QCI	$10^{-9}\text{kg/kg}$	mixing ratio of cloud ice
37 .. SNOW	$0.1\text{g/kg}$	mixing ratio of snow
38 .. GRAUPEL	$0.1\text{g/kg}$	mixing ratio of graupel
39 .. PQCW	$0.1\text{mg/kg/s}$	total production rate of $Qc$ due to cloud micro-physical processes
40 .. PQCI	$0.1\text{mg/kg/s}$	total production rate of $Qi$ due to cloud microphysical processes
41 .. PQS	$0.1\text{mg/kg/s}$	total production rate of $Qs$ due to cloud micro-physical processes
42 .. PQG	$0.1\text{mg/kg/s}$	total production rate of $Qg$ due to cloud micro-physical processes
43 .. RH	Percent	relative humidity
44 .. PPT	$10^{-4}\text{K/s}$	total heating rate of $\Theta$ due to cloud microphysical

		processes
45 . . IWC	0.1g/kg	ice water content ( $Q_i + Q_s + Q_g$ )
46 . . LIWC	0.1g/kg	water content ( $Q_c + Q_r + Q_i + Q_s + Q_g$ )
47 . . DBZ	$10 \times \log_{10}(Z)$	radar reflectivity
48 . .		
49 . .		
50 . . PBUOY	0.1Pascl	pressure component due to buoyancy
51 . . PDRAG	0.1Pascl	pressure component due to water loading
52 . . PDYNA	0.1Pascl	pressure component due to dynamical parts
53 . . PDADVU	0.1Pascl	pressure component due to advection terms of $u$
54 . . PDADVW	0.1Pascl	pressure component due to advection terms of $w$
55 . . PRCP <sub>r</sub>	0.1kg/m <sup>2</sup>	accumulated precipitation amount of rain
56 . . PRCP <sub>s</sub>	0.1kg/m <sup>2</sup>	accumulated precipitation amount of snow
57 . . PRCP <sub>g</sub>	0.1kg/m <sup>2</sup>	accumulated precipitation amount of graupel
58 . . Ni	$10 \times \log_{10}(Ni)$	number concentration of cloud ice (m <sup>-3</sup> )
59 . . Ns	$10 \times \log_{10}(Ns)$	number concentration of cloud snow (m <sup>-3</sup> )
60 . . Ng	$10 \times \log_{10}(Ng)$	number concentration of graupel (m <sup>-3</sup> )
61 . . Nos	$10 \times \log_{10}(Nos)$	intercept parameter of size distribution function of snow (m <sup>-4</sup> )
62 . . Nog	$10 \times \log_{10}(Nog)$	intercept parameter of size distribution function of graupel (m <sup>-4</sup> )

For more detail, see the program PLPMN.

The unit of the contour interval for  $f$  is determined in the program by SCLDT and ICONT as follows:

$$\text{"unit of } f\text{"} \times \text{SCLDT} \times \text{ICONT},$$

where unit of  $f$  is the unit used in the numerical model (ex.  $u$  m/s;  $\theta$ , K; pressure, Pascal;  $Q_v$ , kg/kg). For example, SCLDT for  $Q_v$  is 1000.0, and if you set ICONT=2 for  $Q_v$ , the contour is drawn at intervals of 2g/kg.

### E-3. Plot of the $(x-t; y-t; z-t)$ cross sections at the fixed plane

- i) Set  $(NX, NY, NZ)$  in the parameter statement of the main program PLPMN to be the same as those of the numerical model whose results you want to plot.
- ii) Determine the size of the plotted picture. Set the parameters which relate the real canvas to virtual canvas.
- iii) Designate the plane, kind of data, contour interval of the plot (integer), cross section, portion of area.

$x-t$ cross section	1
$y-t$ cross section	2
$z-t$ cross section	3

Data kind                    the same as E-2.

## E-4. An example of input parameter list for the program "PLPMN"

This is shown in Table E-3.

Table E-3 An example of input parameter list for the program "PLPMN".

```

1MI04.JCL.CNTL

//E01MI04 JOB (XXXXXXXXXXXX),NOTIFY=E01MI04,CLASS=B,REGION=9800K,
//*E01MI04 JOB (XXXXXXXXXXXX),NOTIFY=E01MI04,CLASS=F,REGION=4096K,
//      TIME=30
//*JOBPARM PAGELIM=2800
//*FORT EXEC FORTEC, PARM='RDLINK,DCOM,COMARY,OPT(3)',REGION=4096K
//FORT EXEC FORT7CLG, PARM.FORT='SOURCE,OPT(3),NODCOM',
//      PARM.LKED=(MAP,XREF,LIST,LET,ZCLEAR),
//      COND.LKED=(12,LT,FORT),
//      COND.GO=((12,LT,FORT),(12,LT,LKED))
//*FORT EXEC PGM=JMKFORT,
//*      PARM='NOIAP,SOURCE,SYMDBG,SUBCHK,OPT(0)',REGION=512K
//SYSPRINT DD SYSOUT=A,DCB=BLKSIZE=3429
//SYSPUNCH DD DUMMY
//SYSLIN DD DSN=&SYSLIN,DISP=(MOD,PASS),UNIT=VIRT,
//      SPACE=(3120,(300,15)),DCB=BLKSIZE=3120
//SYSUT2 DD DSN=&SYSUT2,UNIT=VIRT,SPACE=(2048,(10,10))
//*FORT.SYSLIB DD DSN=SLIB13.FORT,DISP=SHR
//FORT.SYSLIB DD DSN=SLSFX.FORT,DISP=SHR
//FORT.SYSIN DD *
*STARTC PLPMN
/*
//*GO.SYSLIB DD DSN=SYS1.FORTHLIB,DISP=SHR
//LKED.SYSLIB DD
//      DD
//      DD
//      DD
//      DD
//      DD DSN=SYS1.GPSL.M24.LOAD,DISP=SHR
//      DD DSN=OPL26A.LOAD,DISP=SHR
//      DD DSN=SYS1.SYSLIB.M24.BGSP,DISP=SHR
//      DD DSN=SYS1.TELCMLIB,DISP=SHR
//GO.STEPLIB DD
//      DD DSN=SYS1.GPSL.M24.LOAD,DISP=SHR
//GO.FILE01 DD DSN=SYS1.GPSL.MOJI.TABLE,DISP=SHR
//GO.SYSDBOUT DD SYSOUT=A
//GO.FT11F001 DD DSN='E01MI04.@SNG33',DISP=(SHR,KEEP)
//GO.FT12F001 DD DSN='E01MI04.@SNG34',DISP=(SHR,KEEP)
//GO.FT13F001 DD DUMMY
//GO.FT14F001 DD DUMMY
//GO.FT20F001 DD DSN=@XY.SKT3,UNIT=SHRT,DISP=(SHR,CATLG),
//      DCB=(RECFM=VS,BLKSIZE=488),
//*      DCB=(RECFM=VS,BLKSIZE=488),VOL=SER=MSS550,
//      SPACE=(CYL,(4,4))
//*      SPACE=(CYL,(4,4))
//*FT20F001 DD DUMMY
//*FT31F001 DD SYSIN
//GO.FT06F001 DD SYSOUT=A
//GO.FT32F001 DD SYSOUT=A
//GO.FT34F001 DD DSN=LYRAN.DATA(SFN4),DISP=(SHR,KEEP)
//*GO.FT34F001 DD DUMMY

```

```

//GO.FT31F001 DD *
4   DEVI(2--XY,4--GLASER)(240,50 --200,30) (150,100:100,120)
24000 16000 60 40   CANVAS 180 120 160.80 180.120 150.30.90
3200   TIME SET (220,120---160,100..SFN)
23     DATA KIND EMAGRAM (150.90 ---- 120,70..SFX)
0     INTVAL ( IX ) MEAN
0 0    POSITION (ISECT==JY ) ICROSS.EQ.0 OR ISECT=0
@
2     CHANGE PARAMETER
16    PRESS
    5 1
213   1 26 1 26   IXBW, IXBE; JYBS,JYBN
@
2     DATA KIND U-V
1     DATA KIND U-V
1 3   1 26 1 26   IXBW, IXBE; JYBS,JYBN
@
2     DATA KIND U-V
1     DATA KIND U-V
114  1 26 1 26   IXBW, IXBE; JYBS,JYBN
@
2     DATA KIND U-W
2     DATA KIND U-W
213   1 26 1 26   IXBW, IXBE; JYBS,JYBN
@
4     DATA KIND PT
1 2   1 26 1 26   IXBW, IXBE; JYBS,JYBN
@
4     DATA KIND PT
10    DATA KIND PT
213   1 26 1 26   IXBW, IXBE; JYBS,JYBN
@
4     DATA KIND PT
1 3   1 26 1 26   IXBW, IXBE; JYBS,JYBN
@
11    DATA KIND W
50    contour interval (cm/s)
213   1 26 1 26   IXBW, IXBE; JYBS,JYBN
@
2     DATA KIND W
10    y-z cross section at x=10
213   1 26 1 26   IXBW, IXBE; JYBS,JYBN
@
11    DATA KIND W
50    contour interval (cm/s)
14    x-y cross section at kz=14
213   1 26 1 26   IXBW, IXBE; JYBS,JYBN
@
11    DATA KIND W
50    contour interval (cm/s)
1 3   1 26 1 26   IXBW, IXBE; JYBS,JYBN
6 ← end of input parameters

```

## **F. References**

- Aihara., M. and H. Okamura, 1985: A numerical simulation of the finite-amplitude mountain waves using a meso-scale nonhydrostatic compressible model. *Pap. Met. Geophys.*, **36**, 119–135 (published by the Meteorological Research Institute attached to Japan Meteorological Agency; hereafter JMA).
- Aihara., M. and M. Hirasawa, 1988a: On severe downslope wind due to the mountain wave-induced critical level. *Pap. Met. Geophys.*, **39**, 59–77.
- Akiyama, To., 1956; On the occurrence of the local severe wind “Yamaji”. Part 1. *J. Meteor. Res.*, **8**, 627–641 (in Japanese).
- Asselin, R. A., 1972: Frequency filter for time integration. *Mon. Wea. Rev.*, **100**, 487–490.
- Bacmeister, J. T. and R. T. Pierrehumbert, 1988: On high-drag states of nonlinear stratified flow over an obstacle. *J. Atmos. Sci.*, **45**, 63–80.
- Berry, E., 1967: Cloud droplet growth by collection. *J. Atmos. Sci.*, **92**, 93–104.
- Berry, E. and R. L. Reinhart, 1974: An analysis of cloud drop growth by collection: Part 1 and 2. *J. Atmos. Sci.*, **31**, 1814–1824, 1825–1831.
- Bigg, E. K., 1953: The supercooling of water. *Proc. Phys. Soc. London*, **B66**, 688–694.
- Carpenter, K. M., 1979: An experimental forecast using a non-hydrostatic mesoscale model. *Quart. J. Roy. Met. Soc.*, **105**, 629–655.
- Clark, T., 1977: A small-scale dynamic model using terrain following coordinate transformation. *J. Comp. Phys.*, **24**, 186–215.
- Clark, T. and W. R. Peltier, 1984: Critical level reflection and the resonant growth of nonlinear mountain waves. *J. Atmos. Sci.*, **41**, 3122–3134.
- Clark, T. L. and W. D. Hall, 1988: Multi-domain simulations of the time dependent Navier Stokes equations: error analysis of nesting procedures (manuscript).
- Cotton, W. R., G. J. Tripoli, R. M. Rauber and E. A. Mulvihill 1986: Numerical simulation of the effects of varying ice crystal nucleation rates and aggregation processes on orographic snowfall. *J. Climate Applied Meteor.*, **25**, 1658–1680.
- Cotton, W. R. and R. A. Anthes, 1989: Cloud and storm dynamics (Chapter 4: parameterization or modelling of microphysical processes in clouds). Academic Press, 880pp.
- Cullen, M. J. P., 1990: A test of a semi-implicit integration technique for a fully compressible non-hydrostatic model. *Quart. J. Roy. Met. Soc.*, **116**, 1253–1258.
- Deardorff, J. W., 1980: Stratocumulus-capped mixed layers derived from a three-dimensional model. *Boundary-Layer Met.*, **18**, 495–527.
- Dröegemeier, K. K. and R. B. Wilhelmson, 1985: Three-dimensional numerical modelling of convection produced by interacting thunderstorm outflows. Parts 1 and 2. *J. Atmos. Sci.*, **42**, 2381–2414.
- Durran, D. and J. Klemp, 1983: A compressible model for the simulation of moist mountain waves. *Mon. Wea. Rev.*, **111**, 2341–2361.
- Durran, D. R., 1986: Another look at downslope windstorms. Part 1. *J. Atmos. Sci.*, **43**, 2527–2543.

- Durrán, D. R. and J. B. Klemp, 1987: Another look at downslope windstorms. Part 2. *J. Atmos. Sci.*, **44**, 3402-3412.
- Fletcher, N. H., 1962: Physics of rain clouds. Cambridge University Press, 179pp.
- Furukawa, T., 1966; On the "Yamaji Wind". *Tenki*, **13**, 261-268 (in Japanese).
- Gal-Chen, T. and R. C. J. Somerville, 1975: On the use of a coordinate transform for the solution of the Navier-Stokes equation. *J. Comp. Phys.*, **17**, 209-228.
- Gouda, H. and K. Kurihara, 1991: Development of a nonhydrostatic model. *Technical Report of Numerical Prediction Division, J. M. A.*, Separate Volume 37, 67-82 (in Japanese).
- Griggs, D. J. and T. W. Choullarton, 1986: A laboratory study of secondary ice particle production by the fragmentation of rime and vapour grown ice crystals. *Quart. J. Roy. Met. Soc.*, **112**, 149-163.
- Gunn, K. L. S. and J. S. Marshall, 1958: The distribution with size of aggregate snowflakes. *J. Meteor.*, **15**, 452-461.
- Hallet, J. and S. C. Mossop, 1974: Production of secondary ice particles during the riming process. *Nature*, **249**, 26-28.
- Harimaya, T. and M. Sato, 1989: Measurement of the riming amount on snowflakes. *J. Fac. Sci., Hokkaido Univ.*, Ser. VII (Geophysics), Vol. 8, 355-366.
- Harimaya, T., 1976: The embryo and formation of graupel. *J. Met. Soc. Japan*, **54**, 42-51.
- Harimaya, T., 1978: Observation of size distribution of graupel and snow flake. *J. Fac. Sci., Hokkaido Univ.*, Ser. VII (geophysics), Vol. 5, 67-77.
- Horibata, Y., 1986: On the stability of the finite difference scheme employed in a rainstorm simulation. *J. Japan Society of Simulation Technology*, **5**, 97-101 (in Japanese).
- Horibata, Y., 1987: Study of a finite difference scheme employed in a rainstorm simulation. Its stability and conservative property. *J. Japan Society of Simulation Technology*, **6**, 90-100 (in Japanese).
- Huffman, P. J. and G. Vali, 1973: The effect of vapor depletion on ice nucleus measurements with membrane filters. *J. Appl. Meteor.*, **12**, 1018-1024.
- Ikawa, M., 1981: The energy conserving scheme of invariant form for the shallow convection. *Pap. Met. Geophys.*, **32**, 65-78.
- Ikawa, M., 1985: Development of convective cloud model, Part 2: Inclusion of orography and 2-dimensional simulation of convective orographic rainfall. Technical Report submitted to the annual meeting of JMA for improvement of forecasting technique, MRI, Forecast Research Department, 16-47 (in Japanese).
- Ikawa, M., H. Sakakibara, M. Ishihara and Z. Yanagisawa, 1987: 2-dimensional simulation of the convective snow band observed over the Japan Sea. —the structure and time evolution of the organized multicellular convection—. *J. Met. Soc. Japan*, **64**, 605-633.
- Ikawa, M., 1988: 2-dimensional simulation of the convective snow band observed over the Japan Sea. Part 2. —Precipitation mechanism of the convective snow band and the effect of the different

- parameterizations of the cloud microphysics on the convective snow band—. *Pap. Met. Geophys.*, **39**, 13–43.
- Ikawa, M., 1988: Comparison of some schemes for nonhydrostatic models with orography. *J. Met. Soc. Japan*, **66**, 753–776.
- Ikawa, M. and Y. Nagasawa, 1989: A numerical study of a dynamically induced foehn observed in the Abashiri-Ohmu area. *J. Met. Soc. Japan*, **67**, 429–458.
- Ikawa, M., 1990a: High-drag states and foehns of a 2-layered stratified fluid past a 2-dimensional mountain. *J. Met. Soc. Japan*, **68**, 163–182.
- Ikawa, M., 1990b: Weakly non-linear aspects of steady hydrostatic mountain waves in a 2-layered stratified fluid of infinite depth over a 2-dimensional mountain. *J. Met. Soc. Japan*, **68**, 357–369.
- Ikawa, M., H. Mizuno, T. Matsuo, M. Murakami, Y. Yamada and K. Saito, 1991: Numerical modeling of the convective snow cloud over the Sea of Japan. —precipitation mechanism and sensitivity to ice nucleation rates—. *J. Met. Soc. Japan*, **69**, 641–667.
- Isono, K., M. Komabayashi, T. Takahashi and T. Tanaka, 1966: A physical study of solid precipitation from convective clouds over the sea: Part 2. *J. Met. Soc. Japan*, **44**, 218–226.
- Kajikawa, M., 1975: Measurement of falling velocity of individual graupel particles. *J. Met. Soc. Japan*, **53**, 476–480.
- Kajikawa, M. and K. Kiba, 1978: Observation of the size distribution of graupel. *Tenki*, **25**, 390–398 (in Japanese).
- Kawamura, T., 1977: The climate of the land-sea breeze. *Investigation report of the atmospheric environment in South Kanto district*, **1**, 46–52 (in Japanese).
- Klemp, J. B. and D. R. Durran, 1983: An upper boundary condition permitting internal gravity wave radiation in numerical mesoscale models. *Mon. Wea. Rev.*, **111**, 430–444.
- Klemp, J. B. and R. B. Wilhelmson, 1978: The simulation of three-dimensional convective storm dynamics. *J. Atmos. Sci.*, **35**, 1070–1096.
- Köenig, L. R., 1971: Numerical modeling of ice deposition. *J. Atmos. Sci.*, **28**, 226–237.
- Kondo, J., 1975: Air-sea bulk transfer coefficients in diabatic conditions. *Boundary-Layer Met.*, **9**, 91–112.
- Konishi, K., T. Endoh and G. Wakahama, 1989: Vertical structure in convective clouds producing graupel and snowflake aggregates. *Proceedings of the NIPR (National Institute of Polar Research) Symposium on Polar Meteorology and Glaciology*, No. 2, 41–47.
- Kurihara, Y., 1965: On the use of implicit and iterative methods for the time integration of the wave equation. *Mon. Wea. Rev.*, **93**, 33–46.
- Lew, J. K., D. C. Montague and H. R. Pruppacher, 1986: A wind tunnel investigation on the riming of snowflakes. Part 1: porous disks and large stellars. *J. Atmos. Sci.*, **43**, 2392–2409.
- Lilly, D. K. and J. B. Klemp, 1979: The effects of terrain shape on non-linear hydrostatic mountain waves. *J. Fluid Mech.*, **95**, 241–261.
- Lin, Y. H., R. D. Farley and H. D. Orville 1983: Bulk parameterization of the snow field in a cloud

- model. *J. Climate and Appl. Meteor.*, 1065–1092.
- Locatteli, J. B. and P. V. Hobbs, 1974: Fall speeds and masses of solid precipitation particles. *J. Geophys. Res.*, **79**, 1914–1932.
- Long, R. R., 1953: Some aspects of the flow of stratified fluids: I. A theoretical investigation. *Tellus*, **5**, 42–58.
- Long, R. R., 1953: Some aspects of the flow of stratified fluids: II. Experiments with a two fluid system. *Tellus*, **6**, 97–115.
- Magono, C. and C. W. Lee, 1973: The vertical structure of snow clouds, as revealed by “Snow Crystal Sondes”, Part 2. *J. Met. Soc. Japan*, **51**, 176–190.
- Matsumoto, S., K. Ninomiya and T. Akiyama, 1967: Cumulus activities in relation to the mesoscale convergence field. *J. Met. Soc. Japan*, **45**, 292–305.
- Matsuo, T., 1986: personal communication.
- Matsuo, T. and H. Mizuno, 1990: personal communication.
- Mizuno, H., 1989: Statistical study on the precipitation characteristics of graupel particles utilizing daily surface observed data at meteorological stations. *Proc. of the spring meeting of Japan Met. Soc.*, **55**, C118 (in Japanese).
- Mizuno, H., 1990a: Parameterization of the accretion process between different precipitation elements. *J. Met. Soc. Japan*, **68**, 395–398.
- Mizuno, H., 1990b: personal communication.
- Mizuno, H. and T. Matsuo, 1990: personal communication.
- Mizuno, H., T. Matsuo, M. Murakami and Y. Yamada, 1990: Characteristics of precipitating particles in the coastal region facing the Sea of Japan when the north-west cold monsoon winds prevails. *Proc. of the spring meeting of Japan Met. Soc.*, **57**, B118 (in Japanese).
- Murakami, M. and T. Matsuo, 1990: Development of the hydrometeor video sonde (HYVIS). *J. Atmos. Ocean Tech.*, **7**, 613–620.
- Murakami, M., H. Mizuno, T. Matsuo and Y. Yamada, 1990: Cloud microphysical structure of convective snow clouds, Part 2: vertical distribution of water content and number concentration of hydrometeors. *Proc. of the spring meeting of Japan Met. Soc.*, **57**, B364 (in Japanese).
- Murakami, M., 1990: Numerical modeling of dynamical and microphysical evolution of an isolated convective cloud—the 19 July 1981 CCOPE cloud—. *J. Met. Soc. Japan*, **68**, 107–128.
- Nakamura, H., 1978: Dynamical effects of mountains on the general circulation of the atmosphere: 1. Development of finite-difference schemes suitable for incorporating mountains. *J. Met. Soc. Japan*, **56**, 317–339.
- Nickerson, E. C., E. Richard, R. Rosset and D. R. Smith, 1986: The numerical simulation of clouds, rain and airflow over the Vosges and Black Forest Mountains: A meso- $\beta$  model with parameterized microphysics. *Mon. Wea. Rev.*, **114**, 398–414.
- Ninomiya, K., 1968: Heat and water budget over the Japan Sea and the Japan Islands in winter season. *J. Met. Soc. Japan*, **46**, 343–372.

- Ogura, M., 1969: A direct method of solving Poisson equation by Dimension Reduction Method. *J. Met. Soc. Japan*, **47**, 319–323.
- Ogura, Y. and N. A. Phillips, 1962: Scale analysis of deep and shallow water convection in the atmosphere. *J. Atmos. Sci.*, **19**, 173–179.
- Orlanski, I., 1976: A simple boundary condition for unbounded hyperbolic flows. *J. Comp. Physics*, **21**, 251–269.
- Passarelli, R. E., 1978: An approximate analytical model of the vapor deposition and aggregation growth of snowflakes. *J. Atmos. Sci.*, **35**, 118–124.
- Peltier, W. R. and T. L. Clark, 1979: The evolution and stability of finite-amplitude mountain waves. Part 2: Surface wave drag and severe downslope windstorms. *J. Atmos. Sci.*, **36**, 1498–1529.
- Pielke, R. A. and C. L. Martin, 1981: The derivation of a terrain-following coordinate system for use in a hydrostatic model. *J. Atmos. Sci.*, **38**, 1707–1713.
- Pielke, R. A., 1984: “Mesoscale meteorological modelling”. Academic Press, 612pp.
- Pierrehumbert, R. T. and B. Wyman, 1985: Upstream effects of mesoscale mountains. *J. Atmos. Sci.*, **42**, 997–1003.
- Pruppacher, H. R. and J. D. Klett, 1978: Microphysics of cloud and precipitation. D. Reidel, 714pp.
- Rutledge, S. A. and P. V. Hobbs, 1984: The mesoscale and microscale structure and organization of clouds and precipitation in midlatitude cyclones. XII: A diagnostic modeling study of precipitation development in narrow cold-frontal rainbands. *J. Atmos. Sci.*, **41**, 2949–2972.
- Saito, K. and M. Ikawa, 1991: A numerical study of the local downslope wind “Yamaji-kaze” in Japan. *J. Met. Soc. Japan*, **69**, 31–56.
- Sakakibara, H., M. Ishihara and Z. Yanagisawa, 1988: Squall line like convective snowbands over the Sea of Japan. *J. Met. Soc. Japan*, **66**, 937–953.
- Simmons, A. J., B. J. Hoskins and D. M. Burridge, 1978: Stability of the semi-implicit method of time integration. *Mon. Wea. Rev.*, **106**, 405–412.
- Smith, R. B., 1980: Linear theory of stratified hydrostatic flow past an isolated mountain. *Tellus*, **32**, 348–364.
- Sommeria, G., 1976: Three-dimensional simulation of turbulent processes in an undisturbed trade wind boundary layer. *J. Atmos. Sci.*, **33**, 216–241.
- Takahashi, T., 1983: A numerical simulation of winter cumulus electrification. Part 1: shallow cloud. *J. Atmos. Sci.*, **40**, 1257–1280.
- Tanguay, M., A. Robert and R. Laprise, 1990: A semi-implicit semi-Lagrangian fully compressible regional forecast model. *Mon. Wea. Rev.*, **118**, 1970–1980.
- Tapp, M. C. and P. W. White, 1976: A non-hydrostatic mesoscale model. *Quart. J. Roy. Met. Soc.*, **102**, 277–296.
- Tatsumi, Y., 1986: A spectral limited area model with time dependent lateral boundary condition and its application to a multilevel primitive equation model. *J. Met. Soc. Japan*, **64**, 637–664.
- Vardiman, L., 1978: The generation of secondary ice particles in clouds by crystal-crystal collision.

*J. Atmos. Sci.*, **35**, 2168-2180.

Yagi, T., H. Uyeda and H. Seino, 1979: Size distribution of snowflakes and graupel particles observed in Nagaoka, Niigata prefecture. *J. Fac. Sci., Hokkaido Univ., Ser. VII (geophysics)*, Vol.6, No.1, 79-92.

Yamada, Y., H. Sakakibara, K. Akaeda, M. Ishihara, Y. Fujiyoshi, K. Tsuboki and S. Sato, 1990: Three-dimensional structure of snow clouds. *Proc. of the spring meeting of Japan Met. Soc.*, **57**, P109 (in Japanese).

Yoshizaki, M., 1988: An explanatory description of the convective cloud model for the simulation of orographic rainfall. (Technical Report, published by Ocean Research Institute, Tokyo University; in Japanese).

Wong, R. K. W. and K. D. Hage, 1983: Comments on terrain-following coordinates and the hydrostatic approximation. *J. Atmos. Sci.*, **40**, 2875-2880.

気象研究所技術報告一覧表

- 第 1 号 バックグラウンド大気汚染の測定法の開発 (地球規模大気汚染特別研究班, 1978)  
Development of Monitoring Techniques for Global Background Air Pollution (MRI Special Research Group on Global Atmospheric Pollution, 1978)
- 第 2 号 主要活火山の地殻変動並びに地熱状態の調査研究 (地震火山研究部, 1979)  
Investigation of Ground Movement and Geothermal State of Main Active Volcanoes in Japan (Seismology and Volcanology Research Division, 1979)
- 第 3 号 筑波研究学園都市に新設された気象観測用鉄塔施設 (花房龍男・藤谷徳之助・伴野登・魚津 博, 1979)  
On the Meteorological Tower and Its Observational System at Tsukuba Science City (T. Hanafusa, T. Fujitani, N. Banno and H. Uozu, 1979)
- 第 4 号 海底地震常時観測システムの開発 (地震火山研究部, 1980)  
Permanent Ocean-Bottom Seismograph Observation System (Seismology and Volcanology Research Division, 1980)
- 第 5 号 本州南方海域水温図——400m (又は 500m) 深と 1000m 深—— (1934-1943 年及び 1954-1980 年) (海洋研究部, 1981)  
Horizontal Distribution of Temperature in 400m (or 500m) and 1000m Depth in Sea South of Honshu, Japan and Western-North Pacific Ocean from 1934 to 1943 and from 1954 to 1980 (Oceanographical Research Division, 1981)
- 第 6 号 成層圏オゾンの破壊につながる大気成分および紫外日射の観測 (高層物理研究部, 1982)  
Observations of the Atmospheric Constituents Related to the Stratospheric Ozone Depletion and the Ultraviolet Radiation (Upper Atmosphere Physics Research Division, 1982)
- 第 7 号 83 型強震形の開発 (地震火山研究部, 1983)  
Strong-Motion Seismograph Model 83 for the Japan Meteorological Agency Network (Seismology and Volcanology Research Division, 1983)
- 第 8 号 大気中における雪片の融解現象に関する研究 (物理気象研究部, 1984)  
The Study of Melting of Snowflakes in the Atmosphere (Physical Meteorology Research Division, 1984)
- 第 9 号 御前崎南方沖における海底水圧観測 (地震火山研究部・海洋研究部, 1984)

- Bottom Pressure Observation South off Omaezaki, Central Honshu (Seismology and Volcanology Research Division and Oceanographical Research Division, 1984)
- 第 10 号 日本付近の低気圧の統計 (予報研究部, 1984)  
Statistics on Cyclones around Japan (Forecast Research Division, 1984)
- 第 11 号 局地風と大気汚染物質の輸送に関する研究 (応用気象研究部, 1984)  
Observations and Numerical Experiments on Local Circulation and Medium-Range Transport of Air Pollutions (Applied Meteorology Research Division, 1984)
- 第 12 号 火山活動監視法に関する研究 (地震火山研究部, 1984)  
Investigation on the Techniques for Volcanic Activity Surveillance (Seismology and Volcanology Research Division, 1984)
- 第 13 号 気象研究所大気大循環モデル-I (MRI・GCM-I) (予報研究部, 1984)  
A Description of the MRI Atmospheric General Circulation Model (The MRI・GCM-I) (Forecast Research Division, 1984)
- 第 14 号 台風の構造の変化と移動に関する研究——台風 7916 の一生—— (台風研究部, 1985)  
A Study on the Changes of the Three-Dimensional Structure and the Movement Speed of the Typhoon through Its Life Time (Typhoon Research Division, 1985)
- 第 15 号 波浪推算モデル MRI と MRI-II の相互比較研究——計算結果図集—— (海洋研究部, 1985)  
An Intercomparison Study between the Wave Models MRI and MRI-II——A Compilation of Results——(Oceanographical Research Division, 1985)
- 第 16 号 地震予知に関する実験的及び理論的研究 (地震火山研究部, 1985)  
Study on Earthquake Prediction by Geophysical Method (Seismology and Volcanology Research Division, 1985)
- 第 17 号 北半球地上月平均気温偏差図 (予報研究部, 1986)  
Maps of Monthly Mean Surface Temperature Anomalies over the Northern Hemisphere for 1891-1981 (Forecast Research Division, 1986)
- 第 18 号 中層大気の研究 (高層物理研究部・気象衛星研究部・予報研究部・地磁気観測所, 1986)  
Studies of the Middle Atmosphere (Upper Atmosphere Physics Research Division, Meteorological Satellite Research Division, Forecast Research Division, MRI and the Magnetic Observatory, 1986)
- 第 19 号 ドップラーレーダによる気象・海象の研究 (気象衛星研究部・台風研究部・予報研究部・応用気象研究部・海洋研究部, 1986)  
Studies on Meteorological and Sea Surface Phenomena by Doppler Radar (Mete-

orological Satellite Research Division, Typhoon Research Division, Forecast Research Division, Applied Meteorology Research Division and Oceanographical Research Division, 1986)

第 20 号 気象研究所対流圏大気大循環モデル (MRI・GCM-I) による 12 年間の積分 (予報研究部, 1986)

Mean Statistics of the Tropospheric MRI・GCM-I based on 12-year Integration (Forecast Research Division, 1986)

第 21 号 宇宙線中間子強度 1983-1986 (高層物理研究部, 1987)

Multi-Directional Cosmic Ray Meson Intensity 1983-1986 (Upper Atmosphere Physics Research Division, 1987)

第 22 号 静止気象衛星「ひまわり」画像の噴火噴煙データにもとづく噴火活動の解析に関する研究 (地震火山研究部, 1987)

Study on Analyses of Volcanic Eruptions based on Eruption Cloud Image Data obtained by the Geostationary Meteorological Satellite (GMS) (Seismology and Volcanology Research Division, 1987)

第 23 号 オホーツク海海洋気候図 (篠原吉雄・四竈信伸, 1988)

Marine Climatological Atlas of the Sea of Okhotsk (Y. Shinohara and N. Shikama, 1988)

第 24 号 海洋大循環モデルを用いた風の応力異常に対する太平洋の応答実験 (海洋研究部, 1989)

Response Experiment of Pacific Ocean to Anomalous Wind Stress with Ocean General Circulation Model (Oceanographical Research Division, 1989)

第 25 号 太平洋における海洋諸要素の季節平均分布 (海洋研究部, 1989)

Seasonal Mean Distribution of Sea Properties in the Pacific (Oceanographical Research Division, 1989)

第 26 号 地震前兆現象のデータベース (地震火山研究部, 1990)

Database of Earthquake Precursors (Seismology and Volcanology Research Division, 1990)

第 27 号 沖縄地方における梅雨期の降水システムの特徴 (台風研究部, 1991)

Characteristics of Precipitation Systems during the Baiu Season in the Okinawa Area (Typhoon Research Division, 1991)

# 気 象 研 究 所

1946 (昭和21) 年 設立

所 長 : 多 田 利 義

予 報 研 究 部	部 長 :	長 谷 川 隆 司
気 候 研 究 部	部 長 :	古 賀 晴 成
台 風 研 究 部	部 長 :	大 塚 伸
物 理 気 象 研 究 部	部 長 :	能 美 武 功
応 用 気 象 研 究 部	部 長 :	理 博 重 原 好 次
気 象 衛 星 ・ 観 測		
シ ス テ ム 観 測 部	部 長 :	田 中 豊 顯
地 震 火 山 研 究 部	部 長 :	理 博 清 野 政 明
海 洋 研 究 部	部 長 :	菊 地 正 武
地 球 化 学 研 究 部	部 長 :	多 田 利 義

## 気 象 研 究 所 技 術 報 告

編 集 委 員 長 : 菊 地 正 武

編 集 委 員 :	三 角 幸 夫	谷 貝 勇	原 昌 弘
	忠 鉢 繁	小 林 隆 久	葦 沢 浩
	伊 藤 秀 美	石 崎 廣	鈴 木 款
事 務 局 :	永 沢 義 嗣	中 島 幸 久	

気象研究所技術報告は、1978(昭和53)年の初刊以来、気象研究所が必要の都度発行する刊行物であり、気象学、海洋学、地震学その他関連の地球科学の分野において気象研究所職員が得た研究成果に関し、技術報告、資料報告および総合報告を掲載する。

気象研究所技術報告の編集は、編集委員会が行う。編集委員会は原稿の掲載の可否を判定する。

本誌に掲載された論文の著作権は気象研究所に帰属する。本誌に掲載された論文を引用する場合は、出所を明示すれば気象研究所の許諾を必要としない。本誌に掲載された論文の全部又は一部を複製、転載、翻訳、あるいはその他に利用する場合は、個人が研究、学習、教育に使用する場合を除き、気象研究所の許諾を得なければならない。

気象研究所技術報告 ISSN 0386-4049

第 28 号

平成 3 年 12 月 25 日 発行

編 集 兼  
発 行 者

気 象 研 究 所

〒305 茨城県つくば市長峰 1-1

TEL. (0298)51-7111

印 刷 所

谷 田 部 印 刷 株 式 会 社

〒305 茨城県つくば市大字谷田部1979-1